



Review Article

A roadmap of MOFs derived porous carbon, oxides, chalcogenides, and phosphides of metals: Synthesis, properties, parameter modulation and their utilization as an electrode for Li/Na/K-ion batteries

Narasimharao Kitchamsetti^{a,b,*}, Jung Sang Cho^{b,**}

^a Department of Electronic Engineering, Institute for Wearable Convergence Electronics, Kyung Hee University, 1732 Deogyong-daero, Giheung-gu, Yongin 17104, Republic of Korea

^b Department of Engineering Chemistry, Chungbuk National University, Chungbuk 361-763, Republic of Korea

ARTICLE INFO

Keywords:

Metal organic frameworks
Porous carbon
Metal oxides
Metal chalcogenides
Metal phosphides
LIBs
SIBs
PIBs

ABSTRACT

Metal-organic frameworks (MOFs) are extensively studied nanomaterials known for their advantageous properties, including good porosity and high surface area. MOFs have garnered significant attention for their role as templates in producing tailored MOF-derived nanomaterials in the realm of energy storage devices. These MOF-derived materials, encompassing metal oxide, porous carbon, and metal oxide@C composites, have exhibited outstanding performance in energy storage devices. While the application of MOFs in deriving phosphides, sulfides and selenides has gained interest, it remains an area with untapped potential. This review provides a comprehensive overview of MOF's evolution from their pristine form to highly functionalized MOF derived composites. Specifically, we delve into present methodologies, challenges, and opportunities for creating MOF derived composites. The distinct advantages of composites derived from MOF are investigated within the context of electrochemical applications, encompassing a range of batteries, involving lithium (Li), sodium (Na), and potassium (K)-ions. In conclusion, the review addresses the existing challenges and outlines the future prospects for MOFs in their journey towards commercialization within the energy storage field.

1. Introduction

In the late 1990s, Professor Omar Yaghi pioneered the development of microporous metal-organic frameworks (MOFs) [1]. These MOFs are self-assembled structures prepared by coordinative bonds involving organic ligands and metal ions (Fig. 1a). Their architecture is characterized by binding organic molecules with metal ions to form alternating layers. This exceptional arrangement provides the distinct structures with governable channels, offering a wide range of functional properties. Consequently, extensive research efforts have been dedicated to MOF synthesis [3–5], as well as the exploration of their diverse properties, structures, and applications [6–8]. Since their initial discovery, MOFs have captured substantial attention within the scientific community (Fig. 1b). Importantly, researchers have extensively investigated various combinations of metal ions and linkers, resulting in the development of MOFs characterized by specific porosity and tailored

properties [8–10]. Among the most renowned structures of MOF, ZIF-7 has attracted considerable interest owing to its substantial surface area, exceptional chemical and thermal stability, distinctive phase transitions, and the fascinating “gate-opening” mechanism, among other remarkable characteristics [11]. ZIF-7 can be readily synthesized using straight forward methods, including microwave synthesis [12] or via the water-in-oil microemulsion approach [13]. Its applicability has highly predictable in membrane technology [14], especially in the processes like CO₂/CH₄ separation [15] and H₂ separation [16]. Another MOF that has been extensively researched is MIL-101, notable for its impressive Langmuir surface area, which can reach up to 5500 m².g^{−1} [17]. This MOF has found utility in various fields, including catalysis, biosensors, drug delivery systems, membranes, and battery technology [18–20]. Given the environmental concerns associated with chromium, researchers have explored several metal analogs of MIL-101, such as vanadium, aluminum, iron, manganese, and titanium, as alternatives [21].

* Correspondence to: N. Kitchamsetti, Department of Electronic Engineering, Institute for Wearable Convergence Electronics, Kyung Hee University, 1732 Deogyong-daero, Giheung-gu, Yongin 17104, Republic of Korea.

** Corresponding author.

E-mail addresses: kitchamsetti.rao@khu.ac.kr (N. Kitchamsetti), jscho@cbnu.ac.kr (J.S. Cho).

<https://doi.org/10.1016/j.est.2024.110947>

Received 14 November 2023; Received in revised form 15 January 2024; Accepted 12 February 2024

Available online 22 February 2024

2352-152X/© 2024 Elsevier Ltd. All rights reserved.

Over the past few decades, MOFs have garnered significant attention for their tailored porous structures and exceptional crystalline properties, particularly in the catalysis and gas storage fields [22]. The utilization of MOFs as initial template to derive nanomaterials has become increasingly prominent, especially in scenarios where pristine MOFs face practical limitations. In recent times, the energy storage field has harnessed MOFs as initial template or precursors to produce metal-based composites or porous carbon (PC) with multifunctional properties [23,24]. These materials have been explored in various energy storage sectors encompassing supercapacitors and batteries [25,26], demonstrating promising features like enhanced material durability, superior rate capability, increased cycle stability, and high specific capacity. Furthermore, the tunability inherent in MOFs make them a valuable resource for crafting electrocatalysts with precisely designed multiscale structures. Such electrocatalysts exhibit remarkable performance in electrochemical activity in terms of durability, selectivity, and stability [27].

In this comprehensive review, our primary attention centers on elucidating the intricate structure-property relationships that emerge during the development of MOF materials. We delve into their transformative journey from MOFs to MOF derived nanomaterials, and their pivotal role in advancing electrochemical energy storage systems as depicted in Fig. 2. Our review takes a holistic approach, encompassing the evolution of MOFs from their inception as single metal core materials to their subsequent progression into binary, ternary metal core, and hybrid materials. Furthermore, we meticulously examine their utilization as precursors for generating a diverse array of MOF-derived nanomaterials. These encompass a spectrum of materials derived from MOFs, including metal oxides, porous carbon, metal oxides@carbon composites, metal chalcogenides, metal phosphides, and metal chalcogenides@carbon composites. Our central discourse revolves prominently around MOF-derived metal compounds emphasizing their pivotal roles in the realm of energy storage systems. This encompasses their applications in batteries involving lithium (Li)-, sodium (Na)-, and potassium (K)-ion batteries. Ultimately, we conclude this review by contemplating the potential and prospects of MOF derived materials in shaping the future of energy storage technologies.

2. Development of MOFs and their derived materials

MOFs have garnered worldwide attention and have distinguished themselves through their diverse array of organic ligands and metal ion cores. The inception of MOF structures can be traced back to pioneering

experimental reports, which initially revolved around copper or cobalt as the central metal ions. Since then, the realm of MOFs has witnessed a remarkable expansion, encompassing well over a thousand distinct variations. As the exploration continued, there arose a pivotal juncture in the evolution of MOFs. This transition involved replacing the central metal core with a repertoire of first-row transition metals, including but not limited to nickel, iron, calcium, zinc, cadmium, magnesium, and barium. These subsequent iterations of MOFs revealed a fascinating propensity—the ease with which their structures could be synthesized and the capacity to impart novel sets of properties and functionalities. Over the years, the trajectory of material development has been nothing short of remarkable. Starting from single-metal cores, the evolution naturally progressed towards the adoption of bi/trimetallic cores as depicted in Fig. 3. This transformative shift allowed for the introduction of binary or ternary combinations of diverse/same metals. Importantly, this expansion didn't compromise the structural integrity of MOFs [28,29]; in fact, it often resulted in enhancements [30]. The synergistic amalgamation of multiple metals within MOFs has yielded remarkable benefits. This includes a reduction in energy barriers in electrocatalysis [31,32], the incorporation of multiple redox-active sites, and the promotion of enhanced conductivity for applications in batteries and supercapacitors [33,34].

Nevertheless, pristine MOFs exhibit inherent limitations, notably poor conductivity, and structural degradation during charge-discharge cycles [35,36]. To circumvent these challenges, innovative strategies have been devised, capitalizing on unique MOF structures. For instance, the adoption of hollow structures has proven effective in enhancing diffusion in catalysts and mass transfer [37,38]. Likewise, oriented structures have demonstrated the ability to promote the creation of superior electrochemically active sites as depicted in Fig. 4 [39,40]. Continual scientific advancements have unveiled MOFs as versatile precursors, capable of giving rise to a diverse array of materials, containing porous carbon, oxides/chalcogenides/phosphides of metals, and more [41,42]. This has not only preserved sophisticated structures but has also imbued them with tailored functional properties. Furthermore, the exploration of hybrid materials and composites has expanded horizons by integrating MOFs with carbon and other materials [43–45], thus propelling the MOF derived nanomaterials development. This portion will delve into the MOFs evolution over the years and their established properties. Key focal points within this section encompass the organic ligands and metal core, the transition from single to multiple cores of metal, oriented and structured MOFs, and hybrid MOF derivatives.

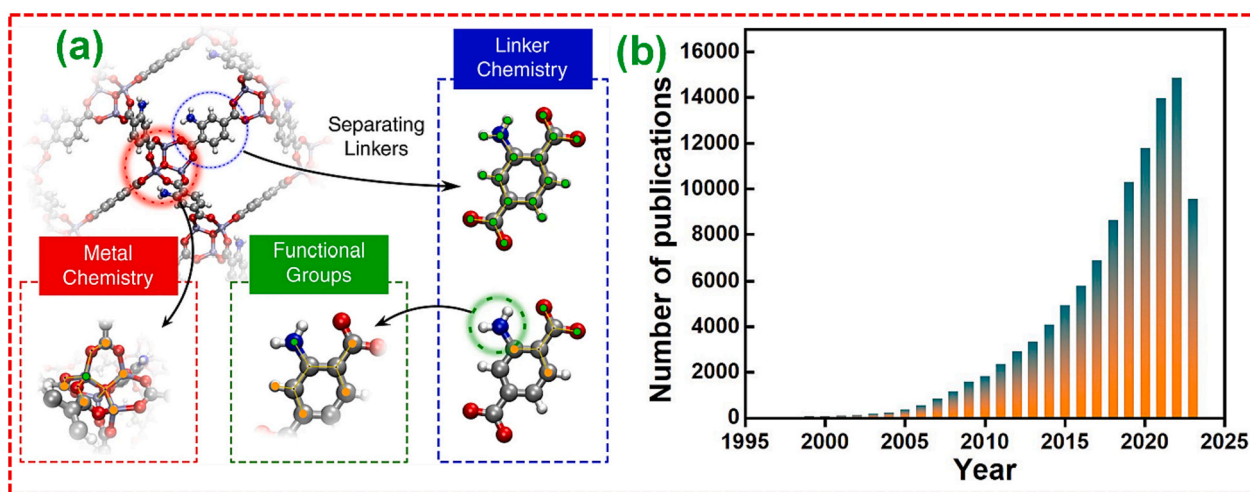


Fig. 1. (a) Illustration of 3 fields of MOF chemistry. Adopted with permission from Ref. [2], Copyright 2020, Springer Nature. (b) The data collected from the web of science by selecting the keyword “Metal-organic framework” (up to September 29, 2023). The publications number of metal-organic frameworks increases every year since 1995.

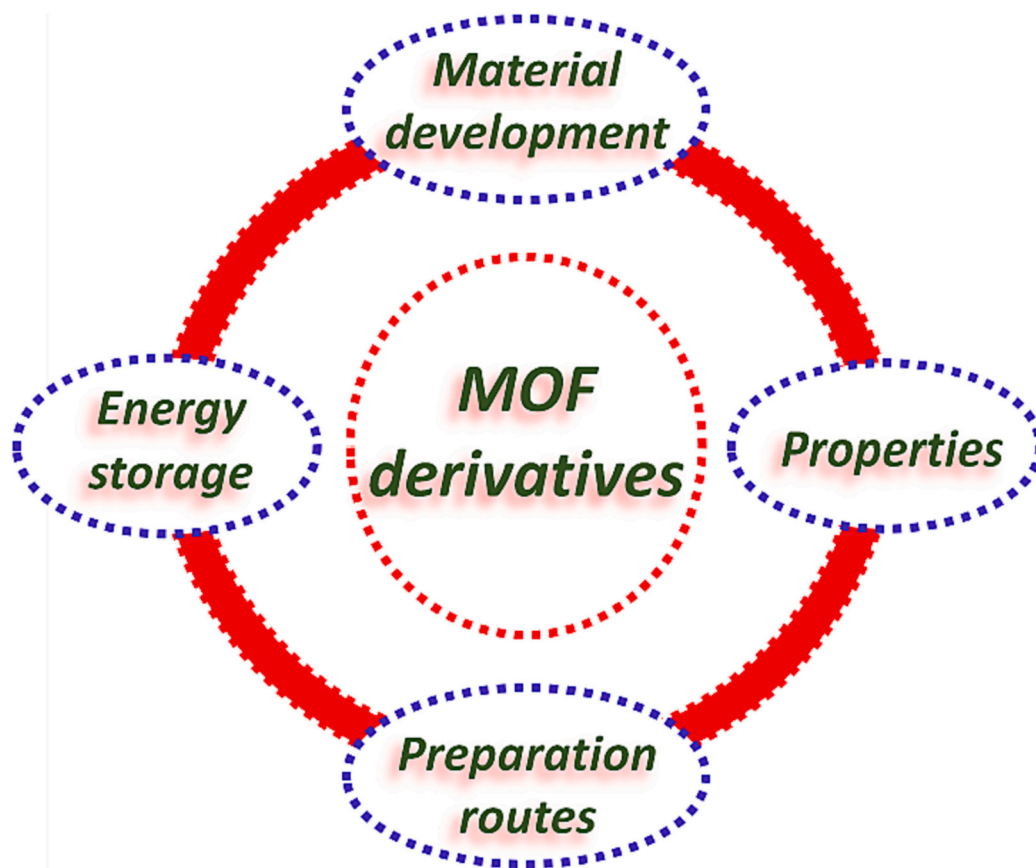


Fig. 2. Schematic outline of the review.

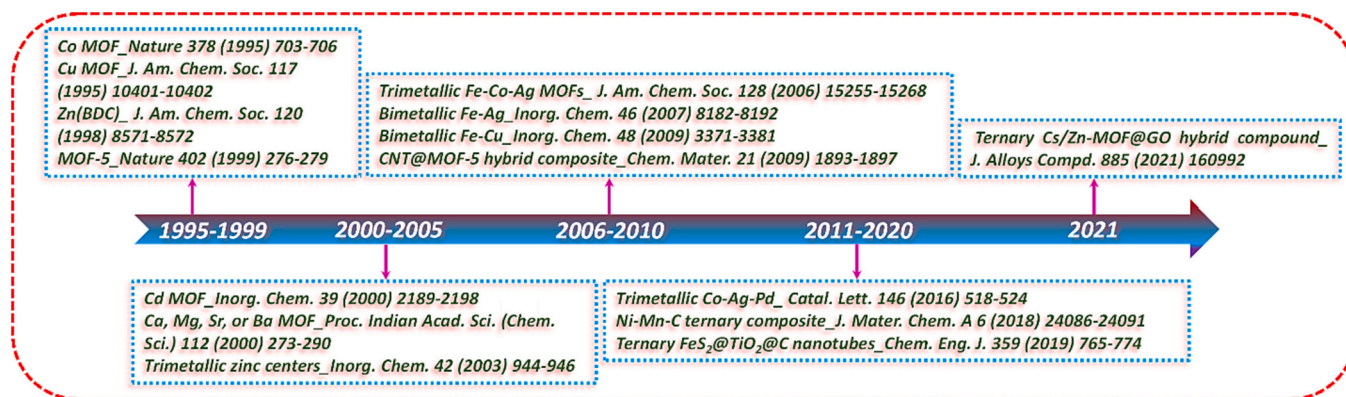


Fig. 3. Progress of the development of MOF with metal cores.

2.1. Metal core and organic ligand

The diverse arrangements of metal ions and organic linkers have unveiled an array of versatile MOF properties. These properties, dependent on the linker utilization, yield varying pore characteristics, ranging from the existence of accessible cages/tunnels to adjustable pores. This diversity significantly impacts the MOFs selectivity and multifunctionality. One exemplary MOF extensively investigated is the family of zeolitic imidazolate frameworks (ZIFs), synthesized using Zn ions and various imidazolate linkers, as illustrated in Fig. 5a [46]. This family has been thoroughly scrutinized by Banerjee et al. [47], who meticulously examined the structures and preparation of 25 distinct ZIFs. Notably, they highlighted the tunability of key parameters such as Langmuir surface area (Fig. 5b) and pore diameter. For instance, ZIF-68

exhibited a pore diameter of 10.2 Å and a Langmuir surface area of 1220 m².g⁻¹, while ZIF-69 featured 7.2 Å and 1070 m².g⁻¹, and ZIF-70 boasted an impressive 15.9 Å and 1970 m².g⁻¹. These tunable characteristics led to various responses in selectivity of gas separation.

Similarly, by varying the metal cores while using the same linker, MOFs have displayed a range of structures and porous characteristics. As depicted in Fig. 6, this variation in metal cores results in distinct topologies, specific pore sizes, and accessible surface areas when terephthalic acid is employed as the linker [48]. Terephthalic acid, with its linear rod-like structure, acts as the linking element between the metal centers, which serve as nodes in the framework.

In terms of ligands, numerous metal centers can be connected, giving rise to a variety of structures based on the number and orientation of their linking sites. This diversity has led to the discovery of various

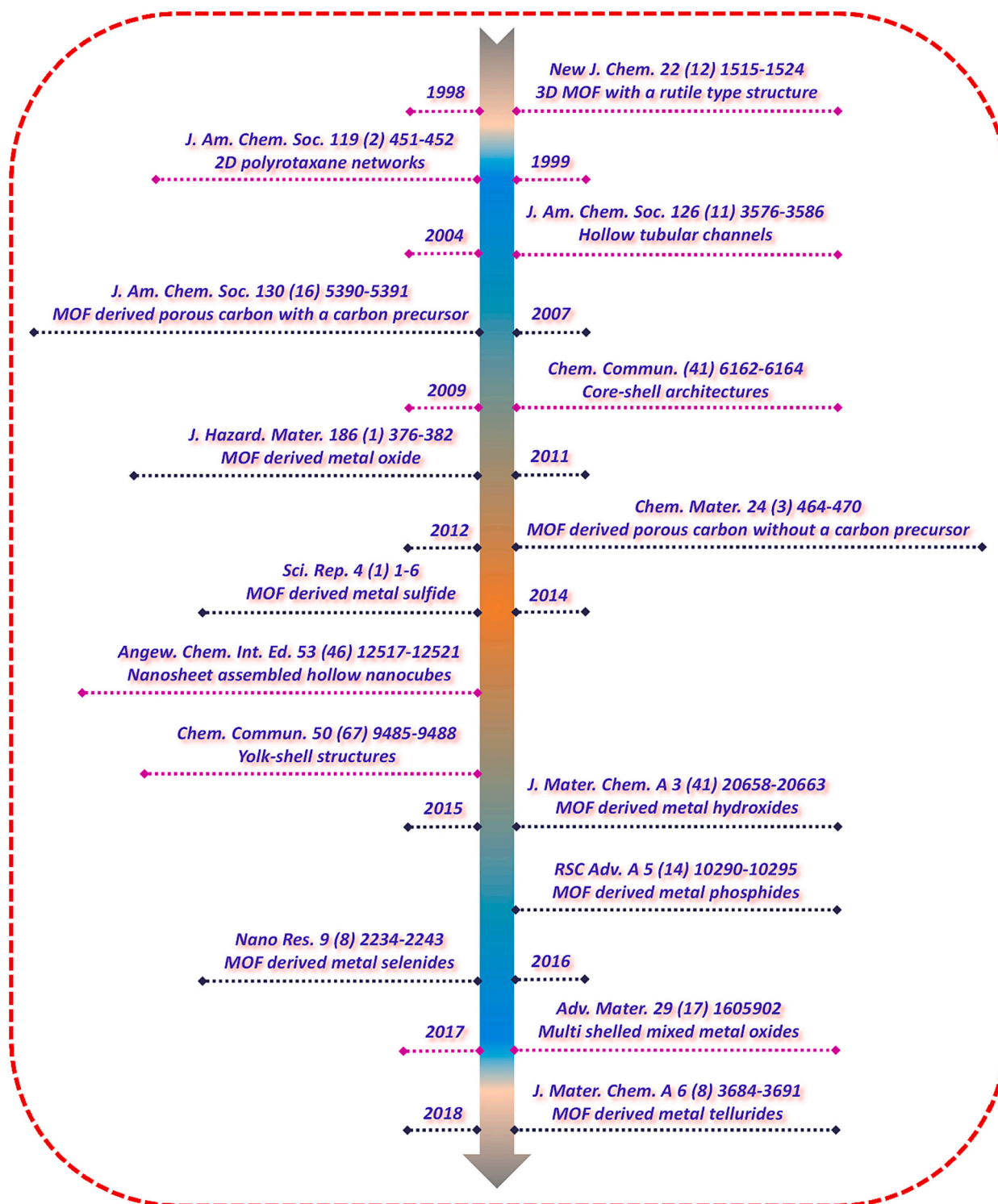


Fig. 4. Progress of MOF development with structures (purple line) and derivatives (dark purple line). (For interpretation of the references to color in this figure legend, the reader is referred to the web version of this article.)

MOFs, as illustrated in Fig. 7. For example, MOF-5 features tetranuclear nodes arranged in an octahedral configuration, resulting in the whole cubic structure. On the other hand, the MIL-101(Cr) comprises trimeric Cr (III) octahedral clusters interconnected by 1,4-benzenedicarboxylate ligands. The 3D structure of MIL-101(Cr) is highly porous, with an impressive BET surface area exceeding $3000 \text{ m}^2 \cdot \text{g}^{-1}$ and large pores measuring 29 and 34°A [50]. The victory in replacing Cr in MIL-101 has paved the way for the exploration of other metal analogs, including

titanium, iron, aluminum, vanadium, scandium, and manganese [51].

2.2. Single to multiple metal core

The adaptability of MOFs in accommodating different metal centers has led to significant advancements in altering their properties and structures for specific applications in materials engineering. MOFs offer a broad variety of advantages ranging from designing material

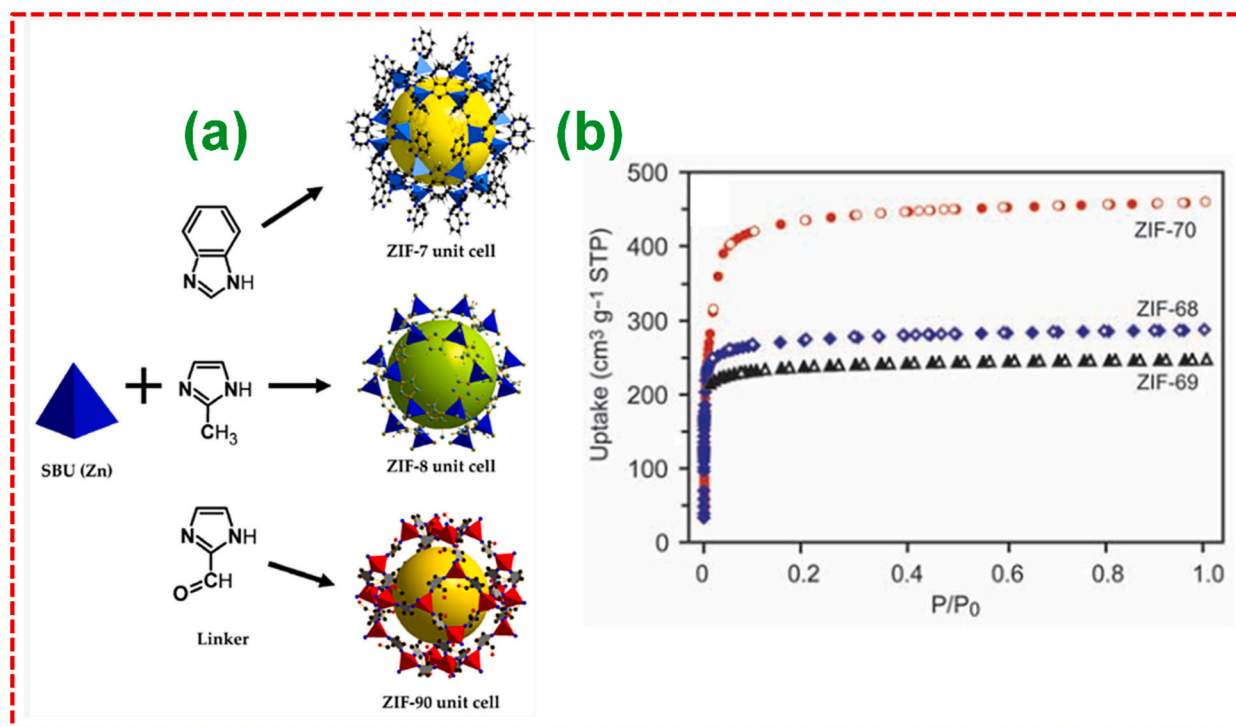


Fig. 5. (a) Preparation of ZIF-7, ZIF-8, and ZIF-90 from imidazolates and a Zn ion. Adopted with permission from Ref. [46], Copyright 2016, MDPI. (b) The N_2 adsorption-desorption study for heterolinked ZIF-68, 69, and 70 at 77 K. Adopted with permission from Ref. [47], Copyright 2008, Science.

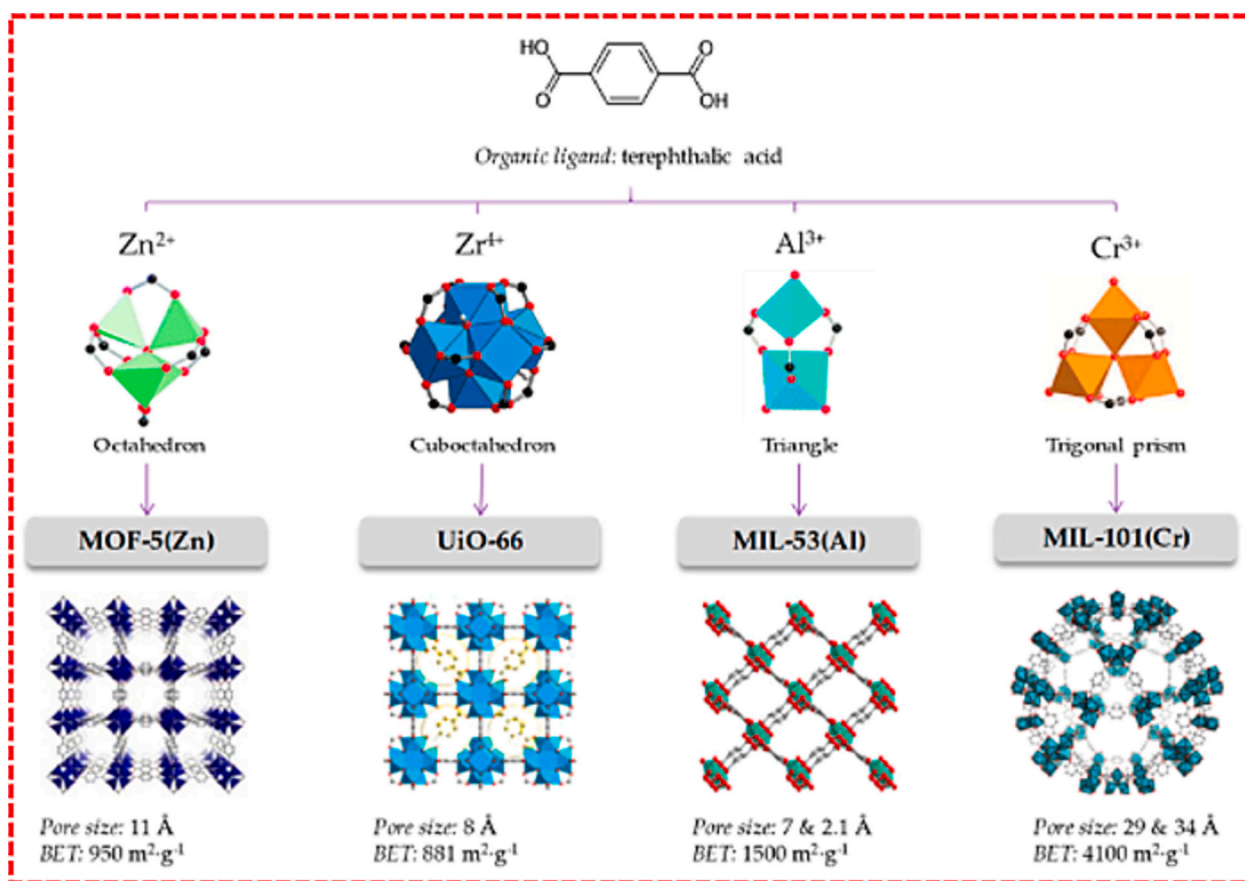


Fig. 6. The careful choice of organic ligand, often linear as in the case of terephthalic acid, and the arrangement of metal clusters determine the desired topology. Each framework topology comes with its unique pore size and surface area. Adopted with permission from Ref. [48], Copyright 2019, MDPI.

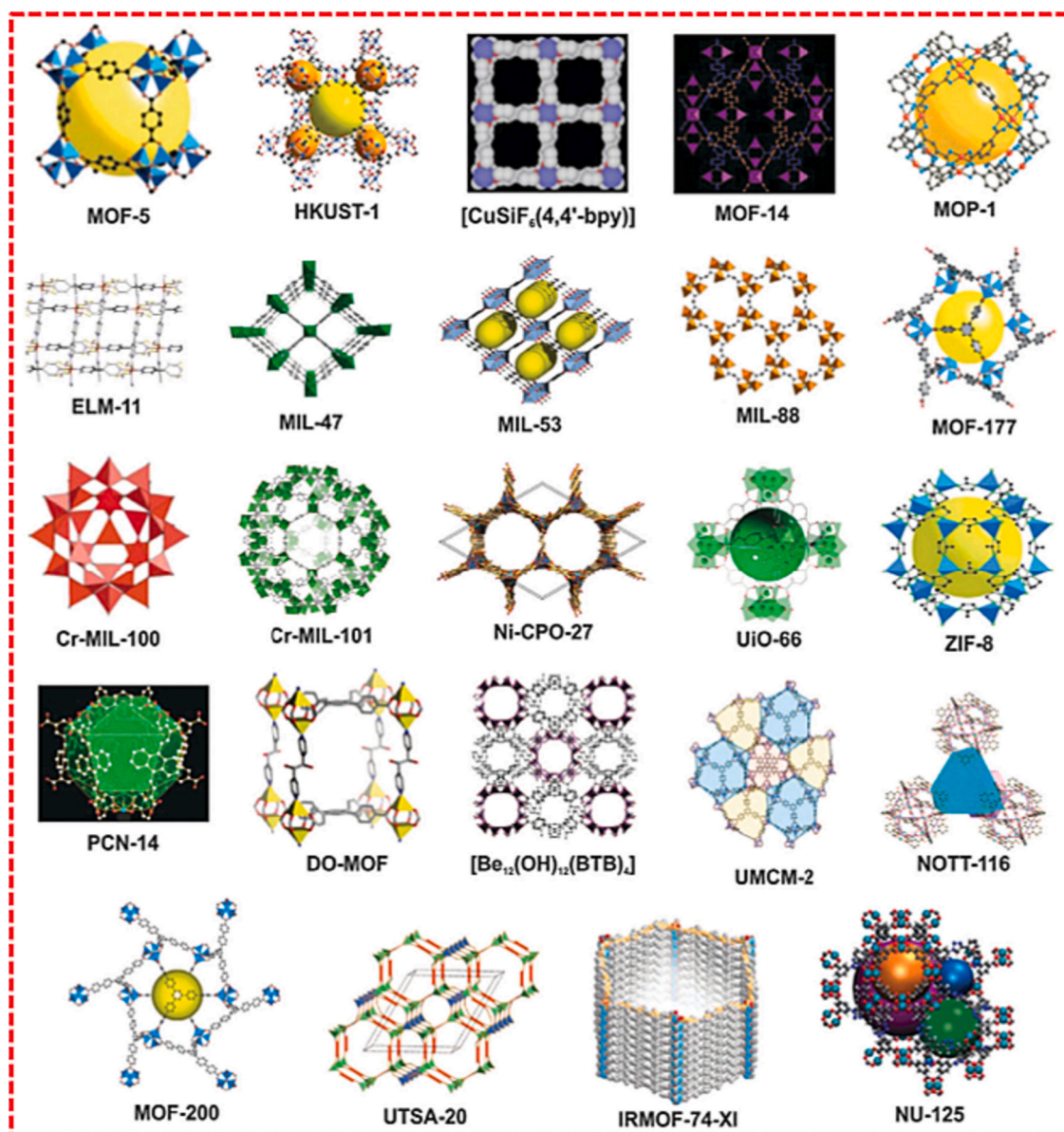


Fig. 7. Various research groups have endeavored to create porous MOFs with the goal of accommodating and retaining chemical species within their channels and pores. Adopted with permission from Ref. [49], Copyright 2015, Royal Society of Chemistry.

structures to imparting important properties for targeted applications. For instance, Gwon et al. [52] investigated the therapeutic potential of hydrogels infused with MOFs containing glutarate and 1,2-bis(4-pyridyl) ethylene linkers. The hydrogel@MOF composites, each incorporating various metal centers within the MOF, exhibited distinct properties, including surface areas and dimensions. Specifically, Cu-MOF 1 featured a 3D structure, Co-MOF 2 had a 2D structure, and Zn-MOF 3 displayed a 3D-type structure formed through hydrogen bonding (Fig. 8a). These structural differences among MOFs with different metal centers performed a crucial task in calculating the released metal ions amount (Fig. 8b). The ions release was estimated in a 0.9 % saline liquid at ambient atmosphere, with the highest release observed for hydrogel@Co-MOF 2, reaching 5.6 ppm after 48 h. Tran et al. [53] synthesized a novel series of isostructural MOFs denoted as M-MOF-184 (Fig. 8c), where M represents different metal centers ($M = \text{Mg, Ni, Co, Zn, Cu, Fe}$) and EDOB^{4-} stands for 4,4'-(ethyne-1,2-diyl)bis(2-oxidobenzoate). Each M-MOF-184 framework, formed with varying central metals ($M = \text{Mg, Co, Ni, Zn}$), exhibited high porosity and available mesopore channels. Additionally, these materials possessed

substantial surface areas ($3200 \text{ m}^2 \cdot \text{g}^{-1}$), with Mg-MOF-184 showcasing the ultimate surface area ($4000 \text{ m}^2 \cdot \text{g}^{-1}$). The catalytic activity of M-MOF-184 was estimated in the cycloaddition of CO_2 (Fig. 8d). Among these, Zn-MOF-184 exhibited exceptional catalytic mechanism, including a high epoxide conversion rate (96 %), yield (82 %), and selectivity (85 %). In an additional investigation [54], three different M-MOF-74 structures, where $M = \text{Zn, Co, and Cu}$ demonstrated a range of properties, containing varying thermal stability ($\text{Cu} < \text{Co} < \text{Zn}$) (Fig. 8e), surface area ($\text{Zn} < \text{Co} < \text{Cu}$) (Fig. 8f), and catalytic action ($\text{Zn} < \text{Co} < \text{Cu}$) (Fig. 8g). There is good agreement on the temperature values at which the different M-MOF-74 decomposition takes place as well as on the shape of the TGA plots and for the linker/residual weight ratio. The thermal stability of any of these samples (decomposition of the less stable Cu-MOF-74 starts above 225°C under air flow) should in principle be enough for being used as catalysts in the conversion of styrene to benzaldehyde under the reaction conditions of this work below 82°C . This ability to tailor the central metal atom in MOFs not only adjusts their structure and porous nature but also results in improved properties tailored for specific advancements.

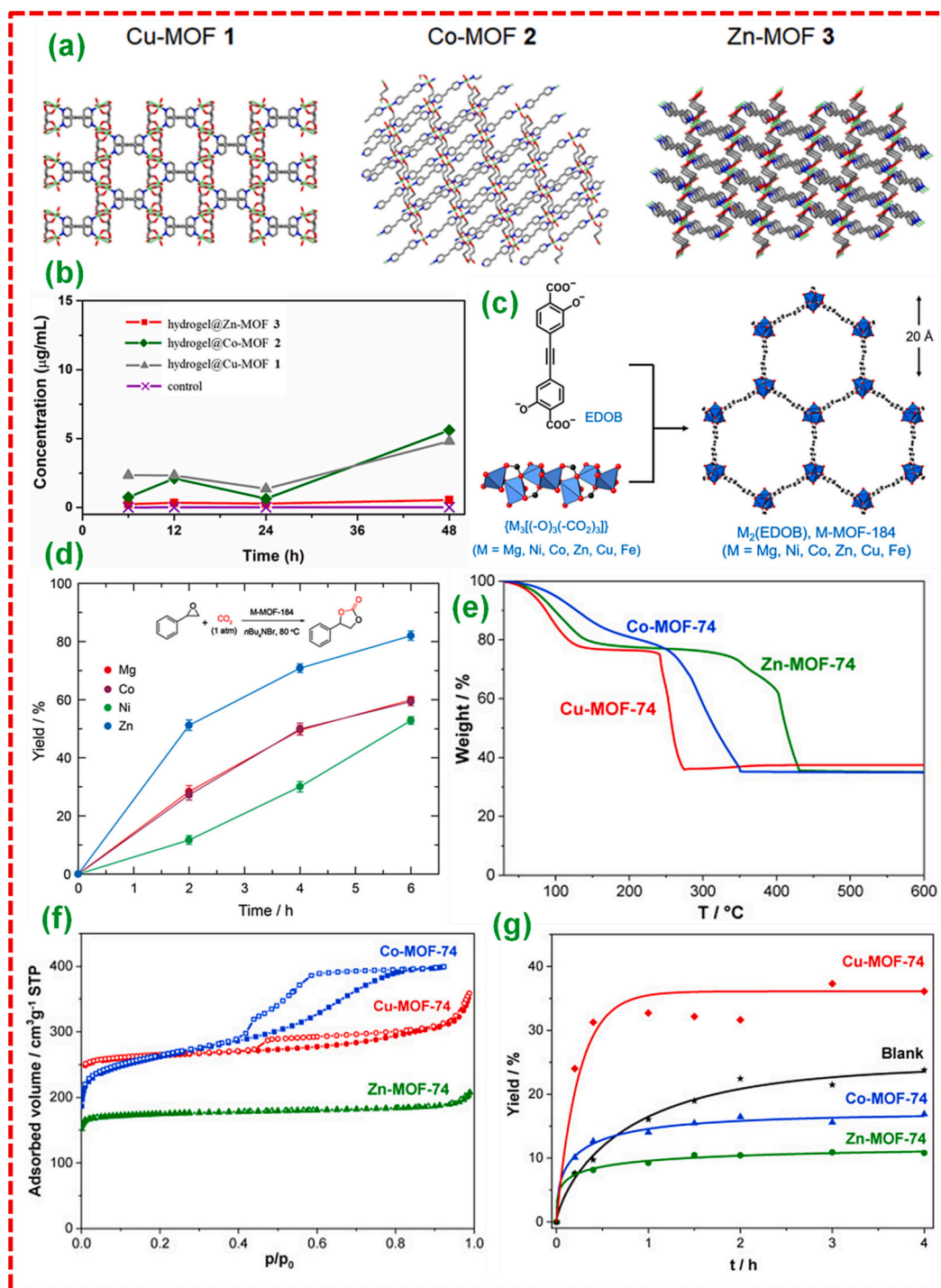


Fig. 8. (a) 3D framework of Cu-MOF 1, the 2D structure of Co-MOF 2, and the hydrogen bonded 3D-like structure of Zn-MOF 3. (b) Concentration of M^{II} released from 1 mg of hydrogel without the MOF and MOF-embedded hydrogels in 1 mL of 0.9 % saline solution. Adopted with permission from Ref. [52], Copyright 2020, American Chemical Society. (c) Crystal structure of M-MOF-184. Infinite, rod-shaped metal clusters, $M_3[(O)_3(-CO_2)_3]_{\infty}$ (where M = Mg, Co, Ni, Zn, Cu, Fe), are joined with EDOB⁴⁻ linkers to form M-MOF-184. (d) Time-dependent yield of styrene carbonate catalyzed by M-MOF-184 (M = Mg, Co, Ni, Zn, Cu, Fe). Adopted with permission from Ref. [53], Copyright 2020, American Chemical Society. (e) TGA plots, (f) N_2 adsorption/desorption study at -196°C of the Co-, Cu- and Zn-MOF-74 products. (g) Kinetics of the yield to benzaldehyde from styrene oxidation for the various M-MOF-74 materials formulated at ambient atmosphere in methanol. Further, a blank investigation without a catalyst is incorporated for evaluation. Adopted with permission from Ref. [54], Copyright 2021, Elsevier B.V.

By restructuring the main metal ion in MOFs, scientists have achieved the preparation of MOFs with a variation of metal centers, allowing the infusion of two or more metals while preserving the overall structural integrity. Two scenarios are possible for the spatial organization of two metals in the framework [55]: initially, two separate metals coexist within the identical secondary building unit (SBU) and

are distributed all over the MOF configuration (Fig. 9a). Next, each SBU contains an identical type of metal, and the two separate SBUs are incorporated within the MOF configuration (Fig. 9b). This enables the uniform arrangement of metals within the porous framework, proposing chances for multifunctionality, and finely tuned properties [56,57]. Heteroatoms at the core of MOFs are able to yield useful hybrid

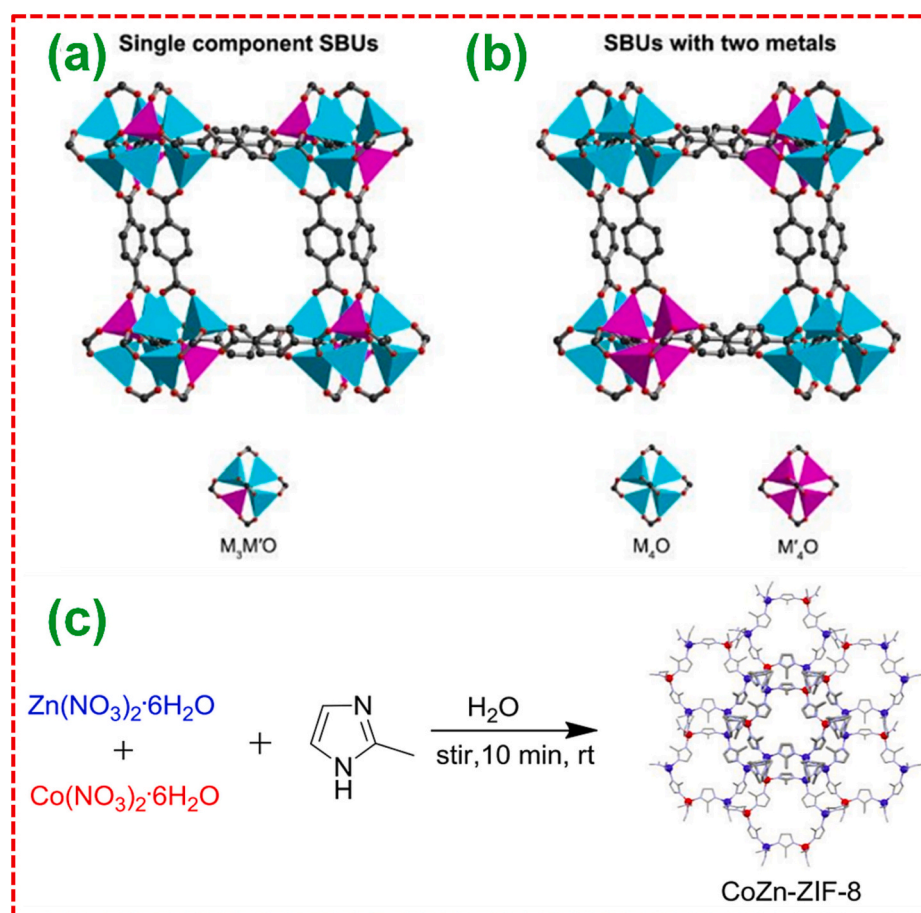


Fig. 9. (a,b) Two spatial assemblies of metals in bimetallic MOFs and their SBUs. Adopted with permission from Ref. [55], Copyright 2020, Royal Society of Chemistry. (c) Schematic representation for the preparation of CoZn-ZIF-8. Adopted with permission from Ref. [59]. Copyright 2016, Royal Society of Chemistry.

properties, containing novel topologies, modified porous structures, improved conductivity, and enhanced redox activity [58]. For instance, Kaur et al. [59] synthesized Co_xZn_{100-x}-ZIF-8 ($x = 0-100$) based ZIFs with changing Co content ($x = 0, 25, 50, 75, 90$, and 100) (Fig. 9c). Surprisingly, no structural alterations were monitored, indicating the effective integration of numerous metals without changing the initial framework. The subsequent Co-substituted ZIF-8 (Co₇₅Zn₂₅-ZIF-8) exhibited an increased surface area, approximately 40 % higher than the Zn-ZIF-8. Notably, by adjusting the Co and Zn precursor contents, the different metal ratios in the CoZn-ZIF-8 led to improved H₂ and CO₂ uptake capacities.

Multiple metals can be introduced into the MOF utilizing various methods, such as employing organic linkers with added metal binding sites (Metallo ligands), post-synthetic ion exchange during single pot production [60,61]. For instance, the connection in chemical valence states and atomic radius between Ni and Co enables the in-situ substitution of metal elements when synthesizing multiple metal MOFs in a single pot preparation [62]. As depicted in Fig. 10a, the amount of metal substitution can be finely tuned by adjusting the primary molar ratio of Ni²⁺ and Co²⁺ without altering the initial MOF's structure (Fig. 10b). The yolk-shell structure of Co-Ni-Fe-type MOFs has demonstrated significant victory in achieving efficient trimetallic integration within the MOF framework (Fig. 10c), leading to improved surface properties and increased electrochemical performance [63]. Other Co/Ni/Fe-type MOFs have revealed effectiveness in applications such as adsorbents [64], electrochemical sensors [65], and electrocatalysts [66–68].

2.3. Hybrid MOF

Hybrid structures in materials engineering are often designed to harness the advantageous properties of a material while mitigating its limitations by initiating a complementary secondary material. This approach aims to combine the strengths of each component. For instance, carbon, known for its large surface area and cycle life but with a low specific capacitance, can be paired with a metal oxide possessing strong redox activity but is electrochemically less stable over extended cycles [69,70]. Similarly, MOFs are frequently integrated with other materials to enhance their properties. These combinations result in hybrid materials like MOF-MOF composites [71–73], MOF-polymer blends [10,74,75], MOF-carbon hybrids [76–78], and more. As an illustration, Fe-Co-Ni MOF was synthesized with a tri-layer structural design using a layer-by-layer (LbL) assembly technique (Fig. 11a, b) [79]. In this controlled electrodeposition process, the Fe-MOF layer was grown initially on Ni foam (NF), followed by the sequential addition of solutions comprising precursors for the second (Co) and third (Ni) layers, all linked together by 2-amino-terephthalic acid connectors. In comparison to the less-ordered mixed metal Fe-Co-Ni MOF synthesized by electrodeposition, the tri-layer Fe-Co-Ni MOF exhibited a highly organized reticular structure. Tailoring catalytically active sites in an LbL fashion affords a highly porous material that exhibits excellent tri-functional electrocatalytic activities towards the hydrogen evolution reaction ($\eta_{j=10} = 116$ mV), oxygen evolution reaction ($\eta_{j=10} = 254$ mV), as well as oxygen reduction reaction (half-wave potential = 0.75 V vs reference hydrogen electrode) in alkaline solutions. The dispersion-corrected DFT calculations suggest that the prominent catalytic activity of the LbL MOF towards the HER, OER, and ORR is due to the initial

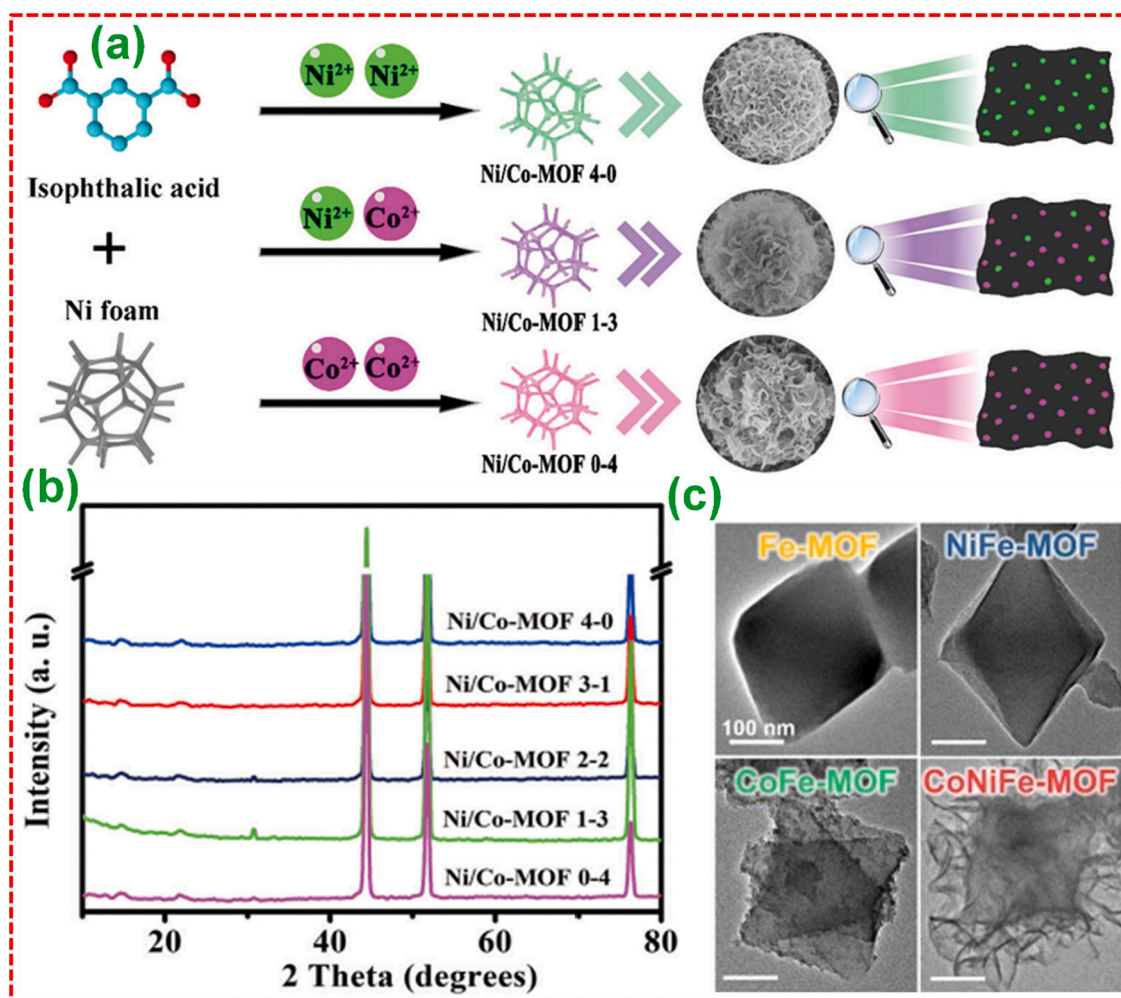


Fig. 10. (a) Schematics of the preparation mechanism and (b) XRD analysis of Ni/Co-MOF with various Ni/Co molar ratios. Adopted with permission from Ref. [62], Copyright 2021, Royal Society of Chemistry. (c) TEM analysis of Fe-MIL-101-NH₂, NiFe/CoFe/CoNiFe-MOFs. Adopted with permission from Ref. [63]. Copyright 2021, Elsevier B.V.

negative adsorption energy of water on the metal nodes and the elongated O—H bond length of the H₂O molecule. The Fe-Co-Ni MOF-based Zn-air battery exhibits a remarkable energy storage performance and excellent cycling stability of over 700 cycles that outperform the commercial noble metal benchmarks. When assembled in an asymmetric device configuration, the activated carbon//Fe-Co-Ni MOF supercapacitor provides a superb specific energy and a power of up to 56.2 W h kg⁻¹ and 42.2 kW kg⁻¹, respectively. This work offers not only a novel approach to prepare an LbL assembled multi-metallic MOF but also provides a benchmark for a multifunctional electrocatalyst for water splitting and Zn-air batteries.

In another investigation, hybrid structures of CNTs@MOF were fabricated by densely packing ZIF-8 MOF onto carbon nanotubes (CNTs) through an in-situ growth process to create hybrids, followed by drying and shrinkage (monolithic densification) at room temperature [80]. When the ZIF-8 content was relatively low (50 wt%), ZIF-8 partially covered the CNTs, leaving noticeable voids and spaces within the 3D CNT network (Fig. 11c). On the other hand, when the ZIF-8 content was increased to 80 wt%, as shown in the SEM image in Fig. 11d, a denser structure with the entire agglomerated monoliths formation was observed. These structures were then altered to allow the infiltration of sulfur (S) through the pores of the MOF hybrids. Remarkably, the S-infiltrated CNTs@ZIF-8 electrode (comprising 50 wt% of ZIF-8 and 40 wt% of S) maintained the higher specific capacity (1480 mAh g⁻¹) than the electrode with a very high ZIF-8 amount (80 wt%) (580 mAh g⁻¹)

(Fig. 11e). This observation underscores the importance of optimizing the carbon-to-MOF ratio for achieving the desired electrochemical performance. MOF-polymer hybrids have also demonstrated excellent processability, making them appropriate for latest protective textiles. Specifically, robust, and flexible MOF-polymer hybrids composed of UiO-66 and UiO-66-NH₂ incorporated with PUU composites (Fig. 11f) were prepared using an electrospinning technique [81]. Fig. 11g showcases the UiO-66-NH₂/PUU electrospun nanofiber (NF) composites covering 20 wt% of MOF. Furthermore, when evaluated against the simulant of a chemical warfare agent, dimethyl-4-nitrophenylphosphate (DMNP), UiO-66 and UiO-66-NH₂ incorporated into mixed matrix membranes with PUU displayed outstanding strength and ductility. The exceptional processability of these hybrid composites, combining MOFs and polymers, for spinning into fibers, along with their high strength and flexibility, positions them as highly promising materials for applications necessitating personal protective equipment (PPE) in countering chemical threats.

2.4. Hierarchical structures of MOF

The wide range of available metal and organic linker precursors has conferred upon MOFs their unique structures and customizable properties. By combining these metal nodes and organic linkers, MOFs display remarkable structural versatility, allowing for the precise design of architectures with controlled features and functional groups. Similar

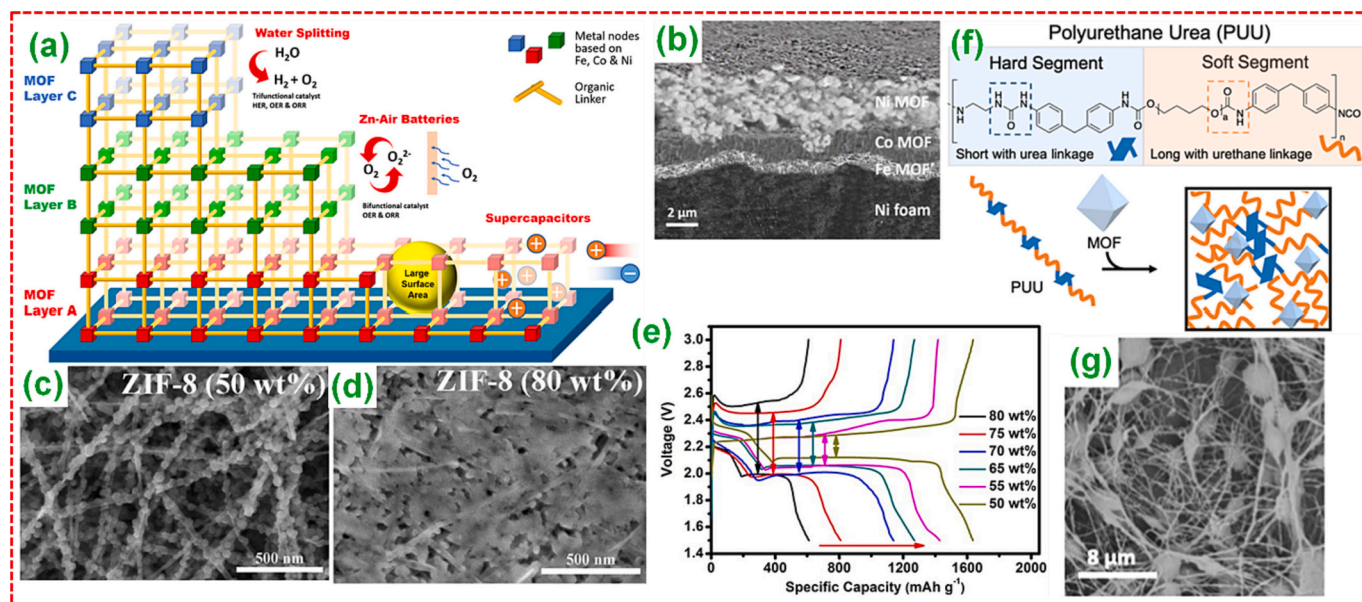


Fig. 11. (a) LbL architectures for the preparation of multi-functional MOFs demonstrating the subsequent deposition of Fe, Co, and Ni MOF layers, (b) side view SEM picture indicating the effective deposition of 3 MOF layers on the NF. Adopted with permission from Ref. [79], Copyright 2022, American Chemical Society. (c, d) SEM analysis of CNTs@ZIF-8 hybrids revealing reliable structure evolution with strengthening MOF amount from 50 to 80 wt%. (e) GCD analysis at 0.2 C rate of the CNTs@ZIF-8 hybrids. Adopted with permission from Ref. [80], Copyright 2019, Royal Society of Chemistry. (f) General overview of the poly (urethane urea) (PUU) polymer, and schematics of the MOF-PUU composites. (g) SEM picture of 20 wt% UiO-66-NH₂/PUU electrospun NF composites. Adopted with permission from Ref. [81], Copyright 2021, American Chemical Society.

to carbon, which can exist as either fullerene (0D) or graphite (3D), MOFs can be engineered to exhibit various dimensionalities, including 0D, 1D, 2D, and 3D structures (Fig. 12). This diversity in structural orientations proves especially valuable in functions that demand distinctive properties. For example, hierarchical structures are highly effective at maximizing surface area while sustaining an integrated framework capable of accommodating numerous electrochemical processes [82]. Conversely, cage type structures excel at trapping compounds, making them valuable in applications that require separation processes [83]. On the other hand, shape-tuned structures portray a pivotal task in enhancing the electrochemical active surface area, enhancing wettability and modifying the current density of reactions, especially in batteries [84].

MOFs initially take shape based on the coordination of metal nodes

and SBUs, which determine their primary configuration. As an illustration, MOF-5 is constructed using an oxide of metal, denoted as a 0D dot (Fig. 13a) [93]. Several benchmark MOFs featuring metal-oxide SBUs in a 0D form consist of MOF-177 (Fig. 13b) [85], MOF-199 [94], and quantum-sized carbon nanodots derived from ZIF-8 [95]. These 0D structures serve as fundamental building blocks that can be constructed and interconnected to form 1D/2D/3D networks. MOFs can be tailored with unique ligand connectivity and topologies by employing various organic ligands. For example, a flexible link-exchange approach was utilized to convert a 0D Cu coordination polyhedron, known as a metal-organic polyhedron (MOP-1), into MOFs of various dimensions [96]. This transformation involved the conversion of 0D MOP-1 into a 1D Cu MOF by 1-methylimidazole. Subsequently, the 1D Cu MOF was further transformed into 2D/3D open frameworks employing 3,5-pyridinedicarboxylic acid (3,5-PDC) and biphenyl-3,3',5,5'-tetracarboxylic acid (BPTC), respectively, all through a single-crystal to single-crystal transformation process.

In the pursuit of preparing 0D MOFs, another approach involves the size reduction of bulk structures. For example, a 0D class MOFs depends on bimetallic Ni-Fe was successfully synthesized, showcasing excellent electronic and structural properties [86]. Initially, the bulk MOF was synthesized conventionally using Ni and Fe salts along with organic linkers. To transform it into a 0D structure, mechanical grinding followed by ultrasonication was employed. This process facilitated the organic hydrocarbon and inorganic metal-oxygen layers destabilization, leading to the formation of NiFe-MOF particles with an average size of 5.5 ± 1.8 nm (Fig. 13c). This 0D MOF exhibited promising characteristics as an electrocatalyst for transforming atmospheric N₂ to valuable NH₃, displaying great faradaic efficiencies and rapid NH₃ production rates.

Yolk-shell structures represent a category of 0D architectures [97], offering novel design possibilities and architectural features. One commonly employed method for creating yolk-shell structures is template-based approach, where the core is deliberately maintained or separated. In the case of hollow structures, various mechanisms beyond template mediation can be utilized, including thermal decomposition,

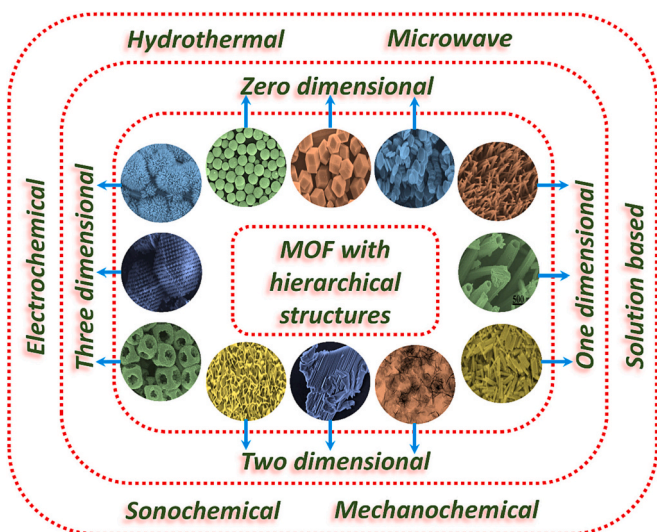


Fig. 12. Hierarchical structures derived from MOF.

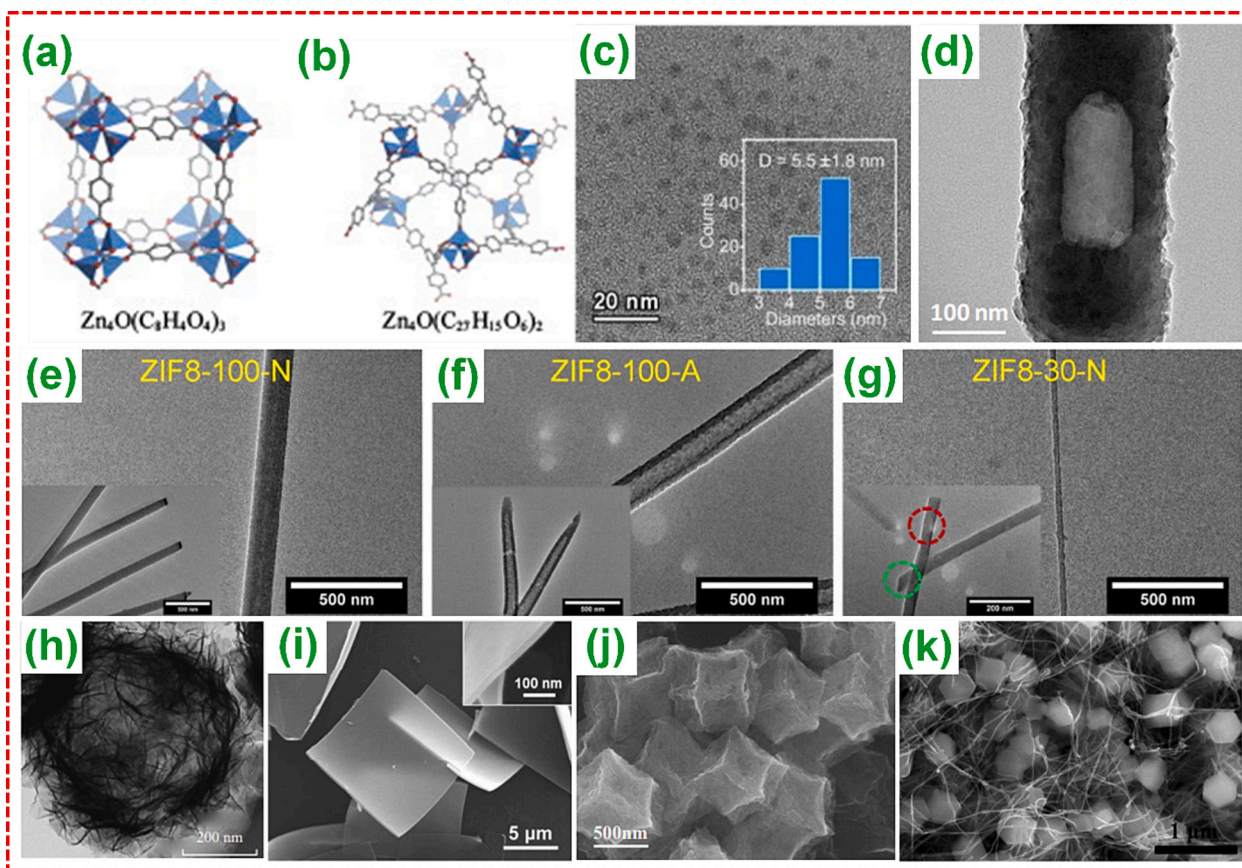


Fig. 13. Pictorial overview of MOFs having metal-oxide SBUs that are (a) MOF-5 and (b) MOF-177 (0D: $\text{Zn}_4\text{O}(\text{CO}_2)_6$). Adopted with permission from Ref. [85], Copyright 2008, Elsevier B.V. (c) HRTEM and the equivalent particle size distribution analysis of the NiFe-MOF. Adopted with permission from Ref. [86], Copyright 2020, Royal Society of Chemistry. (d) TEM analysis of hollow Co-MOF-74 NRs. Adopted with permission from Ref. [87], Copyright 2018, American Chemical Society. TEM analysis of (e) ZIF8-100-N, (f) ZIF8-100-A, and (g) ZIF8-30-N NRs. Adopted with permission from Ref. [88], Copyright 2018, Wiley VCH, Janus. (h) TEM analysis of Ni/Co-MOF NFs. Adopted with permission from Ref. [89], Copyright 2018, Wiley VCH, Janus. (i) SEM analysis (inset shows the side view) of Co-MOF NSs. Adopted with permission from Ref. [90], Copyright 2018, Royal Society of Chemistry. (j) SEM analysis of Co-N-C/SeS₂ composites. Adopted with permission from Ref. [91], Copyright 2018, Royal Society of Chemistry. (k) SEM analysis of CNT networks confined within larger ZIF-8 referred to as L-ZIF-8@CNTs. Adopted with permission from Ref. [92], Copyright 2018, Wiley VCH, Janus.

Ostwald ripening, the Kirkendall effect, ion exchange, galvanic replacement, and more [98]. For example, the Kirkendall effect leverages the differential ions diffusion rates and was utilized to fabricate hollow Co-MOF-74 structure (Fig. 13d) [87]. Primarily, solid Co precursor nanorods (NRs) were prepared with the assistance of PVP and alcohol. The conversion to hollow structures was achieved via introducing a DMF solution of H₄DOBDC. Consequently, the hollow structure emerged owing to the varying Co²⁺ diffusion rates and linker ions over time.

The structure and growth of 1D nanomaterials are significantly persuaded by different physicochemical parameters, including temperature, pH, pressure, molar ratio of the reactants, metal precursor, and the reactant concentration [99]. Different synthetic strategies can be employed to prepare 1D MOFs, either through template-free methods [100] or template-assisted approaches [101]. For instance, growth-controlled method for 1D ZIF-8 was developed via interfacial preparation templated using nano porous polymer membranes [88]. By adjusting the membrane template pores size, as well as the type of Zn salts and concentration, discrete ZIF-8 morphologies were effectively obtained. For example, when using Zn (NO₃)₂, ZIF-8 grew as polycrystalline solid NRs within membrane pores of 100 nm (Fig. 13e), single-crystalline nanowires (NWs) with the size of 30 nm membrane pores (Fig. 13g), and hollow nanotubes (NTs) within 100 nm membrane pores when zinc acetate was employed (Fig. 13f). The application of size-confinement templating techniques in the growth of MOF structures

offers a precise and meticulously controlled approach to attain specific 1D structures.

2D structures possess versatile properties compared to structures of other dimensions like 0D, 1D, and 3D. These properties include a large surface area, atomic-level thickness, and high surface-to-volume ratios [102]. Such attributes make them highly appealing for use in numerous applications like flexible electronics, membranes, and energy storage [103–105]. ZIFs and MOFs, renowned for their substantial surface areas, are frequently employed as precursors for synthesizing nanomaterials. Alongside their preparation, additional components can be presented to provide numerous redox behaviors while preserving strong structural properties. For example, initially, ZIF-67 had a rhombododecahedral structure [89]. However, the structure transformed into a 2D hollow spherical form with the introduction of Ni and Co ions (Fig. 13h). The LBL assembly of NFs in Ni/Co-MOF led to higher capacitance, enhanced rate capacity, and increased electrocatalytic activity compared to Ni-MOF and its parent ZIF-67. In another approach to crafting 2D MOFs, PVP was employed to manipulate the vertical growth of MOF crystals [90]. This method successfully yielded 2D square type NSs of Co-MOF with an intrinsically electropositive zeta potential (Fig. 13i). These NSs were subsequently combined with electronegative graphene oxide (GO) to create a conductive and flexible 2D MOF/rGO paper type electrode through electrostatic self-assembly. Also, 2D MOFs have found applications in perovskite/MOF sheets [106], MOF/graphene derivatives [107], and various other areas.

MOFs have proven greatly valuable as precursors for the growth of transition metal compounds owing to its precisely stated porosity and morphology. A notable example involves a 3D MOF, ZIF-67, with a polyhedral structure, serving as a template for crafting a porous N-doped graphitic carbon (GC)-Co scaffold known as Co-N-C [91]. In this process, the Co particles portion was etched from the MOF, creating channels within the structure. These channels were then loaded with S and selenium (Se) nanoparticles (NPs) using a straightforward melting diffusion method. Effective immobilization of SeS_2 within the porous channels was confirmed by the absence of SeS_2 particles on the surface, indicating successful impregnation (Fig. 13j). This well-designed 3D structure played a critical role in immobilizing lithium polysulfide/polyselenide species, effectively mitigating the volume expansion of S—Se during charge/discharge cycles in Li—S battery (LSB) applications. Besides, researchers achieved the in-situ growth of freestanding 3D networks consisting of porous electrodes derived from MOFs and CNTs through a solvothermal reaction [92]. Illustrated in Fig. 13k are the monolithic

ZIF-8@CNT composites, where the ZIF-8 particles size grown in-situ was precisely controlled to approximately 500 nm via adjusting the concentration of precursor, referred to as L-ZIF-8@CNTs. These L-ZIF-8@CNTs operated as hosts for S loading and exhibited outstanding performance in LSB applications. Various other 3D structures derived from MOFs have been investigated, including highly oriented nano-arrays [108], flower type structures [109], and exceptional combinations of two or more structures through hybrid combinations [110].

2.5. Nanomaterials derived from MOF

The ability to differentiate between two materials and selectively eliminate one while preserving the other is a concept akin to removing a core from core-shell architectures via thermolysis [111] or selectively determining active materials on current collectors via surface acid etching [112]. Similarly, MOFs can be tailored into numerous structures through adjusting specific process conditions. MOF derivatives typically

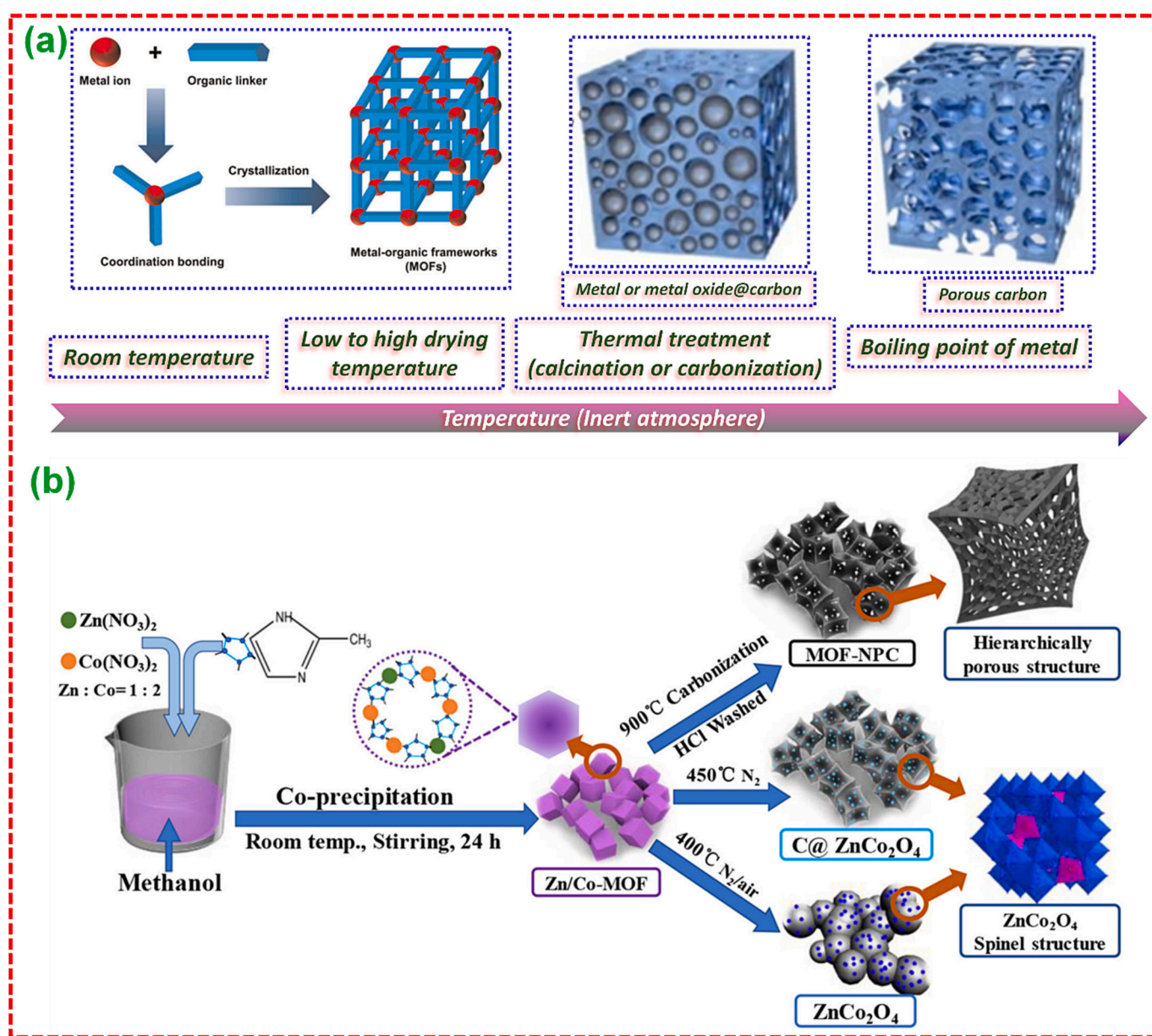


Fig. 14. (a) Pictorial representation of MOF derived porous carbon. Adopted with permission from Ref. [115,116], Copyright 2021, Wiley VCH, Janus, Copyright 2017, Wiley VCH, Janus. (b) Pictorial representation of preparation of nano porous carbons (NPCs) derived from Zn/Co-MOF and ZnCo₂O₄. Adopted with permission from Ref. [117], Copyright 2020, Frontiers.

exhibit a distinct response to precursors, reactive conditions, or elevated temperatures. For instance, MOFs exposed to thermal treatment in an inert atmosphere at temperatures approaching the core metal's melting point can alter their organic linkers into PC [113,114]. These organic linkers contain C, O, N, and some non-metal elements. Monitored heat treatment in an inert atmosphere effectively removes the volatile components, converting C encompassing compounds into PC (Fig. 14a). Wang and colleagues [118] conducted an experiment using ZIF-8 cores encased in polydopamine (PDA) shells. These structures underwent rapid decomposition in a reducing N_2 atmosphere, resulting in the formation of hollow N-doped carbon (NDC). The strong interfacial interactions caused the ZIF-8 cores to expand outward to counteract the induced stress from shrinkage. Nevertheless, as stress accumulated, the ZIF-8 cores ultimately disintegrated, giving rise to hollow carbon structures. In another intriguing transformation, CNTs can be generated through the pyrolysis of ZIF-67 under an Ar atmosphere [119]. Additionally, MOFs exhibit a remarkable stability in water, which has been cleverly manipulated by Bao et al. [120] to create MOF@SiO₂ yolk-shell nanoreactors. Their approach involved a water-etching route applied to the hydrothermally unstable MOF surface, resulting in the formation of a yolk-shell architecture. Finally, PC can be accomplished by selectively removing the metal content from a thermally treated MOF, along with acid washing [121,122]. As of now, numerous MOFs derived carbon have been explored in various forms, as described in Table 1, including PC, NPC, amorphous carbon, CNTs, carbon NRs, GC, and more [27]. This technique for making PC from MOFs can yield novel morphologies and properties that compete favorably with other carbon-based electrode materials, including GO-based [135], glucose-based [136], and coal-based electrode materials [137].

Additionally, apart from the previously discussed approaches, there have been instances where metal dependent compounds were transformed into its metal-oxide counterparts and incorporated into an electrically conductive carbon matrix. For instance, a hybrid composite containing Co₃O₄ embedded within a GC matrix was synthesized by

directly carbonizing Co-MOF in the presence of inert gas temperature at 700 °C [138]. The formation of MOF derived Co@NDC composites could be simply manipulated by adjusting the solvent and anion-to-ligand ratio [139]. It's worth noting that most reported nanomaterials derived from MOF follow a two-step process: first, the M-MOF (M = metal) template preparation, and thereby optimized calcination. He and colleagues [117] conducted an evaluation using Zn/Co-MOFs (Fig. 14b) as precursors, resulting in three distinct products: PC, ZnCo₂O₄, and C@ZnCo₂O₄. For PC, the Zn/Co-MOF underwent heating at 900 °C in N_2 temperature, followed by washing with acid solution. In the case of ZnCo₂O₄, the Zn/Co-MOF underwent initial annealing at 450 °C in N_2 temperature. Subsequently, the N_2 supply was discontinued, and both ends of furnace were exposed to ambient atmosphere. To obtain C@ZnCo₂O₄, the Zn/Co-MOF was heated to 450 °C in N_2 temperature exclusively. Leveraging the distinct properties of metal ions and organic ligands, MOFs can be transformed into various nanomaterials. A classic example involves the direct conversion of MOF precursors into metal oxides, like Co-MOF to Co₃O₄ [140], Ni-MOF to NiO [141], Ce-MOF to CeO₂ [142], and so on, through calcination in air. Remarkably, by carefully controlling the thermal treatment process, variations in composition, morphology, porosity, and electrochemical properties can be achieved [143,144].

While a plethora of metal oxides synthesized from MOFs as illustrated in Fig. 15, it's noteworthy that metal cores have also been utilized as templates for the in-situ preparation of MOF-derived metal oxides [144], sulfides [145], nitrides [146], selenides [147], and more. These materials retain the porous structure that was initially determined by their organic linkers. Research in the realm of MOF-derived nanomaterials has garnered significant attention owing to its novel composition, which suggests distinct benefits. These benefits include rapid ion diffusion rates than metal oxides, a greater theoretical capacity compared to carbon materials, and shorter volume extension in comparison to pure metal and metal alloy electrodes [148]. It's worth highlighting that MOFs act as sacrificial templates capable of providing PC networks with embedded metals, rendering them ideal for applications in electrocatalysis, batteries, and supercapacitors [149,150]. Perhaps, MOFs with substantial surface areas can effectively accommodate high Se/S loading, thus mitigating volume extension concerns in lithium ion batteries (LIBs) [151] and Na-Se batteries [152]. In the following portions, this review will primarily delve into MOF-derived nanomaterials and their applications in energy storage fields. It will comprehensively examine their advantageous properties as well as the current challenges associated with MOF derivatives.

3. Synthesis of MOFs

Various applications require MOFs with different sizes and structures, necessitating the use of diverse synthesis methods. One approach involves manipulating the pH and solvent conditions at ambient atmosphere to expedite precipitation, thereby enabling the creation of large MOF crystals [153]. However, to cater to specific applications, there is a growing need to explore and comprehend innovative, gentle, and swift synthesis techniques. These methods have the potential to facilitate continuous production, allowing for the efficient processing of substantial quantities of uniform samples and ensuring rapid and consistent synthesis outcomes.

The ideal method for material synthesis is one that is straightforward, consistent, and easily adaptable. MOF synthesis relies on fundamental principles, primarily the careful selection of metal centers and linkers. The remarkable diversity in metal centers and linkers available for MOFs allows for virtually limitless organic-inorganic hybrid combinations. Research has revealed certain structural shapes in MOF preparation, aiding in the prediction of architectural outcomes [154,155]. By introducing certain reactive groups, chiral or redox centers into linkers, MOFs with desired properties can be designed. The size, hardness, electronic composition, coordination modes, and other characteristics of

Table 1
Carbon materials derived from MOF.

MOF derived carbon	MOF templates	Heating condition	Ref.
Hollow NDC	ZIF-8	1st: 200 °C for 2 h in N_2	[118]
CNT grafted cobalt/carbon polyhedra grown on Ni foam	dopamine	2nd: 900 °C for 2 h in N_2	
CNRs and graphene nanoribbons	ZIF-67	800 °C for 2 h in H_2 /He	[123]
	MOF-74	CNRs: 1000 °C for 4 h in Ar graphene nanoribbons: CNRs heat-treated to 800 °C for 2 h followed by chemically activated.	[124]
N-CNT	ZIF-67	1st: 435 °C for 8 h in Ar	[125]
CNT-decorated NDC-coated Ni	Ni-MOF	1st: 550 °C for 3 h in Ar	[126]
Hollow PC NCs	melamine	2nd: 700 °C for 3 h in Ar	
	ZIF-8 NCs	900 °C for 3 h in N_2 followed by HF etching	[127]
N-doped PC NSs	ZIF-8	800 °C for 5 h in N_2 followed by HCl washing	[128]
N and S co-doped hollow cellular carbon nanocapsules	LiCl and KCl	900 °C for 5 h in Ar followed by HF washing	[129]
Ultra microporous carbon NPs	MIL-101-NH ₂		
Carbon nanoribbons	thiourea		
	UiO ₆₇	750 °C for 3 h in N_2 followed by HF acid dilution	[130]
Highly porous metal-free carbon material	ZIF-8	1000 °C for 4 h in N_2	[131]
Hollow carbon	nanoribbons		
	Zn-MOF NRs	900 °C for 5 h in N_2 followed by HNO ₃ oxidation	[132]
		800 °C for 2 h in N_2 followed by HCl washing	[133]
3D interconnected hierarchical sponge type PCs	Tannic acid	900 °C for 2 h in Ar	[134]
	Zn(tbip)		

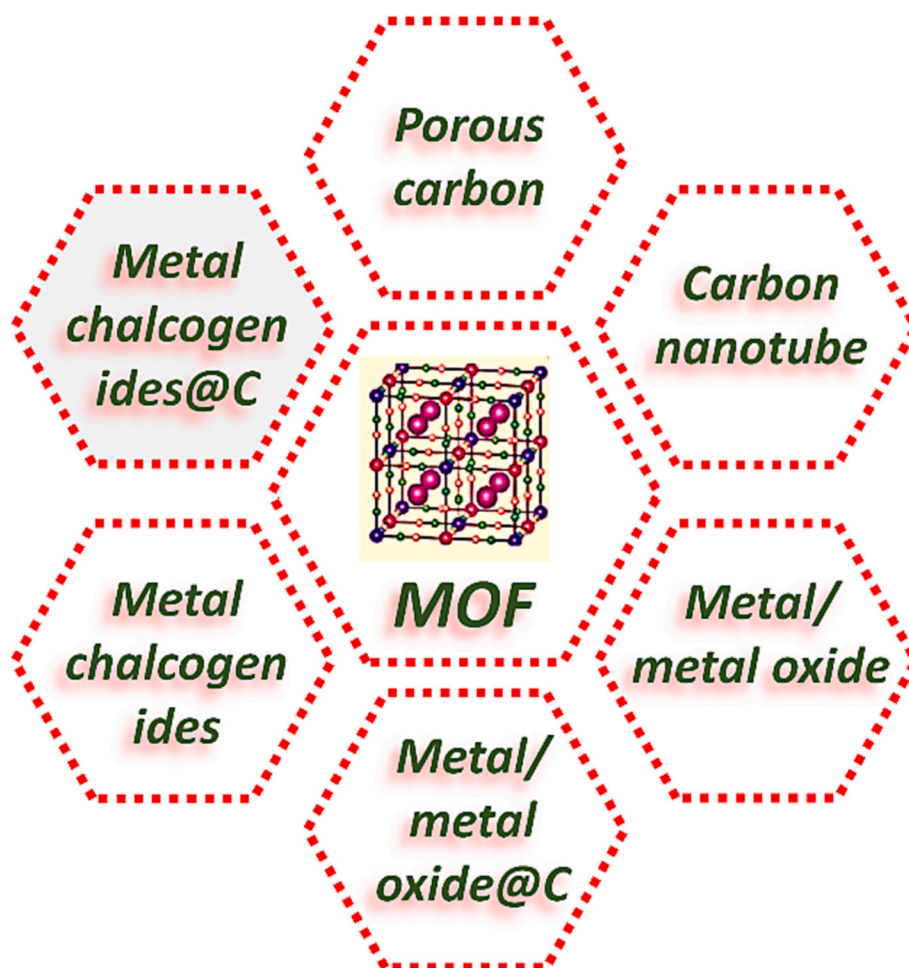


Fig. 15. Pictorial demonstration of nanomaterials derived from MOF.

the metal center influence the final MOF topology [156,157]. Another critical factor influencing the MOFs' properties is the selection of basic building blocks. Additionally, various preparation parameters, including solvent, temperature, pressure, pH, and reaction time, must be carefully studied. Multiple synthesis approaches are available, including conventional solution methods [158,159], hydrothermal processes [160,161], microwave-assisted techniques [162], electrochemical routes [163,164], mechanochemical procedures [165,166], and

sonochemical methods [167,168]. Fig. 16 is a figure that briefly demonstrates the numerous MOF preparation protocols.

3.1. Standard solution approach

The solution approach, conducted at ambient temperature and pressure, is the most straightforward approach for achieving large single crystal MOFs. In the early days of MOF synthesis, Yaghi et al. employed a

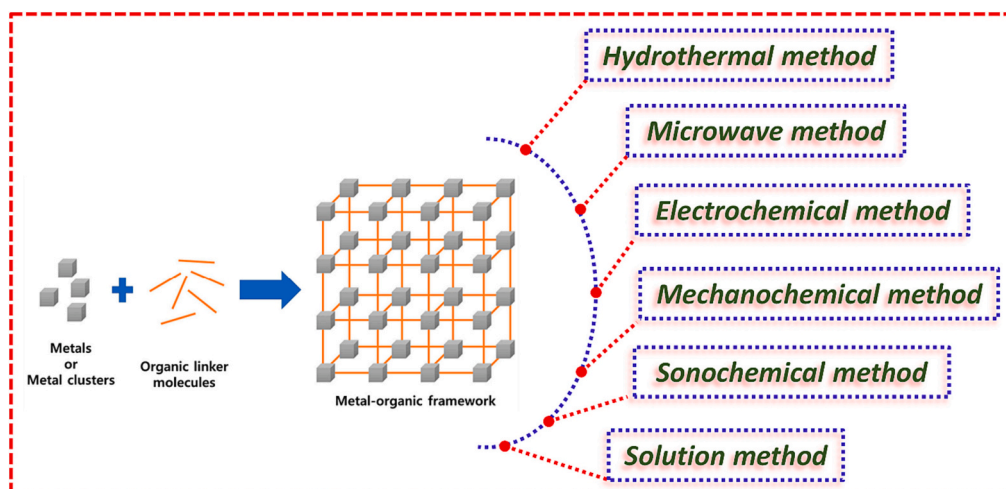


Fig. 16. Pictorial demonstration of various methods for the preparation of MOF. Adopted with permission from Ref. [26], Copyright 2023, MDPI.

diffusion synthesis method, albeit with low yields [169]. Subsequently, a wide range of MOFs, including MIL-53, MIL-88, MIL-110, CAU-1, ZIF-8, ZIF-67, and UiO-66, have been successfully produced utilizing solvents such as water, methanol (MeOH), and dimethylformamide (DMF) [170,171]. Li et al. have even investigated the impact of solvents on the MIL-96(Cr) and MIL-100(Cr) preparation [172]. Dincă et al. conducted research to understand the factors influencing cation exchange in MOFs by investigating the different solvents effect. They achieved this via introducing Ni^{2+} into MOF-5 and Co^{2+} into MFU-4 L (MFU denoting MOF Ulm-University) [173]. The results revealed that while solvents do influence the cation exchange process, only a specific set of pertinent parameters demonstrated correlations with exchange rates. This technique provides valuable insights into critical characteristics of cation exchange in diverse MOFs.

3.2. Hydrothermal approach

The hydrothermal approach, often referred to as solvothermal synthesis, stands as the most commonly employed approach for MOF synthesis [174,175]. In this method, a soluble metal salt, a free ligand, and organic solvent with a high boiling point are combined in a sealed container. The mixture is then heated above the solvent's boiling point. Subsequently, the product is recovered, washed, and the solvent is removed from the MOFs pores. This technique offers several benefits, including the capability to generate uniform MOF particles characterized by high crystallinity, a narrow crystallite size, and exceptional phase purity. These attributes are attributed to the rapid reaction kinetics associated with this method [176,177]. The Yaghi group, renowned pioneers in MOF development, achieved a 90 % yield in synthesizing crystalline MOF-5 by heating an N, N'-diethylformamide (DEF) solution of $\text{Zn}(\text{NO}_3)_2 \cdot 4\text{H}_2\text{O}$ and the acid form of BDC in a sealed container within the temperature range of 85 to 105 °C [178]. Zheng et al. utilized the hydrothermal method to synthesize six distinct types of MOFs. They employed Zn, Co, and Ni as metal ions and H_3BTC , H_2NDC , L_1 , L_2 , and L_3 as ligands ($\text{NDC} = 1,2\text{-benzenebicarboxylate}$, $\text{L}_1 = 1,4\text{-bis(imidazol-1-ylmethyl)benzene}$, $\text{L}_2 = 1,1'-(1,4\text{-butanediyl})\text{bis(imidazole)}$, $\text{L}_3 = 1,1'-(1,4\text{-hexanediyl})\text{bis(imidazole)}$) [179]. The MOFs designed through this method are as follows: (1) $[\text{Co}_3(\text{L}_1)_3(\text{BTC})_2(\mu\text{-H}_2\text{O})_3 \cdot 2\text{H}_2\text{O}]_n$, (2) $[\text{Zn}_2(\text{L}_2)(\text{HBTC})_2 \cdot 2\text{H}_2\text{O}]_n$, (3) $[\text{Co}(\text{L}_3)(\text{HBTC})]_n$, (4) $[\text{Co}(\text{L}_1)(\text{NDC})]_n$, (5) $[\text{Ni}(\text{L}_2)(\text{NDC})]_n$, and (6) $[\text{Co}(\text{L}_3)(\text{NDC})]_n$. Structural analyses revealed that (1) features a rare 4-connected self-penetrating network, (2) exhibits a two-dimensional (2D) (3,4)-connected network, (3) showcases a 2D (3,5)-connected network, while both (4) and (5) display a 4-connected MOF structure akin to the CdSO_4 type

topology, and (6) presents a 2D 4-connected net structure. Despite its advantages, solvothermal synthesis does come with certain drawbacks, including the use of solvents that can have adverse environmental effects, the necessity for costly stainless-steel autoclaves and Teflon reactors, limited potential for mass production, and challenges associated with product cleaning [180].

During hydrothermal activity, a chemical reaction takes place between organic and inorganic components, with the material's structure being shaped by solvent molecules that serve as "pore templates". Subsequently, the trapped solvent within the pores is eliminated through a high temperature washing process [181]. However, under certain reaction conditions, reactive substances like reaction solvents, residual reactants, and by-products might not be entirely removed from the MOF product. This incomplete removal can lead to pore blockages in the process. Pré and colleagues have recently put forward an innovative approach to enhance washing method via implementing adjusted centrifugation techniques at two distinct phases: first, after the initial reaction, and then following the materials washing [182]. Their study focused on Ni-MOF-74 as the target product and the process is outlined in Fig. 17. During the initial set production, the washing activity was repeated, as denoted by the green box in Fig. 17. This repetition significantly enhanced the material separation from the reactive medium. In the second set of production, centrifugation was introduced at two specific spots where solvent drainage occurred, as designated by the red arrows in Fig. 17. They conducted optimization studies for both centrifugation time and rotational speed, both between the reaction and material washing (1) and subsequent material washing stages (2), in order to achieve the highest quality of separation. The 1st centrifugation step in the synthesis technique effectively removed the reactive medium from the product, while the 2nd centrifugation played a crucial role in separating the product from any remaining contaminated MeOH after washing. This approach markedly improved the washing process's effectiveness, ultimately ensuring the complete activation of the MOF pores, thus expanding the potential for future applications.

3.3. Microwave method

In many applications of MOFs, there is often a requirement for small-sized MOFs. The microwave-assisted method proves to be a valuable approach for generating small metal oxide particles. In comparison to the hydrothermal method, this approach offers several benefits, including a reduction in synthesis time by over tenfold, the production of uniformly sized and composed MOFs, and the capability to create MOFs with a wider variety of compositions [162]. Recently, Wright and

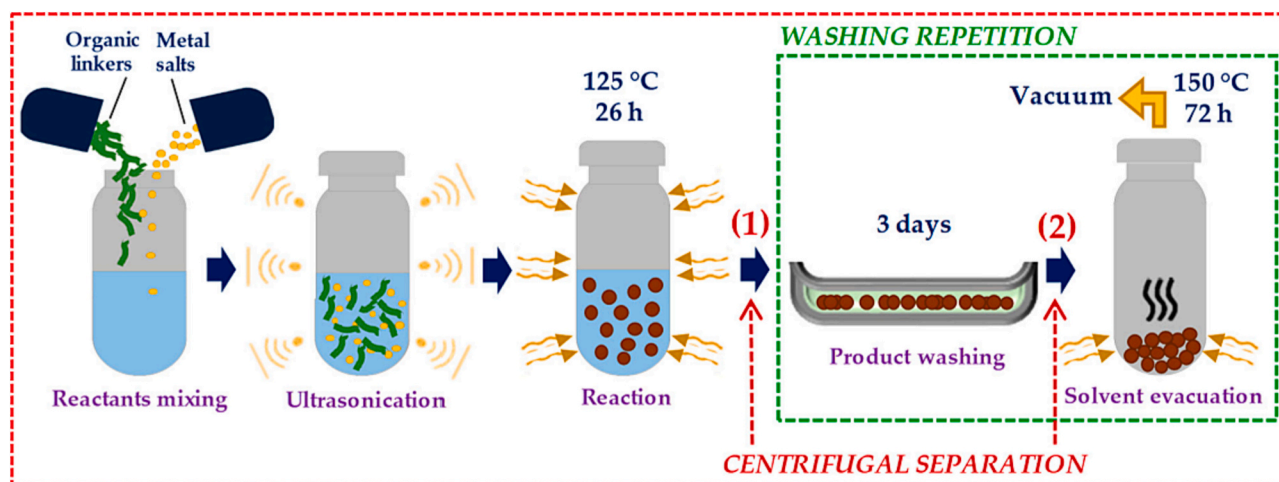


Fig. 17. Pictorial demonstration of Preparation of MOFs using solvothermal technique followed by washing with the help of centrifugal separation. Adopted with permission from [182], Copyright 2020, MDPI.

colleagues demonstrated the synthesis of Zr-based MOFs, specifically UiO-66, in the manner of thin films employing a straightforward and fast microwave aided synthesis [183]. In this investigation, they introduced a swift microwave-based technique to fabricate oriented UiO-66 thin films on both Au and Si substrates. This approach significantly reduced the reaction time, underscoring its capability to synthesize MOFs in the thin films fashion utilizing a straightforward method.

Han and colleagues introduced a novel approach to producing MOFs by mixing the microwave approach with other techniques [184]. In their study, MOF crystals were effectively generated on fiber mats composed of polyacrylonitrile (PAN) and MOF. This innovative method involved merging electrospinning with microwave irradiation. Electrospinning is a straightforward, and scalable manufacturing method for producing constant fibers with diameters spanning from several nanometers to micrometers. This method can be employed to different materials, including polymers, ceramics, and carbon-based constituents, making it highly adaptable and suitable for a range of applications [185]. The integration of microwave and electrospinning techniques enabled the fabrication of nanofiber structures based on MOFs. To optimize the conditions for developing PAN/MOF fiber composites, UTSA-16 (University of Texas at San Antonio) MOFs, specifically UTSA-16(Co) and UTSA-16(Zn), were employed. The UTSA-16(Co) and UTSA-16(Zn) MOFs were synthesized using a microwave-assisted technique. This involved dissolving precursor compounds containing $\text{Co}(\text{OAc})_2$ and $\text{Zn}(\text{OAc})_2$ in a mixed solvent, followed by heating in a microwave oven, washing, and subsequent drying. The PAN/UTSA-16(M) (where M = Co or Zn) fiber template was created by sonicating a mixture of manufactured UTSA-16(M) and DMF until complete dispersion was achieved, after which PAN was added and subjected to further sonication. The resulting electrospinning solution was used to produce fibers on an Al foil, ultimately yielding the electrospun PAN/MOF fiber mat. To vary the composition of the PAN/UTSA-16 fiber mat, the weight ratio of PAN to UTSA-16(X) (where M = Co or Zn and X represents the wt% of UTSA-16) was adjusted. UTSA-16 precursors with various ratios were distributed within the PAN fiber network, and the UTSA-16 growth was promoted under microwave irradiation to form a UTSA-16 crystal layer. The resulting products were designated as PAN/UTSA-16(X)-1st, and the samples undergoing a secondary growth process were labeled as PAN/UTSA-16(X)-2nd. Fig. 18 illustrates the step-by-step production method for the PAN-UTSA-16 fiber mat, encompassing UTSA-16 synthesis, fiber mat organization, and seed growth on the fibers. Both PAN/

UTSA-16(Co) and PAN/UTSA-16(Zn) fibers exhibited micropores within the range of 0.4–1.5 nm and 0.4–1.8 nm, respectively. These pore sizes closely resembled those found in pristine UTSA-16(Co) ranging from 0.3 to 1.45 nm and pristine UTSA-16(Zn) ranging from 0.3 to 1.79 nm [186]. The innovative approach of producing flexible MOF polymer fiber mats in the sequence of microwave and electrospinning methods, as suggested in these findings, offers promising possibilities for a wide array of applications. These applications span areas like energy storage, hazardous chemicals decomposition, filtration, as well as sensor and biomedical applications.

3.4. Electrochemical method

The electrochemical synthesis method entails the production of compounds within an electrochemical cell, offering distinct advantages over traditional solvothermal or microwave synthesis. Notably, this method allows for gentle synthesis conditions compared to more conventional approaches. Furthermore, it stands out as a scalable industrial synthesis method, enhancing selectivity and yield due to its low reaction temperature and rapid synthesis rate [187]. Numerous well-known MOFs, including HKUST-1 [188], ZIF-8 [189], MIL-100(Fe) [190], and MIL-53(Al) [191] have been successfully synthesized using this technique. The underlying principle involves providing metal ions by dissolving the anode within a making mixture covering an electrolyte and organic ligand. Electrochemical method, conducted in the absence of pressure, grants precise constraint over the reactant concentrations throughout the synthesis process. Additionally, it permits the management of anodic oxidation by adjusting the rate at which metals are introduced and continuously incorporating linkers into the solution. Moreover, by controlling the applied electrode voltage, the state of oxidation of the metal can be meticulously regulated. Creating thin MOF film coatings on electrodes via electrochemical methods presents an appealing prospect. Liu et al. [192] introduced an approach for producing a 2D MOF film with large surface area applying electrochemical techniques. Dispersing MOF nanocrystals can be challenging owing to strong interlayer interactions, prompting the exploration of various strategies for addressing this issue [193,194]. In this particular study, they demonstrated the growth of a 2D $\text{Cu}_3(\text{HHTP})_2$ (HHTP: 2,3,6,7,10,11-hexahydroxytriphenylene) film on a Cu foil via a manageable electrochemical fabrication process. The setup involved two Cu foil pieces serving as the anode and cathode, submerged in the

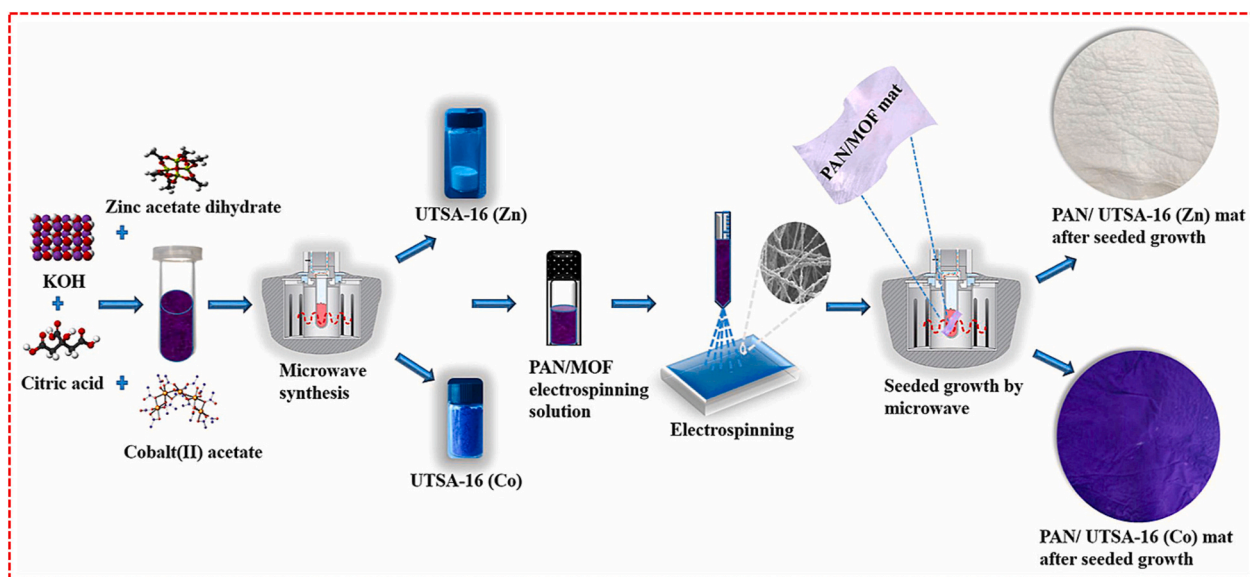


Fig. 18. The fabrication mechanism of PAN-UTSA-16 fiber mat comprises of fiber mat preparation, UTSA-16 production, and seed growth of fibers using electrospinning followed by microwave irradiation. Adopted with permission from [184], Copyright 2021, Elsevier B.V.

solution containing melted HHTP precursor to assemble an electrochemical cell. When a voltage was applied, Cu^{2+} ions were released from the Cu anode and subsequently reacted with HHTP anions, resulting in the deposition of a $\text{Cu}_3(\text{HHTP})_2$ MOF film on the Cu anode. Fig. 19 illustrates the electrochemical approach for synthesizing film-type MOFs. The technique proposed in this study boasts versatility, as it can be applied universally, regardless of the specific ligands used, whether it's benzene-1,3,5-triyltriboronic acid, meso-tetra(4-carboxyphenyl) porphine, or 2,4,6-trihydroxy-1,3,5-benzenetricarboxaldehyde. Furthermore, this MOF film can be seamlessly transferred to any substrate using PMMA transfer technology without sustaining damage. This advancement opens up possibilities for an efficient and convenient electrochemical method suitable for large-scale MOF film synthesis, with potential applications in nanoelectronic devices and beyond.

3.5. Mechanochemical method

Mechanochemical preparation is a highly regarded method that combines chemical and mechanical processes at the molecular level, and it is considered one of the suggesting approaches for large-scale MOF production [166]. The appeal of MOF synthesis through mechanochemical methods lies in the fact that it occurs at room temperature, without the need for solvents or with minimal additional heat, and is remarkably swift, typically taking only 10–60 min to reach completion, yielding high quantities of the desired product. Mechanochemical approaches can be categorized into 3 primary types: (1) neat grinding (NG), which eschews solvents entirely, (2) liquid-assisted grinding (LAG), which utilizes a small volume of liquid to enhance reactant mobility, and (3) ion-and-liquid assisted grinding (ILAG), which employs a catalytic liquid comprising minute quantities of salt additives to expedite formation of MOF.

James et al. achieved a breakthrough by demonstrating the production of microporous MOFs through neat grinding (NG) for the first time in 2006 [195]. Later, they also created HKUST-1 by milling $\text{Cu}_2(\text{OAc})_4$, H_2O and H_3BTC [196]. This NG technique has proven effective with other metal ions, including Cd-based MOFs. One notable benefit of this method is that it produces only water as a by-product and involves no purification [197]. While some MOFs can be produced via a solvent-free NG technique, metal carbonates and metal oxides without crystal water, as opposed to metal acetates and nitrates, often need the addition of a solvent to facilitate the reaction activity [198]. Hence, the liquid-assisted grinding (LAG) technique has been introduced. Braga et al. [199] investigated that the presence of small amounts of solvent can enhance MOF crystallization and reaction rates. In a specific examination, 1D porous coordination polymer- CuCl_2 (trans-1,4-

diaminocyclohexane, denoted as dace) was produced by grinding CuCl_2 , H_2O and dace in the presence of water or DMSO, followed by heat and vacuum treatment to remove the water or DMSO. Jones et al. [200] shown that some inorganic salts can facilitate MOF preparation through the LAG method. Since then, research has been conducted on the MOFs preparation using the ILAG approach, which involves a catalytic liquid containing trace volumes of salt additives. For instance, zeolitic imidazolate frameworks (ZIFs) were created using grinding solutions like DMF, EtOH, and DEF, with $\text{NH}_4\text{CH}_3\text{SO}_3$, NH_4NO_3 , and $(\text{NH}_4)_2\text{SO}_4$ as salt additives [201].

Ni-based MOFs have garnered substantial interest and have predominantly been produced using hydrothermal methods [202] and precursor heat treatment in ambient atmosphere [203]. However, these preparation activities typically demand elevated temperatures, substantial quantities of solvents, and extended reaction durations [204]. Jin et al. [205] introduced a relatively simple solution-phase technique for swiftly producing $\text{Ni}_3(\text{BTC})_2 \cdot 12\text{H}_2\text{O}$, but it required the laborious deprotonation of the ligand and the utilization of organic solvent. Subsequently, there were efforts to synthesize Ni-MOFs through mechanochemical methods, although each study had its limitations, and none reported entirely satisfactory results [206]. Wang et al. [207] achieved the synthesis of a Ni-based MOF in an incredibly brief time frame of just 1 min, capitalizing on the advantages of the mechanochemical approach. Interestingly, variations in grinding time had minimal impact on the yield, which consistently fell within the range of 66 % to 72 %. Irrespective of the auxiliary liquid type (water, MeOH, EtOH, or DMF) included in minute quantities, the material was produced within 1 min, with yields ranging from 60 % to 70 %. In summary, this study's proposed method was found to be rapid, efficient, environmentally friendly, cost-effective, and highly scalable. Furthermore, it advised that both yield and reaction performance could be improved by adjusting preparation conditions.

ZIF-8 stands out as one of the broadly researched MOFs types, primarily owing to their straightforward preparation process and impressive structural resilience [208]. Within the same structural framework as ZIF-8, ZIF-67 substitutes Co for Zn. By skillfully manipulating the quantities of Zn and Co, researchers have successfully crafted bimetallic ZIFs. Numerous studies have detailed a preparation pathway for generating CoZn-ZIFs within liquid-based preparation systems [209]. An alternative approach involves transforming ZnO into ZIF using a solvent-free method suitable for mechanochemical applications [210]. Tanaka et al. introduced a straightforward acetate-assisted mechanochemical preparation that employs $\text{Co}(\text{OAc})_2$ as part of the strategy to enable the large-scale production of CoZn-ZIFs [211]. Fig. 20 provides a schematic representation of the mechanochemical method alongside images

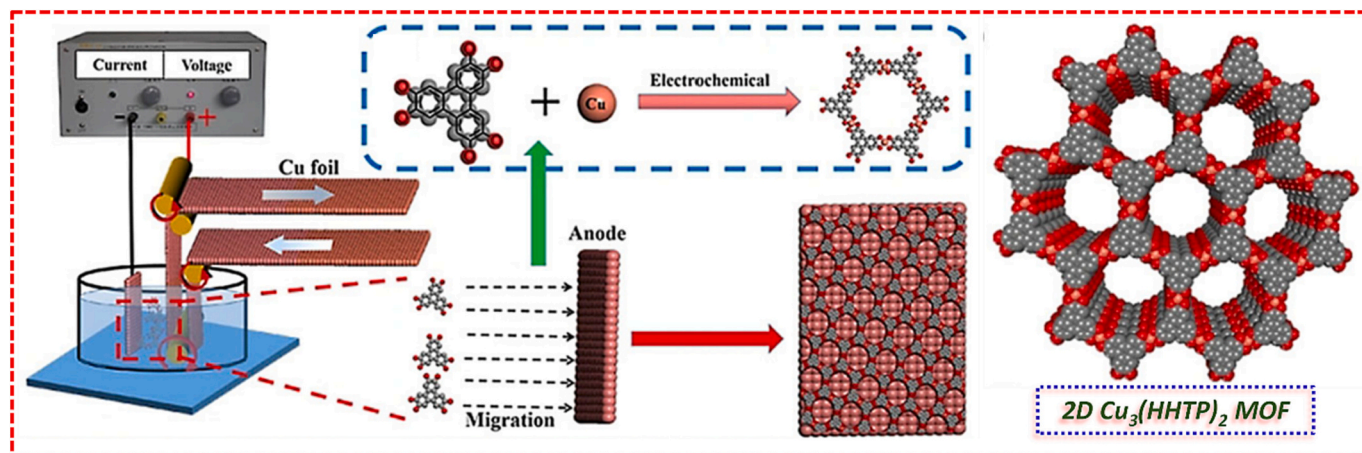


Fig. 19. Schematic demonstration of preparing 2D $\text{Cu}_3(\text{HHTP})_2$ MOF film via the electrochemical technique. Adopted with permission from Ref. [192], Copyright 2021, Wiley VCH, Janus.

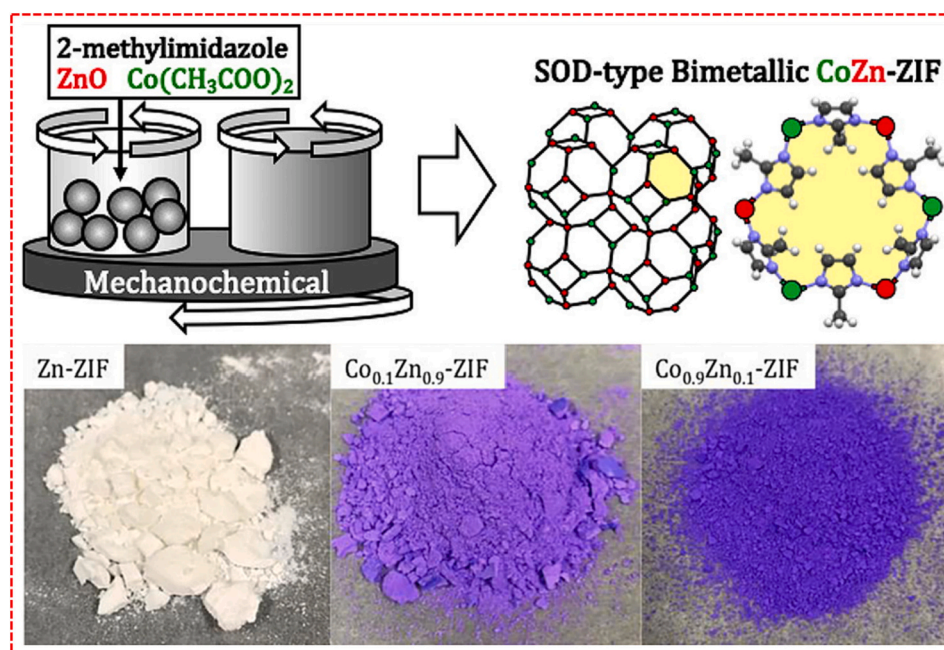


Fig. 20. Pictorial illustration of mechanochemical technique for the Zn-ZIF and CoZn-ZIFs preparation along with the desired products images. Adopted with permission from Ref. [211], Copyright 2019, Elsevier B.V.

depicting Zn-ZIF and bimetallic-ZIF precursors produced using this technique. The resulting powders showcase distinctive colors: Zn-ZIF appears as a white powder, ZIF-67 exhibits a deep purple, while Co_xZn_(1-x)-ZIF ranges from light to dark purple, depending on the value of *x*. The addition of cobalt acetate in the acetate-assisted mechano-synthesis prompts a reaction where acetic acid is released, subsequently reacting with 2-MIM. This process enhances the solubility of ZnO in acids and facilitates mass transfer via hydrated water and autoacetic acid. These factors collectively advance the complex reaction between the ionized metal and 2-MIM [212]. The acetate-aided milling technique suggested in these findings offers the advantage of controlling the Co/Zn ratio by regulating the acetate amount added. Furthermore, this method eliminates the need for solvents, treating the starting materials as solids. It holds significant promise in revitalizing industrial applications of ZIFs and opens new avenues for the development of multi-metal ZIF nanomaterials.

3.6. Sonochemical method

The sonochemical approach harnesses the chemical effects produced by subjecting a mixture to high-energy ultrasound during a reaction. This approach offers several notable advantages when applied to MOF synthesis, including rapid reaction kinetics, environmental friendliness, energy efficiency, and user-friendliness. Its potential for facilitating quick reactions makes it a promising candidate for the future mass production of MOFs [167]. Ahn and colleagues pioneered the sonochemical synthesis of MOF-177 in 2010 [213]. They also synthesized CuTATB-*n* (TATB = 4,4',4''-s-triazine-2,4,6-triyltribenzoate; *n* = power level), known as PCN-6, with an isorecticular structure akin to HKUST-1, using an innovative sonochemical route [214]. In this investigation, both catenated PCN-6 and non-catenated PCN-6' were produced by solely optimizing the ultrasonic power level within a span of 1 h, utilizing a DMF solution containing Cu(NO₃)₂ and H₃TATB as reactants. Similarly, IRMOF-9 (catenated) and IRMOF-10 (non-catenated) were also prepared using the identical approach, employing 4,4'-biphenyldicarboxylic acid (BPDC) as a linker. The application of higher ultrasonic power levels resulted in increased surface areas and improved porosity in the sonochemically synthesized products. Notably, particle size

exhibited gradual increments with higher ultrasonic power levels.

Morsali et al. [215] employed the sonochemical method to synthesize TMU-5 (bearing the acronym TMU for Tarbiat Modares University, formulated as [Zn(oba)(4-bpdh)_{0.5}]_n(DMF)_{1.5}) and TMU-6 ([Zn(oba)(4-bpmb)_{0.5}]_n(DMF)_{1.5}) (where oba stands for 4,4'-oxybisbenzoic acid; 4-bpdh = 2,5-bis(4-pyridyl)-3,4-diaza-2,4-hexadiene; 4-bpmb = 1,4-bis(pyridine-4-ylmethoxy)benzene). Their study delved into the impact of ultrasonic irradiation time and initial reagent concentration on the size and morphology of the resulting MOF particles. Their investigations revealed that a high initial reagent concentration led to the production of larger particles and induced a non-uniform distribution of particle sizes. Conversely, when the initial reagent concentration was low, the size of the MOF particles decreased. To facilitate nucleation, triethylamine (TEA) was introduced, which had the effect of boosting the nucleation rate. When TEA was utilized, fast nucleation occurred due to the deprotonation of the oba ligand. This accelerated nucleation process contributed to a reduction in particle size. A variety of metal ions are promptly integrated within molecular units to impart a broad spectrum of optoelectronic functionalities. In MOFs, the porphyrin units within the linker component form robust coordination bonds with valuable metal nodes, leading to enhanced chemical stability [216]. This feature is particularly advantageous as the well-dispersed and isolated porphyrin units in rigid porphyrinic MOFs prevent catalyst deactivation resulting from porphyrin molecule dimerization. Consequently, porphyrin is extensively utilized in MOFs constructed from tetrakis(4-carboxyphenyl)-porphyrin (TCPP) and metal nodes like Fe, Al, and Zr [217]. Zr-based MOFs, including MOF-525, MOF-545 (also known as PCN-222), PCN-221, PCN-223, PCN-224, PCN-225, and NU-902, are also under investigation [218]. Among these, MOF-525 and MOF-545 are produced using the same substrate as the Zr metal source and TCPP. Due to the frequent occurrence of mixed-phase particles, a variety of strategies, such as high-throughput combination, seed-mediated preparation, solvent-assisted separation, exploration of modulators, and the application of kinetic and thermodynamic control, have been employed to obtain pure phases of these MOFs [218,219].

Ahn et al. introduced a straightforward synthesis method for obtaining pure-phase MOF-525 and MOF-545 through modulation preparation using the sonochemical approach [220]. The synthesis of

MOF-525 and MOF-545 involved zirconyl chloride octahydrate, benzoic acid, trifluoroacetic acid, DMF, and TCPP. The resulting samples were designated as S-MOF-525 and S-MOF-545, respectively. For evaluation, conventional solvothermal synthesis was employed to produce MOF-525 and MOF-545, which were referred to as C-MOF-525 and C-MOF-545. Fig. 21 provides a pictorial representation of the sonochemical approach, depicting the structures of MOF-525 and MOF-545, and showcases the SEM images of MOF-525 and MOF-545 prepared under optimal conditions. Upon examining the morphology of S-MOF-525 and S-MOF-545 grown under various conditions, cubic and needle-shaped particles were observed, with some samples exhibiting a mixture of both morphologies as shown in the middle SEM image in Fig. 21. MOF-525 exhibits a ftw topology, comprising $Zr_6(OH)_4O_4(CO_2)_{12}$ clusters, whereas MOF-545 features a csq topology, composed of $Zr_6O_8(CO_2)_8(H_2O)_8$ clusters. The presence of mixed-form particles can be attributed to variations in the connectivity of Zr_6 clusters during the synthesis process [221]. In summary, sonochemical synthesis generates intense local temperatures and pressures due to acoustic cavitation, resulting in rapid heating and cooling rates. This phenomenon accelerates homogeneous nucleation and significantly reduces crystallization times [222]. As a result, this method offers several advantages, including shortened synthesis duration, reduced energy consumption, the formation of defect sites, improved textural properties of the material, and scalability for large-scale preparation [223]. This study demonstrates that the sonochemical approach for preparing Zr–/porphyrin-based MOFs yields highly pure, uniformly sized particles while drastically reducing synthesis times.

Table 2 provides a summary of merits and demerits associated with the various MOF preparation techniques discussed. MOFs hold immense potential for an extensive array of applications, making it crucial for industrial implementation to progress hand in hand. Luckily, as indicated throughout this review, new preparation techniques have emerged, blurring the lines between laboratory-scale and industrial production [224]. While it remains uncertain whether MOFs can rival established industrial compounds like zeolites, silica, or activated carbon, the extensive attention from researchers towards MOF applications suggests that this possibility is increasingly within reach.

Table 2

Merits and demerits of the preparation routes of MOF.

Preparation route	Merits	Demerits
Microwave	Quick preparation time and increased yield Simple and energy-efficient approach Easy transformation and tight control of response parameters Morphology control, phase selectivity, and particle distribution	Difficulty separating large single crystals
Conventional solution	MOFs crystallinity arises in a quick time Ambient atmosphere synthesis Normal, simple, easy	Small amount synthesis Relatively slow process
Sonochemical	Uniform shape and particle size can be obtained in a short time Energy efficient, and environmentally friendly. An appropriate method for the nanosized MOFs preparation	Sonication can shatter the crystallites and block the large single crystal formation
Electrochemical	Fast and clean synthesis Beneficial for batch scale preparation by providing enhanced selectivity and yield Equivalent MOF growth and direct deposition on platforms Precise layer deposition growth	—
Hydro/Solvothermal	Easy industrial transposition Broad working temperature range (e.g., 80–250 °C) A heating and cooling method can assist crystal growth.	Long reaction time High cost of purchasing the equipment required for the preparation High energy consumption
Mechanochemical	No particular pressure and temperature needed Solvent-free method	Secondary phases are usually obtained. Difficulty separating large single-crystals.

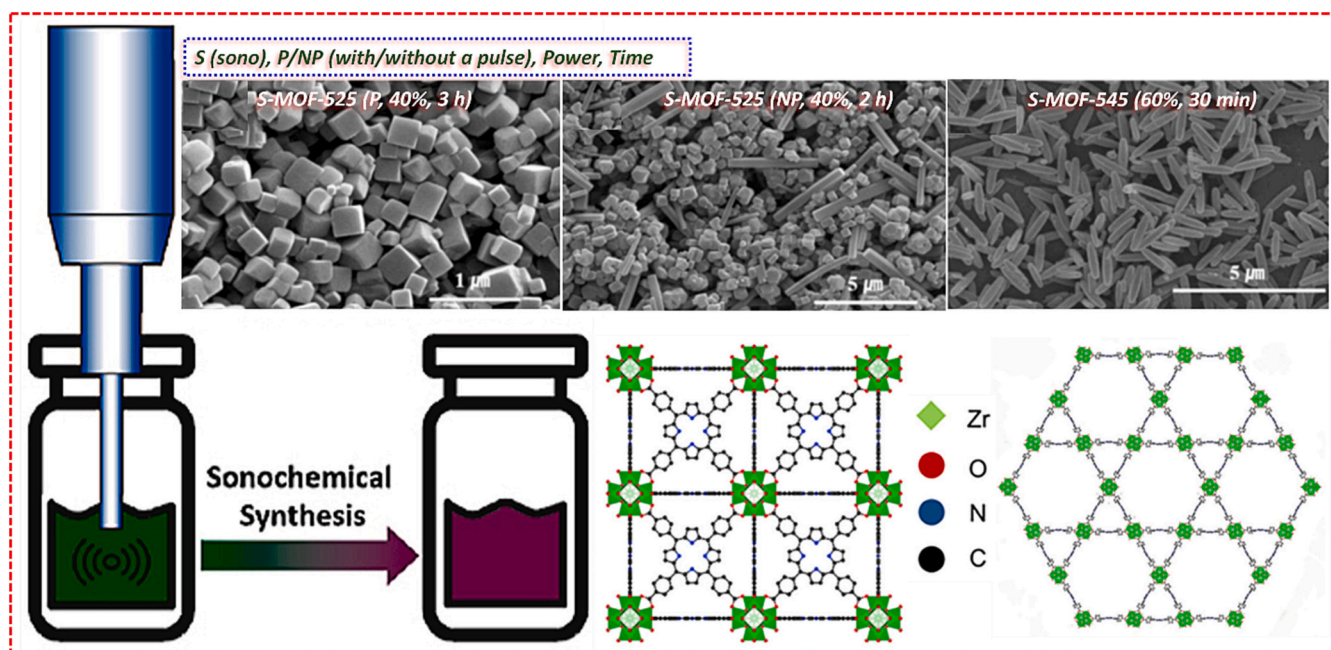


Fig. 21. Pictorial demonstration of the sonochemical technique, structures, and SEM analysis of MOF-525 and MOF-545. Adopted with permission from Ref. [220], Copyright 2021, Elsevier B.V.

4. Characteristics of MOF derived nanomaterials

MOFs present a class of highly structured materials with remarkable attributes, including useful compositions, high surface area, adjustable pores, even component distribution, and precisely described active sites [225]. Notably, MOFs are renowned for their exceptional surface area. In 2018, Hönicke et al. [226] introduced a novel mesoporous MOF (DUT-60) boasting an experimental record-breaking specific surface area of approximately $7800 \text{ m}^2 \cdot \text{g}^{-1}$, surpassing MIL-101 ($\sim 5900 \text{ m}^2 \cdot \text{g}^{-1}$) [35] and MOF-210 ($\sim 6240 \text{ m}^2 \cdot \text{g}^{-1}$) [227]. While numerous factors influence the design, structures, and properties of MOFs, the novel selection and coordination of metal cores, ligands, and solvents perform pivotal roles [228]. For instance, Farha et al. [229] examined the substitution of phenyl groups with ethynyl units as ligand expansion components. Theoretical calculations suggest a hypothetical maximum surface area of around $14,600 \text{ m}^2 \cdot \text{g}^{-1}$ with ethynyl units compared to phenyl units ($9950 \text{ m}^2 \cdot \text{g}^{-1}$) and phenyl ethynyl units ($12,250 \text{ m}^2 \cdot \text{g}^{-1}$). In the conventional solvothermal synthesis of MOF precursors, the organic linkers typically stay intact throughout the preparation route, leading to slow growth of crystal [230]. As a result, MOFs retain their distinctive frameworks, making them excellent templates for producing MOF-derived nanomaterials. Table 3 provides a summary of the porosity and surface characteristics of these nanomaterials derived MOF. These materials often exhibit larger surface areas compared to their MOF counterparts due to the specific temperature treatment circumstances applied during their transformation. Fig. 22 offers a concise overview of the characteristics of nanomaterials derived from MOF, highlighting their significant advantages, many of which are inherited from the pristine MOFs. Moreover, nanomaterials derived from MOF can be improved with post-functionalities, containing enhanced conductivity and increased stability of the material [234], in comparison to their pristine forms. While there are numerous reviews on metal/metal oxides derived from MOF [235], and PC [236], this particular review is focused on derivatives of TMCs (Sulfur, and Selenium), and phosphides derived from MOFs along with the metal/metal oxides derived from MOF, and PC for the applications in energy storage sectors.

5. Parameter alteration

While nanomaterials derived from MOF have demonstrated remarkable potential in various established energy storage and conversion devices, the quest for nanomaterials derived from MOF with superior performance compared to traditional inorganic materials remains a formidable challenge. This challenge is intimately tied to the morphology, composition, particle size, and surface area of nanomaterials derived from MOF. By carefully controlling the conversion

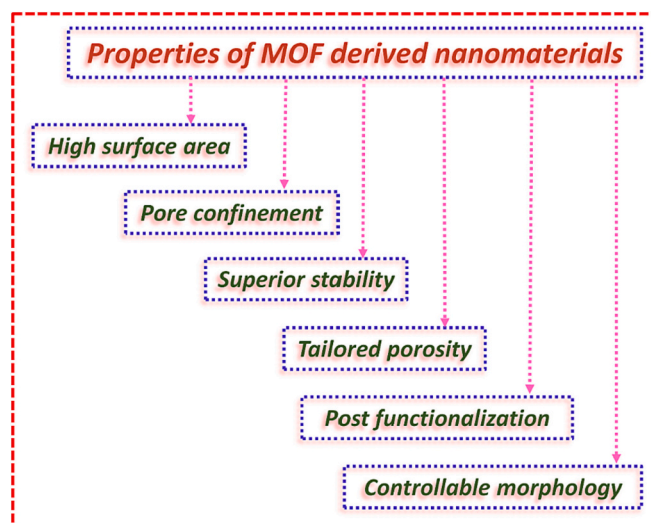


Fig. 22. Properties of MOF-derived nanomaterials.

mechanism parameters, including heating rate, temperature, time, and gas medium, it becomes possible to obtain derivatives with a wide range of morphologies, and compositions from MOF templates.

5.1. Temperature

The thermolysis activity of MOF templates is heavily influenced by temperature, which ultimately dictates the morphology, composition, surface area, and porous nature of resulting derivatives. In the case of carbon materials derived from MOF, greater temperatures promote the well-ordered GC structures formation with excellent conductivity. Nevertheless, extreme heating often leads to the loss of unique MOF morphology and partial or complete collapse of the porous structure. Moreover, elevated temperatures can significantly decrease the presence of heteroatoms (e.g., N, S, P), which typically serve as operational locations for rapid electrochemical reactions. In the context of metallic compounds, higher calcination temperatures tend to increase particle size substantially, resulting in a reduction of surface area. Thus, precise temperature control is crucial for achieving nanomaterials derived from MOF with exceptional physicochemical characteristics.

Zn dependent MOFs, such as ZIF-8 and MOF-5 are considered excellent sacrificial templates for producing ZnO@C nanocomposites (NCs) and PC products. Park and colleagues conducted a study in which they created ZnO QDs@PC NCs. These NCs featured uniformly distributed ZnO QDs measuring 2.3 nm in size, embedded within a carbon matrix. They achieved this by subjecting an IRMOF-1 precursor to thermal treatment at various temperatures. As the pyrolysis temperature increased, the ZnO particle size grew from 2.3 nm to 20 nm (Fig. 23a-c) [237]. In another investigation, researchers transformed well-distributed ZIF-8 polyhedra into 3D N-doped graphene-like particles (denoted as N-C-t, where t denotes the temperature of carbonization) through thermolysis [238]. When the heat treatment was elevated from 700 to 900 °C, the N-C products morphologies remained intact. However, the surface areas diminished, and the N doping content dropped significantly from 24.45 to 10.73 wt% (Fig. 23d-g). Typically, excessive N amount can lead to structural uncertainty, while short N amount may result in limited active sites. Consequently, an adjusted sample, N-C-800, with N amount of 17.72 wt%, exhibited tremendous performance in LIBs with impressive cycle stability and rate performance. Furthermore, Wei and his research team informed the preparation of N-doped PC materials derived from ZIF-8 [239]. When the pyrolysis temperature was increased to 1100 °C, the original ZIF-8 morphology was lost, and the porous structure collapsed (Fig. 23h-k). Consequently, these materials exhibited poorer electrochemical performance.

Table 3

Pore characteristics of MOF as well as MOF derivatives.

MOF	MOF derivatives	MOF transformation	Ref.
MOF-5 SSA_477 $\text{m}^2 \cdot \text{g}^{-1}$ PV_0.33 $\text{cm}^3 \cdot \text{g}^{-1}$	Porous carbon SSA_1884 $\text{m}^2 \cdot \text{g}^{-1}$ PV_1.84 $\text{cm}^3 \cdot \text{g}^{-1}$	Ar (1000 °C/2 h) followed by washing with HCl	[231]
Ni-Zn-MOF SSA_46 $\text{m}^2 \cdot \text{g}^{-1}$ PD_24 nm	NiO@ZnO SSA_67 $\text{m}^2 \cdot \text{g}^{-1}$ PD_17 nm	Ar (800 °C/2 h)	[232]
MOF-5 SSA_835 $\text{m}^2 \cdot \text{g}^{-1}$ PV_0.38 $\text{cm}^3 \cdot \text{g}^{-1}$	Porous carbon SSA_2393 $\text{m}^2 \cdot \text{g}^{-1}$ PV_1.13 $\text{cm}^3 \cdot \text{g}^{-1}$	Ar (1000 °C/5 h)	[233]

SSA_ specific surface area, PV_ pore volume, PD_ pore diameter.

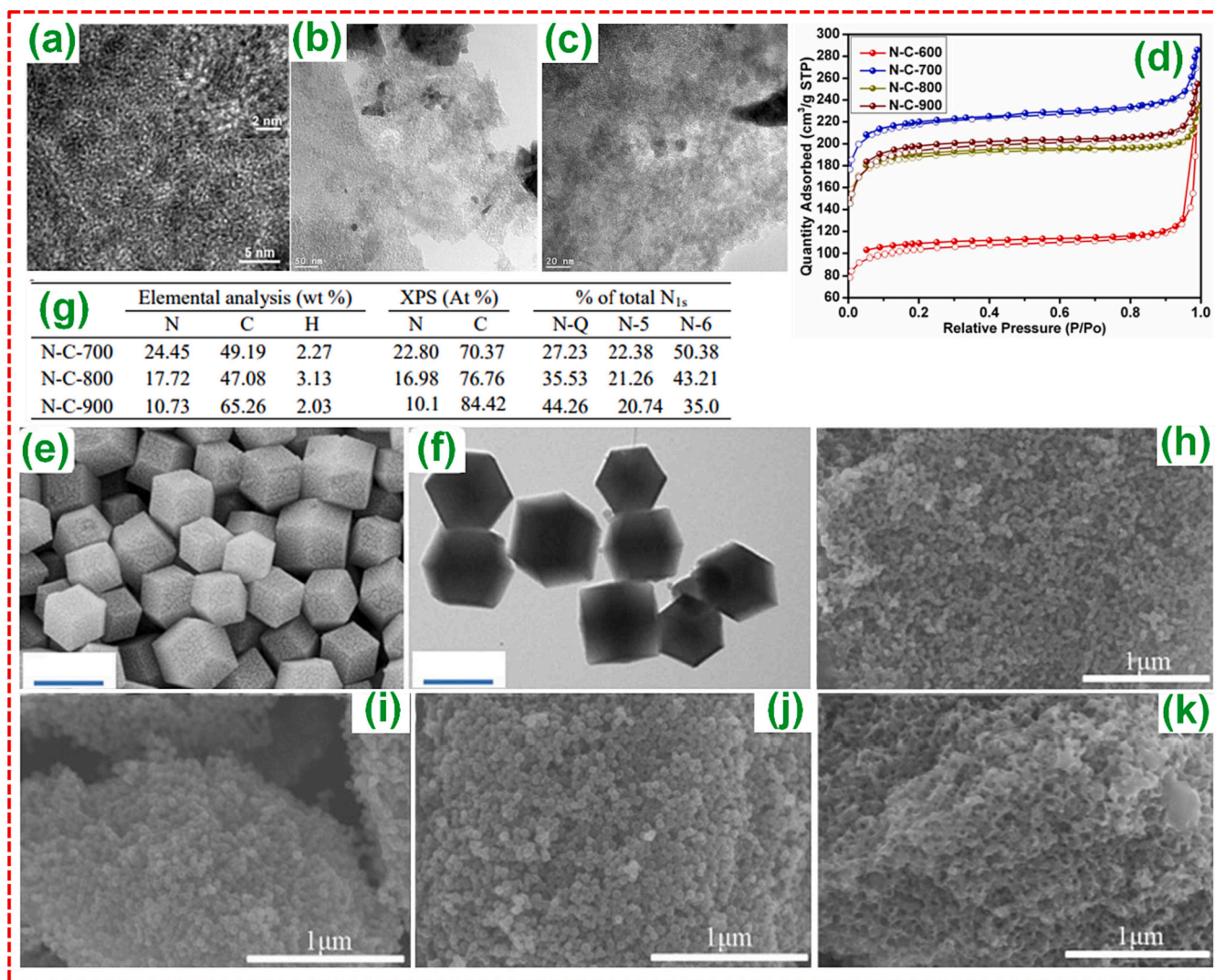


Fig. 23. (a-c) TEM analysis of ZnO QDs@PC-550, ZnO QDs@PC-600, and ZnO QDs@PC-700 derived from IRMOF-1, respectively. Adopted with permission from Ref. [237], Copyright 2013, American Chemical Society. (d) N₂ adsorption/desorption isotherm study, (e,f) SEM analysis, and (g) configuration of NDC products produced at various temperatures. Adopted with permission from Ref. [238], Copyright 2014, Springer Nature. (h-k) SEM analysis of ZIF-8 derived PC products achieved at 800, 900, 1000, and 1100 °C, respectively. Adopted with permission from Ref. [239], Copyright 2016, Elsevier B.V.

Co-based MOFs, particularly ZIF-67, which consists of Co²⁺ ions and methylimidazole ligands, are commonly employed templates for producing numerous materials, including metal/metal oxides, PC, and its NCs. Interestingly, the pyrolysis temperature appears to have a minimal influence on overall morphology of the MOF-derived materials. These materials essentially comprise composites containing metal/metal oxides within NDC matrices or CNTs. However, the pyrolysis temperature portrays a crucial job in determining the NP size of the metals/metal oxides and the extent of N-doping. For instance, when the temperature was increased from 435 to 800 °C, the morphologies of maximum ZIF-67 derivatives underwent a transformation characterized by the CNTs growth on the surface of carbon shells. This transformation was primarily driven by the catalytic activity of Co NPs (Fig. 24) [125,240–242].

However, the surface area and NP diameter of these NCs were significantly affected. Cobalt NP sizes obtained at 435 °C and 550 °C were measured at 5 nm and 10 nm, respectively. In addition to ZIF-67, other Co-based MOFs have been explored as templates to understand the impact of heat treatment temperature on the physicochemical characteristics of their derived materials [243]. Recently, Co/Co₃O₄ NPs enclosed within NDC shells were synthesized using Co-based MOF

templates. This was achieved by adjusting the temperature from 600 °C to 800 °C [244]. It is observed that temperature really had a significant impact on surface area, particle size, and the N-doped content, with trends like those observed in the ZIF-67 derived NCs mentioned earlier. Moreover, the thermolysis temperature influenced the phase composition of the resultants. Wu and colleagues exhibited a strategy involving MoO₃@ZIF-67 to produce various 1D Mo dependent/carbon composites with diverse architectures. When the temperature was raised from 600 °C to 700 °C, core shelled MoO₃/C and Mo₂C/C materials were achieved (Fig. 25a) [245]. Precisely, a Co-based MOF containing cages and modified with Fe and dicyandiamide was exposed to various temperatures (800 °C, 900 °C, and 1000 °C) in the inert atmosphere, resulting in the Fe₃C/N-doped PC materials formation with varying carbon morphologies, including onion type carbon, tubular carbon, and tubular graphene/N-doped graphene structures (Fig. 25b) [246].

Indeed, it appears that the morphologies of Fe containing MOF derived NCs are more influenced by the heating temperature. This could be attributed to an arbitrary distribution of Fe species within the templates. For example, in a study conducted by Chen and colleagues, Fe-MIL-88 loaded with melamine was subjected to pyrolysis in a N₂ atmosphere, resulting in the formation of Fe₃C NRs enclosed within a

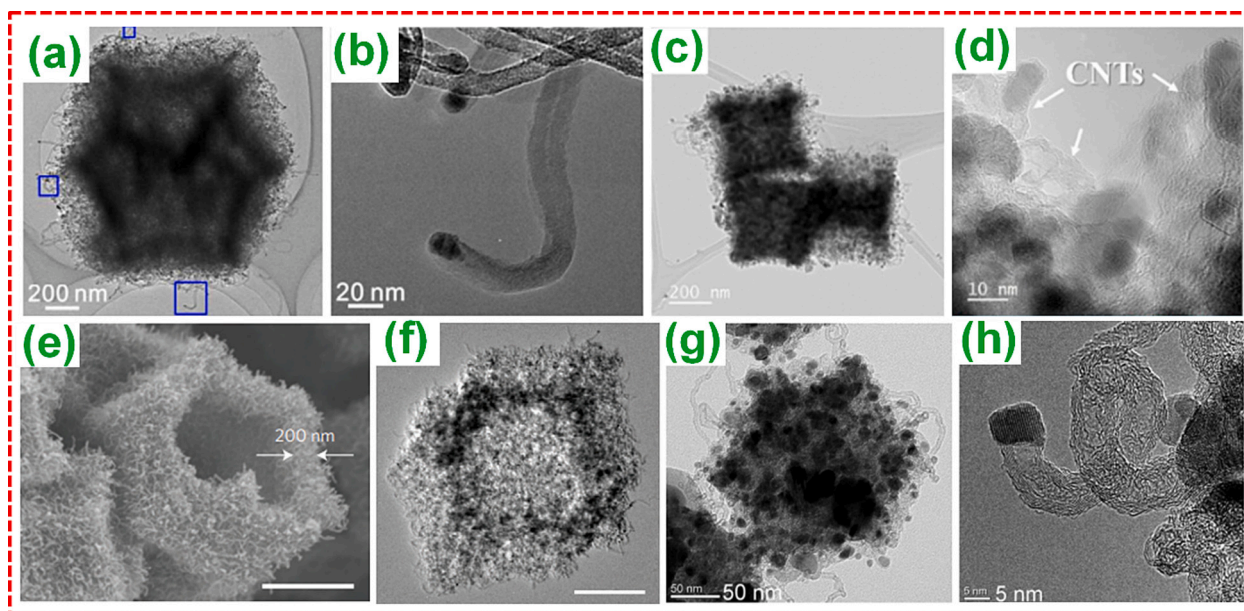


Fig. 24. (a, b) TEM analysis of N-CNT-assembled hollow dodecahedra derived from ZIF-67 achieved at 435 °C. Adopted with permission from Ref. [125], Copyright 2017, American Chemical Society. (c, d) TEM analysis of CoSe₂@N-PGC/CNTs nano cubes derived from ZIF-67 achieved at 550 °C. Adopted with permission from Ref. [240], Copyright 2017, Elsevier B.V. (e, f) SEM and TEM analysis of N-doped CNT frameworks derived from ZIF-67 attained at 700 °C. Adopted with permission from Ref. [241], Copyright 2016, Springer Nature. (g, h) TEM analysis of Co@Co₃O₄/NC derived from ZIF-67. Adopted with permission from Ref. [242], Copyright 2016, Wiley VCH, Janus.

porous carbon structure [247]. When the temperature was varied from 700 °C to 900 °C, the morphology of the carbon component slowly transformed from wrinkled NDC layers to N-doped CNTs (Fig. 26a). Specifically, after annealing at 800 °C, N-doped CNTs were observed to grow on a N-doped PC sheet (NCNT/NCP). Concurrently, the alteration in N amount indicated that greater temperatures led to the carbon component formation with superior conductivity (Fig. 26b). Besides the studies mentioned above, temperature variation has been employed in the study of various other MOFs, including V-MOF [248], Cu-MOF [249], In-MOF [250], Ti-MOF [251], and Ni-MOF [252], with detailed results summarized in Table 4.

5.2. Gas atmosphere

The composition of materials derived from MOF is indeed determined by the gas medium used during the heat treatment process. When MOFs are pyrolyzed in ambient atmosphere, they typically yield subsequent metal oxides. Conversely, pyrolysis of MOFs in inert gases like N₂ or Ar, without subsequent acid etching, results in the formation of NCs composed of metals, oxides/carbides/sulfides of metals, and carbon. The specific inorganic elements formed depend largely on the metal type and the synthesis conditions. In general, pyrolyzing MOF precursors in an inert atmosphere led to the production of metal NP/single metal atom/carbon composites. These materials find significant interests in electrocatalysis and metal-air batteries [254]. For instance, a highly reactive and stable isolated single-atom Fe/N-doped PC (ISA Fe/CN) catalyst, with Fe loading till 2.16 wt%, was recently produced from Fe-doped ZIF-8 precursors through thermal treatment in an Ar environment [255]. Afterward, Li and colleagues expanded this approach to create a single metal atom/carbon catalysts by pyrolyzing MOF templates in Inert gas atmospheres, incorporating N species stabilized Ru₃ clusters and single W atoms assisted by NDC products [256]. Moreover, it's important to note that these materials often exhibit poor electrochemical performance and provide minimal capacity contribution when employed in metal ion batteries, specifically LIBs and SIBs. Hence, it is crucial to employ a mixture of inert and ambient atmospheres during pyrolysis. Under these conditions, the metal/PC composites can be

further transformed into metal oxides/porous carbon composites, resulting in increased performance for LIBs, SIBs, and PIBs. Certainly, various gas atmospheres perform a pivotal task in shaping the composition and morphology of nanomaterials derived from MOF during the pyrolysis route. Here are some examples:

Inert Atmosphere (N₂ or Ar): Pyrolyzing MOFs in these atmospheres can lead to the formation of metal nitrides and highly N-doped PC. For instance, micro spherical Ni-MOF was annealed in Inert atmosphere to produce a Ni/graphene composite. Subsequent pyrolysis in air resulted in hierarchical NiO/Ni/graphene composites with a hollow and ball-in-ball structure [257]. NH₃ atmosphere has also been used as a N source for creating highly N-doped PC [258]. Additionally, post-treatment processes like sulfuration and phosphorization have been integrated with inert atmospheres to derive sulfides/phosphides of metals [259,260].

Mixed Atmosphere (e.g., H₂/Ar, C₂H₂/N₂, H₂/He): The use of mixed atmospheres enables the regulation of composite materials and morphology. For instance, a thermal treatment in H₂/Ar environment at 700 °C, followed by acid leaching of ZIF-67 particles, induces the hollow structure formation. In the absence of H₂, polyhedron-shaped particles are derived [242]. Another study involves choosing a mixed C₂H₂/N₂ environment during heat treatment, resulting in Co/Co₃ZnC@N-CNT derived from a Co/Zn-ZIF-67 template. Importantly, C₂H₂ gas acts as the carbon source for forming CNTs catalyzed by the Co metal catalyst. If N₂ replaces C₂H₂/N₂, no CNTs are formed after heat treatment (Fig. 27) [261]. These examples illustrate how tailoring the gas atmosphere during pyrolysis offers precise control over the composition and morphology of MOF-derived materials, expanding their potential applications.

5.3. Duration time

Indeed, the duration time performs a significant role in modulating the properties of materials derived from MOF other than temperature and gas medium. Here are some examples illustrating its significance:

Porous Carbon Formation: Sun et al. developed a straightforward approach for creating PC by in-situ ZIF-8 carbonization in an Ar

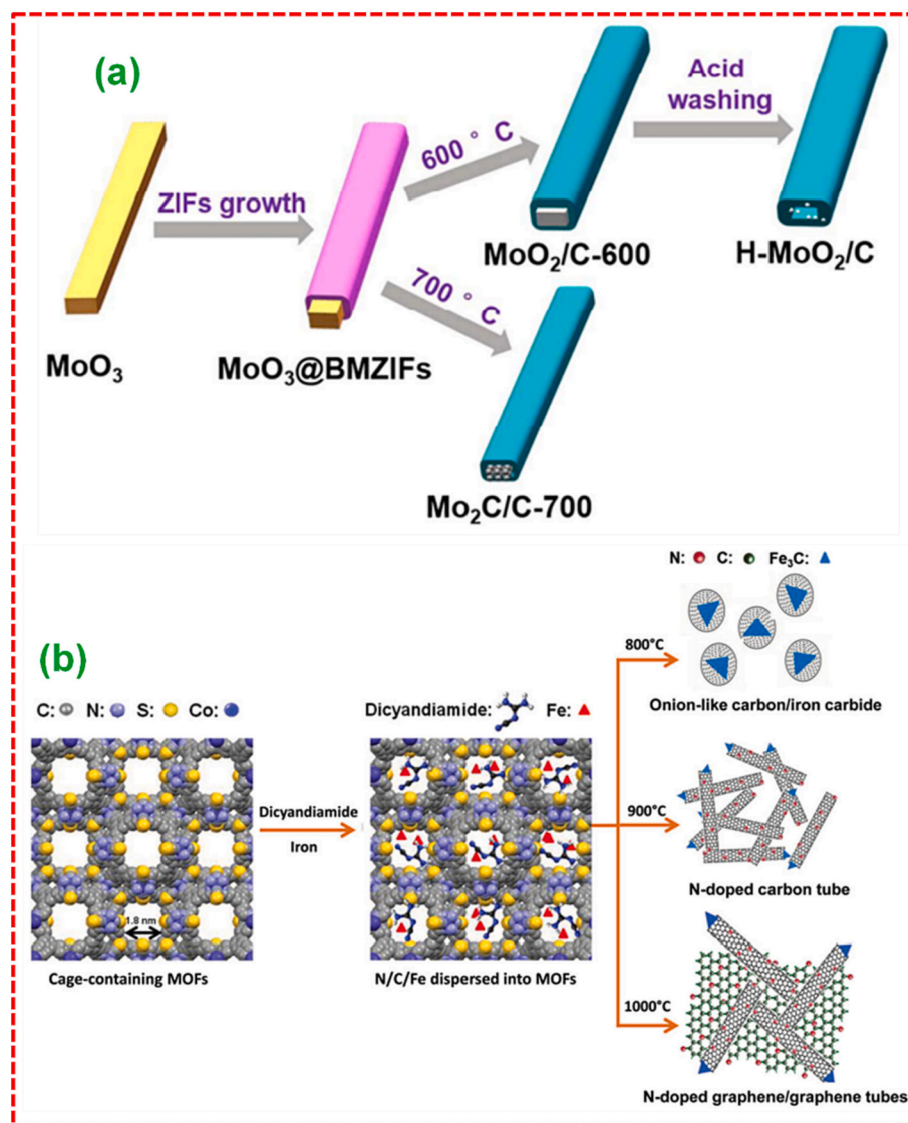


Fig. 25. (a) Schematics of carbon deposited Mo-based composites. Adopted with permission from Ref. [245], Copyright 2018, American Chemical Society. (b) Pictorial demonstration of carbon nanomaterials formation prepared at various calcination temperatures. Adopted with permission from Ref. [246], Copyright 2013, Wiley VCH, Janus.

atmosphere followed by NH_3 treatment. The duration time in NH_3 atmosphere significantly impacted the surface area and porous structure of the resulting PC materials. Extending the treatment time from 3 to 5 and 7 min led to an increase in pore volume and the construction of a hierarchically nano PC material [262].

Phase Composition Control: In recent work, different cobalt sulfides were prepared by handling the Co-MOF template with varying duration times. A pure phase $\text{CoS}_{1.097}$ was achieved under 1 h of treatment, while increasing the duration time to 2 h resulted in the formation of a mixed phase Co_9S_8 and $\text{CoS}_{1.097}$ (Fig. 28). Interestingly, a single-phase Co_9S_8 could be achieved by replace with H_2/Ar for Ar atmosphere [263]. These examples demonstrate that adjusting the duration time during MOF-derived material synthesis can be a powerful tool for tailoring properties such as surface area, pore structure, and phase composition.

To gain a comprehensive understanding of how the duration time during the thermolysis activity influences the composition, morphology, and size of MOF-derived materials, advanced characterization methods like X-ray absorption fine structure spectroscopy (XAFS), high-energy X-ray diffraction (HEXRD), and hard X-ray photoelectron spectroscopy (HAXPES) have been employed. Sakata and colleagues conducted an in-

depth investigation into the alterations in local geometrical and electronic properties of thermally decomposed Ni-MOF-74 at numerous temperatures and duration times [264]. Their findings, based on HEXRD and Fourier transform (FT) analysis, revealed that extending the duration time facilitated the complete precipitation of face-centered cubic (fcc) Ni metallic clusters and the orderly growth of fcc-Ni metal nanoclusters within the MOF matrix. Specifically, when the duration time was increased from 12 to 24 h, the particle size of Ni NPs grew from 4.5 ± 1.2 nm to 5.0 ± 1.2 nm. Furthermore, EXAFS data indicated that the larger NP size of Ni resulted in a notably lower coordination number, a characteristic that can be advantageous for selective catalysis. Despite these insights, it's worth noting that there is a limited body of research dedicated to systematically exploring the relationship between duration time and the structural, compositional, particle size, and surface area properties of nanomaterials derived from MOF.

5.4. Heating rate

The heating rate performs an important role in determining the graphitization degree of the carbon component, controlling the particle size of MOF-derived materials, and influencing whether the initial

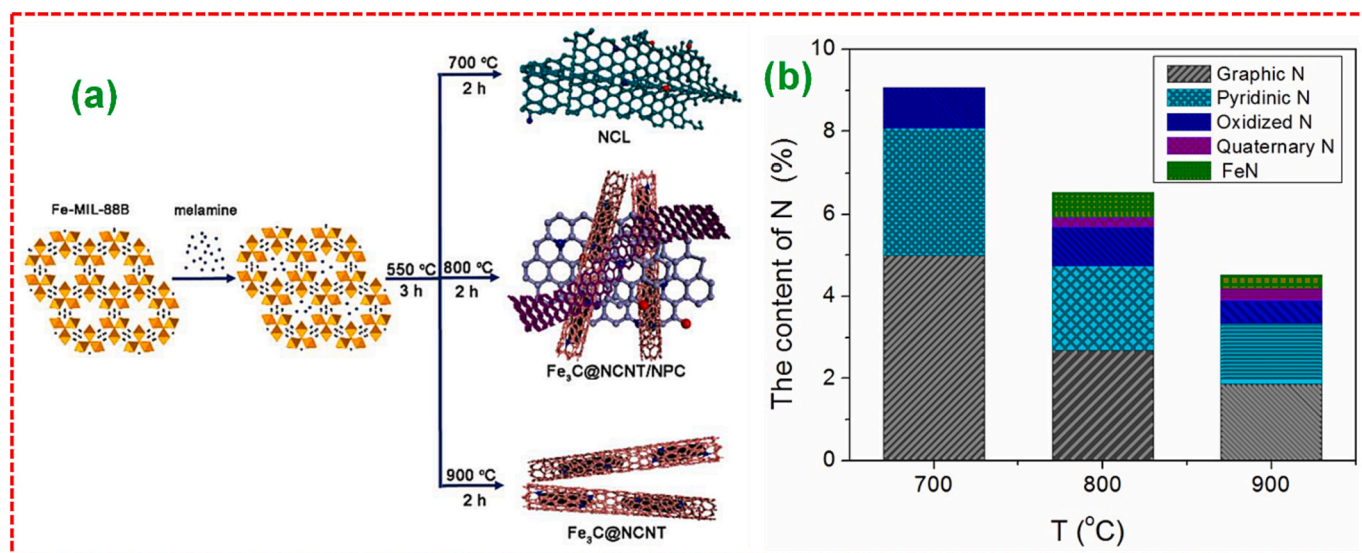


Fig. 26. (a) Pictorial demonstration of morphology dependent preparation and (b) the amount of N in Fe-N-C catalysts. Adopted with permission from Ref. [247], Copyright 2016, Royal Society of Chemistry.

Table 4

Parameters of MOF derived nanomaterials obtained by the annealing of pristine MOFs at various temperatures.

MOF derivatives	MOF Precursors	Temperature (°C)	Morphology	Surface area (m ² g ⁻¹)	Pore Volume (cm ³ g ⁻¹)	N amount (wt%)	Ref.
In ₆ S ₇ -confined PC materials	In-MOF	700	Micro-particles	408	0.29	0.4	[250]
		800		338	0.2	0.58	
		900		448	0.4	0.35	
Hierarchical VO _x /PCs	V-MOF	500	Rods	—	—	—	[248]
		600	Rod morphology consists of slit type pores	84.92	—	—	
		700	—	—	—	—	
		800	—	—	—	—	
		900	—	—	—	—	
Anatase TiO ₂ /C	MIL-125 (Ti)	600	Tablet morphology with decrease in size and surface roughness increased	227.5	0.161	—	[251]
Anatase TiO ₂ /C		700		275.8	0.171	—	
Anatase/rutile TiO ₂ /C		800		350.9	0.2199	—	
Rutile TiO ₂ /C	Cu-MOF	900	Highly disordered structure	406.5	0.28	—	[249]
NDC materials		600		37	0.14	29.42	
		700		27	0.13	25.78	
		800		35	0.13	20.38	
		900		29	0.10	13.32	
Mesoporous NiO NRs	Ni-MOF	500	NP-integrated NRs to NPs	30.2	—	—	[253]
		600		18.5	—	—	
		700		11.2	—	—	
Ni confined in N doped carbon	Ni-MOF	600	Sphere-type structure bounded by few-layered graphene	116.5	—	0.89	[252]
		700		114.6	—	1.31	
		800		122.9	—	0.95	
		850		101.3	—	—	
		900		80.7	—	0.37	

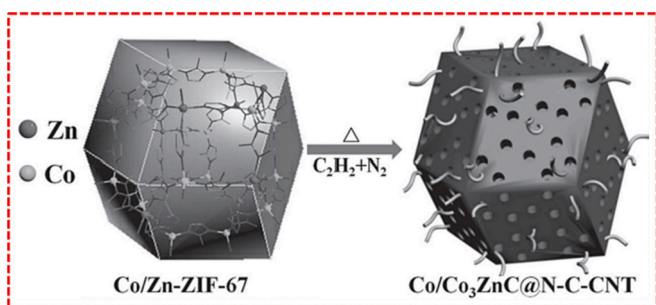


Fig. 27. Pictorial demonstration of the preparation of Co/Co₃ZnC@N-C-CNT rhombic dodecahedron composite. Adopted with permission from Ref. [261], Copyright 2016, Wiley VCH, Janus.

morphology of MOFs can be preserved. To illustrate this, Ji and colleagues conducted a study where they carried out controlled thermolysis of PB with Se, resulting in the series of rod type NDC-coated FeSe₂ NCs. They systematically increased the ramping rate from 1 °C min⁻¹ to 5 °C min⁻¹ and 10 °C min⁻¹ [265]. Their findings revealed that a faster heating rate led to an improvement in the crystallinity of the derived materials. However, this increase in crystallinity did not translate into enhanced capacitive behaviors when these materials were utilized as anodes for SIBs. Additionally, faster heating rates resulted in the formation of larger particles. This effect can be attributed to the fact that a rapid heating rate reduced the activation energy required for grain growth, leading to faster grain growth and a broader size distribution of particles. In contrast, a slower heating rate favored the orderly construction of carbon structures, resulting in thinner and more uniform carbon layers as depicted in Fig. 29 due to more controlled growth processes. In another illustrative study, Chen and colleagues successfully

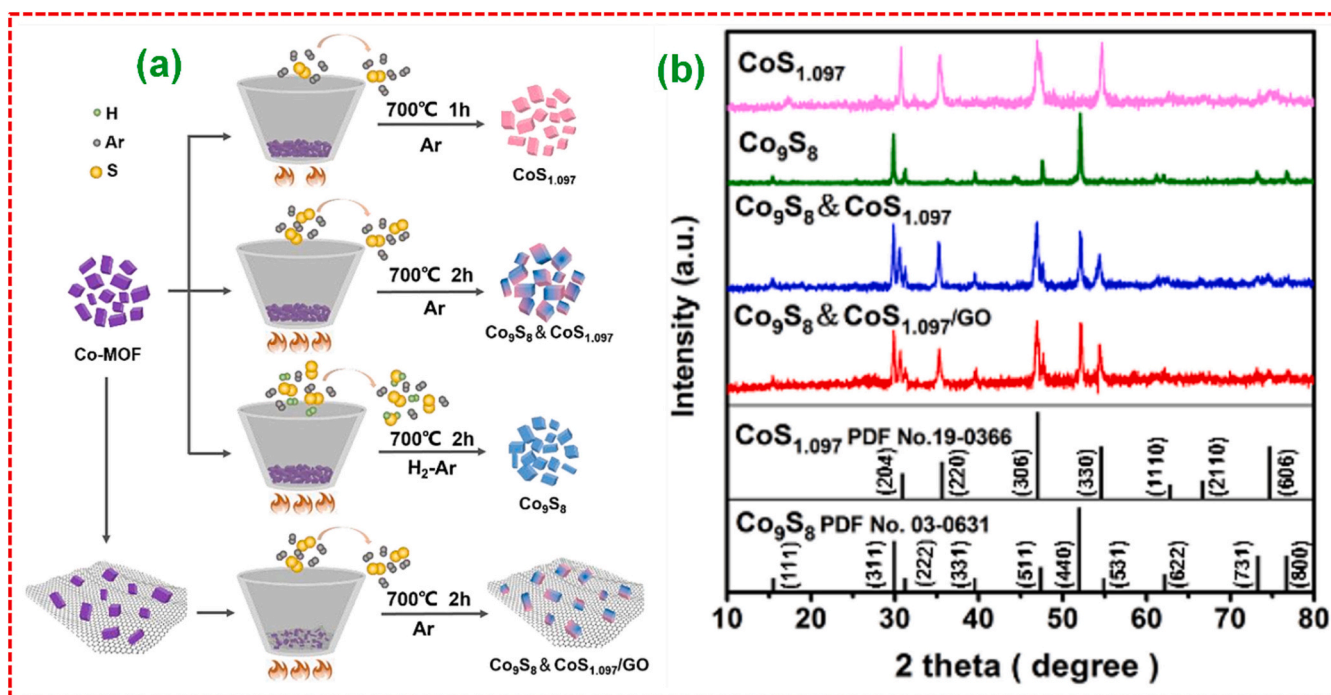


Fig. 28. (a) Pictorial demonstration of preparation of CoS_{1.097}, Co₉S₈&CoS_{1.097}, and Co₉S₈ by varying the atmosphere and operating time. (b) XRD analysis of all the prepared moieties. Adopted with permission from Ref. [263], Copyright 2018, Wiley VCH, Janus.

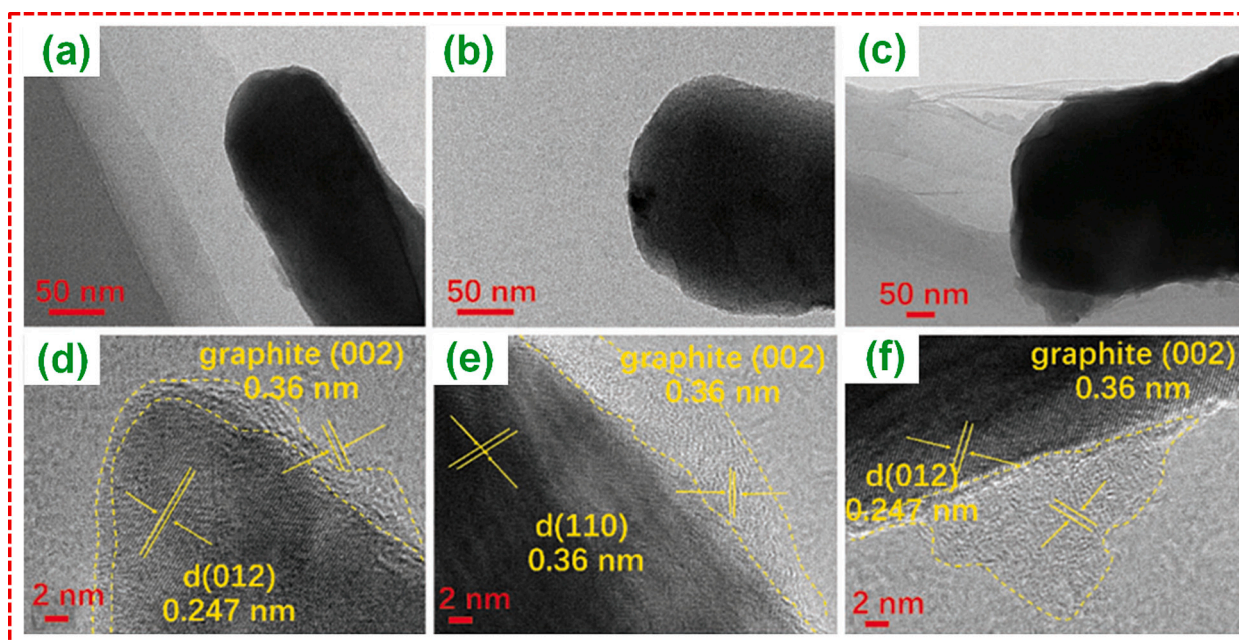


Fig. 29. TEM and HRTEM analysis of FeSe₂ coated with NDC derived from PB at various ramping rates: (a, d) 1 °C min⁻¹, (b, e) 5 °C min⁻¹, (c, f) 10 °C min⁻¹. Adopted with permission from Ref. [265], Copyright 2018, Wiley VCH, Janus.

produced hierarchical ZnO/NiO microstructures with varying morphologies by precisely controlling the ramping rate during the thermolysis process [266]. Their results showcased that a seaweed-like morphology, characterized by abundant nanosheets (NSs), was achieved when employing a higher ramping rate of 5 °C min⁻¹. Conversely, a lower heating rate of 1 °C min⁻¹ led to the formation of aggregates consisting of NPs. This study highlights the undeniable influence of the ramping rate on the morphology, particle size, and the presence of carbon in materials derived from MOF. It also underscores the feasibility

of tailoring the morphologies of these materials to meet specific requirements by selecting an appropriate heating rate.

The various studies mentioned above clearly demonstrate the substantial impact of pyrolysis parameters on the physicochemical properties of nanomaterials derived MOF. The choice of temperature of heat treatment can govern the extent of framework maintenance, the quantity of heteroatoms, particle size, and electrical conductivity. In contrast, the gas medium primarily influences the composition of MOF derived nanomaterials, whether they consist of carbon/metal oxides/

composites. Furthermore, the duration time plays a crucial role in determining the particle size of nanomaterials derived from MOF, while the ramping rate straight affects the degree of graphitization of the carbon materials, the particle size of MOF derived nanomaterials, and the preservation of morphological features. Although each of these pyrolysis parameters individually contributes to the alteration of the physicochemical properties of MOF derived nanomaterials, it's essential to recognize that the alteration from MOF templates to high-quality nanomaterials relies on the synergistic interplay of temperature, gas medium, duration time, and ramping rate. Hence, in the MOF pyrolysis process, a comprehensive consideration of these factors is imperative to enhance the physicochemical properties and, subsequently, the electrochemical performance of nanomaterials derived from MOF.

6. Electrochemical applications

Over the past decade, there has been a substantial emphasis on advancing energy storage devices, particularly in the context of LIBs, SIBs, and PIBs. These endeavors are driven by the urgent need to tackle rising energy consumption and the resulting environmental concerns. Given the shared physical and chemical properties of Li, Na, and K, LIBs, SIBs, and PIBs operate on similar principles of energy storage. A pivotal aspect in enhancing the electrochemical performance of both these technologies revolves around the identification and development of advanced electrodes. Consequently, the pursuit of highly promising, high-performance materials for use in LIBs, SIBs, and PIBs has emerged as a prominent research area in the fields of electrochemistry and materials science. In essence, the ideal electrode materials for achieving exceptional Li/Na/K storage performance should meet several critical criteria:

- They should feature nanoscale voids and open channels that facilitate thorough infiltration by the electrolyte.
- A high specific surface area is crucial to maximize the interface between the electrode and electrolyte.
- Exceptional electrical conductivity is essential to promote efficient transfer of both mass and electrons.
- The presence of hollow or porous structures is necessary to accommodate the volume changes that occur during the cycling activity.

MOFs have emerged as highly favorable sacrificial templates for crafting porous nanomaterials that align perfectly with these requirements. Nanostructures derived from MOFs offer several advantages, including precise control over chemical composition, tunable porosity, a substantial surface area, and reduced distances for both electron and ion transport [267]. Furthermore, when considering their use in LIBs, SIBs, and PIBs, MOF-derived nanostructures exhibit two additional strengths compared to other materials. Initially, their exceptional porosity and extensive surface area play a pivotal role in expediting ion transport and insertion processes, ensuing in improved reversible capacity and more efficient kinetics. Additionally, the presence of ample cavities, often accompanied by carbonaceous components, helps to alleviate structural strain during the repetitive insertion and extraction of Li/Na/K-ions, thus promoting an extended cycle life [268]. These remarkable characteristics are closely associated with the thermolysis activity of MOF templates. This segment provides a comprehensive overview of recent notable advancements in utilizing MOF-derived nanostructures as an anode for LIBs, SIBs, and PIBs, while also exploring the intricate relationship between pyrolysis parameters, nanomaterials derived from MOF, and its performance in LIBs, SIBs, and PIBs.

6.1. Li-ion batteries

Since their commercial debut in the 1990s [269], LIBs have become emblematic representatives of next-generation electrochemical energy

storage sector, offering significant utility in the realm of portable electronic devices. This recognition is primarily attributable to their relatively high theoretical energy density, enduring cycle stability, and minimal self-discharge [270]. Despite notable advancements, such as the integration of LIBs into hybrid electric vehicles, their energy density and intrinsic low power density still require enhancement to meet the escalating demands of future markets. LIBs comprise various components, including the cathode, anode, separator, and electrolyte. Among these, the anode is particularly crucial as it facilitates the reversible absorption and release of Li-ions originating from the cathode. The widely adopted graphite anode, known for its low specific capacity of 372 mAh g^{-1} , falls short of satisfying the growing market demands. Therefore, the development of promising anodes with improved electrochemical performance is of paramount significance. MOF-derived nanostructures, renowned for their high chemical and mechanical stability, extensive surface area, and adaptable pore structure, have proven to be formidable alternatives to conventional inorganic materials and NCs for addressing this challenge [268].

6.1.1. Metal oxides derived from MOF

Metal oxides (MOs) are gaining prominence as favorable options to the industrial graphite anode owing to its abundant resources, cost-effectiveness, and higher reversible capacities, which often exceed 600 mAh g^{-1} . These capacities are attained via conversion reactions that occur during the charge/discharge processes [271]. Though, traditional MOs as anodes often face challenges such as limited rate performance and poor capacity retention. As a result, there is a growing interest in exploring novel MOs, especially those with adjustable sizes and controllable morphologies. The pyrolysis of MOFs in an air environment has proven to be an effective method for producing various types of MOs with enhanced Li storage performance. The specific enhancements typically depend on the kinds of metal ions used and the inherent structures of the MOFs. Recent developments in MOF-derived MOs, featuring varied morphologies, and their applications in LIBs are summarized in Table 5.

MOFs can act as sacrificial templates for the synthesis of MOs. Mixed-valence Co_3O_4 has attracted significant interest due to their impressive theoretical capacity of 890 mAh g^{-1} , depending on an 8-electron conversion mechanism. Various Co_3O_4 related materials have been successfully synthesized through the Co-MOFs calcination and have been explored for their potential as an anode in LIBs [281]. For example, the Xu research group developed agglomerated Co_3O_4 NPs, with a diameter of approximately 250 nm, consisting of smaller Co_3O_4 NPs, each around 25 nm in size. This material was created by heating Co-MOFs to 600°C in ambient environment with a ramping rate of $10^\circ\text{C min}^{-1}$ [299]. While this material revealed a high reversible capacity of 965 mAh g^{-1} after 50 cycles, it faced challenges in terms of rate capacity and cycle stability. Subsequently, numerous Co_3O_4 heterostructures were synthesized by Co-MOFs as either sacrificial templates or precursors, revealing that morphology shows a critical role in influencing the electrochemical performance of Co_3O_4 .

Han and colleagues successfully prepared a hollow Co_3O_4 with enhanced Li-storage through a two-way annealing process using parallel-leveled Co-MOF in an air environment (Fig. 30a) [300]. Moreover, Tian et al. also achieved Co_3O_4 hollow tetrahedra by calcination of a Co-MOF at 500°C in ambient environment (Fig. 30b) [301]. The distinctive structure of Co_3O_4 contributed to its outstanding rate capabilities with capacities of 1196 mAh g^{-1} at 50 mA g^{-1} and 1052 mAh g^{-1} at 200 mA g^{-1} after 60 cycles, respectively. Furthermore, the same research group reported 2D Co-BDC nanoplates composed of Co^{2+} and BDC^{2-} by the diffusion-mediated control technique in the absence of structure directing agents. Subsequently, in another study wrinkled porous Co_3O_4 NSs prepared through annealing process (Fig. 30c) [272]. These Co_3O_4 NSs offered increased porosity, larger surface areas, higher aspect ratios, and more accessible sites, resulting in improved retention in capacity and rate capacity compared to bulk-type Co_3O_4 . The material

Table 5

Metal oxides derived from MOF for LIBs.

MOF derived MOs	Pristine MOF	Initial discharge/charge capacity (mAh g ⁻¹)	Current density (A g ⁻¹)	Cycle number	Capacity after cycles (mAh g ⁻¹)	Ref.
Co ₃ O ₄ NSs	Co-BDC nanoplates	1392/961	1.0	200	775	[272]
Co ₃ O ₄ hollow dodecahedrons	ZIF-67	1735/1083	0.1	140	1265	[273]
NiCo ₂ O ₄ /NiO hollow dodecahedron	ZIF-67	1622/1030	0.2	100	1497	[274]
Zn-doped hollow core-shell Co ₃ O ₄ (Cu _{0.3} OCo _{0.7})Co ₂ O ₄ /CuO	Zn-ZIF-67 (Cu, Co) ₃ (BTC) ₂ MOF	—/— 712/324	1.0 1.0	700 1000	1600 610	[275] [276]
Hierarchical Porous Te@ZnCo ₂ O ₄ NFs	Co-Zn-ZIF-8, Te NWs	1364/839	0.1	100	956	[277]
Co ₃ O ₄ /MoS ₂	ZIF-67, ammonium molybdate, thiourea	1136.4/912.4	0.1	100	1200	[278]
Multishelled Ni _x Co _{3-x} O ₄ Hollow Microspheres	Ni-Co-BTC MOF	1619.2/1139.3	1.0/2.0	300	832/673	[279]
Mesoporous NiMn ₂ O ₄	MnNi-BTC MOF	1738/1049	0.503	400	413	[280]
Co ₃ O ₄ film on Ti NWAs	ZIF-67, Ti NWAs	—/—	20.0	2000	300	[281]
GeO ₂ NSs	Ge-MOF	2079/1315	0.1	350	1393	[282]
CoMoO ₄ /Co ₃ O ₄ hollow porous octahedrons	Co ₂ [Mo(CN) ₆].xH ₂ O	1175.1/1021.3	0.2	100	1050.3	[283]
Porous Ni _x Fe _{3-x} O ₄ Nanotubes-0.25	Fe-Ni-BDC MOF	1466/1223	0.25	200	1184	[284]
Hollow H-Fe ₂ O ₃ -NSA	MIL-88 microrods	1308/1025	1.0	400	973	[285]
Mesoporous NiO NR-500	Ni-BTC MOF	1309/942	0.1	100	1019	[253]
Co ₃ O ₄ -CoFe ₂ O ₄ -12	MOF-74-FeCo	1328/918	0.1	80	940	[286]
Porous Mn _{1.8} Fe _{1.2} O ₄ NCs	Prussian blue analogues (PBA)	2312/1337	0.2	60	827	[287]
α-Fe ₂ O ₃	Fe-BDC MOF	1487/1024	0.1	40	Ca. 920	[288]
Co ₃ V ₂ O ₈	V-Co-BDC MOF	1536/934	1.0	700	501	[289]
Porous Fe ₂ O ₃ NCs	PB	1269/914	0.2	50	800	[290]
Mesoporous hetero-ZnFe ₂ O ₄ /ZnO NSs	PBA	1156/839	1.0	500	383	[291]
Hierarchical meso-/macroporous anatase TiO ₂	MIL-125(Ti)	304/219	0.84	200	155	[292]
Porous NiO NRs	Ni-MIL-77	743/519	0.1	60	700	[293]
Mesoporous Ni _{0.3} Co _{2.7} O ₄ NR	Co/Ni-MOF-74	1666/1189	2.0/5.0	500	812/656	[294]
Porous Mn ₂ O ₃	[Mn(Br ⁴⁻ bdc)(4,4'-bpy)(H ₂ O) ₂] _n	1158/852	1.0	250	705	[295]
Fe ₂ O ₃ @NiCo ₂ O ₄ porous nanocages	Core-shell Co ₃ [Fe(CN) ₆] ₂ @Ni ₃ [Co(CN) ₆] ₂ NCs	1311.4/902.7	0.1	100	ca. 1000	[296]
Mini-Hollow Mn ₂ O ₃	Mn-MOF	—/—	2.0	1000	760	[297]
Spindle-like porous α-Fe ₂ O ₃	MIL-88-Fe	1372/940	0.2	50	911	[298]

maintained a capacity of 1477 mAh g⁻¹ at a rate of 100 mA g⁻¹ after 160 cycles. Even when cycled at 1 A g⁻¹, a substantial capacity of 775 mAh g⁻¹ was still retained after 200 cycles. Porosity also plays a significant role in electrochemical performance beyond morphology helping to mitigate volume changes and facilitating Li⁺ diffusion during the charge/discharge activity. Li and colleagues employed a MOF-71 as a template to create Co₃O₄ materials, represented as MOF-71@300 N and MOF-71@450 N, using a calcination process at various temperatures (300 °C and 450 °C) and durations (12 h and 1.5 h). MOF-71@300 N exhibited distinct mesoporous characteristics, smaller particle size and higher surface area, compared to MOF-71@450 N. Consequently, MOF-71@300 N demonstrated good cycle stability and superior rate capability when used as an electrode of LIB (Fig. 30d) [302].

Fe₂O₃ is a promising and competitive anode material that has garnered significant attention, owing to its advantages such as lower cost and conversion-type mechanism compared to Co₃O₄ [303]. Xu and colleagues stated an innovative approach using MOFs as templates for the synthesis of Fe₂O₃ as an anode for LIBs [298]. They employed a two-way heat treatment approach (500 °C in N₂ and 380 °C in air) to produce α-Fe₂O₃ while preserving the parent MOF morphology (Fig. 30e). The resulting mesoporous spindle-type material had dimensions of 800 nm in length, 400 nm in width, and was composed of clustered Fe₂O₃ NPs, each under 20 nm in size (Fig. 30f, g). This exceptional structure conferred significantly improved Li-storage performance upon α-Fe₂O₃, including capacity of 911 mAh g⁻¹ at 0.2 C after 50 cycles and excellent rate capacity compared to bulk Fe₂O₃ obtained by direct calcination of Fe-MIL-88 at 380 °C in the air atmosphere (Fig. 30h, i). In contrast, Banerjee and colleagues employed a calcination approach for the Fe-MIL-88 at 550 °C in the air atmosphere, resulting in the formation of α-Fe₂O₃ nanospindles [288]. Although they observed comparable

capacity retention compared to α-Fe₂O₃ obtained through the two-way heat treatment approach, the initial step produced α-Fe₂O₃ showed inferior rate capacity, highlighting the crucial role of calcination conditions in determining the performance of MOs derived from MOF. Additionally, PB and its analogs, a type of MOF have also been used for producing porous Fe₂O₃ NCs with enhanced Li-storage, particularly in terms of rate performance [290].

Besides the previously mentioned MOs, various other MOF derived MOs have been investigated as an anode for LIBs, including ZnO [304], NiO [293], GeO₂ [282], and TiO₂ [292], all of which have exhibited impressive electrochemical performance. Furthermore, Mn-based oxides derived from MOFs, particularly Mn₂O₃, have gained attention as favorable anode of LIBs owing to their low transition potential and voltage hysteresis. For instance, Bai and colleagues utilized cost-effective and an easily synthesized Mn-MOF to prepare Mn₂O₃ at 600 °C with the ramping of 10 °C min⁻¹ for 3 h. For comparison, they also prepared micro-sized nonporous Mn₂O₃ from industrial MnO₂ [295]. The porous structure offered a larger surface area, effective electrode-electrolyte contact, and the ability to accommodate significant volume changes, resulting in exceptional retention in capacity (705 mAh g⁻¹ at 1 A g⁻¹ after 250 cycles) and outstanding rate capability. Consequently, they produced polyhedron-shaped Mn₂O₃ by the heat treatment of Mn-MOF at 750 °C with a ramping of 5 °C min⁻¹ for 4 h. This material exhibited outstanding performance, characterized by prolonged cycle performance, a high specific capacity, and exceptional rate performance (819.8 mAh g⁻¹ after 1200 cycles at 1 A g⁻¹ and 760 mAh g⁻¹ after 1000 cycles at 2 A g⁻¹) [297].

Furthermore, CuO derived from MOF also found utility as an anode for LIBs. For illustration, Banerjee and colleagues informed the synthesis of CuO NPs resultant from the MOF-199 at 550 °C for 2 h and employed

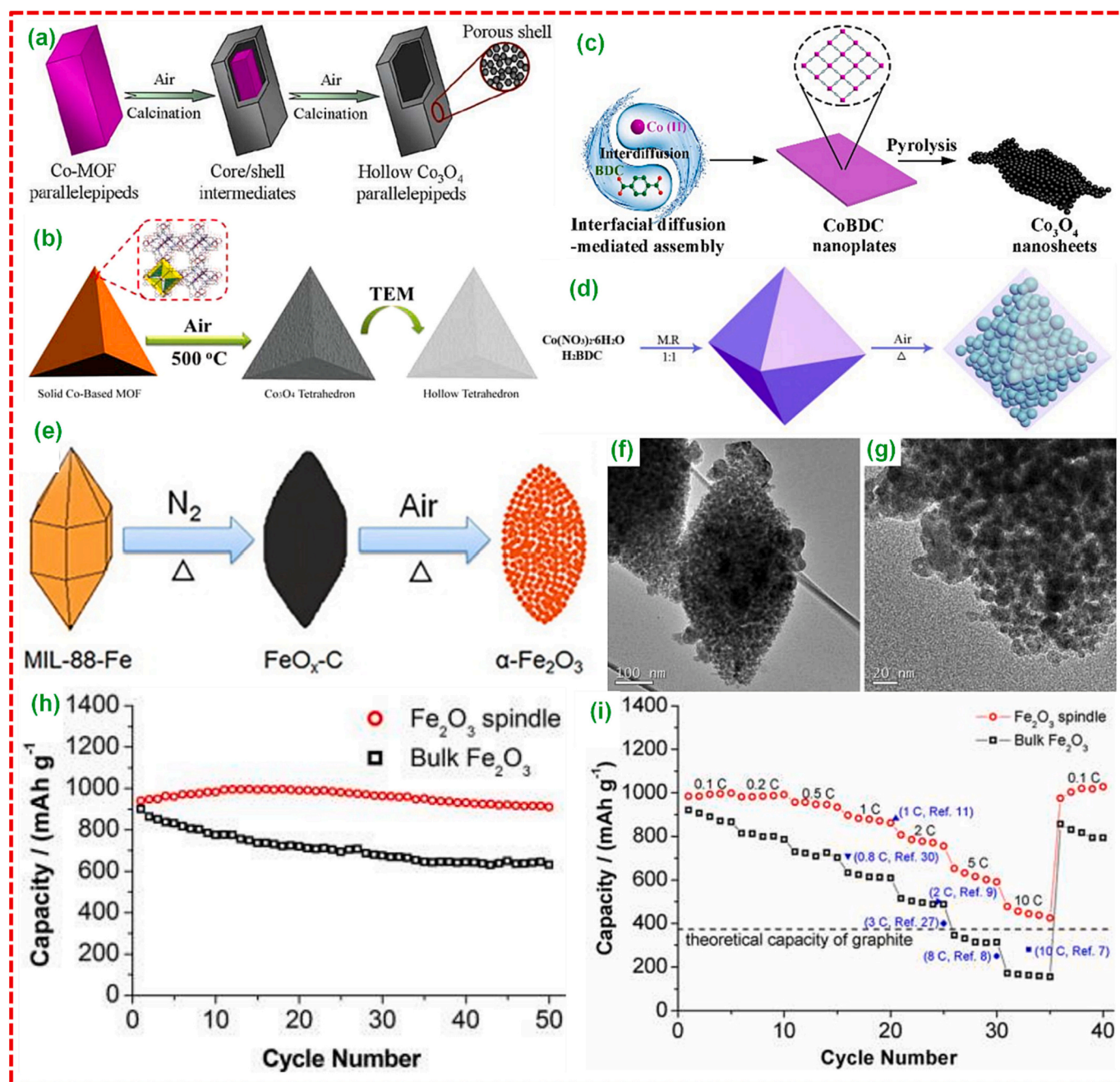


Fig. 30. (a) Schematics of hollow Co_3O_4 parallelepipeds. Adopted with permission from Ref. [300], Copyright 2015, American Chemical Society. (b) Pictorial demonstration of the preparation route of Co_3O_4 hollow tetrahedra. Adopted with permission from Ref. [301], Copyright 2015, Royal Society of Chemistry. (c) Schematics of wrinkled porous Co_3O_4 NS formation. Adopted with permission from Ref. [272], Copyright 2018, Royal Society of Chemistry. (d) Pictorial demonstration of nanostructured Co_3O_4 . Adopted with permission from Ref. [302], Copyright 2015, Royal Society of Chemistry. (e) Schematics, (f, g) TEM analysis, (h) stability study, and (i) rate capability of spindle-like mesoporous $\alpha\text{-Fe}_2\text{O}_3$ derived from MIL-88-Fe. Adopted with permission from Ref. [298], Copyright 2012, American Chemical Society.

as an anode in LIBs [305]. They adopted a two-way heat treatment route (300°C with a ramping of $10^\circ\text{C min}^{-1}$ for 30 min in N_2 followed by another 60 min in ambient atmosphere) to produce a porous CuO hollow octahedron using the MOF-199 template. This product demonstrated significantly improved Li-storage activity, boasting capable rate performance and tremendous cycle stability [306]. Further, the growth of MOs on 3D electroconductive substrates has proven efficient to increase the electrical conductivity of resulting MO electrodes. As an illustrative example, Liang and co-workers coated ZnO or Co_3O_4 NSs onto NF or CF substrate by annealing in the air temperature [307]. Leveraging the merits of NS structures and 3D electroconductive substrates, these

composite materials, particularly $\text{Co}_3\text{O}_4/\text{3DNF}$, demonstrated exceptional cycle stability and rate capacity enduring till 2000 cycles at 5 and 20 A g^{-1} . It's evident that the several MOs discussed above are primarily obtained from single-metallic MOFs. While these materials have achieved superior energy storage performance compared to MOs prepared using traditional inorganic techniques, they still face challenges related to poor rate/cycle performance. These challenges have the potential to impede their future development. Researchers have been working on the preparation of binary-, ternary-, and even multi-doped MOs through the calcination of bimetallic or polymetallic MOF precursors to address this issue. This multi-element doped MOs have shown significant

improvements in Li-storage performance compared to their single MOs counterparts.

Through a two-step process involving the synthesis of bimetallic-doped MOF precursors and subsequent calcination, binary MOs are created. In one such example, bimetallic NiFe-MIL-88 with needle shaped morphology was initially synthesized using a co-precipitation process. Then it was subjected to thermal treatment at 500 °C for 1 h in the Ar environment followed by another 1 h heating step at 500 °C in an air environment. This process yielded porous $\text{Ni}_x\text{Fe}_{3-x}\text{O}_4$ (NFO) NTs (Fig. 31a, b) [284]. The NFO-0.25 sample, optimizing the molar ratio of

Fe^{3+} to Ni^{2+} , exhibited superior Li-storage activity (1184 mAh g^{-1} at 0.25 A g^{-1} after 200 cycles) shown in Fig. 31c. In another study, Zhang and colleagues successfully produced $\text{Ni}_x\text{Co}_{3-x}\text{O}_4$ by utilizing a bimetallic NiCo-MOF as the self-sacrificing template and precursor [279]. During the heat treatment process, the heterogeneous reduction phenomenon generated by nonequilibrium calcination led to the formation of a multi-shelled hollow structure (Fig. 31d). The novel morphology and compositions of $\text{Ni}_x\text{Co}_{3-x}\text{O}_4$ resulted in good cycle stability and high capacity when utilized as an anode for LIBs (Fig. 31e). Moreover, bimetallic MOFs have been employed as templates or precursors to

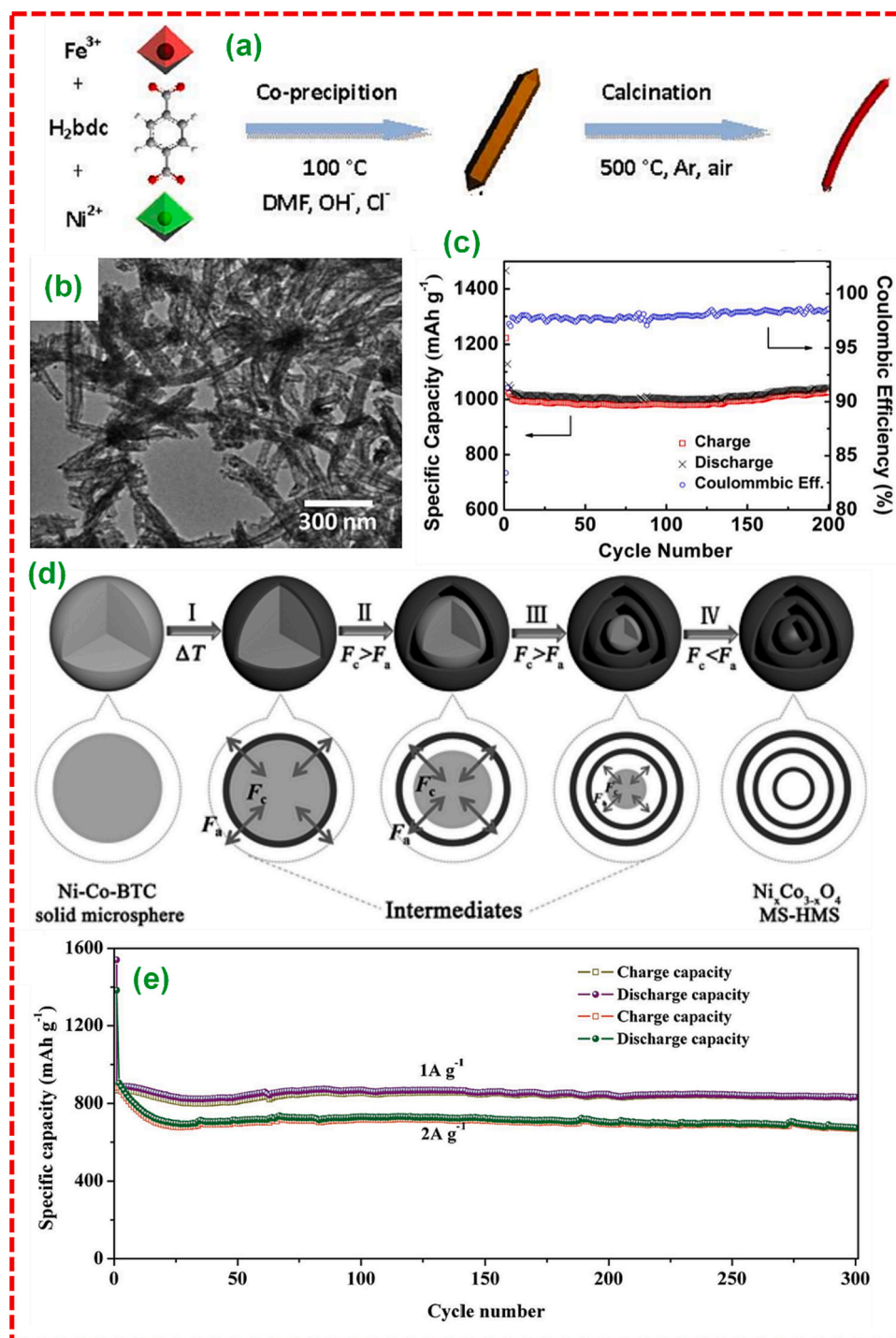


Fig. 31. (a) Pictorial demonstration, (b) TEM analysis, and (c) stability study of the $\text{Ni}_x\text{Fe}_{3-x}\text{O}_4$ NTs. Adopted with permission from Ref. [284], Copyright 2015, Wiley VCH, Janus. (d) The preparation mechanism and (e) stability study of multi-shelled hollow $\text{Ni}_x\text{Co}_{3-x}\text{O}_4$ microsphere. Adopted with permission from Ref. [279], Copyright 2017, Wiley VCH, Janus.

prepare binary MOs with remarkable energy storage performance. For instance, MnFe-PBA was subjected to a heat treatment in the air environment for 2 h at 450 °C, resulting in the formation of $\text{Mn}_{1.8}\text{Fe}_{1.2}\text{O}_4$ NCs [287]. This material exhibited a remarkable Li-storage capacity and exceptional cycle stability. Likewise, Wang and colleagues initially synthesized Fe-PBA and subsequently underwent an ion exchange process to obtain MgFe-PBA [308]. By subjecting the MgFe-PBA precursor to a heat treatment in air atmosphere at 700 °C for 6 h, they successfully derived MgFe_2O_4 microboxes, which demonstrated improved Li-storage and rate performance. Additionally, porous nanostructured ZnCo_2O_4 was synthesized from ZnCo-MOF and utilized as an anode for LIBs [309]. These materials hold great promise for enhancing LIB performance.

Moreover, multi-component binary or multi-MO composites have been successfully synthesized by utilizing yolk-shell MOF templates or adjusting the molar ratios of metal ions during the preparation process or by selecting suitable calcination conditions. Huang and colleagues employed a hydrothermal route to create yolk-shell $\text{NiFe-MIL-88/Fe-MIL-88}$ structures, which served as precursors for the subsequent synthesis of hierarchical $\text{NiFe}_2\text{O}_4/\text{Fe}_2\text{O}_3$ NTs through heat treatment for 6 h in an air atmosphere at 450 °C (Fig. 32a-c) [310]. The resulting NT structure, characterized by a hierarchical porous and hollow design, effectively reduced diffusion distances, enhanced electrode-electrolyte interactions, and accommodated volume changes. These features endowed $\text{NiFe}_2\text{O}_4/\text{Fe}_2\text{O}_3$ NTs with outstanding electrochemical performance. In a related study, they utilized yolk-shell CoFe-PBA@NiCo-PBA nanocubes (NCs) as self-sacrificial template to produce $\text{Fe}_2\text{O}_3@\text{NiCo}_2\text{O}_4$ nanocages, featuring an average diameter of 213 nm (Fig. 32d-h) [296]. Leveraging the morphological advantages of these nanocages, the resulting material exhibited improved capacity and rate capability. Furthermore, in a recent development, Yuan and colleagues investigated the preparation of hollow $\text{CoMoO}_4/\text{Co}_3\text{O}_4$ octahedrons after the heat treatment of PBA precursor in an ambient temperature for 2 h at 450 °C with a ramping of 2 °C min^{-1} [283]. Our group also successfully prepared a $\text{Co}_3\text{O}_4\text{-CoFe}_2\text{O}_4$ composite with superior Li-storage performance than the pure Co_3O_4 by utilizing the FeCo-MOF-74 precursor [286]. Additionally, other mixed MO composite materials have been developed using bi/multi-metallic MOF templates. These include porous $\text{NiCo}_2\text{O}_4/\text{NiO}$ hollow dodecahedrons [274], self-assembled $\text{ZnO/Co}_3\text{O}_4$ NC

clusters, hollow CuO@NiO spheres [311], and $\text{Fe}_2\text{O}_3/\text{ZnO}$ composites [312]. These materials have exhibited even better energy storage performances compared to its equivalent single-component counterparts.

6.1.2. Porous carbon derived from MOFs

Traditional porous carbon materials are typically obtained through the physical/chemical carbonization methods or direct carbonization of organic precursors. However, these carbon materials have specific limitations, like disordered structure, lower surface area, and non-uniform size distribution, which restrict its utilization in LIBs [313]. To overcome these drawbacks, researchers have turned to carbon materials derived from MOFs. MOFs are uniquely suited to serve as templates or precursors for creating PC materials owing to their open-framework structure, organic moieties, and high surface area. These porous carbon materials can be derived by the heat treatment of MOFs in an inert temperature, like N_2 , Ar, or Ar/H_2 . Xu et al. studied the first instance of nanoporous carbon (NPC) derived from MOF [314], numerous PC products have been prepared from MOF templates. These materials have demonstrated significantly improved electrochemical performance compared to industrial graphite when used as an anode for LIBs (Table 6) [311]. Furthermore, carbonaceous products doped with heteroatoms can also be synthesized by either directly carbonizing MOFs with organic ligands containing heteroatoms like N and S or by introducing a secondary N species. For example, Shen and colleagues conducted a study where they synthesized N-modified carbon from MOF template through a process involving treatment in an Ar atmosphere at 700 °C, along with subsequent HNO_3 and HCl etching processes [318]. The resulting electrode made of nanocarbon displayed a discharge capacity of 853.1 mAh g^{-1} at 500 mA g^{-1} after 800 cycles. An impressive breakthrough in the realm of heteroatom-doped PC derived from MOF as an anode for LIBs was achieved by the Chen research team shown in Fig. 34a-b (Fig. 33a-b) [238]. In this pioneering work, they crafted a N-doped graphene particle analogue with an astonishing N amount till 17.7 wt% by carbonizing polyhedron-type ZIF-8 precursors. Thanks to its distinctive structure and substantial N doping, the adjusted N-C-800 product demonstrated extraordinary Li-storage activity. It reached a specific capacity of 2132 mAh g^{-1} at 100 mA g^{-1} after 50 cycles, and an impressive 785 mAh g^{-1} at a current density of 5 A g^{-1} after 1000 cycles.

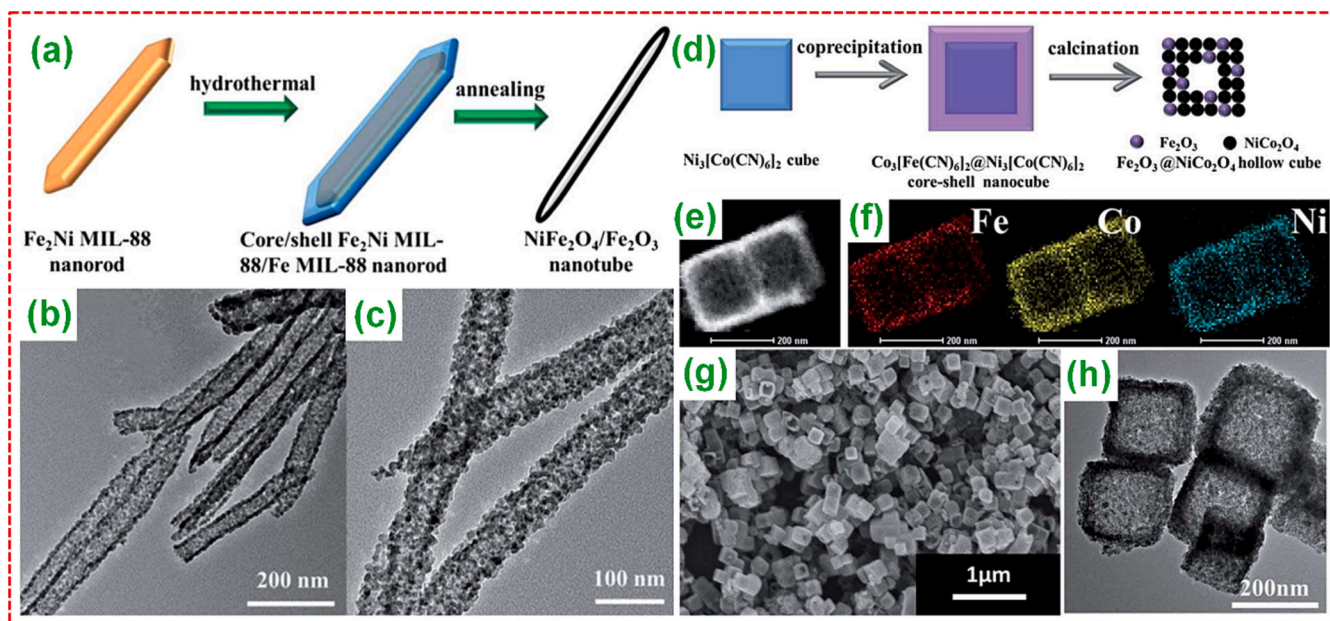


Fig. 32. (a) Schematics of preparation mechanism (b, c) TEM analysis of $\text{NiFe}_2\text{O}_4/\text{Fe}_2\text{O}_3$ NTs. Adopted with permission from Ref. [310], Copyright 2014, Royal Society of Chemistry. (d) The formation process and (e-h) TEM analysis of porous $\text{Fe}_2\text{O}_3@\text{NiCo}_2\text{O}_4$ nanocages. Adopted with permission from Ref. [296], Copyright 2014, Royal Society of Chemistry.

Table 6

Porous carbon derived from MOFs for LIBs.

MOF derived porous carbon	MOF templates	Initial discharge/charge capacity (mAh g ⁻¹)	Current density (A g ⁻¹)	Number of cycles	Capacity after cycles (mAh g ⁻¹)	Ref.
PNCs@Gr	ZIF-8, GO sheets	—/—	5.0	400	530	[315]
Porous carbon	[Cd ₃ (TCPB) ₂ (H ₂ O) ₂ (DMF) ₂].7H ₂ O	2486/1683	0.3	300	1285	[316]
N-doped PC coated graphene	ZIF-8, GO	1391/873	0.5	200	1040	[317]
N-modified carbon	Cu-MOF	1584.4/942.1	0.5	800	853.1	[318]
Highly N-doped PC-800	ZIF-8	3487/2037	5.0	1000	785	[238]
N-C-550	TCNQ-based Sr-MOF	1043/675	0.1	50	736.8	[319]
Multifractal PC	MOF-5	—/—	0.74	50	2016	[320]

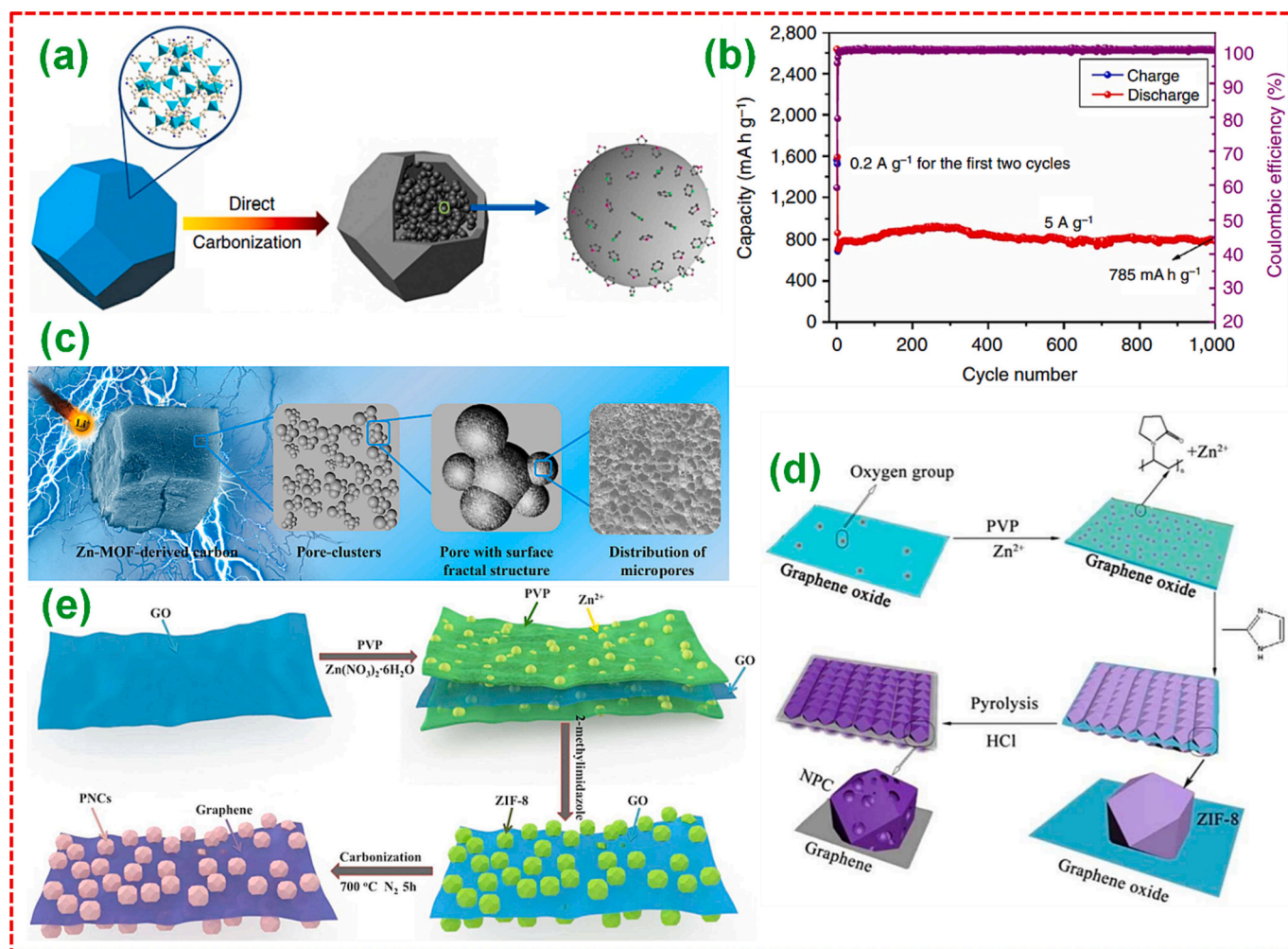


Fig. 33. (a) Formation mechanism and (b) Cycle stability at current densities of 5 A g⁻¹ of N-doped PC. Adopted with permission from Ref. [238], Copyright 2014, Springer Nature. (c) Preparation of porous carbon. Adopted with permission from Ref. [320], Copyright 2017, Springer Nature. (d) Formation of N-doped PC deposited graphene sheets. Adopted with permission from Ref. [317], Copyright 2017, Royal Society of Chemistry. (e) Preparation of graphene dependent NDC. Adopted with permission from Ref. [315], Copyright 2016, Royal Society of Chemistry.

Density functional theory (DFT) analysis proposed that by preventing oxidation at the graphene sheets edges, an abundance of active sites for attaching N atoms, particularly pyridinic/pyrrolic N could be provided, thus enhancing the performance of electrochemical activity. Subsequently, they derived porous carbon products with disordered structures from a Zn-MOF template, which exhibited an ultrahigh specific capacity along with promising rate capability (Fig. 33c) [320]. Small-angle X-ray scattering (SAXS) analysis validated that the thermolysis activity in the vacuum atmosphere induced the multi-fractal structure formation of PC and the creation of additional closed pores. These structural characteristics reduced the electrolyte penetration distance and provided

numerous active sites for Li-storage, contributing to remarkable electrochemical activity of the material.

To further augment the Li-storage capabilities of MOF-derived carbonaceous products, researchers have integrated additional conductive substrates during the preparation of MOF templates to enhance the kinetics of electrochemical activity. Zhang and their research team introduced an N-doped PC-rGO sheet, referred to as NPCGS, through a simple heat treatment of sandwich-type ZIF-8/GO moiety as depicted in Fig. 33d [317]. Hierarchical pores were formed by selectively removing residual Zn and ZnO using HCl. This novel structural characteristic conferred superior LIB performance compared to

conventional N-doped PC. Similarly, Liu and their colleagues employed the ZIF-8/GO template to effectively craft a sandwich-type, graphene-based porous NDC (PNCs/Gr) (Fig. 33e) [315]. This material exhibited amazing capacity, outstanding rate/cycle performance. It sustained a capacity of 530 mAh g^{-1} at 5 A g^{-1} after 400 cycles, with a capacity retention rate of 84.4 %. These results outperform the performance of many other carbonaceous products and MOF-type anodes derived from MOFs.

6.1.3. Metal chalcogenides derived from MOF

LIBs have risen to prominence as a preferred choice among energy storage devices, attracting growing interest from researchers owing to its high operating voltage, impressive energy density, and reduced ecological impact [326]. Nonetheless, the traditional graphite anodes used in LIBs have a restrained theoretical capacity of 372 mAh g^{-1} . Thus, there exists a critical need to significantly improve the LIBs performance [327]. One effective strategy is the development of innovative electrode materials with exceptional electrochemical characteristics. Transition metal chalcogenides (TMCs), including Sulfides (S), Selenides (Se), and Tellurides (Te), have displayed immense potential due to their improved conductivity and higher Li-storage capabilities compared to

MOs. Chalcogenides have been successfully synthesized from MOFs [328]. Nanomaterials derived from MOF can inherit the morphology of their templates, offering improved electrochemical advantages by shortening the Li^+ diffusion pathways and facilitating rapid electrolyte penetration. However, researchers have targeted various strategies to improve the performance of electrodes due to the thermal stability and low conductivity of MOFs. These strategies encompass doping with both metals as well as non-metals, additional heat treatments through calcination, and the incorporation of graphene to fabricate hybrid materials. Cobalt sulfide (Co_xS_y) stands out as a highly favorable material for conversion-type electrodes, falling under the chalcogenides category. It exhibits exceptional electrochemical activity and an impressive theoretical capacity exceeding 400 mAh g^{-1} . To harness the potential of MOF-based nanomaterials, researchers have explored the synthesis of cobalt sulfide hybrids containing carbon. This approach effectively enhances both conductivity and stability. As an example, Shanguan and colleagues [321] introduced a MOF-derived structure in the form of a hollow polyhedron composite, $\text{Co}_9\text{S}_8/\text{HNCS}$, which features an NDC shell with dimensions of approximately 900 nm. Within this structure, uniform Co_9S_8 NPs of around 11 nm are uniformly enveloped (Fig. 34a). This unique architecture significantly improves the electrical

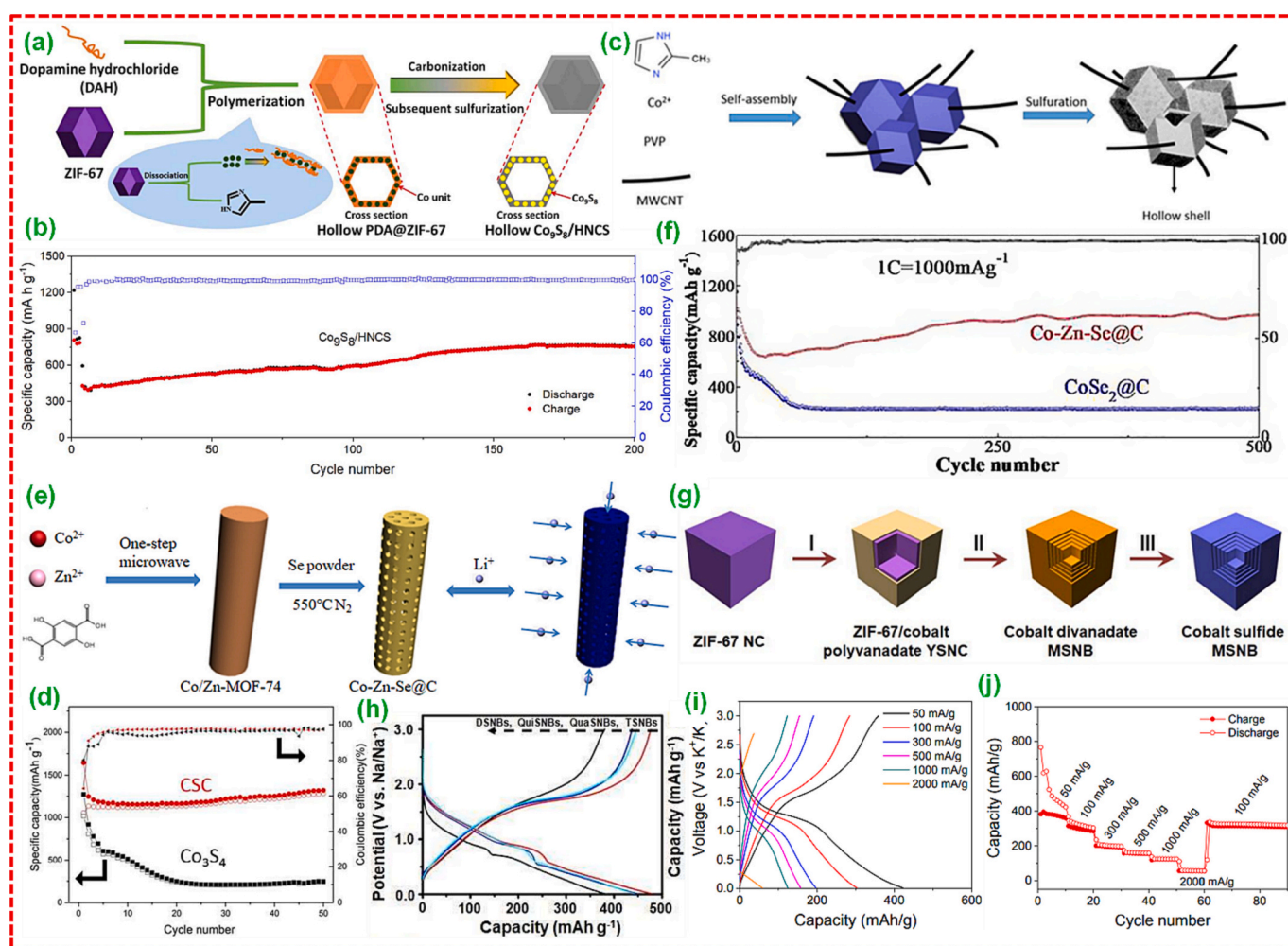


Fig. 34. (a) Pictorial demonstration of formation process. (b) Cycle stability at 500 mA g^{-1} of $\text{Co}_9\text{S}_8/\text{HNCS}$ composite. Adopted with permission from Ref. [321], Copyright 2019, Elsevier B.V. (c) Pictorial representation of formation mechanism. (d) Cycle stability of the $\text{Co}_3\text{S}_4/\text{MWCNT}$ composite and Co_3S_4 electrode at 200 mA g^{-1} . Adopted with permission from Ref. [322], Copyright 2018, American Chemical Society. (e) Schematic illustration of the preparation. (f) Cycle stability of Co-Zn-Se@C and $\text{CoSe}_2@C$ at 1 A g^{-1} . Adopted with permission from Ref. [323], Copyright 2018, Elsevier B.V. (g) Schematic illustration of the synthesis process. (h) The GCD plots of cobalt sulfide multi-shelled nanoboxes (MSNBs) at 500 mA g^{-1} with various shell numbers. Adopted with permission from Ref. [324], Copyright 2019, Wiley VCH, Janus. (i) Voltage plots at different current densities and (j) rate capability test. Adopted with permission from Ref. [325], Copyright 2022, Royal Society of Chemistry.

conductivity, increases the active sites, shortens the Li^+ diffusion pathways, and accommodates the volume changes throughout Li^+ insertion/extraction. Impressively, the composite demonstrates an outstanding capacity of 755 mAh g^{-1} at 0.5 A g^{-1} after 200 cycles (Fig. 34b).

Metal sulfides and selenides are highly promising as probable anodes due to their impressive theoretical capacities. However, it has become essential to incorporate carbon materials to enhance cycle stability and rate capacity. Carbon materials serve multiple purposes, such as enhancing conductivity, preventing the agglomeration and suspension of active compounds, and providing structural support to withstand volume fluctuations. A thoughtfully fabricated porous structure with a great surface area can successfully assist the volume changes that occur during repeated cycling [329]. In a noteworthy study conducted by Jin et al. [330], a composite material was developed, comprising binary metal selenides (ZnSe/CoSe) encapsulated within NDC polyhedra organized with CNTs. This composite, known as ZCS@NC/CNTs , established a strong and interconnected conductive network with porous structures that significantly reduced the diffusion pathways for Li^+ ions within the hierarchical structure. The observed synergistic effects resulted from two critical factors: (1) the ZIF derived ZnSe/CoSe possessed substantial surface area and capacity, and (2) the CNTs and NDC polyhedra collaboratively created interconnected conductive networks, reducing the diffusion pathways for both Li^+ ions and electrons, thereby enhancing Li^+ insertion capabilities, particularly in terms of rate performance. The porous NDC polyhedra portray a dual function in ion storage and facilitating transfer of charge at the electrode and electrolyte interface. Furthermore, the voids within the carbon polyhedra efficiently assist the volume variations that occur during the Li^+ insertion/extraction activity, contributing to stable cycle performance. When utilized as an anode for LIBs, the synthesized ZCS@NC/CNTs displayed remarkable attributes, including high capacity, and exceptional rate/cycle performance. Notably, the material maintained a stable capacity of 768 mAh g^{-1} at 1 A g^{-1} after 1000 cycles. Similar cycle performance of chalcogenides derived from MOF with the incorporation of carbon was noticed in MOF-derived hollow $\text{Co}_3\text{S}_4/\text{MWCNT}$ NCs (Fig. 34c, d) [322]. While Co_3S_4 exhibited electrolyte decomposition and the formation of an irreversible Solid Electrolyte Interphase (SEI) layer, the presence of MWCNTs permitted volumetric expansion/contraction, reducing the active material loss. Furthermore, the mixed metals incorporation during MOF preparation not only resulted in improved capacity but also enhanced stability of material when utilized as an electrode for LIBs. As depicted in Fig. 34e, f, the cycle performances of MOF-derived Co-Zn-Se@C , in comparison to $\text{CoSe}_2@\text{C}$ [323], demonstrated that the inherent porous nature and the synergistic effect of the two metal species contributed to the excellent cycle stability and high specific capacity of Co-Zn-Se@C for LIBs. Moreover, Lou et al. [324] report the synthesis of cobalt sulfide multi-shelled nanoboxes through MOF-engaged complex anion conversion and exchange processes. The polyvanadate ions transformed from metavanadate ions in alkaline media first react with ZIF-67 nanocubes to form ZIF-67/cobalt polyvanadate yolk-shelled particles. Afterwards, the as-formed ZIF-67/cobalt polyvanadate yolk-shelled particles are gradually converted to cobalt divanadate multi-shelled nanoboxes by a solvothermal treatment under neutral condition. The cobalt sulfide multi-shelled nanoboxes are produced through the ion exchange reaction with S^{2-} ions and a subsequent annealing treatment as shown in Fig. 34g. The as-obtained cobalt sulfide multi-shelled nanoboxes exhibit enhanced sodium storage properties when evaluated as anodes for SIBs. For example, a high specific capacity of 438 mAh g^{-1} can be retained after 100 cycles at the current density of 500 mA g^{-1} for the triple-shelled nanoboxes (Fig. 34h). Besides, Cobalt telluride anchored to N-rich carbon dodecahedra (CoTe@NCD) was synthesized by simultaneous pyrolysis-tellurium melt impregnation of ZIF-67 MOFs [325]. The purely thermal method involved no secondary chemicals and no waste byproducts. The result is a microstructure consisting of nanoscale 86 wt% CoTe intermetallic nanoparticles contained within a thin N-rich carbon matrix. During electrochemical

cycling, the 21 nm average diameter CoTe provides short diffusion paths for Na^+ ions, which in conjunction with the electrically conducting carbon matrix allow for rapid sodiation. As SIB anodes, CoTe@NCD demonstrates attractive reversible capacity, promising cycling stability, and state-of-the-art rate performance (Fig. 34i, j).

Post-treatments of MOF-derived NCs, like sulfurization, selenization, and phosphorization, offer effective strategies to further enhance their Li-storage performance. For instance, Lou and colleagues developed hollow CoS_2 prisms composed of two-step process involving sulfidation followed by heat treatment for 2 h at 350°C in N_2 atmosphere with a ramping of 2°C min^{-1} (Fig. 35a-c) [331]. Utilizing its novel hollow structure, these CoS_2 prisms exhibited improved performance, delivering a capacity of 737 mAh g^{-1} at 1000 mA g^{-1} after 200 cycles (Fig. 35d). In a similar manner, Yu and collaborators synthesized hollow Co_9S_8 NPs embedded in a GC NC through heat treatment at 500°C for 4 h in Ar/H_2 gas with a rate of 1°C min^{-1} , connected with the process of sulfurization of ZIF-67 template [333]. In another study, Zaworotko et al. investigated a Cu_xS NW-in-carbon composite via the direct Cu-MOF sulfurization in the Ar environment (Fig. 35e, f). The phase of the material can be able to change by optimizing the temperature for sulfurization, and the adjusted $\text{Cu}_{1.8}\text{S/C-500}$ composite exhibited superior performance [332]. Another valuable approach involves selenization to prepare metal selenides/carbon NCs from MOF templates. Zhao et al. prepared the ZnSe/CoSe confined in NDC polyhedra interconnected with CNTs (ZCS@NC/CNTs) through in-situ heat treatment followed by selenization of ZnCo-ZIF [330]. The resulting ZCS@NC/CNTs demonstrated a high capacity of 768 mAh g^{-1} at 1000 mA g^{-1} after 1000 cycles (Fig. 35g, h).

Furthermore, the incorporation of metallic Sn or SnO_2 in MOF-derived NCs represents another effective strategy for enhancing their performance of electrochemical activity. Mai et al. pioneered a method in which a combination of H_2BDC and CoSn(OH)_6 was initially heated to produce a $\text{CoSnO}_3@\text{MOF}$ precursor. Subsequently, this precursor was carbonized to create carbon encapsulated SnO_2/Co ($\text{SnO}_2/\text{Co@C}$) NCs in the inert environment (Fig. 36a) [334]. These NCs exhibited exceptional cycle life and rate performance. Remarkably, they maintained a high capacity of approximately 400 mAh g^{-1} at 5 A g^{-1} after 1800 cycles (Fig. 36b). In a similar fashion, our group prepared a hybrid material consisting of SnO_2 NPs enveloped by NDC composite [336]. In this work, NDC was first synthesized from ZIF-8 through carbonization followed by etching with HCl . Subsequently, SnO_2 NPs were encapsulated within the MOF-derived carbon matrix by the heat treatment of blend of NDC and tetraphenyltin in the presence of vacuum. The novel structural features of this material endowed it with outstanding Li-storage capability and cycle life. Similarly, Lu and colleagues described a NC composed of 3D NPC frameworks encapsulating Sn NPs (Sn@3D-NPC) by directly pyrolyzing MOFs to obtain 3D NPC frameworks followed by a reduction to convert Sn^{4+} to Sn NPs within the carbon matrix [337]. This composite exhibited high capacity, outstanding rate performance and cycle stability.

6.1.4. Metal phosphides derived from MOF

Moreover, phosphorization represents another valuable technique for improving energy storage activity of MOF-derived NCs in LIBs. Wang and colleagues reported the creation of novel ball-cactus type microsphere consisting of carbon-coated $\text{NiP}_2/\text{Ni}_3\text{Sn}_4$ with deeply embedded CNTs (Ni-Sn-P@C-CNT) (Fig. 36c) [335]. This material was synthesized by carbonization of Ni-Sn-MOF template in a mixed $\text{C}_2\text{H}_2/\text{Ar}$ atmosphere (5 %/95 %) followed by a phosphorization. The presence of Ni-Sn catalyzed the CNTs formation, and when the gas medium was replaced with Ar , a Ni-Sn@C NC without CNTs was achieved. The synergistic effects among the numerous components contributed to the enhanced Li-storage activity of this item. It revealed a specific capacity of 704 mAh g^{-1} at 100 mA g^{-1} after 200 cycles, and a comparable capacity of 504 mAh g^{-1} at 1 A g^{-1} was still maintained after 800 cycles (Fig. 36d). Furthermore, a novel material consisting of Bi NPs anchored

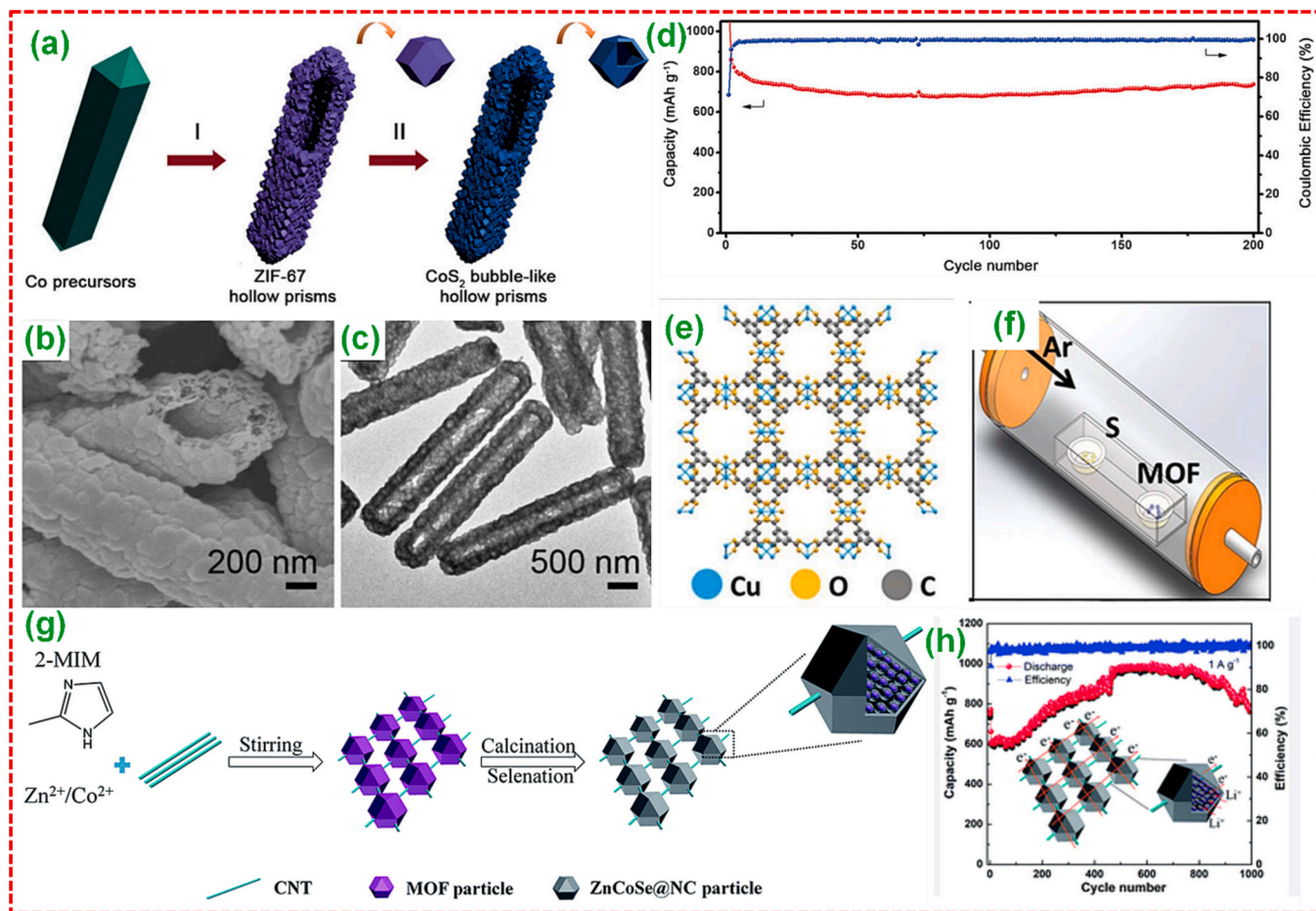


Fig. 35. (a) Pictorial demonstration of preparation mechanism hollow prisms covered with CoS₂ nanobubble, (b) SEM analysis, (c) TEM analysis and (d) cycle stability study. Adopted with permission from Ref. [331], Copyright 2016, Wiley VCH, Janus. (e) Cu-MOF structure along the c-axis; (f) Pictorial demonstration of Cu₂S/C composite formation. Adopted with permission from Ref. [332], Copyright 2018, Wiley VCH, Janus. (g) Schematics of preparation process and (h) cycle stability of ZnSe/CoSe/N-C composite. Adopted with permission from Ref. [330], Copyright 2018, Royal Society of Chemistry.

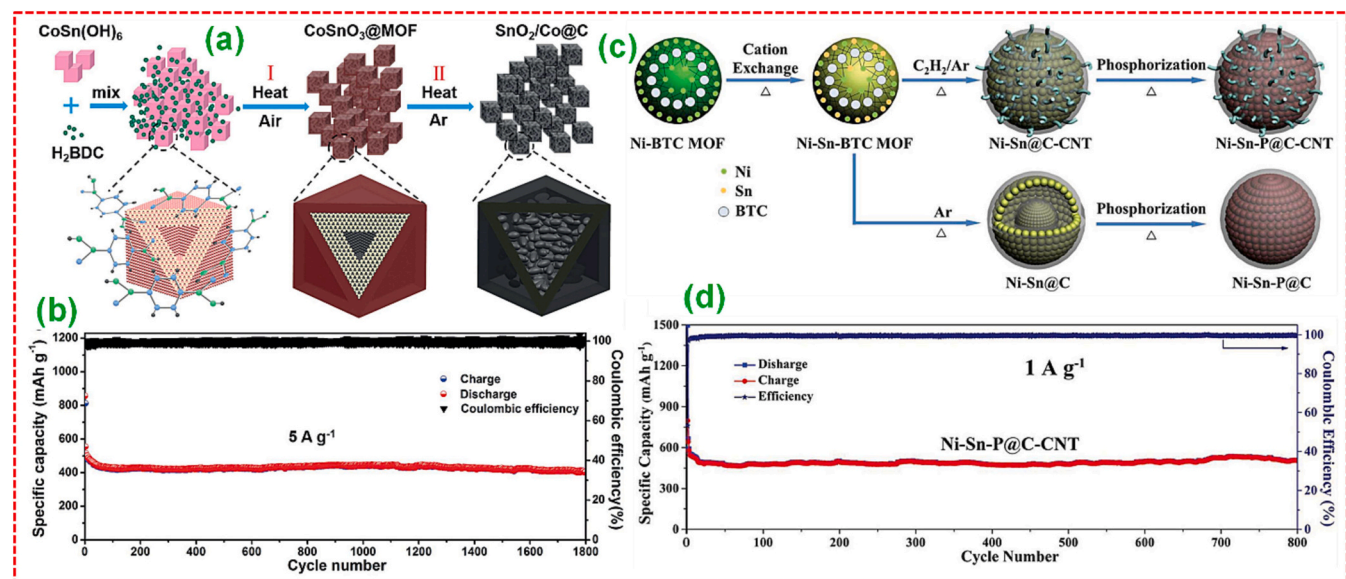


Fig. 36. (a) Formation of SnO₂/Co@C NC, and (b) cycle stability. Adopted with permission from Ref. [334], Copyright 2017, Wiley VCH, Janus. (c) Pictorial demonstration of Ni-Sn-P@C-CNT and (d) cycle stability. Adopted with permission from Ref. [335], Copyright 2017, Wiley VCH, Janus.

in NDC was synthesized from a ZIF-8 template through heat treatment in H_2/Ar medium at 600°C followed by a replacement reaction between Bi^{3+} and Zn ($\text{Bi}^{3+} + \text{Zn} \rightarrow \text{Zn}^{2+} + \text{Bi}$) [338]. During the discharge/charge activity, the NDC matrix enhanced the electrical conductivity and alleviated the mechanical strain of Bi NPs upon Li insertion/extraction, thanks to the larger void space. This resulted in an excellent cycle life, and rate capacity observed in the as-prepared sample.

6.2. Sodium ion batteries

Despite the significant impact of LIBs on the energy storage market, they confront several challenges, including safety concerns, low power density, and a limited supply of lithium in the Earth's crust. As an appealing alternative, SIBs have gained traction owing to the sodium abundance, its cost-effectiveness, and the low electrochemical potential (-2.71 V vs SHE) [339]. Nevertheless, the molar mass and larger ionic radius of sodium ions pose a challenge. Many electrode materials appropriate for LIBs no longer meet the SIBs requirements in the aspect of energy density, cycle/rate performance. Consequently, there is an urgent need to identify suitable anode materials for SIBs. While various materials, including MOs [340], PB [7], and small organic molecules [341], have served as cathode for SIBs, discovering favorable anode with superior cycle/rate performance, greater capacity, and extreme energy density remains a significant challenge. Fortunately, the emergence of MOF-derived NMs specifies a promising avenue for the SIB anodes advancement with outstanding energy storage performance.

6.2.1. Metal oxides derived from MOF

Given the exceptional electrochemical performance of MOs derived from MOF as an anode for LIBs, significant research efforts assigned to exploring their Na-storage potentials, as summarized in Table 7. Pan and collaborators adopted a straightforward method concerning the synthesis of Ti-MIL-125 precursor, followed by annealing to produce a cake-type TiO_2 material [347]. This material demonstrated remarkable rate performance and maintained good cycle performance after 2500 cycles. The mesoporous Co-doped TiO_2 nano disk was derived from the Ti-MIL-125@Co precursor to enhance the electrical conductivity of TiO_2 . This modification resulted in enhanced Na-storage capability compared to pristine TiO_2 [344]. The same research group utilized a different approach to derive hollow $\text{CuO}/\text{Cu}_2\text{O}$ octahedron from Cu-MOF, which was estimated as an anode for SIBs [343]. The findings emphasized the critical role of calcination temperature in determining the Na-storage capability of the $\text{CuO}/\text{Cu}_2\text{O}$ NCs. The elevated $\text{CuO}/\text{Cu}_2\text{O}$ -300 exhibited remarkable retention in capacity, exceptional rate performance and extended cycle life.

Beyond the MOs derived from MOF discussed previously, Prussian blue analogues (PBAs), which are part of the MOF family, have proven to be valuable templates for crafting MOs with exceptional Na-storage capability. As an illustration, Lu and their team effectively produced CoFe_2O_4 NCs utilizing a CoFe-PBA template [342]. The resulting material demonstrated a noteworthy capacity of 394 mAh g^{-1} at 50 mA g^{-1} , accompanied by an impressive retention in capacity (91.4 %). The

capacity remained substantial even when subjected to high current density of 2.5 A g^{-1} , reaching 152.6 mAh g^{-1} over 500 cycles. Furthermore, hollow MnFe_2O_4 micro boxes were derived by utilizing MnFe-PBA template [346]. When assessed as an anode for SIBs, the MnFe_2O_4 showed exceptional cycle performance and rate capacity.

6.2.2. Porous carbon derived from MOF

Just as with LIBs, porous carbon (PC) materials derived from MOFs emerge as an ideal class of anodes for SIBs (Table 8) [356]. Ji and their research team employed MOF-5 as a template to craft porous cube-shaped carbon. When applied as an anode, this resultant carbon showcased exceptional Na-storage capability, achieving a capacity of 240 mAh g^{-1} at 100 mA g^{-1} of current density after 100 cycles. Impressively, it sustained a capacity of 100 mAh g^{-1} at 3.2 A g^{-1} of current density after 5000 cycles [353]. Moreover, Al-MOFs served as templates for fabricating accordion-like NPC with superb capacity, rate performance, and cycle durability [352]. Nonetheless, it's worth noting that Na-ions have a larger diameter compared to Li-ions, presenting challenges in terms of efficient insertion. Consequently, the imperative lies in the development of PC materials with unique morphologies, like hollow configurations, ultrathin 2D structures, doping, and NFs, to amplify the performance of SIB anodes [116]. Hu and their research team achieved a significant milestone by creating ZIF-8 NBs using a tannic acid etching method. These hollow ZIF-8 nanobubbles underwent heat treatment at 600°C in N_2 environment for 5 h, followed by an extensive HCl etching to yield hollow carbon NBs [357]. The hollow carbon NBs had an average size of approximately 60 nm with a shell thickness of 10 nm . Thanks to their surface area of $700\text{ m}^2\text{ g}^{-1}$ and porous structure containing micropores with diameters less than 2 nm , as well as mesopores with diameters of 6 nm and 40 nm , these carbon NBs demonstrated exceptional Na-storage performance. They exhibited remarkable cycle performance at 10 A g^{-1} after 1000 cycles, along with excellent rate capacity. Furthermore, Mn-MOF was prepared using a microemulsion-assisted approach, serving as a precursor to produce 3D hollow PC microspheres [350]. As the anode material, this material displayed an excellent rate capacity and good specific capacity.

Furthermore, along with the hollow structure, utilizing MOFs as templates to create heteroatom-doped carbon has proven to be an efficient approach in enhancing Na-storage capability. Zou and their research team synthesized a hollow S, N doped PC materials (S/N@C) with shell-type morphology by a process that involved MOF gel carbonization at various temperatures followed by acid etching (Fig. 37a) [358]. The carbon resultant exhibited several advantageous characteristics, comprising thin walls with 0.375 nm interplanar spacing, a high surface area, mesopores distribution, and a hollow porous interconnected carbon shell. Consequently, when utilized as an anode for SIBs, this carbon demonstrated a discharge capacity of 448 mAh g^{-1} at 100 mA g^{-1} . In another noteworthy instance, a novel and effective Cu-MOF was employed as a template to produce highly NDC [249]. Initially, the MOF was stabilized at 200°C and subsequently treated with a mixed $\text{H}_2\text{O}_2/\text{HCl}$ precursor to eliminate any remaining Cu NPs. Lastly, it was transformed into highly NDC (HNC) at temperatures

Table 7
Metal oxides derived from MOF for SIBs.

MOF derived metal oxides	MOF templates	Initial discharge/charge capacity (mAh g^{-1})	Current density (A g^{-1})	Cycle number	Capacity after cycles (mAh g^{-1})	Ref.
Porous CoFe_2O_4 NCs	PB	573/394	2.5	500	152.6	[342]
Hollow octahedral porous $\text{CuO}/\text{Cu}_2\text{O}$ -300	Cu-MOF	—/—	1.0/2.0	400/600	212/165	[343]
Mesoporous Co^{2+} - TiO_2 Nanodisks-32	Ti-MIL-125@Co	498/232	0.5	500	140	[344]
SnO_2 nanospheres	Sn-MOF	—/—	—	100	970	[345]
MgFe_2O_4 hollow microboxes	PBA	406/207	0.05	150	135	[346]
Porous cake-type TiO_2	Ti-MIL-125	—/—	1.0	2500	173	[347]
$\text{Co}_3\text{O}_4/\text{ZnO}$ hybrids	Co-Zn-ZIF	—/—	2.0	1000	242	[348]

Table 8

Porous carbon derived from MOF for SIBs.

MOF derived porous carbon	MOF templates	Initial discharge/charge capacity (mAh g ⁻¹)	Current density (A g ⁻¹)	Number of cycles	Capacity after cycles (mAh g ⁻¹)	Ref.
N-rich PC NSs-1	2D hexamine-type MOF	425/318	5.0	1000	170	[349]
3D hollow PC-800	Mn-MOF	—/—	0.1	100	313.8	[350]
HNC-800	HMT-based MOFs	441/254	2/5/10	500	145/123/95	[249]
S-doped meso PC	MOF-5, S powders	1491.5/296.5	0.2	500	173.7	[351]
Accordion-like NPC	Al-MOF	912/307	0.1	200	210	[352]
Cube-shaped PC	MOF-5	1822.8/626	3.2	5000	100	[353]
Amorphous carbon nitride	ZIF-8	640/430	1.67	2000	175	[354]
N-doped PC	ZIF-67	576/231	0.5	500	182	[355]

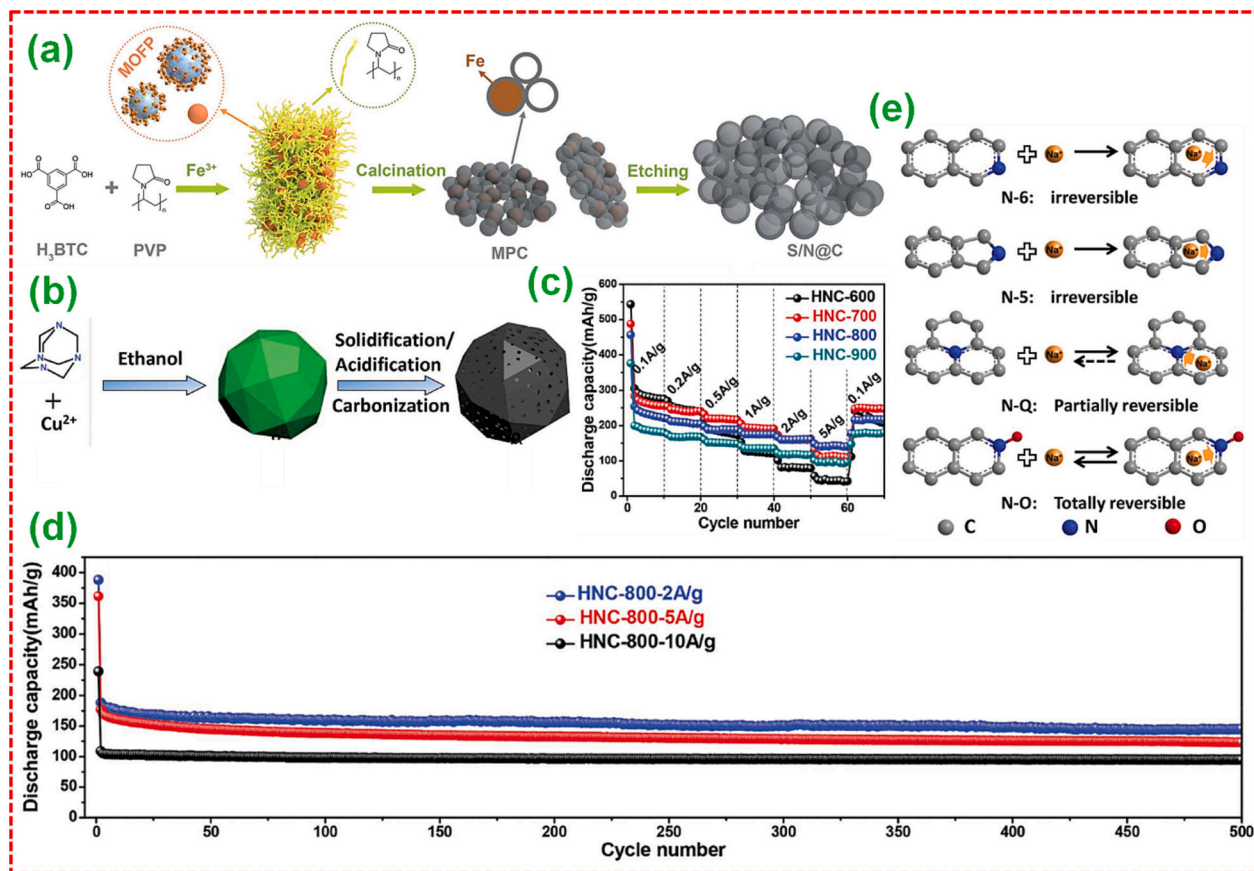


Fig. 37. (a) Preparation of S, N doped thin carbon. Adopted with permission from Ref. [358], Copyright 2018, Wiley VCH, Janus. (b) Pictorial demonstration of Cu-MOF derived NDC material, (c) rate performance achieved at various annealing temperatures, (d) Cycle stability at various current densities of HNC-800, (e) Reaction models of various N configurations with Na ions. Adopted with permission from Ref. [249], Copyright 2018, Wiley VCH, Janus.

ranging from 600 to 900 °C in an inert environment (Fig. 37b). The optimized product (i.e., HNC-800) exhibited exceptional rate performance and cycle stability shown in Fig. 37c, d. The presence of nitrogen atoms (N-6, N-5, N-Q, N—O) portrayed a pivotal function in Na-storage. Specifically, the reversibility of sodiations followed this order: N-6 < N-5 < N-Q < N-O, with the neighboring carbon of N-6 acting as active sites. The N-6/N-Q ratio had a significant impact on capacity and rate performance (Fig. 37e).

Similarly, the research team chose another Zn-MOF as a precursor to derive N-rich PC nanosheets (NSs) (Fig. 38a) [349]. This carbon material displayed an extended lifespan after 1000 cycles with a 76.9 % retention in capacity revealed in Fig. 38b. In addition to the approaches stated earlier, electro spun carbon nanofibers (CNFs), or hollow CNFs derived from MOF often possess a porous structure, high surface area and good electrical conductivity making them promising anode for SIBs.

Goodenough and their team showed the preparation of hollow N-doped CNFs (HPCNFs-N) through the in-situ growth of Zn-Co-ZIF over the PAN polymer [359]. The carbonization was accomplished at 700 °C in an inert environment with a ramping of 2 °C min⁻¹ for 20 h, followed by acid etching (Fig. 38c). It's noteworthy that expanding the zinc acetate amount led to the transformation of ZIF derived materials from NFs to hollow tubes. The resulting hollow tubes contained a significant carbon amount with an interplanar spacing of 0.38–0.44 nm, which facilitated rapid Na-ion intercalation. Thanks to these unique structural characteristics, the final hollow tubes demonstrated outstanding Na-storage activity, including a high capacity of 346 mAh g⁻¹ and outstanding cycle life after 10,000 cycles with negligible capacity decay when used as an anode for SIBs (Fig. 38d-f).

In recent advancements, our research team has made substantial progress in the field of MOF-derived heteroatom-doped PC as an anode

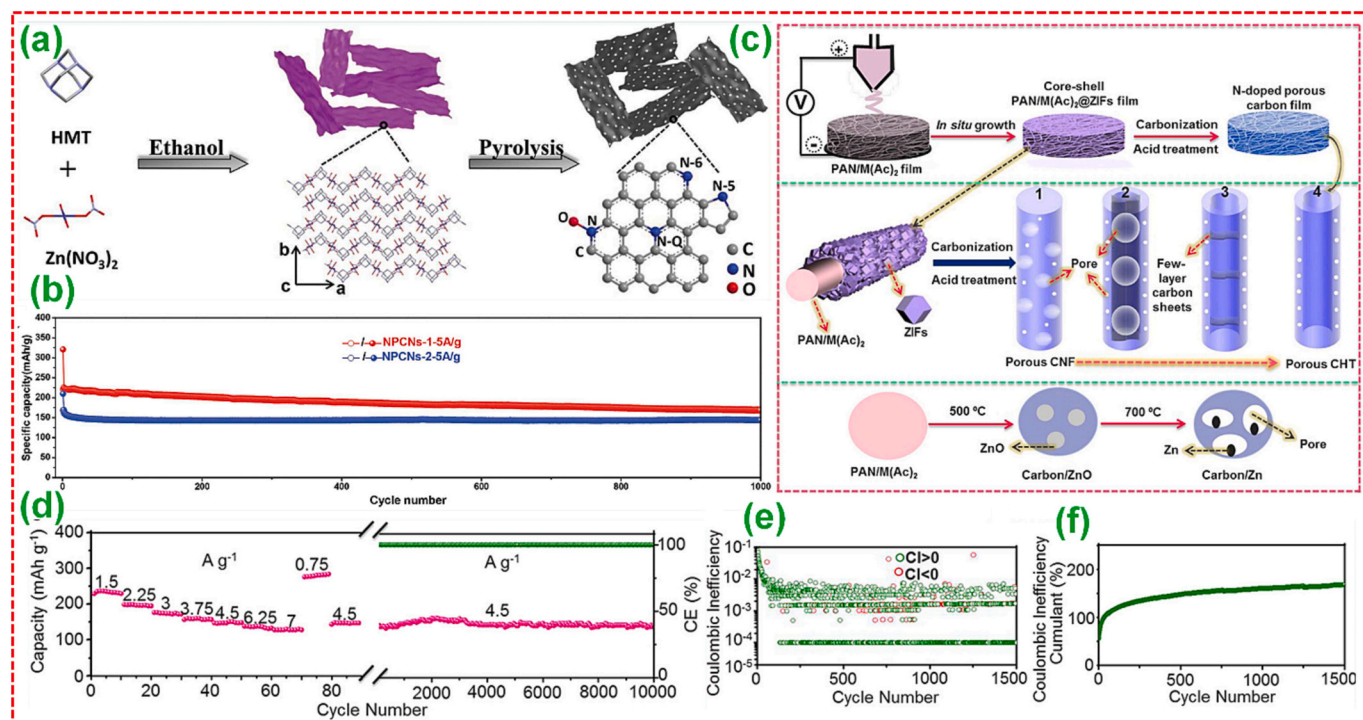


Fig. 38. (a) Pictorial demonstration of N-doped PC NSs and (b) Cycle stability. Adopted with permission from Ref. [349], Copyright 2018, Wiley VCH, Janus. (c) Preparation and (d-f) cycle life of a series of 1D nanocarbons from N-doped CNFs to CHTs. Adopted with permission from Ref. [359], Copyright 2017, Elsevier B.V.

for SIBs, showcasing impressive energy storage capacity. One noteworthy accomplishment involved the fabrication of NDC foils (NC-1) derived from Mn-MOF via a two-way methodology. This strategy included the controlled preparation of 2D Mn-MOF and subsequent heat treatment of prepared Mn-MOF in the presence of NH_3 environment. Following this, an acid etching activity was applied to produce NDC foils with a multiscale pore structure, encompassing micro-, meso-, and macropores, and an abundance of N moieties (Fig. 39a) [258]. TEM analysis highlighted the ultrathin thickness of the initially synthesized 2D Mn-MOF precursor. After the pyrolysis process, substantial amounts of Na_2CO_3 components and MnO NPs were evenly distributed on the surface or within the layers, which were subsequently eradicated to achieve NDC foils (Fig. 39b-d). This novel structural benefit established a continual electron-conductive platform and summarized the transport of ions pathway, ultimately equipping the elevated NC-1 sample with remarkable capacity and cycle performance. Furthermore, it achieved a high capacity of 150 mAh g^{-1} at 10 A g^{-1} of current density (Fig. 39e, f), surpassing the performance of bulk MOF-derived NDC and many reported results.

6.2.3. Metal chalcogenides derived from MOF

SIBs, resembling LIBs in their electrochemical Na-storage and release mechanisms, hold significant promise as an energy storage device. Consequently, the pursuit of innovative anode materials with exceptional Na-storage capability for SIBs remains critically important. MOF-derived MO, encompassing selenides, sulfides, and phosphides, when combined with PC composites, not only retains the benefits of porous nature and high surface area but also bolsters structural stability and conductivity. This underscores their increasing relevance in the realm of SIBs (Table 9).

Much like in the case of LIBs, applying post-treatments to MOF-derived NCs, like sulfurization, selenization, and phosphorization, can significantly boost their Na-storage capabilities. Metal chalcogenides were created by carbonizing MOF templates followed by sulfurization/selenization processes, and these materials have been employed as an anode in SIBs. This is due to the fact that S, Se, and O belong to the same

chemical group, implying that their compounds of metals share comparable physicochemical characteristics. For example, Mai and colleagues effortlessly produced PC confined CoS NPs (7-CoS/C) through in-situ carbonization followed by sulfidation of Co-MOF template at 600°C for 2 h (Fig. 40a) [365]. Thanks to the synergistic effects arising from chemical and structural interactions among porous NRs and CoS NPs, the 7-CoS/C NCs exhibited outstanding Na-storage activity, including extended cycle life, a high capacity of 542 mAh g^{-1} at 1 A g^{-1} , and exceptional rate capacities (Fig. 40b, c). Further, metal sulfides like NiS_2 [360], WS_2 [375], and MnS [362], were synthesized using a similar approach outlined earlier, involving the utilization of MOF templates. To enhance electrical conductivity and facilitate rapid kinetic reactions, graphene has been incorporated. For instance, Huo, Lu, and other researchers presented a MIL-88 derived composite. This composite comprised FeS_2 , N, S co-doped PC (NSC), and reduced graphene oxide (rGO) ($\text{FeS}_2/\text{NSC}/\text{G}$). Remarkably, it maintained a capacity of 203.5 mAh g^{-1} at 10 A g^{-1} even after 400 cycles, as illustrated in Fig. 40d-i [385]. The primary capacity contribution originated from the redox mechanism of FeS_2 , in addition to the EDLC and surface pseudo capacitance of the NSC and rGO. Likewise, additional composite material derived from GO and ZIF-67, featuring rGO and hollow carbon-confined Co_9S_8 QDs ($(\text{Co}_9\text{S}_8 \text{ QD@HCP})/\text{rGO}$), was described as shown in Fig. 40j [378]. This NC exhibited 92.6 % retention in capacity at 300 mA g^{-1} after 500 cycles as shown in Fig. 40k. In addition to oxides, and sulfides, selenides of metals have also been synthesized from MOF templates and utilized as an anode for SIBs. Hu and their research team employed Cu-MOF, Fe-MOF, and Ni-MOF as templates to fabricate $\text{Cu}_2\text{Se}/\text{C}$ octahedra, NiSe/C microspheres, and $\text{Fe}_7\text{Se}_8/\text{C}$ NRs, respectively, by in-situ carbonization followed by selenization activity [328]. These composites exhibited remarkable cycle stability during cycling at high current density and supported outstanding rate performance.

6.2.4. Metal phosphides derived from MOF

MOF derived metal phosphides from have been extensively examined as promising anodes in SIBs, showcasing impressive energy storage

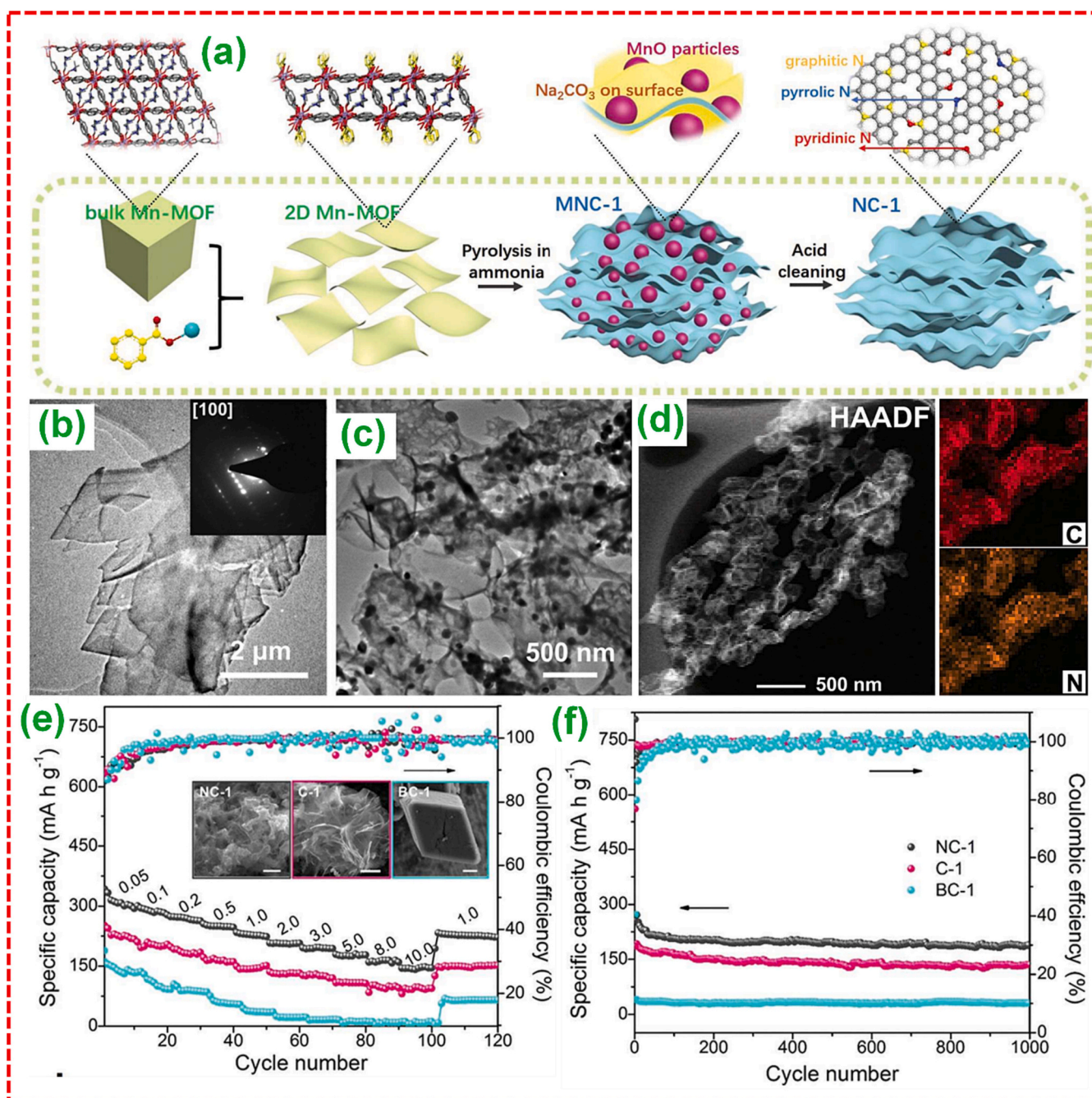


Fig. 39. (a) Pictorial demonstration of PC foils preparation, (b-c) TEM analysis of NDC foils, (d) STEM and the equivalent EDS elemental mapping analysis of C, and N elements of PC foil, (e) rate performance and (f) cycle stability of PC foils. Adopted with permission from Ref. [258], Copyright 2018, Wiley VCH, Janus.

phenomena. For example, Kang and their colleagues presented a CoP/C NC synthesized from Co-MOF and red phosphorus (P) templates [259]. The use of numerous additional sequences resulted in the formation of two distinct NCs: CoP-O (indicating direct heat treatment) and CoP-T (indicating two-way heat treatment) (Fig. 41a). The CoP-O material retained a remarkable capacity of 598 mAh g^{-1} at 0.1 A g^{-1} after 200 cycles due to the presence of a conversion type mechanism instead of alloying type mechanism. It still delivered a substantial capacity of 386 mAh g^{-1} after 900 cycles even when cycled at a higher rate of 1.0 A g^{-1} as illustrated in Fig. 41b, c. This exceptional activity was attributed to the existence of the highly conductive nature of NDC NSs and a P—C chemical interface. Yin and colleagues introduced an innovative approach by anchoring graphene oxide (GO) on PDDA-modified Ni-foam, followed by the growth of ZIF-67 on the substrate. This process led

to the formation of a yolk-shell CoP@C-RGO-NF NC shown in Fig. 41d [374]. The resulting composite exhibited exceptional cycle/rate performance when utilized as a binder-free anode in SIBs. In addition to the previously mentioned studies, composites derived from MOF with various post-modifications were developed and applied as an anode for SIBs. For instance, researchers created a core-shelled $\text{Co}_9\text{S}_8/\text{MoS}_2\text{-CN}$ composite by introducing ammonium molybdate in ZIF-67 derived Co/NDC [361]. This material displayed remarkable cycle stability and rate performance when utilized in SIBs. Furthermore, a blend comprising porous carbon derived from Co-MOF grown on carbon cloth (CC) and $\text{Na}_2\text{MoO}_4 \cdot 2\text{H}_2\text{O}$ was subjected to hydrothermal conditions to produce free-standing CC@CN@MoS₂ nano-wall arrays and directly employed as an anode for SIBs [371]. The high surface area, novel array architecture, and the introduction of nitrogen-induced defects collectively endowed

Table 9

Metal chalcogenides derived from MOF for SIBs.

MOF derived chalcogenides	MOF templates	Initial discharge/charge capacity (mAh g ⁻¹)	Current density (A g ⁻¹)	Number of cycles	Capacity after cycles (mAh g ⁻¹)	Ref.
TiO ₂ /C NC-700	MIL-125 (Ti)	—/—	5.0	10,000	120	[251]
VO _x /PCs-2	V-MOF	—/—	0.5/1.0	2000	152/123	[248]
NiS ₂ /NC	Ni-BTC-MOF, thiourea	759.2/559.1	0.5	300	356.2	[360]
Cu ₂ Se@C	Cu-BTC MOF, Se powder	—/—	1.0	200	207	[328]
NiSe@C,	Ni-BTC MOF, Se powder		3.0	2000	160	
Fe ₇ Se ₈ @C	Fe-BDC MOF, Se powder		3.0	550	219	
H-FeSe ₂ /GC	MIL-88, Se powder	642/511	0.2	100	587	[285]
yolk-shelled Co ₉ S ₈ /MoS ₂ -CN	ZIF-67, (NH ₄) ₂ MoS ₄ , S powder	840/604	2	250	421	[361]
CoP/CNS-O	Co-BTC MOF, red P	—/—	1.0	900	386	[259]
Carbon coated MnS	Mn-BTC MOF	—/—	1.0	5000	148.3	[362]
Co ₂ P@N-C@rGO	ZIF-67, NaH ₂ PO ₂ , GO	—/—	1.0	1000	100	[363]
Porous shuttle like V ₂ O ₃ /C	MIL-88B-V	630/404	2.0	1000	133	[364]
7-CoS/C NRs	Co-BTC MOF, sublimed S	—/—	1.0/5.0	2000	542/504	[365]
Fe ₇ S ₈ @C-G	MIL-88Fe, S power, GO	714/426	0.5	150	449	[366]
3DG/FeS@C	PB, GO, S powders	—/—	1.0	300	358	[367]
FTO c CNTs	Core-shell Fe-MOF@TiO ₂	956.0/543.6	2.0	3500	210.5	[368]
N-doped Yolk-Shell-Structured CoSe/C	ZIF-67, Se powder	—/—	0.5	50	531.6	[369]
Co/(NiCo)Se ₂ box-in-box hollow NCs	ZIF-67, Se powder	661/574	0.2	80	497	[370]
CC@CN@MoS ₂	Co-MOF, CC, Na ₂ MoO ₄ ·2H ₂ O	1288/659	1.0	1000	265	[371]
Hollow Ni ₃ S ₂ /Co ₉ S ₈ /NDC	Ni-Co-MOF, thiourea	554/425	1.0	300	300	[372]
Ni-doped Co/CoO/NC	Ni-Co-ZIF-67	—/—	0.5	100	218.7	[373]
CoP@C-rGO-NF	ZIF-67, NF, NaH ₂ PO ₂ , GO	2455.6/1163.5	0.1	100	473.1	[374]
WS ₂ @NC	PB, ammonium tetrathiotungstate	—/401	5.0	500	78	[375]
ZnS-Sb ₂ S ₃ @C Core-Double Shell Polyhedron	ZIF-8, TAA, Sb ²⁺	1675/1029	0.1	120	630	[376]
P@N-MPC	ZIF-8, red P	1312/710	1.0	1000	450	[377]
NDC	Zn-Co-ZIF, PAN,	735/346	4.5	10,000	140	[359]
Co ₉ S ₈ (QD@HCP)@rGO sponge-like composites	ZIF-67, GO, S powder	679/604	0.3	500	628	[378]
Carbon-coated rutile TiO ₂	Ti-MOF	324.7/136.4	3.36	2000	70	[379]
G-NC@TiO ₂	MIL-125(Ti), GO	—/—	1.0	5000	—	[380]
CuO/Cu ₂ O-GPC	Cu-BTC MOF	780/—	0.05	170	302.9	[381]
Co ₃ O ₄ @NC	ZIF-67	813/516	1.0	1000	175	[382]
N-doped hollow MoS ₂ /C nanospheres	Mo-MOF	972/600	2.0	5000	128	[383]
Fe ₃ O ₄ QD@C-GN	MIL-88-Fe-NH ₂ , GO	1081/971	2/5/10	1000	343/234/149	[384]
Hollow NiO/Ni/Graphene	Ni-BTC MOF	992/483	1.0	200	248	[257]

this composite with an outstanding Na-storage capacity of 265 mAh g⁻¹ at 1.0 A g⁻¹ of current density after 1000 cycles.

6.3. Potassium ion batteries

Energy storage plays a pivotal role in advancing PIBs as long-lasting devices. To fulfill this essential requirement, numerous approaches have been proposed for crafting electrode materials, with a particular focus on anodes. Among the most promising approaches, derivation of carbonaceous materials and metal compounds from MOF templates stands out. This method is highly favored because it enables the retention of the MOFs' inherent hierarchical architectures, and uniform porosity. Achieving these characteristics through MOF template-based preparation is quite challenging to replicate using other techniques. Pristine MOFs act as sacrificial precursors, undergoing heat treatment in the presence of air or inert environment. The resulting structures inherit enhanced stability, rendering them well-suited for energy storage applications [386]. While MOF precursors exhibit commendable performance, their limited conductivity and structural stability during prolonged cycling have restricted their utility as electrodes for PIBs. Consequently, scientists have shifted their focus to MOF derived materials and utilized them as anodes for PIBs. A diverse range of carbonaceous materials has been synthesized through the MOF precursors carbonization thereby subsequent acid etching to vaporize metal

constituents. These carbonaceous products offer doping with N, P, S, F, and O along with the distinctive structural attributes. These dopants enable the successful intercalation/deintercalation of K-ions. Likewise, metal compounds and metal compounds/carbon composites derived via thermal treatment of MOF precursors, demonstrate outstanding K-ion storage due to their porous nature and ordered structures contribute to advanced K-storage via an alloying/conversion reaction compared to conventional metal compounds or physically blended composites of metal compounds and carbon. Furthermore, MOF derived materials exhibit fascinating thermal stability, enabling the operation of PIBs at elevated temperatures. To offer a comprehensive understanding, this section subdivided into porous carbon/metal alloys/metal chalcogenides/metal phosphides derived from MOF as anodes for PIBs. It delves into the K-ion storage depending on the interplay between structure, properties, and performance.

6.3.1. Porous carbon derived from MOF

Although the intercalation/deintercalation of K-ions into the GC structures has been investigated, their K-ion storage has been somewhat unsatisfactory. As shown in the previous portion, the anode made of graphite did achieve a 273 mAh g⁻¹ reversible capacity close to its theoretical limit at the rate of C/40, resulting in the KC₈ formation. However, the unstable structure and initial capacity degradation observed during extended cycles did not undergo the needs of energy

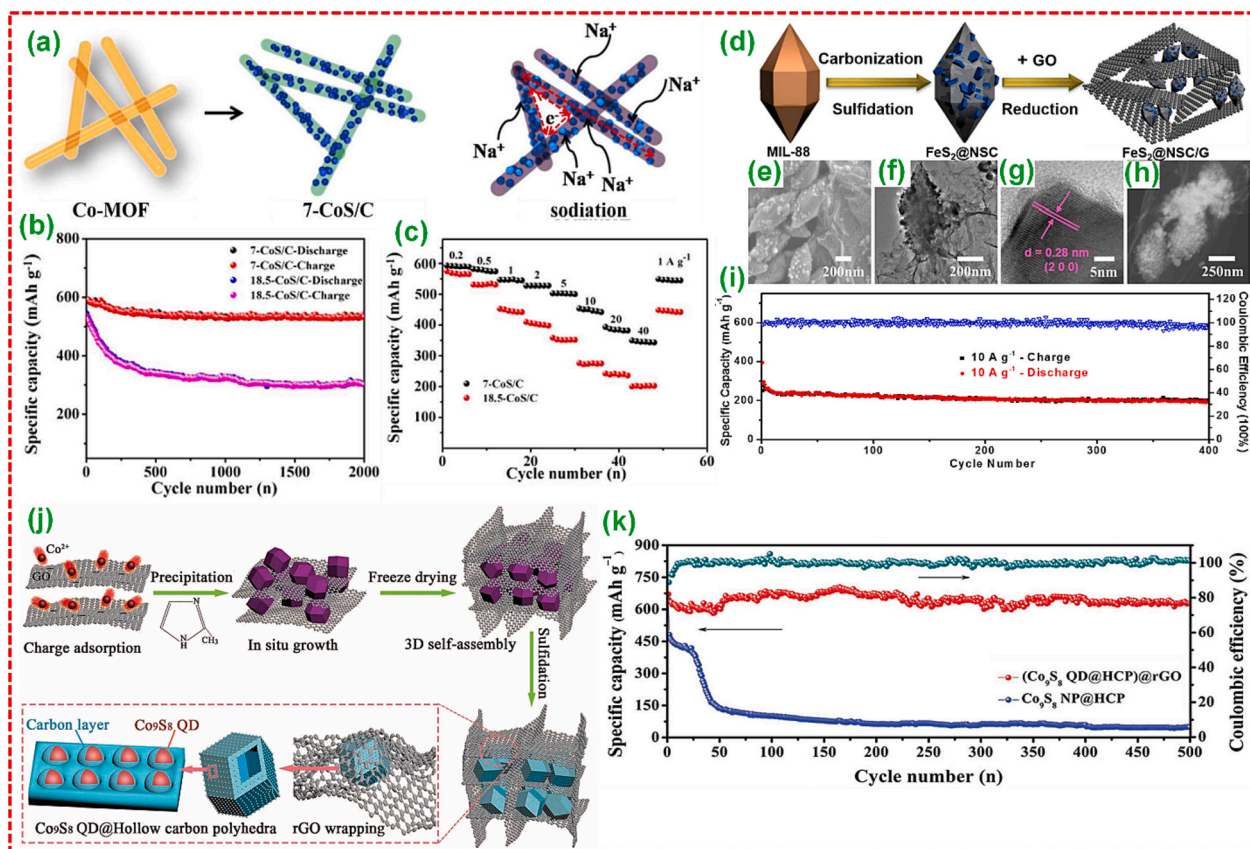


Fig. 40. (a) Pictorial demonstration of Na-storage mechanism of 7-CoS/C composite, (b) cycle stability and (c) rate performance. Adopted with permission from Ref. [365], Copyright 2017, Elsevier B.V. (d) Preparation of FeS₂@NSC/G NC, (e-h) TEM analysis, and (i) cycle stability. Adopted with permission from Ref. [385], Copyright 2018, American Chemical Society. (j) Schematics of (Co₉S₈ QD@HCP)@rGO NC formation, (k) cycle performance. Adopted with permission from Ref. [378], Copyright 2017, Wiley VCH, Janus.

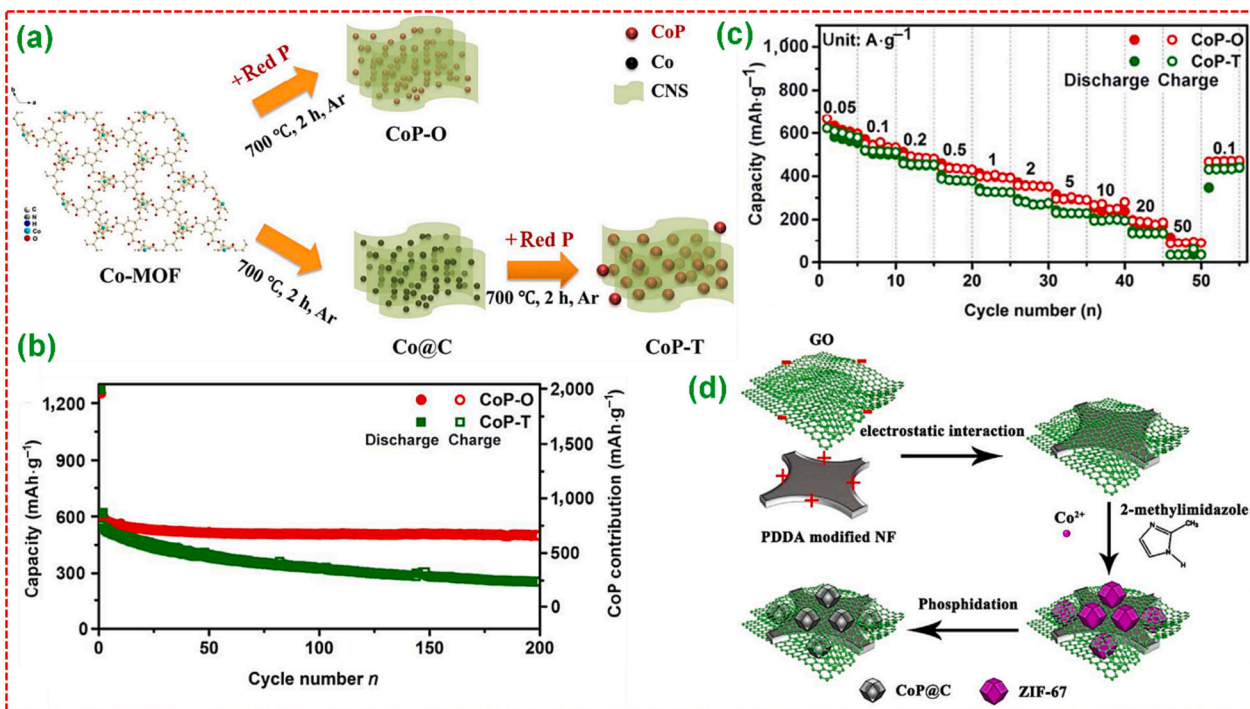


Fig. 41. (a) Pictorial demonstration of CoP-O and CoP-T NCs formation, (b) cycle stability and (c) rate performance. Adopted with permission from Ref. [259], Copyright 2017, Springer Nature. (d) Schematics of CoP@C-RGO-NF composite formation. Adopted with permission from Ref. [374], Copyright 2017, Elsevier B.V.

storage in the case of present PIBs [387]. Numerous carbonaceous products like CNTs, hard/soft carbon, rGO, and CNFs, have been explored as probable anodes for PIBs. Unfortunately, these materials have exhibited inadequate K-storage with reversible capacity falling below 300 mAh g^{-1} , and often showing insignificant retention in capacity over 150 cycles [388,389]. This type of performance results due to several factors, including greater K-ion size than Li-ion, the inherently lower theoretical capacity of carbon products in PIBs, and the greater demand for interlayer distance during intercalation of K-ion, which leads to structural breakdown and, consequently, poor cycle capacity. To address these challenges, researchers have turned to the surface dominated activity (i.e., pseudocapacitive effect) that promotes the K-ions absorption over the surface of carbon products. This effect increases

the rate of K-ion transport during the repeated GCD analysis. It has been noticed that the effect of pseudocapacitive nature can be increased by introducing doping of N into the carbon products, specifically pyridinic N, which contains a lone pair of electrons and donates electrons to the conjugated π bond. Pyridinic N successfully adsorbs K-ions, leading to increased rate performance, cycle life, and reversible capacity. However, controlling the amount of pyridinic N in conventional carbonaceous materials has proven challenging. Therefore, researchers have proposed an efficient preparation strategy, namely MOF precursor derivation, to boost the pyridinic N amount which may further increase the carbon products performance in PIBs [389].

The expanding MOFs family boasts meticulously structured constructions with impressive surface areas ranging from 1000 to 10,000

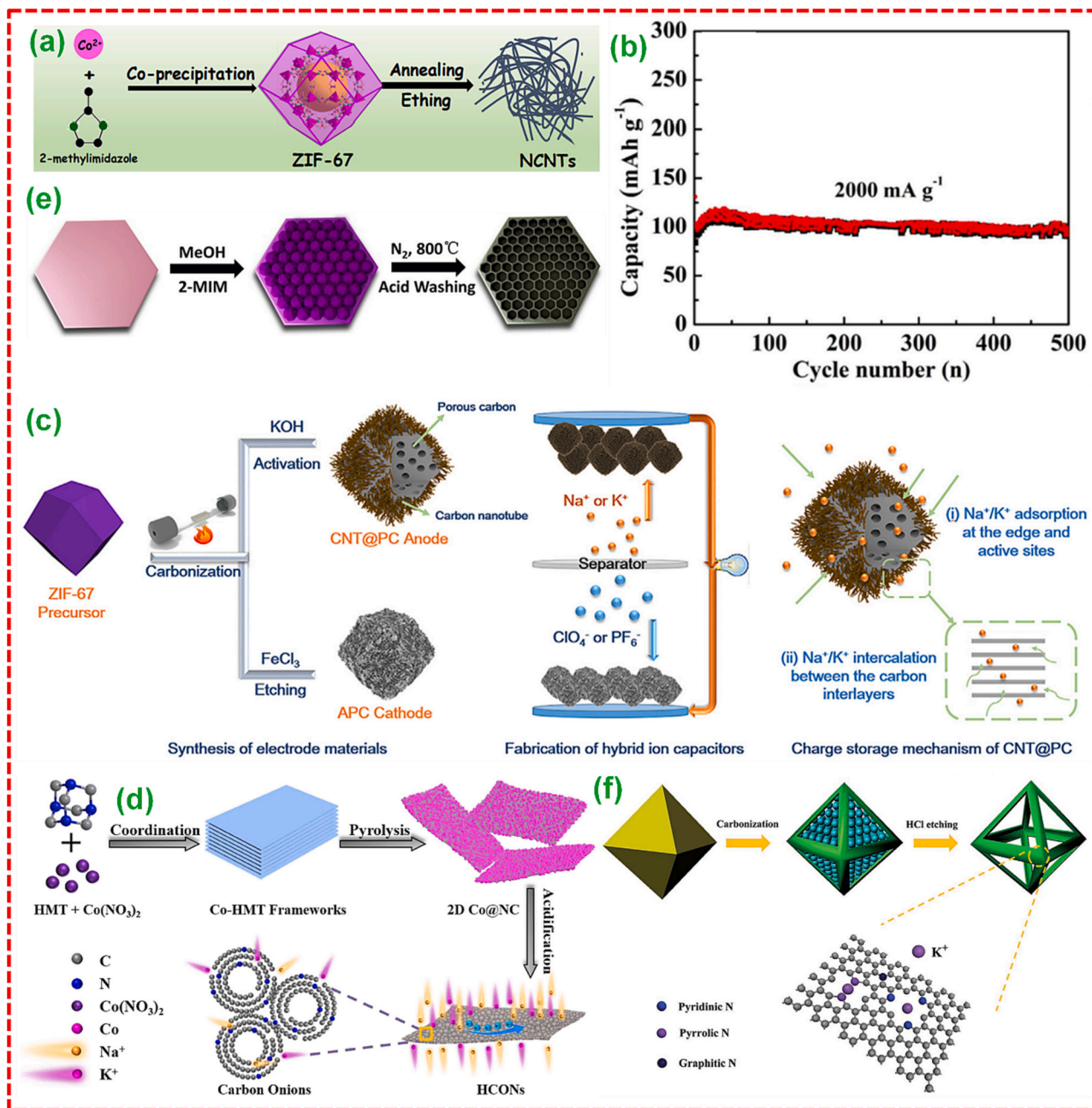


Fig. 42. Pictorial demonstration of (a) NCNTs formation, (b) rate capability. Adopted with permission from Ref. [391], Copyright 2017, Wiley VCH, Janus. (c) N-doped CNT@PC. Adopted with permission from Ref. [392], Copyright 2019, Elsevier B.V. (d) HCONs. Adopted with permission from Ref. [393], Copyright 2019, Royal Society of Chemistry. (e) Cellular N—C. Adopted with permission from Ref. [394], Copyright 2020, Elsevier B.V. and (f) NPCFs. Adopted with permission from Ref. [395], Copyright 2020, Wiley VCH, Janus.

$\text{cm}^2 \text{g}^{-1}$, along with exceptional porosity. These characteristics provide ample opportunities to tailor their structural properties for specific applications during the synthesis process. A paramount approach in utilizing MOFs is the creation of nano porous carbon (NPC) materials through controlled temperature thermal treatments, using MOFs as sacrificial templates or precursors. This method offers several advantages, including:

- Suitability for large-scale synthesis: NPC materials could be efficiently prepared on a bulk range.
- Simplicity and cost-effectiveness: Pristine MOFs can be synthesized under straightforward and cost-effective conditions.
- Enhanced interlayer spacing: The resulting NPC materials exhibit expanded interplanar distance, which is advantageous to achieve high capacity.
- In-situ doping of heteroatom: NPC structure readily accommodates in situ heteroatom doping during a heat treatment process.
- Doping of single or multiatom: Single or dual elemental doping, involving elements such as N, P, F, O, and S, would be attained easily through a heat treatment process. This type of doping enhances diffusion kinetics and further enlarges the interlayer spacing.

These attributes make the application of MOFs as sacrificial templates for NPC materials highly advantageous for various applications.

In a study conducted by Zhang and colleagues, they explored the process of pyrolyzing ZIF-67 polyhedra followed by etching with acid, to create three-dimensional networks of graphitic carbon (GC). The primary objective was to enhance the connectivity and conductivity among carbon particles and potassium ions (K-ions) [390]. In their research, the authors investigated size-supported thermolysis, wherein the ZIF-67 polyhedrons size was decreased from a macro to a nano scale. This reduction in size led to the instinctive 3D carbon networks formation with highly graphitized structures, complemented by the catalytic effect of Co NPs. The resulting graphitic networks exhibited electrochemical performance equivalent to that of conventional carbonaceous anode materials, achieving a specific capacity of 190 mAh g^{-1} with an impressive retention in capacity of 75 % after 500 cycles at 50 mA g^{-1} . Moreover, these graphitic networks demonstrated excellent cycle performance in comparison to standard carbonaceous anodes. Another team investigated the use of ZIF-67 derived N-doped CNTs (NCNTs) as depicted in Fig. 42a as anodes in PIBs and achieved favorable rate capability [391]. These NCNTs possessed a distinctive edge-open layer-arrangement structure, facilitating the rapid K-ions intercalation. This structural feature contributed to better rate capacity, as evidenced by the high retention in capacity of 102 mAh g^{-1} over 500 cycles at 2 A g^{-1} illustrated in Fig. 42b. As previously discussed, a high pyridine N amount enhances the performance of carbon anodes. To leverage this, Li and colleagues synthesized high pyridine N-doped PC derived from ZIF-67 polyhedra [389]. Enhanced pyridine N content in N-doped PC, along with a minor variation in interlayer spacing, provided bonus adsorption positions for K-ions during the insertion/extraction activity. Consequently, this material achieved a great reversible capacity of 587.6 mAh g^{-1} at 50 mA g^{-1} , outstanding rate performance of 186.2 mAh g^{-1} at 2 A g^{-1} , and impressive cycle performance of 231.6 mAh g^{-1} at 500 mA g^{-1} after 2000 cycles. Additionally, Fe-ZIF-8 derived Fe-induced CNT/NDC (FNC) material was investigated as an anode for PIBs [396]. The incorporation of CNTs enhanced the contact area and conductivity, resulting in high reversible capacity of 268 mAh g^{-1} at 0.1 A g^{-1} after 200 cycles. Furthermore, it exhibited an exceptionally long cycle stability, retaining a capacity of 169 mAh g^{-1} at 1.0 A g^{-1} after 5000 cycles, along with an outstanding rate capacity. This impressive performance was accredited to the unique amorphous carbon structure. In a different research endeavor, an abundant ZIF-8 was vertically cultivated on the 3D Cu substrate using a binary-solvent technique. Afterwards, this array underwent heat treatment to yield a graphene-type N-doped PC array on the 3D Cu substrate, denoted as NPC/Cu [397]. During the heat

treatment activity, the Zn component vaporized, resulting in the formation of NPC/Cu. This material was utilized as a binder-free and self-standing anode for PIBs at numerous electrolytes. Remarkably, it showed outstanding electrochemical activity, including high reversible capacity of 315 mAh g^{-1} at 50 mA g^{-1} after 500 cycles, greater rate capacity of 120 mAh g^{-1} at a charge-discharge rate of 21 C , and comparatively stable capacity of 129 mAh g^{-1} at 2 A g^{-1} after 20,000 cycles. These impressive results were achieved using a 5 M concentrated ether electrolyte containing KFSI in DME.

Indeed, it is worth noting that materials derived from MOFs and doped with N tend to exhibit increased defect density, thereby enhancing electronic conductivity and enabling exceptionally long cycling stability. For instance, MOF-derived 3D interconnected N-doped PC [398], N-doped CNT-coated PC [392], and N abundant hollow carbon onion assembled NSs (HCNs) [393] have all demonstrated impressive capacity retention and unprecedented cycling stability in PIBs. Specifically, these materials achieved a remarkable cycle performance of 157 mAh g^{-1} after 12,000 cycles at 2.0 A g^{-1} , 141 mAh g^{-1} after 1000 cycles at 1.0 A g^{-1} , and 132 mAh g^{-1} after 5000 cycles at 2.0 A g^{-1} , respectively. Fig. 42c shows the process of preparing an activated PC (APC) cathode and a CNT@PC anode for hybrid SCs. Additionally, the figure illustrates the adsorption-intercalation process involved in the K-ion storage within PIBs. Likewise, in Fig. 42c and Fig. 42d, we can observe the pictorial representation of the preparation approach for N-HPC [398] and HCNs [393]. Additionally, various NDC materials were examined as an anode for PIBs, each showcasing remarkable cycle performance:

1. A NDC with a honeycomb construction known as cellular N—C (Fig. 42e) [394].
2. N-doped PC framework (NPCF) with a high N amount of 13.57 %, primarily consisting of pyrrolic N/pyridinic N (Fig. 42f) [395].
3. 3D N-doped micro-PC polyhedra (NMCP) encased by 2D rGO, denoted as NMCP@rGO [399].

These materials, derived from MOFs, delivered remarkable cycling stability in PIBs:

- Cellular N—C exhibited a capacity of 143 mAh g^{-1} at 1 A g^{-1} over 2000 cycles.
- NPCF achieved a capacity of 258.9 mAh g^{-1} after 2000 cycles at 1 A g^{-1} .
- NMCP demonstrated a capacity of 151.4 mAh g^{-1} after 6000 cycles at 5.0 A g^{-1} .

The cyclic voltammetry (CV) analysis of NPCFs revealed an initial large peak at 0.6 V during the cathodic inspection. Interestingly, in subsequent scans, this peak disappeared, and the CV curves overlapped. This behavior strongly suggested the SEI formation and demonstrated the reversibility of K-ion intercalation and deintercalation into and from NPCFs. These materials displayed exceptional morphological characteristics, including a high surface area, well-distributed micro/meso/macropores, pyrrolic/pyridinic N doping, and extended interlayer distances. Collectively, these features greatly facilitated the K-ion diffusion kinetics, ultimately enhancing the capacity of these electrodes to hold a higher quantity of K-ions. Liu and colleagues introduced a novel approach for synthesizing NPC using a double-solvent diffusion-heat treatment technique. They utilized UIO-66- NH_2 adsorbed with NH_4Cl as the template [400]. When employed as an anode for PIBs, the resulting NPC exhibited an impressive reversible capacity of 346 mAh g^{-1} at 100 mA g^{-1} and maintained a capacity of 187 mAh g^{-1} after 800 cycles. However, quantitative kinetic studies revealed that this anode exhibited activities akin to traditional graphite anodes, with potassiation/depotassiation mechanisms taking place primarily on the PC surface rather than within the interlayer distance. This led to a less favorable cycle performance. Moreover, significant studies have been directed towards

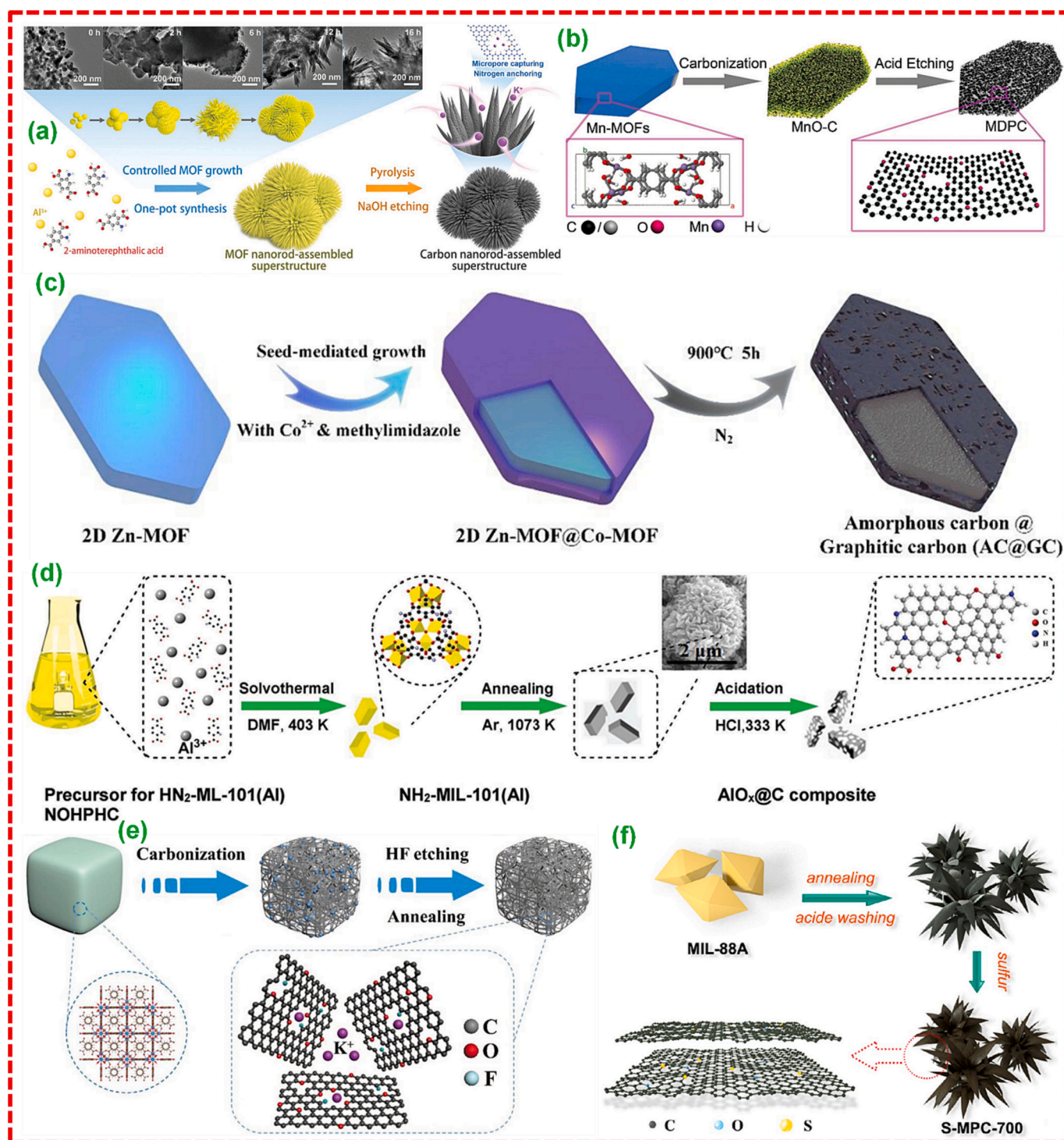


Fig. 43. (a) Pictorial demonstration of CNS formation and equivalent TEM analysis. Adopted with permission from Ref. [401], Copyright 2021, Wiley VCH, Janus. Pictorial demonstration of formation for the (b) MDPC [402], Copyright 2019, Royal Society of Chemistry. (c) AC@GC. Adopted with permission from Ref. [403], Copyright 2017, Wiley VCH, Janus. (d) NOHPHC. Adopted with permission from Ref. [404], Copyright 2019, Wiley VCH, Janus. (e) OFPCN. Adopted with permission from Ref. [405], Copyright 2021, American Chemical Society. and (f) S-MPC. Adopted with permission from Ref. [406], Copyright 2020, Wiley VCH, Janus.

the optimization of MOF architecture and calcination temperature to synthesize exceptional carbonaceous materials. Notable examples include the highly porous NDC NR-assembled superstructure (NCS) (Fig. 43a) [401], porous carbon derived from Mn-MOF (MDPC) (Fig. 43b) [402], amorphous carbon within a GC matrix (AC@GC) (Fig. 43c) [403], and Cu-MOF derived C500 [407]. These studies shed light on the potential of structural engineering to increase the carbon-

based anodes performance for PIBs.

A variety of innovative NPC materials have been designed, showcasing impressive performance in PIBs. These materials include the N/O dual-doped hard PC (NOHPHC) (Fig. 43d) [404], Meso-PC octahedrons (MCOs) [408], N/S co-doped carbon microboxes (NSC) [409], O/F dual-doped PC nanopolyhedra (OFPCN) (Fig. 43e) [405], P/N co-doped porous CNFs (PN-HPCNFs) [410], B/O/N co-doped hollow PC spheres

(HPCS) [411], O/S co-doped PC (S-MPC) (Fig. 43f) [406]. These remarkable carbon anodes are derived from the carbonization-etching of MOF templates and have demonstrated long cycle performance with excellent retention in capacity for PIBs. The outstanding activity of these carbon anodes for PIBs can be largely attributed to their expanded interlayer spacing resulting from dual-elemental doping, along with their high surface areas and distinctive morphological structures. It's worth noting that all the carbonaceous anodes derived from MOFs mentioned above exhibited exceptional cycling stability in PIBs, as summarized in Table 10.

Carbon materials derived from MOFs have emerged as highly attractive anode materials for PIBs. These materials largely fulfill the criteria for commercial electrode materials, including attributes such as non-toxicity, abundance, durability, and extreme cycle performance. They demonstrate commendable performance, offering moderate capacities varying from 200 to 400 mAh g⁻¹. They also exhibit low migration barriers and favorable intercalation potential for the diffusion of K-ions. This suggests a favorable potential for widespread practical applications, particularly after optimization. However, there are still significant challenges to overcome, such as relatively minimal volumetric densities and initial coulombic efficiencies, which currently stand at less than 60 %. Addressing these disparities is crucial, and it necessitates further improvement efforts. The use of theoretical calculations and the application of acquired knowledge can serve as a foundation for optimization and problem-solving. Consequently, we anticipate the development of various carbon-based anodes derived from MOFs that not only enhance the overall energy density of batteries but also have the potential for scalability. These advancements signify a bright future in the energy storage sector.

6.3.2. Metal alloys derived from MOF

Alloying-type materials have garnered significant attention as emerging anodes in rechargeable batteries due to their high capacity, appropriate electrochemical potential, and safety features that contribute to attractive overall performance. Extensive research has focused on elements from Group 10 to 15, thanks to their abundant availability, eco-friendly nature, and cost-effectiveness. All these elements can be employed in various forms, such as metals in crystalline, amorphous, or thin-film configurations, and have the inherent capability to form alloys during the alloying/dealloying processes. Anodes derived from alloying materials, synthesized using conventional methods, typically exhibit tremendous electrochemical activity,

featuring high coulombic efficiency and great reversible capacities. But their application as viable anodes for PIBs are hindered by limitations such as minimal cycle performance and significant capacity loss [412]. Notably, MOFs containing Bi and Sb metal centers have pointed promising potential in the context of PIBs. This is primarily due to its appealing theoretical capacities, namely 385 mAh g⁻¹ for Bi and 660 mAh g⁻¹ for Sb. Further, the incorporation of Bi into PC materials through the MOF templates calcination has been explored for PIBs as an anode. Sun and colleagues introduced a solvothermal followed by carbothermic reduction method to prepare Bi confined within a 3D NDC nanocages (Bi@N-CNCs) framework. This innovative approach utilized a flower typed Bi-MOF compiled with porous 2D NSs as a template (Fig. 44a-e) [413]. When evaluated as an anode, the produced Bi@N-CNCs displayed a substantial reversible capacity of 224 mAh g⁻¹ and impressive cycle life (1200 cycles), as depicted in Fig. 44f, g. In-situ TEM studies revealed the enhanced structural stability achieved through thoughtful void construction. The remarkable electrochemical K-storage activities of Bi@N-CNCs were assigned to the synergistic contributions of the 3D conductive N-CNCs network and the nanosized effects of Bi NPs. To gain a deeper investigation of the electrochemical K-storage activities of Bi@N-CNCs, the researchers also operated SAED and XRD investigations. Additionally, carbon deposited double-shell Bi hollow boxes (C@DSBC) were synthesized using a cation exchange method involving amorphous double-shell ZnS boxes, initially synthesized from the ZIF-8 precursors sulfidation. This process, carried out at room temperature, replaced zinc cations with Bi cations through successive heat treatment [414]. When assessed as a PIB anode material, the C@DSBC composite demonstrated reversible capacity of 351 mAh g⁻¹ with a coulombic efficiency of 52 %. It stated a retention in capacity over 200 mAh g⁻¹, corresponding to a capacity decay of only 0.13 % per cycle, indicating excellent durability and establishing it as a favorable anode for PIBs.

Similarly, anode materials incorporating Bi have demonstrated remarkable performance. Ultrathin carbon film@carbon NRs@Bi NPs composite, referred to as UCF@CNs@BiN, were prepared through the Bi-MOFs heat treatment, as depicted in Fig. 45a [415]. The potassiation/depotassiation behavior of the material was compared to that of traditional Bi nanoparticle electrodes. The stable rod structure of the UCF@CNs@BiN electrode remained intact over numerous cycles, in contrast to traditional Bi NPs that experienced a repeated SEI film formation, resulting in immediate capacity decay and low coulombic efficiency. The UCF@CNs@BiN presented exceptional reversible capacity,

Table 10
Porous carbon derived from MOF for PIBs.

Carbon derived from MOF	MOF template	Voltage (V vs. K/K ⁺)	Current density (A g ⁻¹)	Capacity (mAh g ⁻¹)	Cycle number	Ref.
NCNTs	ZIF-67	0.01–3.0	2	102	500	[391]
FNC	Fe-ZIF-8	0.01–2.5	1	169	5000	[396]
CNT@PC	ZIF-67	0.001–3.0	1	171	1000	[392]
3D carbon networks	ZIF-67	0.001–3.0	0.05	~202.5	500	[390]
N-HPC	3DOM-ZIF-8@PS	0.01–3.0	2	157	12,000	[398]
Cellular N-C	CoAl-LDH@ZIF-67	0.01–3.0	1	143	2000	[394]
NPC	UiO-66-NH ₂ with NH ₄ Cl	0.01–3.0	0.1	187	800	[400]
NPC/Cu	ZIF-8/Cu	0.01–3.0	2	129	20,000	[397]
NMCP@rGO	ZIF-8@GO	0.01–3.0	5	151.4	6000	[399]
NPC	ZIF-67	0.1–3.0	0.5	231.6	2000	[389]
HPCS	Ni-MOF	0.01–2.0	1	190	1000	[411]
C ₅₀₀	Cu-MOF	0.01–3.0	5	210	500	[407]
NCS	NH ₂ -MIL-101(Al)	0.0–3.0	1	166	100	[401]
NOHPHC	NH ₂ -MIL-101(Al)	0.001–3.0	1.05	~130	1100	[404]
S-MPC	MIL-88 A	0.01–3.0	1	206.3	700	[406]
NSC	S-ZIF-67	0.01–3.0	0.5	180.5	1000	[409]
AC@G	Zn-MOF@Co-MOF	0.01–3.0	1	192	5200	[403]
OFFCN	UiO-66(Zr)	0.01–3.0	1	218	2000	[405]
PN-HPCNFs	ZIF-8	0.01–3.0	2.0	226	10,000	[410]
MCOs	Cu-BTC	0.01–3.0	2	80	3000	[408]
MDPC	Mn(BDC)(H ₂ O) ₂	0.01–3.0	0.2	150.2	1000	[402]
NPCF	MET-6	0.01–3.0	1	258.9	2000	[395]
HCONs	Co-HMT	0.01–2.8	2	132	5000	[393]

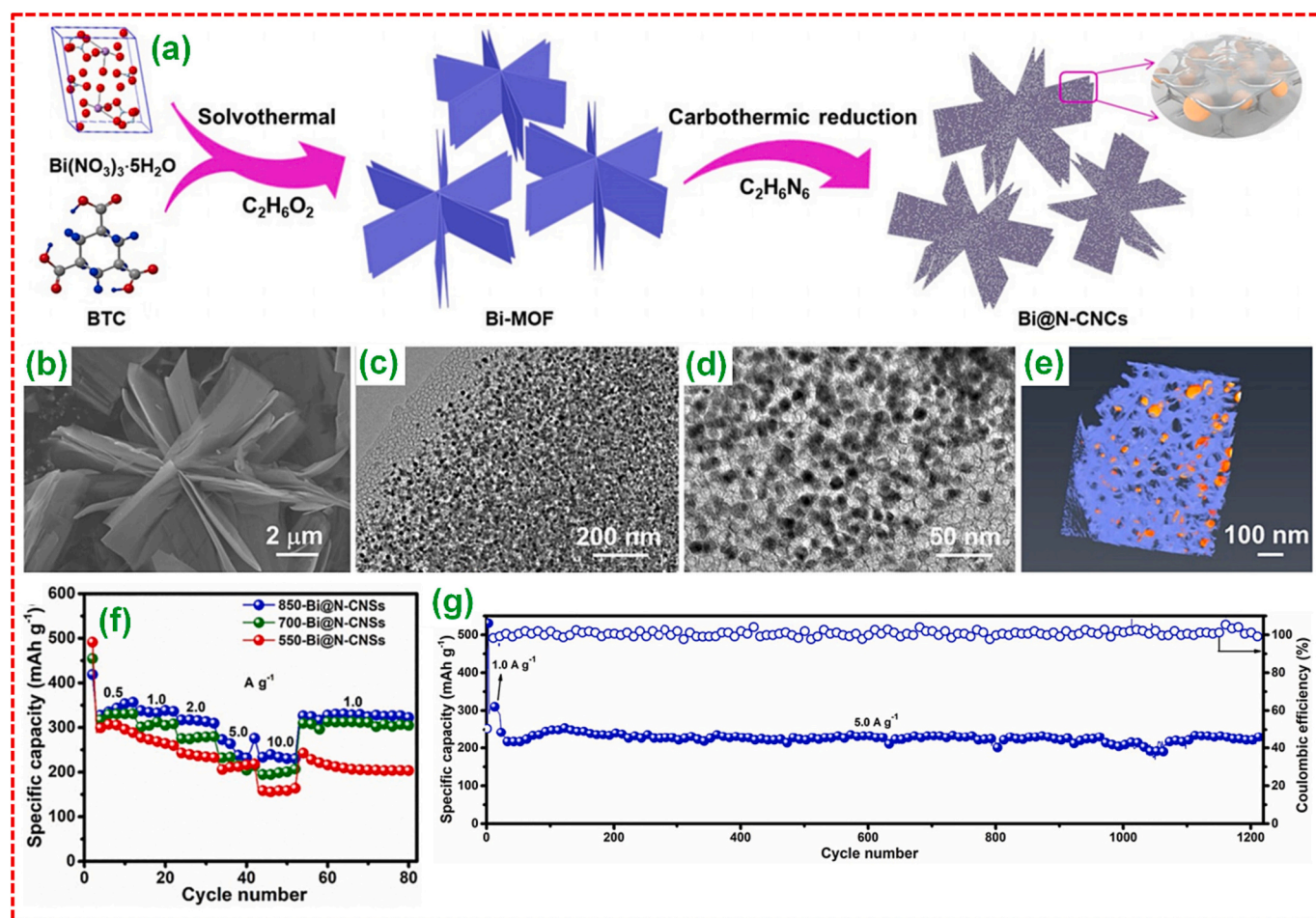


Fig. 44. (a) Pictorial demonstration of Bi@N-CNCs preparation and (b–e) the equivalent FESEM, TEM studies, and restructured 3D tomograms, respectively. Adopted with permission from Ref. [413], Copyright 2021, Wiley VCH, Janus. (f) Rate behaviors of three Bi@N-CNCs anodes, and (g) cycle stability of 850-Bi@N-CNCs at 5 A g⁻¹ after activation for 20 cycles at 1 A g⁻¹. Adopted with permission from Ref. [413], Copyright 2021, Wiley VCH, Janus.

delivering 425 mAh g⁻¹ at 100 mA g⁻¹, with a minimal capacity decay of 0.038 % per cycle over 600 cycles and 0.036 % per cycle during 700 cycles at 1 A g⁻¹ of current density (Fig. 45b, c). In a separate study, Cheng et al. [416] informed Sb NPs (approximately 19 nm) inserted within a PC network derived from Sb-MOF, denoted as Sb-NPs@PC (Fig. 45d). These nano-sized Sb NPs underwent alloying/dealloying processes, with the PC serving as a buffer against volume expansion, mechanical strain, and nanoparticle agglomeration. The Sb-NPs@PC anode material achieved high discharge/charge capacities of 750 mAh g⁻¹/551 mAh g⁻¹ at 50 mA g⁻¹ of current density, while maintaining a remarkable retention in capacity of 94.6 % after 100 cycles (Fig. 45e, f).

Another innovative approach involved the use of MOF-based electrospinning combined with ion-exchange followed by annealing to create yolk-shell Sb@C NBs surrounded within CNFs (Sb@CNFs), as depicted in Fig. 46a [417]. This design capitalizes on rational structural engineering, resulting in Sb@CNFs with spacious voids and elastic carbon shells. These features effectively mitigate the substantial volume changes experienced during cycling, ensuring a capacity of 227 mAh g⁻¹ at a 1 A g⁻¹ of current density after 1000 cycles (Fig. 46b). In this investigation, the researchers conducted in-situ TEM observations of Sb@CNFs during the alloying/dealloying activity, as presented in Fig. 46c–f. These observations revealed substantial volume expansion and contraction of inner Sb NPs, while the void space adeptly accommodated the whole volume variation. The flexible carbon shell holds the structural integrity throughout these transformations. The hypothetical structural changes in this anode during charge/discharge processes

unveiled a sequence in which K⁺ ions first insert into the carbon matrix before penetrating the Sb@C nanoboxes. Over time, the Sb NPs gradually expanded, filling the internal void space within the carbon shell.

Lastly, Yan and colleagues explored the impact of metalation with Zn on the performance of nano porous carbon during the potassiation/depotassiation process for PIBs [418]. Through calcination of ZIF-8 template at 600 °C in N₂ temperature, they achieved a highly dispersed configuration of Zn NPs confined within a nano PC network, referred to as ZNP/C. When employed as an anode in PIBs, ZNP/C displayed a high capacity of 200 mAh g⁻¹ over 100 cycles at 0.1 A g⁻¹ and maintained a stable capacity of 145 mAh g⁻¹ over 300 cycles at 0.5 A g⁻¹. Table 11 provides a summary of K-storage performance of alloying-type metal anodes derived from MOF.

6.3.3. Metal chalcogenides derived from MOF

To propel the advancement of PIB technology, there is an immediate need for electrode materials that exhibit efficient performance and excellent electrochemical activity. In previous sections, numerous electrode materials based on both pristine MOFs and MOF-derived nano PC materials were explained for efficient K-ion storage. Moreover, there have been reports on MOF-derived composites as an electrode, especially those composed of metal selenides distributed within a nano porous carbon framework. This involves a single-step thermal conversion process in which a MOF precursor is heated with selenium powder under inert atmospheric conditions. This process results in the formation of metal selenides distributed within PC, where the metal amount of the MOF blends with Se to create metal selenide, while the organic linker

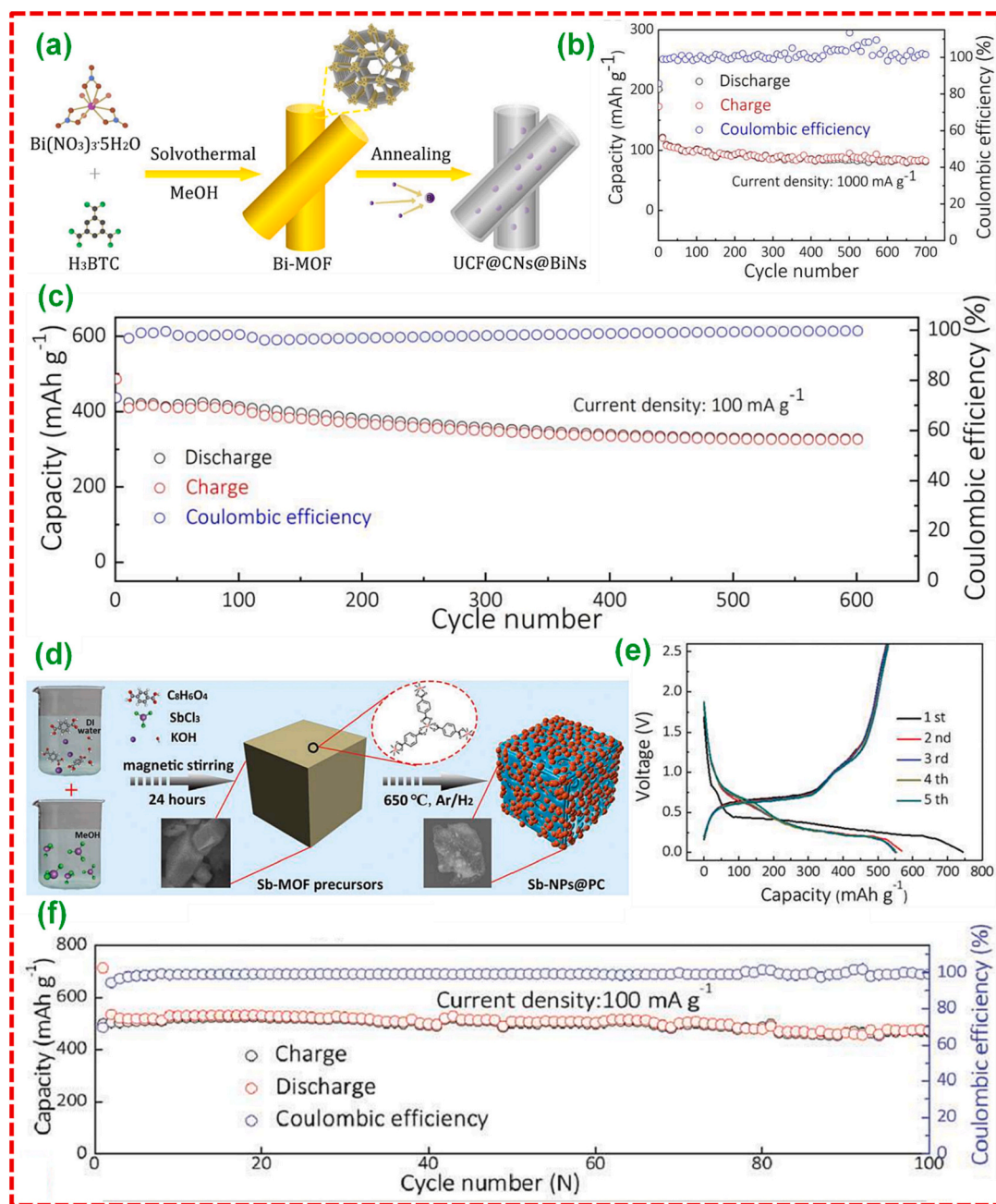


Fig. 45. (a) Pictorial demonstration of UCF@CNs@BiN composites formation, (b) cycle stability at the 1000 mA g⁻¹ of current density, (c) cycle stability at the 100 mA g⁻¹ of current density. Adopted with permission from Ref. [415], Copyright 2019, American Chemical Society. (d) Scheme illustrating the preparation procedure of Sb-NPs@PC material, (e) galvanostatic charge/discharge curves for the first 5 cycles, and (f) cycle stability at 100 mA g⁻¹ of current density. Adopted with permission from Ref. [416], Copyright 2019, Royal Society of Chemistry.

transformed into nano porous carbon. In most cases, ZIF-67 and ZIF-8 serve as the templates for producing metal selenides. One advantage of this approach is that the in situ created PCs can mitigate the significant volume alterations associated with metal selenides and enhance their electronic conductivity.

Ma et al. conducted a MOF template preparation to create Co_{0.85}Se NPs dispersed within NDC (Co_{0.85}Se@NC), employing ZIF-67 as a sacrificial template (Fig. 47a). When evaluated as an anode for PIBs, this composite exhibit enhanced electron conductivity due to the presence of NDC. It also effectively mitigated volume fluctuations and prevented the Co_{0.85}Se agglomeration during cycling [419]. Additionally, the mesoporous composite structure diminished the diffusion length for K-ions and improved electrolyte-electrode interaction, resulting in a capacity of

114.7 mAh g⁻¹ at 1 A g⁻¹ over 250 cycles (Fig. 47b). Furthermore, Co_{0.85}Se QDs/carbon polyhedra (Co_{0.85}Se-QDs/C) (Fig. 47c) [420], S-doped Co_{0.85}Se_{1-x}S_x NPs encapsulated within double carbon shells (CoSeS@C/G) (Fig. 48a), and Co_{0.85}Se@carbon NBs confined in CNFs (Co_{0.85}Se@CNFs) [423] were prepared utilizing ZIF-67 as a template and assessed for its working for PIBs. The FESEM and TEM analysis revealed an identical ZIF-67 polyhedral structure and small divergent lamellas on the Co_{0.85}Se-QDs/C composite surface (Fig. 47d-m). SAED images and elemental analysis through EDS scanning proved the polycrystalline nature and even allocation of C, Co, and Se in the Co_{0.85}Se-QDs/C composite. The ductile and multidimensional C matrix helped the Co_{0.85}Se-QDs/C expansion, reducing the stress caused by K-ion intercalation and preventing the active material accumulation. As a

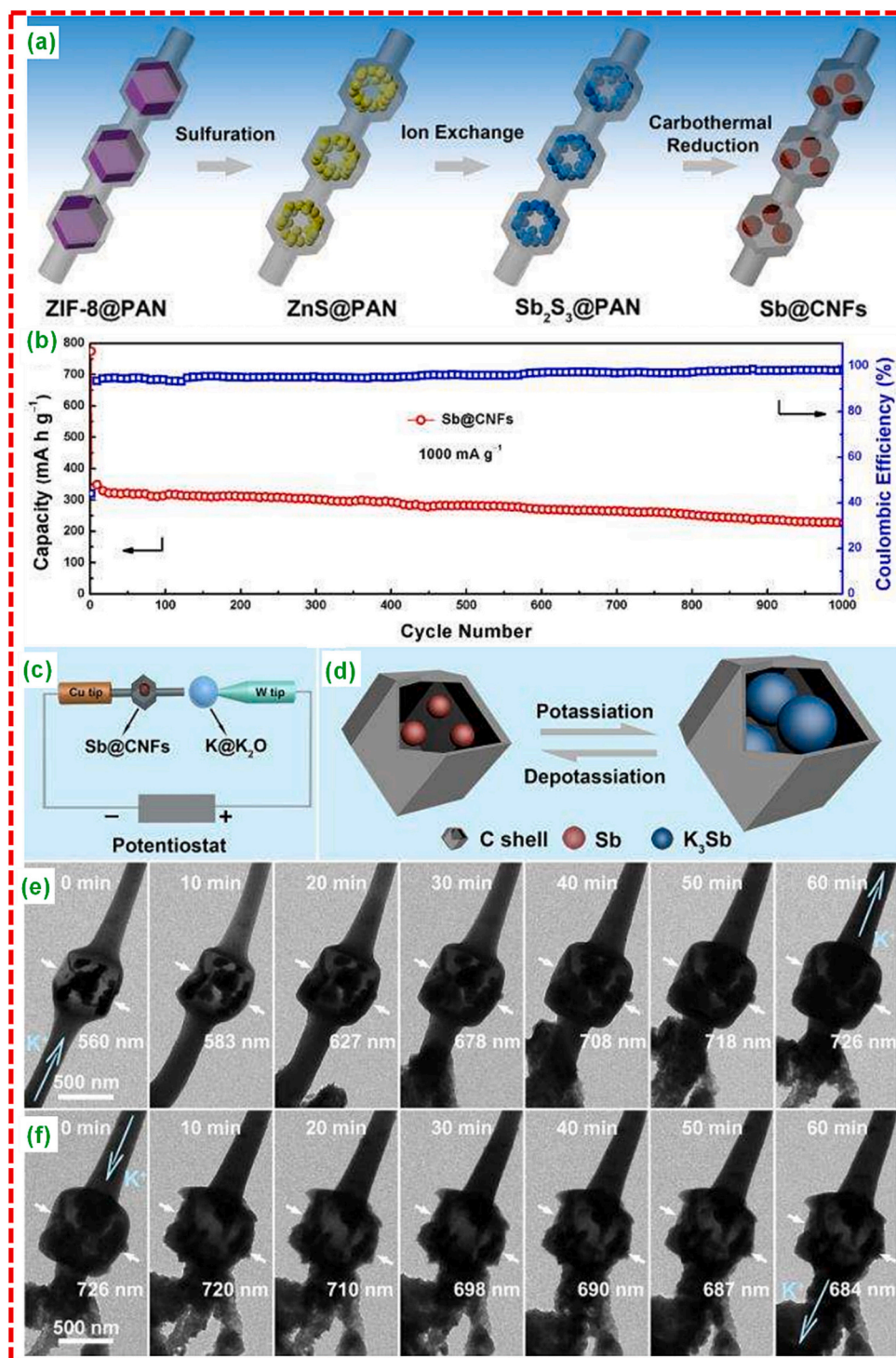


Fig. 46. (a) Pictorial demonstration of Sb@CNFs preparation, (b) cycle stability of Sb@CNFs at a 1000 mA g⁻¹ over 1000 cycles, (c) Pictorial demonstration of the in-situ TEM device, (d) Pictorial demonstration of the potassiation/depotassiation processes of Sb@CNFs, Sb NPs confined in the carbon shell. Time lapse TEM images of the single Sb@CNFs during the (e) first potassiation and (f) first depotassiation. The size of Sb@C nanoboxes in (e) and (f) is measured and indicated by white arrow and light blue arrow represents the transportation direction of K⁺ during the potassiation/depotassiation activities. Adopted with permission from Ref. [417], Copyright 2020, Wiley VCH, Janus. (For interpretation of the references to color in this figure legend, the reader is referred to the web version of this article.)

result, this composite exhibited remarkable K-storage behavior, delivering a capacity of 402 mA h g⁻¹ at 50 mA g⁻¹ over 100 cycles, thanks to its structural integrity and enhanced conductivity.

Furthermore, the CoSeS@C/G and Co_{0.85}Se@CNFs (Fig. 48a) anodes retained a reversible capacity of 208.1 mA h g⁻¹ at 0.2 A g⁻¹ after 100 cycles and 299 mA h g⁻¹ at 1 A g⁻¹ after 400 cycles. Similarly, ZnSe

NP@NHC [424], ZnSe@NDPC [425], ZnSe/C (Fig. 48b) [422], and ZnSe-FeSe₂/rGO [426] were obtained from the ZIF-8 as a sacrificial template and evaluated as anode for PIBs. The ZnSe NP@NHC composite, when used as an anode, displayed a capacity of approximately 132.9 mA h g⁻¹ over 1200 cycles at 0.1 A g⁻¹. This impressive performance was attributed to the well-decorated ZnSe NPs on the hollow

Table 11

Metal alloys derived from MOF for PIBs.

Alloys derived from MOF	MOF template	Voltage (V vs. K/K ⁺)	Current density (A g ⁻¹)	Capacity (mAh g ⁻¹)	Cycle number	Ref.
UCF@CNs@BiN	Bi-BTC	0.01–3.0	0.1	~327	600	[415]
ZNP/C	ZIF-8	0.01–3.0	0.5	145	300	[418]
Bi@N-CNCs	Bi-MOF	0.1–1.5	5	224	1200	[413]
Sb-NPs@PC	Sb-TPA	0.01–2.6	0.1	497	100	[416]
C@DSBC	ZIF-8	0.0–1.5	0.4	~220	200	[414]
Sb@CNFs	ZIF-8@PAN	0.01–2.0	1	227	1000	[417]

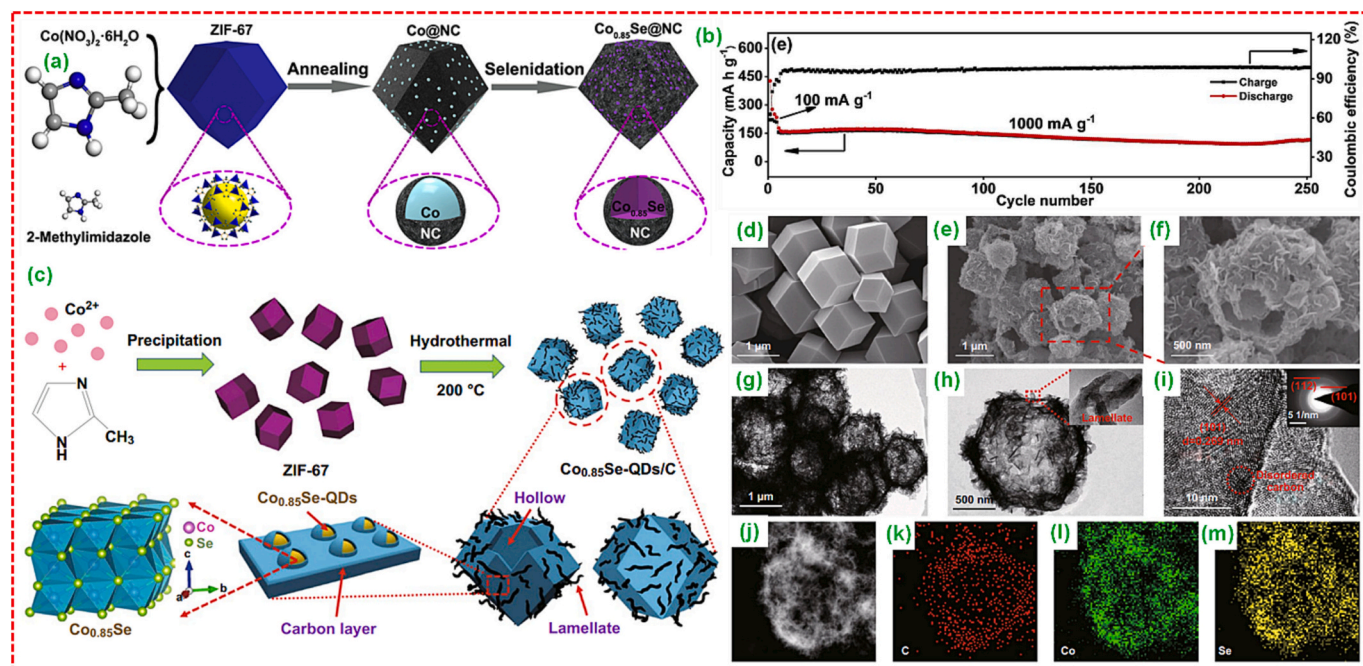
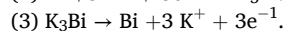
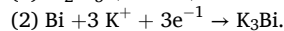
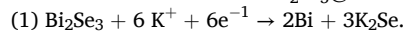


Fig. 47. (a) Pictorial demonstration of Co_{0.85}Se@NC formation, (b) cycle stability of Co_{0.85}Se@NC-650 at 1000 mA g⁻¹. Adopted with permission from Ref. [419], Copyright 2018, Elsevier B.V. (c) Pictorial demonstration of Co_{0.85}Se-QDs/C composite formation, and (d-m) SEM, TEM, HRTEM, and SAED pattern analysis of Co_{0.85}Se-QDs/C-20. Adopted with permission from Ref. [420], Copyright 2019, Springer Nature.

carbon polyhedra, which provided numerous active sites and mitigated volume expansion, thereby enhancing charge-transfer kinetics. Additionally, the N doping enhanced the interfacial adsorption among carbon and active species. The ZnSe@NDPC anode done well with a capacity of 262.8 mAh g⁻¹ at 100 mA g⁻¹ after 200 cycles. This performance was due to the stress-buffering effect, which allowed the anode to deliver a stable and high reversible capacity. The ZnSe/C electrode achieved a reversible capacity of 318 mAh g⁻¹ at 50 mA g⁻¹ with exceptional cyclability, retaining 189 mAh g⁻¹ after 1000 cycles at 500 mA g⁻¹. This remarkable performance was accredited to the favorable synergistic effect and the distinctive design of the nanocages. Structural alterations of ZnSe/C nanocages during the potassiation/depotassiation activity are effectively clarified in Fig. 48c, where the ZnSe NPs can be envisioned buffering the large volume alterations and preventing the electrode fracture due to their stress-buffering effect.

In pursuit of achieving a higher potassium storage capacity, Yang and their research team introduced a novel composite material composed of Bi₂Se₃@C with a rod type construction. This composite was synthesized utilizing an in-situ selenization protocol with a Bi-MOF template [427]. The resulting anode material for PIBs exhibited remarkable behavior, with an excellent capacity of 305 mAh g⁻¹ at 0.1 A g⁻¹ even after 400 cycles of use. The K-storage process, elucidated depends on CV tests conducted with ester/ether electrolytes, involves conversion and alloying reactions. The first CV displayed two reduction curves at 0.64 V and 0.04 V. The first peak corresponds to the conversion reaction among Bi₂Se₃ and K-ion, leading to the Bi and K₂Se phases

formation. The successive reduction peak at 0.04 V signifies the alloying mechanism. In the anodic test, an oxidation peak observed at 0.65 V is corresponding to the dealloying mechanism of K₃Bi phase. Additionally, an oxidation peak ranging from 1.21 to 2.50 V is assigned to the reversion reaction. Subsequent scans showed great reversibility in the cathodic/anodic peaks, revealing that K-ions exhibited highly reversible behavior within the Bi₂Se₃@C anodes.



Ultrafine iron selenide (Fe₃Se₄) NPs incorporated into 1D carbon fibers (Fe₃Se₄@CFs) were successfully produced through the heat treatment of Fe-BTC/PAN precursor. This innovative material was explored as an anode in PIBs and revealed an outstanding retention in capacity, retaining 161 mAh g⁻¹ even after 300 cycles at 1 A g⁻¹ [428]. Additionally, Wang and their team developed Mn-Fe-Se/CNTs derived from PBA for utilization as an anode for PIBs [429]. The as-prepared Mn-Fe-Se/CNTs demonstrated a discharge capacity of 141 mAh g⁻¹ at a current density of 50 mA g⁻¹ after 70 cycles. Further, Table 12 reveals the comprehensive comparison of the energy storage performance of MOF-derived metal selenide-based anodes for PIBs.

While LIB technology has gained immense popularity owing to its lightweight nature, high energy density, and exceptional cycle stability, there is growing concern about the limited availability of lithium resources in the future. As a promising alternative, PIBs have emerged;

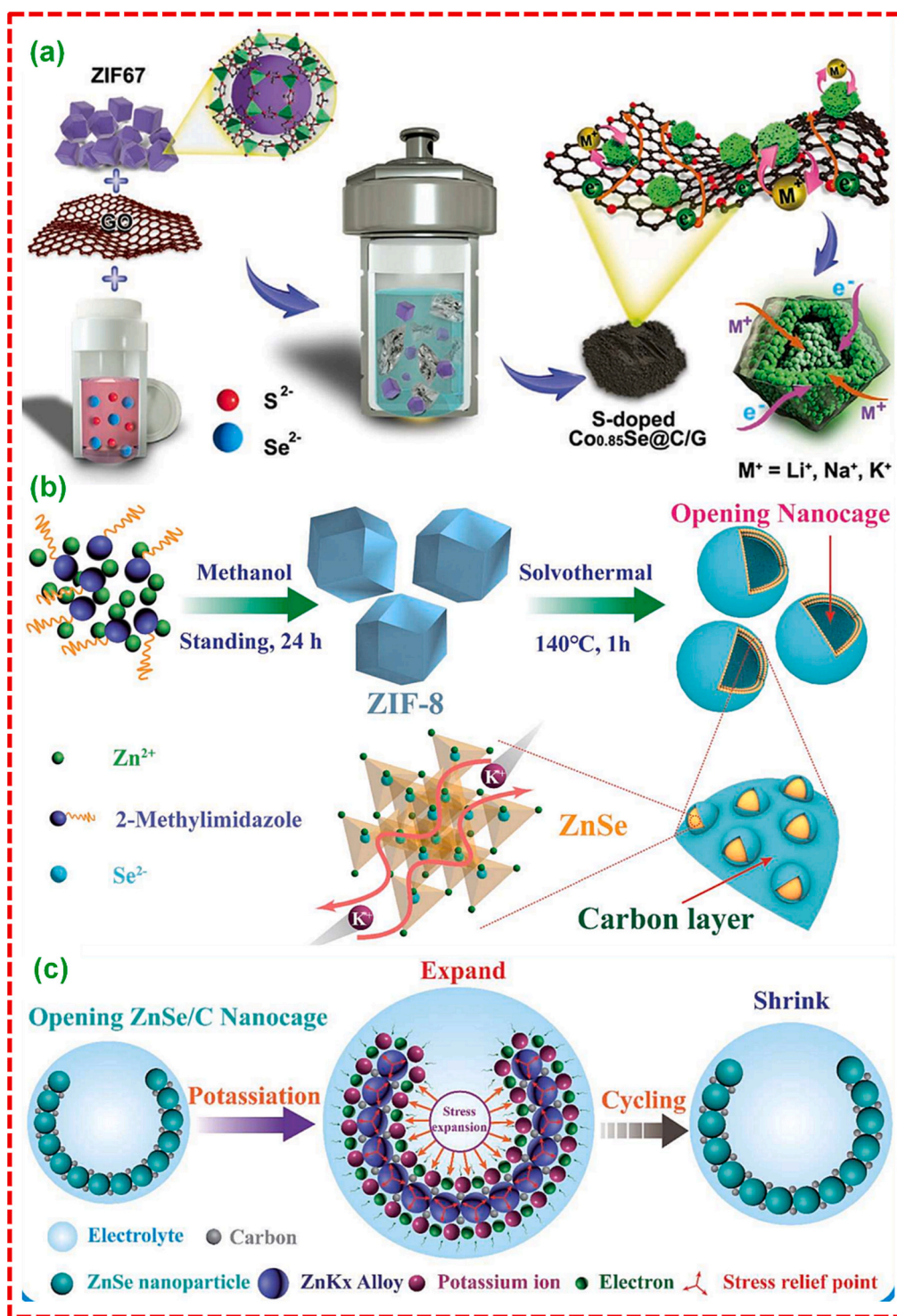


Fig. 48. (a) Pictorial demonstration of CoSeS@C/G composite preparation. Adopted with permission from Ref. [421], Copyright 2020, Wiley VCH, Janus. (b) Pictorial demonstration of ZnSe CS/C preparation. Adopted with permission from Ref. [422], Copyright 2020, Royal Society of Chemistry. (c) Pictorial demonstration of morphology evolution of the potassiation/depotassiation mechanism in open nanocage ZnSe-type anodes. Adopted with permission from Ref. [422], Copyright 2020, Royal Society of Chemistry.

however, this technology faces challenges due to the less favorable potassiation/depotassiation processes caused by the large ionic radius of K-ions than Li-ions. Conventional metal sulfides were initially studied for K-ion storage, but the outcomes proved to be disappointing, exhibiting lower capacities and shorter cycle lifespans. Drawing inspiration from the excellent energy storage performance of MOF-derived metal sulfides as anodes for LIBs, scientists have now turned their attention to

investigating their suitability as anode in PIBs [432].

Xie et al. introduced a unique attempt involving the preparation of MOF derived $FeS_2@RGO$ as an electrode for PIBs (Fig. 49a). This anode material demonstrated impressive behavior with a capacity of 264 mAh g^{-1} after 50 cycles at 50 mA g^{-1} and a sustained capacity of 123 mAh g^{-1} after 420 cycles, even when subjected to a high current density of 500 mA g^{-1} . These exceptional results were accredited to the synergistic

Table 12

Metal selenides derived from MOF for PIBs.

MOF-derived metal selenide	MOF templates	Voltage (V vs. K/K ⁺)	Current density (A g ⁻¹)	Capacity (mAh g ⁻¹)	Cycle number	Ref.
CoSe ₂ @NC/HMCS	ZIF-67/HMCS	0.001–3.0	0.1	442	120	[430]
ZnSe-FeSe ₂ /RGO	Fe-Zn-MOF-5	0.01–3.0	0.05	363	100	[426]
ZnSe@NDPC	ZIF-8	0.01–3.0	0.1	262.8	200	[425]
Co _{0.85} Se@CNFs	ZIF-67@PAN	0.01–2.60	1	299	400	[423]
CoSeS@C/G	ZIF-67	0.01–3.0	0.2	208.1	100	[421]
Co _{0.85} Se@NC	ZIF-67	0.01–3.0	1	114.7	250	[419]
Fe ₃ Se ₄ @CFs	Fe-BTC/PAN	0.01–2	1	161	300	[428]
ZnSe@NDPC	ZIF-8	0.01–3.0	0.1	262.8	200	[425]
Mn-Fe-Se/CNTs	Mn-Fe-PBA/CNTs	0.0–3.0	0.05	141	70	[429]
ZnSe NP@NHC	ZIF-8	0.3–2.9	0.1	132.9	1200	[424]
ZnSe CS/C	ZIF-8	0.01–2.5	0.5	189	1000	[422]
Co-Se@CNCP	ZIF-8@ZIF-67	0.01–2.60	0.5	253	200	[431]
Bi ₂ Se ₃ @C	Bi-BTC	0.01–3.0	0.1	305	400	[427]
Co _{0.85} Se-QDs/C	ZIF-67	0.01–2.5	0.05	402	100	[420]
Zn-Co-Se@NCP	ZIF-8@ZIF-67	0.01–2.60	0.5	42	200	[431]

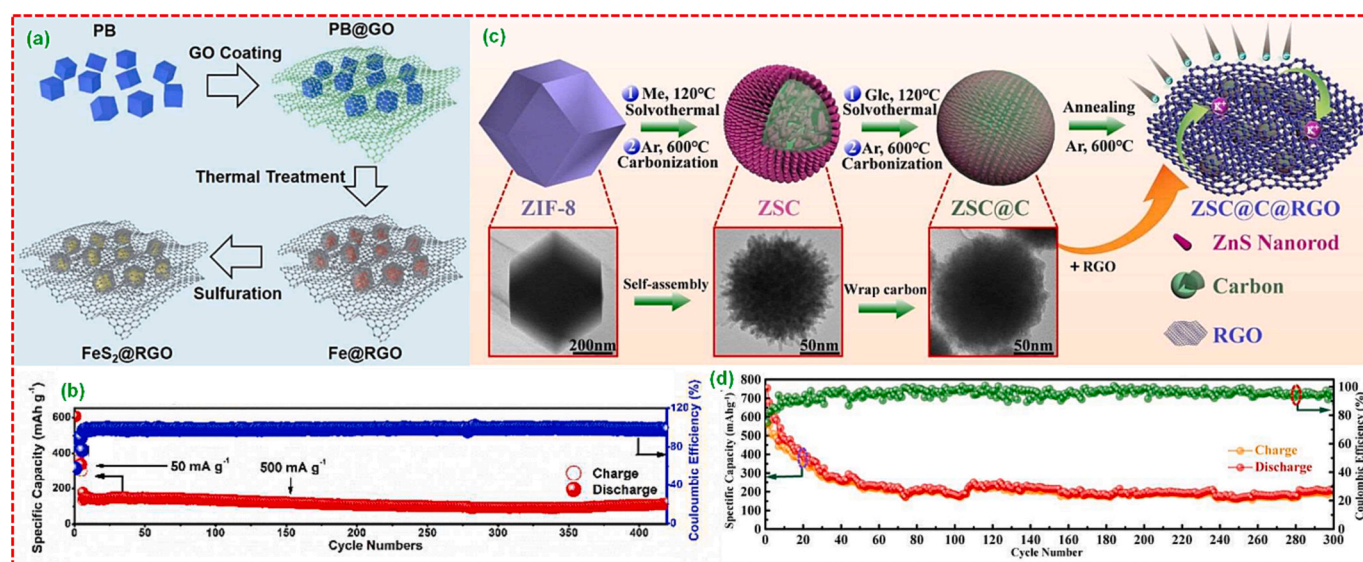


Fig. 49. (a) Pictorial demonstration of FeS₂@RGO preparation, (b) cycle stability of FeS₂@RGO-2 at 500 mA g⁻¹. Adopted with permission from Ref. [433], Copyright 2018, Royal Society of Chemistry. (c) Pictorial representation of synthesis route of ZSC@C@RGO composite, and (d) cycle stability of the ZSC@C@RGO composite at 500 mA g⁻¹ over 300 cycles. Adopted with permission from Ref. [434], Copyright 2019, American Chemical Society.

effects among the FeS₂ and the RGO shells (Fig. 49b) [433]. Rui et al. [435] achieved uniform coating of ultrathin MoS₂ NSs onto ZIF-67 resultant carbon polyhedra (ZIF-67-C@MoS₂) NCs. These materials served as efficient anodes for PIBs, delivering a high discharge capacity of 199.8 mAh g⁻¹ after 50 cycles at a 0.1 A g⁻¹ of current density, with a Coulombic efficiency close to 100 %. A tertiary hierarchical structure, comprising primary ZnS NRs, secondary carbon nanospheres, and tertiary carbon confined ZnS subunit nanospheres wrapped in RGO networks (ZSC@C@RGO), was designed for efficient K-ion storage (Fig. 49c). This novel strategy delivered a stable diffusion pathway and improved conductivity for potassium ions and electrons, while also mitigating volume fluctuations and facilitating the stable SEI formation during cycling. These features resulted a reversible capacity of 330 mAh g⁻¹ after 100 cycles at 50 mA g⁻¹ and 208 mAh g⁻¹ at 500 mA g⁻¹ over 300 cycles (Fig. 49d) [434].

To enhance potassium-ion performance, scholars have developed an anode for PIBs based on bimetallic sulfides, capitalizing on synergistic effects to improve their energy storage behavior. Han et al. [436] introduced the preparation of dodecahedral heterogeneous nanocages (DHNCs) consisting of Co₉S₈/N-C@MoS₂. This electrode exhibited a reversible capacity of approximately 100 mAh g⁻¹ at 1 A g⁻¹ after 100 cycles. This impressive performance was attributed to the synergistic effects of metal sulfides and the unique hollow polyhedra structure,

combined with the conductive N-doped PC (Fig. 50a). Another innovative PIB anode material was developed using a 3D amorphous carbon condensed CoS/NCNTs framework sustained on CoS-coated CNFs (AC@CoS/NCNTs/CoS@CNFs). This advanced material exhibited a capacity of 401 mAh g⁻¹ at 0.1 A g⁻¹ after 100 cycles, showcasing remarkable rate capacities. Even at a high current density of 3.2 A g⁻¹, it maintained a capacity of 130 mAh g⁻¹ after 600 cycles. These exceptional results were made possible by the 3D-ordered anode design, which reduced the diffusion length of ions, improved electronic conductivity, and enhanced mechanical stability (Fig. 50b, c) [437]. Likewise, anode materials for PIBs have been developed using MOF derived NCS@RGO [439] and Ni-Fe-S-CNT to enhance K-ion storage (Fig. 50d). NCS@RGO demonstrated a long cycle life, maintaining a reversible capacity of 495 mAh g⁻¹ at 200 mA g⁻¹ over 1900 cycles, surpassing the performance of most previously reported MOF-derived metal sulfides. Additionally, the researchers conducted an extensive study on the composition of the SEI layer and the roughness of electrodes after 50 cycles employing various electrolytes. In contrast, the Ni-Fe-S-CNT NCs exhibited poor rate capacity than NCS@RGO, maintaining a charge capacity of 181 mAh g⁻¹ after 50 cycles at 0.1 A g⁻¹ (Fig. 50e) [438]. Qin et al. described the preparation of Co₃O₄@C@MoS₂ anode for K-ion storage. This anode material offered a large surface area for electrode/electrolyte contact, sufficient interstitial space to accommodate volume

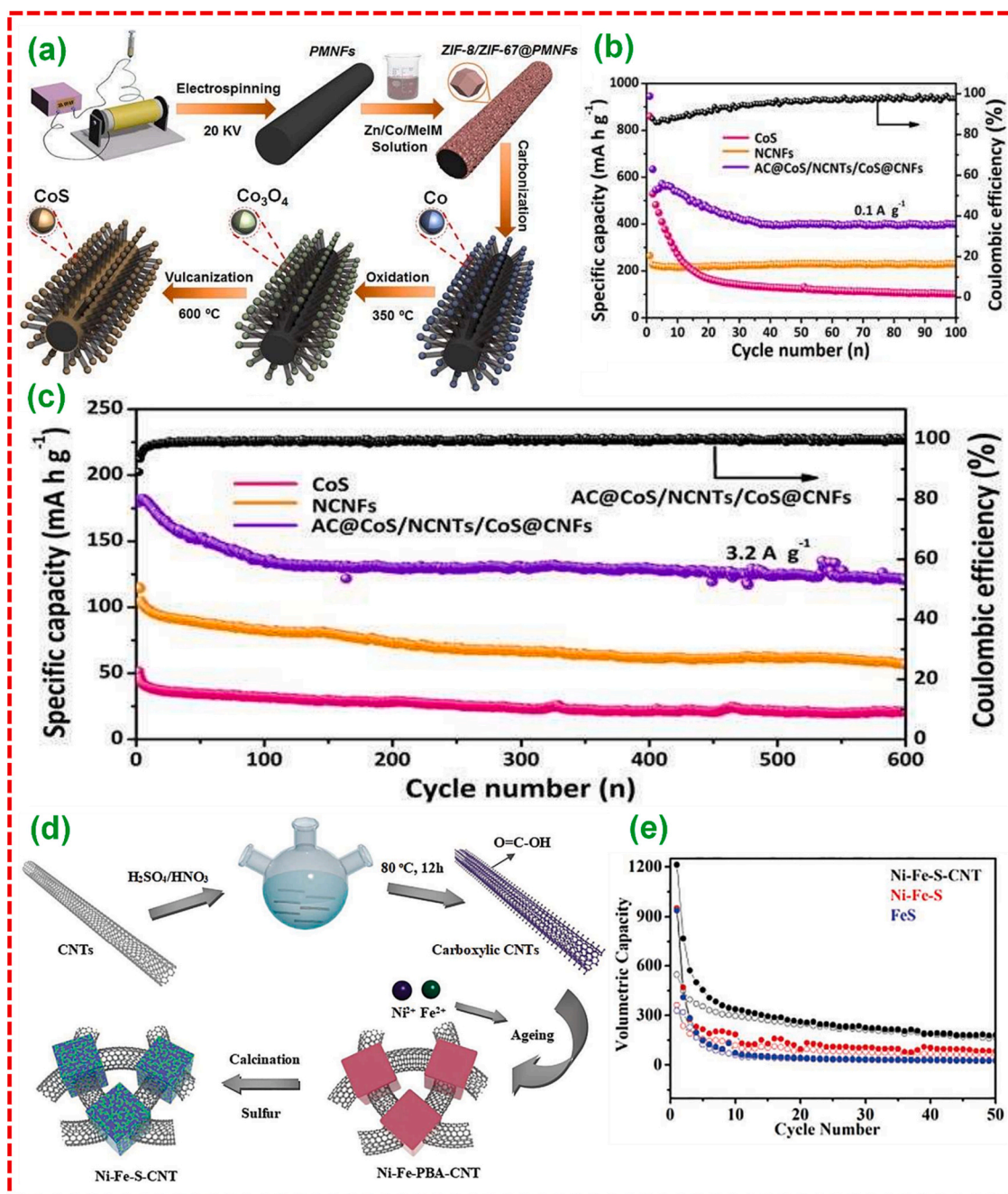


Fig. 50. (a) Pictorial demonstration of AC@CoS/NCNTs/CoS@CNFs formation, (b) cycle stability at the 0.1 A g⁻¹ of current density, (c) cycle stability at the 3.2 A g⁻¹ of current density. Adopted with permission from Ref. [437], Copyright 2019, Royal Society of Chemistry. (d) Pictorial demonstration of Ni-Fe-S-CNT formation, and (e) cycling performance of Ni-Fe-S-CNT, Fe—S, and Ni-Fe-S at 0.1 A g⁻¹. Adopted with permission from Ref. [438], Copyright 2020, Wiley VCH, Janus.

Table 13

Metal sulfides derived from MOF for PIBs.

MOF derivatives	MOF templates	Voltage (V vs. K/K ⁺)	Current density (A g ⁻¹)	Capacity (mAh g ⁻¹)	Cycle number	Ref.
Fe _{1-x} S/SC	Fe-MOF	0.01–3.0	0.05	430	300	[441]
Co ₉ S ₈ /NSC@MoS ₂ @NSC	ZIF-67	0.01–2.6	3	141	800	[442]
NCS@RGO	MOF-74	0.01–3.0	0.2	495	1900	[439]
FeS ₂ @RGO	PB@GO	0.01–3.0	0.5	123	420	[433]
2ZIF-67-C@MoS ₂	ZIF-67	0.01–3.0	0.1	199.8	50	[435]
Fe ₇ S ₈ /C@d-MoS ₂	MIL-88B(Fe)	0.01–3.0	4	286	500	[443]
Co ₃ O ₄ @C@MoS ₂	PBA@RF	0.001–3.0	0.05	~365.2	100	[440]
AC@CoS/NCNTs/CoS@CNFs	ZIF-8/ZIF-67	0.01–3.0	3.2	130	600	[437]
ZSC@C@RGO	ZIF-8	0.0–2.5	0.5	208	300	[434]
Ni-Fe-S-CNT	Ni-Fe-PBA-CNT	0.0–3.0	0.1	181	50	[438]
Co ₉ S ₈ /N-C@MoS ₂	ZIF-67	0.01–3.0	1	100	100	[436]

alterations throughout K-ion intercalation/deintercalation and exhibited valuable synergistic effects. It showed a high capacity of 256 mAh g^{-1} and retained a high capacity of 88.3 % at 500 mA g^{-1} of current density after 500 cycles [440]. The performance of MOF-derived metal sulfide-based anodes for PIBs is summarized in Table 13 for ease of comparison.

6.3.4. Metal phosphides derived from MOF

The demand for highly efficient electrode materials in PIBs has surged, challenging the dominant position of LIBs. One of the primary issues faced by electrode materials in PIBs is the tendency to aggregate

or undergo pulverization during cycling. This problem arises because the ionic radius of K^+ is greater than that of Li^+ and Na^+ , owing to undesirable volume variations. Nevertheless, the limited availability of Li-resources has further intensified the demand for alternatives. Metal phosphide-based anodes have recently gained considerable interest due to its high theoretical capacity, abundance in nature, and non-toxic properties [444]. Furthermore, as discussed in earlier sections of this review, the optimization of K-storage and enhancement of charge transfer kinetics in electrode materials heavily rely on nano structural engineering, such as the design of nano cubes, nanowires, core-shell structures, and so on. The methodology for preparing metal

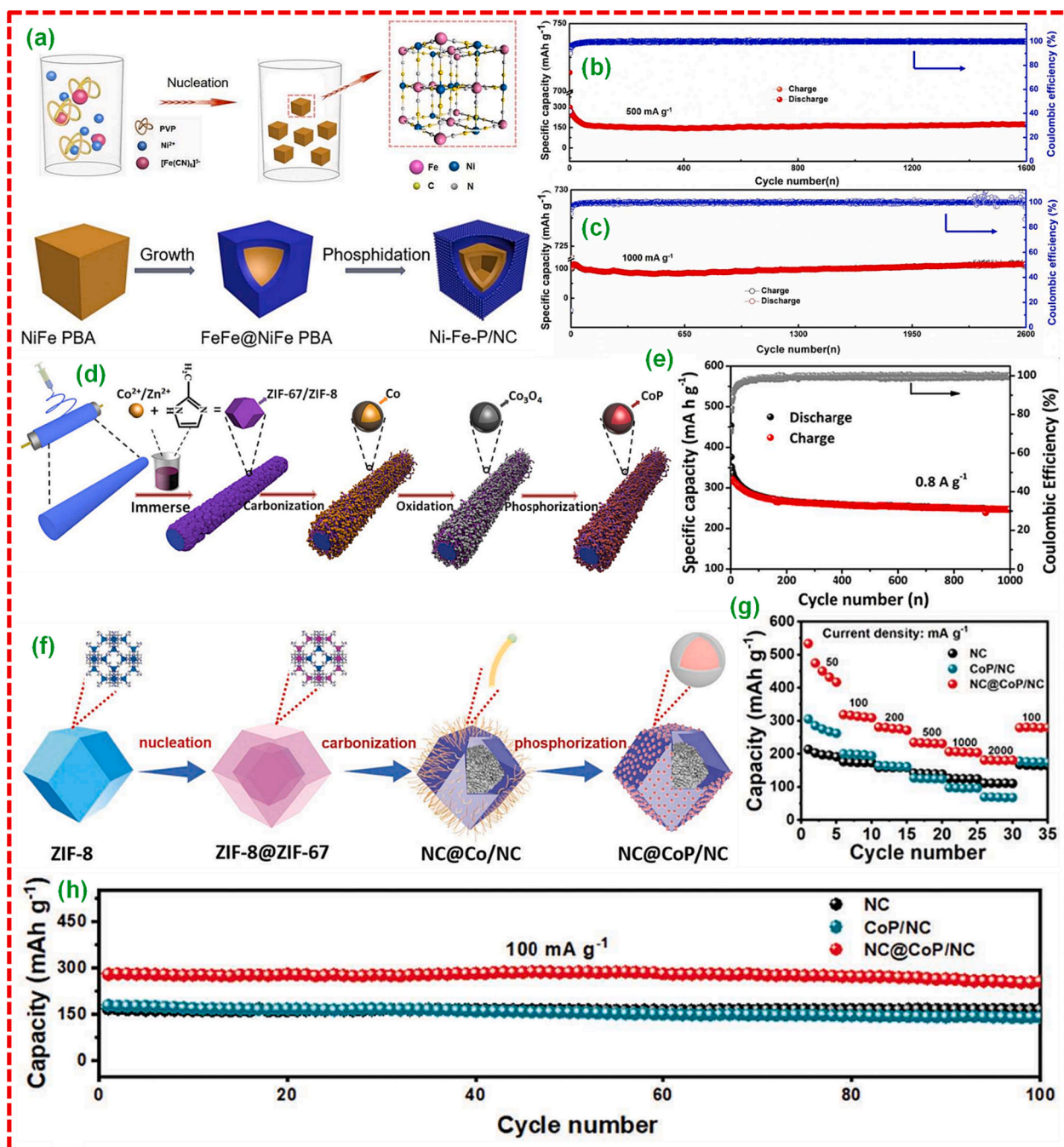


Fig. 51. (a) Pictorial demonstration of Ni-Fe-P/NC preparation mechanism, (b) cycle stability study at 500 mA g^{-1} , (c) cycle stability study at 1000 mA g^{-1} of current density. Adopted with permission from Ref. [446], Copyright 2019, American Chemical Society. (d) Schematic of preparation process of AC@CoP/NCNTs/CNFs composite, (e) cycle stability study at 0.8 A g^{-1} of current density over 1000 cycles. Adopted with permission from Ref. [447], Copyright 2019, Elsevier B.V. (f) Pictorial demonstration of NC@CoP/NC NCs, (g) rate capacities, and (h) cycle stability study of NC, CoP/NC, and NC@CoP/NC at 100 mA g^{-1} . Adopted with permission from Ref. [448], Copyright 2020, Wiley VCH, Janus.

phosphide-based anodes is similar to that used for metal selenide/sulfide-based anodes. The key difference is that in the case of metal phosphide electrodes, carbonization during MOF template-mediated preparation is carried out in the existence of a phosphorus source.

Yi et al. [445] developed an innovative flexible MoP@NPCNFs membrane. This free-standing PIB anode, prepared through an electrospinning followed by carbonization and phosphorization, exhibited impressive performance. It revealed a high capacity of 320 mAh g^{-1} at 100 mA g^{-1} , excellent rate performance with 220 mAh g^{-1} at 2 A g^{-1} , and excellent retention in capacity over 90 % even after 200 cycles. These outstanding results were accredited to the synergistic effects among the MoP NPs and 3D conductive matrix of N,P co-doped CNFs. Chen et al. synthesized double-shelled Ni-Fe-P/NDC NBs (referred to as Ni-Fe-P/NC) through epitaxial deposition followed by phosphorization (Fig. 51a) [446]. When used as an anode for PIBs, Ni-Fe-P/NC exhibited higher cycle stability, retaining a capacity of 172.9 mAh g^{-1} after 1600 cycles at 500 mA g^{-1} and 115 mAh g^{-1} after 2600 cycles at 1 A g^{-1} . This improved performance was credited to the unique core-shell architecture as shown in Fig. 51b, c. Miao et al. [447] introduced a 3D structural AC@CoP/NCNTs/CNFs material derived from ZIF-67/ZIF-8 template (Fig. 51d). The CoP NPs served as the core, while the amorphous carbon layer played as the shell. This design effectively mitigated the volume expansion of active materials during charge and discharge cycles, resulting in a reversible capacity of 247 mAh g^{-1} after 1000 cycles at 0.8 A g^{-1} , as demonstrated in Fig. 51e. A flexible porous anode material, composed of 3DG/FeP has been developed for PIBs [449]. This material features an interconnected porous conducting network, tight contact between graphene and FeP hollow nanospheres, and appropriately buffered nano-hollow spaces. These characteristics efficiently encourage the transport of charge and keep structural integrity, resulting in a high reversible capacity of 323 mAh g^{-1} at 0.1 A g^{-1} and exceptional cycle stability with a retention in capacity of 97.6 % at 2 A g^{-1} after 2000 cycles. Yi et al. [448] synthesized N-doped PC confined CoP polyhedron architectures (NC@CoP/NC) derived from ZIF-8@ZIF-67 precursors (Fig. 51f). These architectures were employed as an anode for PIBs and exhibited remarkable electrochemical behavior. The composite delivered a reversible capacity of nearly 200 mAh g^{-1} at 2000 mA g^{-1} and maintained a retention in capacity of 93 % at 100 mA g^{-1} after 100 cycles (Fig. 51g, h). These excellent results can be attributed to the quick electron conductive pathways and promising mechanical robustness of the material. For a comprehensive comparison, the electrochemical performance of MOF-derived metal phosphide-based anodes in PIBs is summarized in Table 14.

7. Conclusions and outlook

In the realm of electrochemical energy storage systems, active electrode materials are pivotal, exerting a profound influence on the overall battery performance. This review has systematically outlined the advantages and challenges associated with MOFs and how these challenges have been effectively addressed through the derivation of valuable MOF-derived products. These products encompass a wide range of materials, including PC, metal/metal oxide, metal/metal oxide@C composites, metal chalcogenides, and phosphides. However, it's crucial to recognize that the electrochemical performance of electrodes can be influenced by a multitude of factors beyond just the choice of active

materials. One noteworthy factor is the composition of active electrode materials, which can be tailored to incorporate multiple metals, oxides, or chalcogenides [7,116]. Such compositional diversity offers opportunities for enhanced electrochemical performance. Furthermore, the structure and morphology of these materials are equally significant, as they dictate the presence of conductive pathways and the quality of the electrode/electrolyte interfaces [8,69]. Variations in nanostructure growth can significantly impact electrochemical activity [42]. Additionally, components other than active materials can also play a pivotal role. For instance, current collectors can serve as substrates for the direct growth of active materials, reducing the need for multiple additives such as binders and conductive carbon, which can introduce resistance and affect overall performance [57].

Since the discovery of MOFs in the 1990s, they have garnered significant attention across various fields, including sensing, catalysis, energy storage, and more. Over time, MOFs have undergone transformations into desired materials such as metal-based oxides, chalcogenides, phosphides, and carbon-based materials. In this comprehensive review, we have summarized recent advancements, developments, structural formations, properties, applications, and future prospects of both MOFs and MOF-derived nanomaterials. For a multitude of applications, MOFs are highly sought after due to their ability to offer tailored surface area, controllable porosity, precise pore size, and composition customization as critical attributes. However, original MOFs have inherent limitations, notably their weak conductivity and structural stability, which restrict their use in electrochemical systems. MOF derivatives have emerged as promising materials to address these limitations and find applications in various electrochemical fields. These materials serve as effective templates, enabling precise control over morphology, functionalization, heteroatom doping, enhanced surface area, and structural modifications. Nonetheless, there are certain challenges associated with MOFs that need to be addressed to facilitate their widespread commercialization, as depicted in Fig. 52.

1. Certainly, to further enhance the electrochemical activities of MOF derivatives and address aggregation issues, coupling them

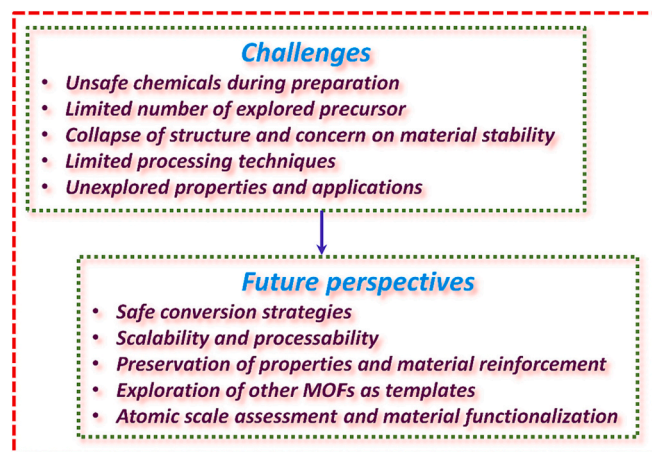


Fig. 52. Challenges and perspectives of commercialization of MOF and their derivatives.

Table 14

Metal phosphides derived from MOF for PIBs.

MOF derivatives	MOF templates	Voltage (V vs. K/K ⁺)	Current density (A g ⁻¹)	Capacity (mAh g ⁻¹)	Cycle number	Ref.
AC@CoP/NCNTs/CNFs	ZIF-67/ZIF-8	0.01–3.0	0.8	247	1000	[447]
Ni-Fe-P/NC	FeFe@NiFe PBA	0.01–3.0	1	115	2600	[446]
3DG/FeP	3DG/PB	0.01–3.0	2	~124	2000	[449]
MoP@NPCNFs	ZIF-8@PAN/DMF	0.01–3.0	0.1	280	200	[445]
NC@CoP/NC	ZIF-67/ZIF-8	0.01–2.5	0.5	110	800	[122]

- with 2D conductive materials like graphene, MXene, and rGO is a promising approach. These conductive materials can not only improve the overall electrical conductivity but also help mitigate aggregation, thereby maximizing the active surface area and enhancing electrochemical performance.
- Improving the structural stability of MOFs and their derived composites is crucial. This can involve investigating specific orientation techniques, utilizing conductive organic linkers, and optimizing the formation of in-situ heterostructures, including p-n heterojunctions. These strategies can enhance the robustness of MOF-based materials, making them more suitable for various applications.
 - Furthermore, thorough research into the effects of heat treatment on the structure, composition, and morphology of MOF derivatives is essential. This should encompass a systematic examination of parameters such as heating rate, duration, cooling rate, and gas atmosphere. Understanding these factors will enable precise control over the properties of MOF-derived materials.
 - Incorporating modern in-situ techniques like high-energy XRD (HE-XRD), X-ray absorption fine structure (XAFS), and hard X-ray photoelectron spectroscopy (HAXPES) is highly recommended. These techniques can provide detailed insights into the synthesis and heat treatment parameters, allowing for a better understanding of the local geometry, composition, and electrical properties of MOF-derived functional materials.
 - For tracking the structural evolution of MOFs and MOF-derived composites during electrochemical methods, in-situ structural characterizations using methods like Raman spectroscopy and surface-enhanced Raman spectroscopy (SERS) are also strongly advised. These techniques can provide real-time information on structural changes, helping researchers optimize and tailor MOF-based materials for specific applications.
 - To gain a comprehensive understanding of energy storage systems, it's essential to delve into the mechanisms and reaction processes involved. The inherent complexity of MOF materials can pose challenges in pinpointing and optimizing the actual active sites within these energy storage devices. To achieve peak performance in energy storage systems, it's critical to identify key components of MOF derivatives, such as the redox-active centers, cycle stability, rate performance, and more. Therefore, in-situ measurements employing techniques like Raman spectroscopy, XRD, X-ray absorption spectroscopy (XAS), ambient-pressure XPS, and electrochemical mass spectrometry (MS), coupled with theoretical calculations, can be invaluable for unraveling the mechanisms underlying energy storage systems.
 - Safety and environmental concerns should guide the design and synthesis of new MOFs. Some elements used in MOF fabrication can be toxic and carcinogenic, emphasizing the importance of exploring cleaner and safer synthesis routes.
 - To ensure excellent material stability, electronic properties, and electrochemical performance, the structural design of MOF derivatives should be highly tailored. The high-temperature treatment involved in the conversion of MOFs into carbon-, oxides-, phosphides, and chalcogenides-based materials can potentially lead to the collapse of the original pore structure and the management of new pore structures is challenging. Therefore, a comprehensive optimization of heat treatment parameters, including temperature and atmosphere, is essential.
 - While there are over 20,000 MOFs known, only a small fraction, including ZIF-67, ZIF-8, and other ZIF-based MOFs, have been successfully transformed into useful products. Exploring the transformation of other MOFs into valuable products is highly recommended. This exploration can uncover diverse precursors, morphologies, properties, and potential applications, expanding the utility of MOFs in various fields.
 - Functionalizing MOF derivatives remains relatively limited, but there is potential to enhance their electrochemical properties by encapsulating functional groups and multiple species within their frameworks. This approach can lead to synergistic effects, such as catalytic enhancements and improved electronic conductivity, which can significantly benefit their performance.
 - The study of MOF-derived materials in practical energy storage applications is still in its early stages. It is essential to develop a comprehensive understanding of charge-storage mechanisms, particularly in materials that offer high capacity, high-rate capability, and long-term stability. This understanding can be achieved through the application of advanced techniques and methodologies.
 - To create high-performance energy storage devices, it's crucial to identify suitable MOF derivatives for both anodes and cathodes. Achieving a match between positive and negative electrodes, along with mass balancing, is a critical aspect that needs thorough investigation for the successful implementation of high-performance devices in real-world applications.
 - Exploring state-of-the-art manufacturing techniques for flexible devices, which involve depositing nanomaterials derived from MOFs onto flexible and conductive substrates (such as carbon cloths, MXene films, fibers/textiles, etc.), should be a subject of investigation.
 - There is a pressing need for the development of solid-state flexible and wearable micro-batteries based on MOF-derived composites. These batteries should exhibit controlled properties, ensuring safety, reliability, and intelligent electronic features. This area of research warrants further exploration.
 - Additionally, machine learning techniques, including artificial intelligence, can be leveraged to investigate the phase formation of MOF-derived composites. These advanced computational methods can assist in predicting novel materials and deepening our understanding of their mechanisms for advanced applications.

Overall, this comprehensive review has highlighted recent advancements, developments, properties, and applications of MOFs and MOF-derived composites. The significant contributions of MOF-derived nanomaterials in the realm of energy storage have yielded promising results. Beginning with the inception of MOFs, their evolution into diverse metal MOFs and hybrid composites, and subsequent transformations into hierarchical nanomaterials, this review has provided a chronological overview of the progress in MOF electrode fabrication. Consequently, this critical review offers a profound insight into the current advancements, preparation methodologies, and potential applications of MOF-derived composites in the context of metal ion batteries.

CRediT authorship contribution statement

Narasimharao Kitchamsetti: Conceptualization, Data curation, Formal analysis, Investigation, Methodology, Validation, Visualization, Writing – original draft, Writing – review & editing. **Jung Sang Cho:** Funding acquisition, Resources, Supervision, Writing – review & editing.

Declaration of competing interest

The authors declare that they have no known competing financial interests or personal relationships that could have appeared to influence the work reported in this paper.

Data availability

Data will be made available on request.

Acknowledgements

Narasimharao Kitchamsetti acknowledges Prof. Daewon Kim at Kyung Hee University, Republic of Korea for helping him in gaining in-depth knowledge and advancing his career in the field of energy storage and environmental applications. This work was supported by the National Research Foundation of Korea (NRF) grant funded by the Korea government (MSIT) [No. RS-2023-00217581]. This work was also supported by the Commercialization Promotion Agency for R&D Outcomes (COMPA) grant funded by the Korea government (Ministry of Science and ICT) [No. RS-2023-00304768]. This work was also supported by the Ministry of Education and National Research Foundation of Korea (NRF) for "Leaders in Industry-University Cooperation 3.0" project.

References

- [1] O.M. Yaghi, G.M. Li, H.L. Li, Selective binding and removal of guests in a microporous metal-organic framework, *Nature* 378 (1995) 703–706, <https://doi.org/10.1038/378703a0>.
- [2] S.M. Moosavi, A. Nandy, K.M. Jablonka, D. Ongari, J.P. Janet, P.G. Boyd, Y. J. Lee, B. Smit, H.J. Kulik, Understanding the diversity of the metal-organic framework ecosystem, *Nat. Commun.* 11 (2020) 4068, <https://doi.org/10.1038/s41467-020-17755-8>.
- [3] W. Zhang, M.J. Boddys, N. Pinna, A universal synthesis strategy for tunable metal-organic framework nanohybrids, *Angew. Chem. Int. Ed.* 62 (2023) e202301021, <https://doi.org/10.1002/anie.202301021>.
- [4] Z.X. Lin, J.J. Richardson, J.J. Zhou, F. Caruso, Direct synthesis of amorphous coordination polymers and metal-organic frameworks, *Nat. Rev. Chem.* 7 (2023) 273–286, <https://doi.org/10.1038/s41570-023-00474-1>.
- [5] N. Kitchamsetti, J.S. Cho, A roadmap of recent advances in MXene@MOF hybrids, its derived composites: synthesis, properties, and their utilization as an electrode for supercapacitors, rechargeable batteries and electrocatalysis, *J. Energy Storage* 80 (2024) 110293, <https://doi.org/10.1016/j.est.2023.110293>.
- [6] N. Muzaffar, A.M. Afzal, H.H. Hegazy, M.W. Iqbal, Recent advances in two-dimensional metal-organic frameworks as an exotic candidate for the evaluation of redox-active sites in energy storage devices, *J. Energy Storage* 64 (2023) 107142, <https://doi.org/10.1016/j.est.2023.107142>.
- [7] N. Kitchamsetti, A review on recent advances in Prussian blue, its analogues, and their derived materials as electrodes for high performance supercapacitors, *J. Energy Storage* 73 (2023) 108958, <https://doi.org/10.1016/j.est.2023.108958>.
- [8] N. Kitchamsetti, D. Kim, High performance hybrid supercapacitor based on hierarchical MOF derived CoFe_2O_4 and NiMn_2O_4 composite for efficient energy storage, *J. Alloys Compd.* 959 (2023) 170483, <https://doi.org/10.1016/j.jallcom.2023.170483>.
- [9] J.L. Song, L. Chai, A. Kumar, M. Zhao, Y.Z. Sun, X.G. Liu, J.Q. Pan, Precise tuning of hollow and pore size of bimetallic MOFs derivative to construct high-performance nanoscale materials for supercapacitors and sodium-ion batteries, *Small* 2306272 (2023), <https://doi.org/10.1002/smll.202306272>.
- [10] N. Kitchamsetti, D. Kim, A facile method for synthesizing MOF derived ZnCo_2O_4 particles on MXene nanosheets as a novel anode material for high performance hybrid supercapacitors, *Electrochim. Acta* 441 (2023) 141824, <https://doi.org/10.1016/j.electacta.2023.141824>.
- [11] R. Bose, V. Bon, N. Bonisch, P. Selvam, N.S. Kaisare, S. Kaskel, Crystal size dependent flexibility in ZIF-7: from macro-to nanoscale, *Chem. Mater.* 35 (2023) 7825–7838, <https://doi.org/10.1021/acs.chemmater.3c01840>.
- [12] Y. Shu, X.Y. Linghu, Y. Zhao, Z. Chen, J.W. Zhang, D. Shan, W.Q. Liu, M.Y. Di, B. Q. Wang, Photodynamic and photothermal therapy-driven synergistic cancer treatment assisted by zeolitic imidazolate framework-8: a review, *J. Drug Deliv. Sci. Technol.* 81 (2023) 104272, <https://doi.org/10.1016/j.jddst.2023.104272>.
- [13] Q. Zhang, S.G. Yan, X.T. Yan, Y. Lv, Recent advances in metal-organic frameworks: synthesis, application and toxicity, *Sci. Total Environ.* 902 (2023) 165944, <https://doi.org/10.1016/j.scitotenv.2023.165944>.
- [14] S. Li, W.Y. Han, Q.F. An, K.T. Yong, M.J. Yin, Defect engineering of MOF-based membrane for gas separation, *Adv. Funct. Mater.* 33 (2023) 2303447, <https://doi.org/10.1002/adfm.202303447>.
- [15] W.F. Zhu, L.Z. Wang, H.H. Cao, R. Guo, C.F. Wang, Introducing defect-engineering 2D layered MOF nanosheets into Pebax matrix for CO_2/CH_4 separation, *J. Membr. Sci.* 669 (2023) 121305, <https://doi.org/10.1016/j.memsci.2022.121305>.
- [16] G.N.B. Durmuş, E.O. Eren, Y. Devrim, C.O. Colpan, N. Ozkan, High-temperature electrochemical hydrogen separation from reformate gases using PBI/MOF composite membrane, *Int. J. Hydrog. Energy* 48 (2023) 23044–23054, <https://doi.org/10.1016/j.ijhydene.2023.03.192>.
- [17] Y.Z. Chun, Y.J. Cheng, Z. Wen, Y.W. Hui, G. Jianyu, L. Li, X. Hong, The preparation and adsorption performance of Co-doped MIL-101 (Cr) for low-concentration C_3F_8 , *Chem. Eng. Sci.* 282 (2023) 119302, <https://doi.org/10.1016/j.ces.2023.119302>.
- [18] J. Munawar, M.S. Khan, S.E.Z. Syeda, S. Nawaz, F.A. Janjhi, H.U. Haq, E. U. Rashid, T. Jesionowski, M. Bilal, Metal-organic framework-based smart nanoplateforms for biosensing, drug delivery, and cancer theranostics, *Inorg. Chem. Commun.* 147 (2023) 110145, <https://doi.org/10.1016/j.inoche.2022.110145>.
- [19] K. Sun, Y. Qian, H.L. Jiang, Metal-organic frameworks for photocatalytic water splitting and CO_2 reduction, *Angew. Chem. Int. Ed.* 62 (2023) e202217565, <https://doi.org/10.1002/anie.202217565>.
- [20] S. Jo, N. Kitchamsetti, H.W. Cho, D. Kim, Microwave-assisted hierarchically grown flake-like NiCo layered double hydroxide nanosheets on transitioned polystyrene towards triboelectricity-driven self-charging hybrid supercapacitors, *Polymers* 15 (2023) 454, <https://doi.org/10.3390/polym15020454>.
- [21] Z.Y. Xiao, R. Wu, T.T. Shu, Y.X. Wang, L. Li, Synthesis of Co-doped Fe metal-organic framework MIL-101(Fe,Co) and efficient degradation of organic dyes in water, *Sep. Purif. Technol.* 304 (2023) 122300, <https://doi.org/10.1016/j.seppur.2022.122300>.
- [22] A.F. Sahayaraj, H.J. Prabu, J. Maniraj, M. Kannan, M. Bharathi, P. Diwihar, J. Salamon, Metal-organic frameworks (MOFs): the next generation of materials for catalysis, gas storage, and separation, *J. Inorg. Organomet. Polym. Mater.* 33 (2023) 1757–1781, <https://doi.org/10.1007/s10904-023-02657-1>.
- [23] Y.J. Ren, X. Wang, J.X. Ma, Q. Zheng, L.J. Wang, W. Jiang, Metal-organic framework derived carbon based composites for electromagnetic wave absorption: dimension design and morphology regulation, *J. Mater. Sci. Technol.* 132 (2023) 223–251, <https://doi.org/10.1016/j.jmst.2022.06.013>.
- [24] W.X. Zhou, Y.J. Tang, X.Y. Zhang, S.T. Zhang, H.G. Xue, H. Pang, MOF derived metal oxide composites and their applications in energy storage, *Coord. Chem. Rev.* 477 (2023) 214949, <https://doi.org/10.1016/j.ccr.2022.214949>.
- [25] X.T. Hou, J.X. Sun, M.Y. Lian, Y. Peng, D.W. Jiang, M.J. Xu, B. Li, Q. Xu, Emerging synthetic methods and applications of MOF based gels in supercapacitors, water treatment, catalysis, adsorption, and energy storage, *Macromol. Mater. Eng.* 308 (2023) 2200469, <https://doi.org/10.1002/mame.202200469>.
- [26] S. Dutt, A. Kumar, S. Singh, Synthesis of metal organic frameworks (MOFs) and their derived materials for energy storage applications, *Clean Technol.* 5 (2023) 140–166, <https://doi.org/10.3390/cleantechnol5010009>.
- [27] H. Gunaseelan, A.V. Munde, R. Patel, B.R. Sathe, Metal-organic framework derived carbon-based electrocatalysis for hydrogen evolution reactions: a review, *Mater. Today Sustain.* 22 (2023) 100371, <https://doi.org/10.1016/j.mtsust.2023.100371>.
- [28] N. Kitchamsetti, C.S. Chakra, A.L.F. deBarros, D. Kim, Development of MOF based recyclable photocatalyst for the removal of different organic dye pollutants, *Nanomaterials* 13 (2023) 336, <https://doi.org/10.3390/nano13020336>.
- [29] N. Kitchamsetti, D. Narsimulu, A. Chinthakuntla, C.S. Chakra, A.L.F. deBarros, Bimetallic MOF derived ZnCo_2O_4 nanocages as a novel class of high performance photocatalyst for the removal of organic pollutants, *Inorg. Chem. Commun.* 144 (2022) 109946, <https://doi.org/10.1016/j.inoche.2022.109946>.
- [30] W. Huang, M. Chai, R. Lin, V. Chen, J.W. Hou, Mechanism comprehension and design of MOF catalysts for photocatalytic ammonia production, *Ind. Eng. Chem. Res.* 62 (2023) 14130–14143, <https://doi.org/10.1021/acs.iecr.3c02177>.
- [31] C.L. Wang, Z.H. Lv, W.X. Yang, X. Feng, B. Wang, A rational design of functional porous frameworks for electrocatalytic CO_2 reduction reaction, *Chem. Soc. Rev.* 52 (2023) 1382–1427, <https://doi.org/10.1039/D2CS00843B>.
- [32] Z. Li, Y.M. Guo, K. Li, S. Wang, E.D. Bonis, H. Cao, S.F.L. Mertens, C. Teng, Shape control of bimetallic MOF/Graphene composites for efficient oxygen evolution reaction, *J. Electroanal. Chem.* 930 (2023) 117144, <https://doi.org/10.1016/j.jelechem.2023.117144>.
- [33] N. Kitchamsetti, M. Samtham, D. Singh, E. Choudhary, S.R. Rondiya, Y.R. Ma, R. W. Cross, N.Y. Dzade, R.S. Devan, Hierarchical 2D MnO_2 @1D mesoporous NiTiO_3 core-shell hybrid structures for high-performance supercapattery electrodes: theoretical and experimental investigations, *J. Electroanal. Chem.* 936 (2023) 117359, <https://doi.org/10.1016/j.jelechem.2023.117359>.
- [34] N. Kitchamsetti, R.S. Kalubarme, P.R. Chikate, C.J. Park, Y.R. Ma, P.M. Shirage, R.S. Devan, An investigation on the effect of Li-ion cycling on the vertically aligned brookite TiO_2 nanostructure, *ChemistrySelect* 4 (2019) 6620–6626, <https://doi.org/10.1002/slct.201900395>.
- [35] H. Wang, Q. Yang, N. Zheng, X.W. Zhai, T. Xu, Z.X. Sun, L. Wu, M. Zhou, Roadmap of amorphous metal-organic framework for electrochemical energy conversion and storage, *Nano Res.* 16 (2023) 4107–4118, <https://doi.org/10.1007/s12274-022-5114-8>.
- [36] J.H. Park, Y.S. Kim, N. Kitchamsetti, S. Jo, S.J. Lee, J. Song, W. Park, D. Kim, FeV LDH coated on sandpaper as an electrode material for high-performance flexible energy storage devices, *Polymers* 15 (2023) 1136, <https://doi.org/10.3390/polym15051136>.
- [37] N. Kitchamsetti, M.S. Ramteke, S.R. Rondiya, S.R. Mulani, M.S. Patil, R.W. Cross, N.Y. Dzade, R.S. Devan, DFT and experimental investigations on the photocatalytic activities of NiO nanobelts for removal of organic pollutants, *J. Alloys Compd.* 855 (2021) 157337, <https://doi.org/10.1016/j.jallcom.2020.157337>.
- [38] K.A. Adegoke, N.W. Maxakato, Porous metal-organic framework (MOF)-based and MOF-derived electrocatalytic materials for energy conversion, *Mater. Today Energy* 21 (2021) 100816, <https://doi.org/10.1016/j.mtener.2021.100816>.
- [39] N. Kitchamsetti, R.J. Choudhary, D.M. Phase, R.S. Devan, Structural correlation of a nanoparticle-embedded mesoporous CoTiO_3 perovskite for an efficient electrochemical supercapacitor, *RSC Adv.* 10 (2020) 23446–23456, <https://doi.org/10.1039/D0RA04052E>.
- [40] N. Kitchamsetti, Y.R. Ma, P.M. Shirage, R.S. Devan, Mesoporous perovskite of interlocked nickel titanate nanoparticles for efficient electrochemical

- supercapacitor electrode, *J. Alloys Compd.* 833 (2020) 155134, <https://doi.org/10.1016/j.jallcom.2020.155134>.
- [41] A. Zhang, Q. Zhang, H.C. Fu, H.W. Zong, H.W. Guo, Metal-organic frameworks and their derivatives based nanostructure with different dimensionalities for supercapacitors, *Small* (2023) 2303911, <https://doi.org/10.1002/smll.202303911>.
- [42] N. Kitchamsetti, P.R. Chikate, R.A. Patil, Y.R. Ma, P.M. Shirage, R.S. Devan, Perforated mesoporous NiO nanostructures for an enhanced pseudocapacitive performance with ultra-high rate capability and high energy density, *CrystEngComm* 21 (2019) 7130–7140, <https://doi.org/10.1039/C9CE01475F>.
- [43] K. Boukayouh, L. Bazzi, S.E. Hankari, Sustainable synthesis of metal-organic frameworks and their derived materials from organic and inorganic wastes, *Coord. Chem. Rev.* 478 (2023) 214986, <https://doi.org/10.1016/j.ccr.2022.214986>.
- [44] C.W. Jiao, Z. Cao, J. He, Z.W. Liu, L.F. Xu, C. Zheng, S. Peng, G. Haldun, B. Chen, Facile strategy of directing metal-organic frameworks into hollow nanostructures by halide ions, *J. Phys. Chem. C* 127 (2023) 5702–5712, <https://doi.org/10.1021/acs.jpcc.3c00083>.
- [45] M.T. Anwar, M.R. Asghar, A. Ahmed, S. Fareed, H.I. Khan, T. Rasheed, Metal organic frameworks-carbon based nanocomposites for environmental sensing and catalytic applications, *Adv. Chem. Pollut. Environ. Manag. Prot.* 9 (2023) 301–320, <https://doi.org/10.1016/bs.amp.2022.12.002>.
- [46] E.V. Perez, C. Karunaweera, I.H. Musselman, K.J. Balkus, J.P. Ferraris, Origins and evolution of inorganic-based and MOF-based mixed-matrix membranes for gas separations, *Processes* 4 (2016) 32, <https://doi.org/10.3390/pr4030032>.
- [47] R. Banerjee, A. Phan, B. Wang, C. Knobler, H. Furukawa, M.O. Keffe, O.M. Yaghi, High-throughput synthesis of zeolitic imidazolate frameworks and application to CO₂ capture, *Science* 319 (2008) 939–943, <https://doi.org/10.1126/science.1152516>.
- [48] P.R. Bautista, I.T. Mancera, J. Pasan, V. Pino, Metal-organic frameworks in green analytical chemistry, *Separations* 6 (2019) 33, <https://doi.org/10.3390/separations6030033>.
- [49] P. Silva, S.M.F. Vilela, J.P.C. Tome, F.A.A. Paz, Multifunctional metal-organic frameworks: from academia to industrial applications, *Chem. Soc. Rev.* 44 (2015) 6774–6803, <https://doi.org/10.1039/C5CS00307E>.
- [50] S. Bhattacharjee, C. Chen, W.S. Ahn, Chromium terephthalate metal-organic framework MIL-101: synthesis, functionalization, and applications for adsorption and catalysis, *RSC Adv.* 4 (2014) 52500–52525, <https://doi.org/10.1039/C4RA11259H>.
- [51] M.Y. Zorainy, M.G. Alalm, S. Kaliaguine, D.C. Boffito, Revisiting the MIL-101 metal-organic framework: design, synthesis, modifications, advances, and recent applications, *J. Mater. Chem. A* 9 (2021) 22159–22217, <https://doi.org/10.1039/D1TA06238G>.
- [52] K. Gwon, I. Han, S.H. Lee, Y.M. Kim, D.N. Lee, Novel metal-organic framework-based photocrosslinked hydrogel system for efficient antibacterial applications, *ACS Appl. Mater. Interfaces* 12 (2020) 20234–20242, <https://doi.org/10.1021/acsami.0c03187>.
- [53] Y.B.N. Tran, P.T.K. Nguyen, Q.T. Luong, K.D. Nguyen, Series of M-MOF-184 (M = Mg, Co, Ni, Zn, Cu, Fe) metal-organic frameworks for catalysis cycloaddition of CO₂, *Inorg. Chem.* 59 (2020) 16747–16759, <https://doi.org/10.1021/acs.inorgchem.0c02807>.
- [54] J.G. Flores, M.D. Garcia, I.A. Ibarra, J.A. Pliego, M.S. Sanchez, Sustainable M-MOF-74 (M = Cu, Co, Zn) prepared in methanol as heterogeneous catalysts in the synthesis of benzaldehyde from styrene oxidation, *J. Solid State Chem.* 298 (2021) 122151, <https://doi.org/10.1016/j.jssc.2021.122151>.
- [55] L.Y. Chen, H.F. Wang, C.X. Li, Q. Xu, Bimetallic metal-organic frameworks and their derivatives, *Chem. Sci.* 11 (2020) 5369–5403, <https://doi.org/10.1039/D0SC01432J>.
- [56] N. Kitchamsetti, P.N. Didwal, S.R. Mulani, M.S. Patil, R.S. Devan, Photocatalytic activity of MnTiO₃ perovskite nanodisks for the removal of organic pollutants, *Heliyon* 7 (2021) e07297, <https://doi.org/10.1016/j.heliyon.2021.e07297>.
- [57] N. Kitchamsetti, D. Kim, Facile synthesis of hierarchical core-shell heterostructured ZnO/SnO₂@NiCo₂O₄ nanorod sheet arrays on carbon cloth for high performance quasi-solid-state asymmetric supercapacitors, *J. Mater. Res. Technol.* 21 (2022) 590–603, <https://doi.org/10.1016/j.jmrt.2022.09.041>.
- [58] N. Kitchamsetti, M. Samtham, P.N. Didwal, D. Kumar, D. Singh, S. Bimli, P. R. Chikate, D.A. Basha, S. Kumar, C.J. Park, S. Chakraborty, R.S. Devan, Theory abide experimental investigations on morphology driven enhancement of electrochemical energy storage performance for manganese titanate perovskites electrodes, *J. Power Sources* 538 (2022) 231525, <https://doi.org/10.1016/j.jpowsour.2022.231525>.
- [59] G. Kaur, R.K. Rai, D. Tyagi, X. Yao, P.Z. Li, X.C. Yang, Y. Zhao, Q. Xu, S.K. Singh, Room-temperature synthesis of bimetallic Co-Zn based zeolitic imidazolate frameworks in water for enhanced CO₂ and H₂ uptakes, *J. Mater. Chem. A* 4 (2016) 14932–14938, <https://doi.org/10.1039/C6TA04342A>.
- [60] S.J. Lee, S.G. Telfer, Multicomponent metal-organic frameworks, *Angew. Chem. Int. Ed.* (2023) e202306341, <https://doi.org/10.1002/anie.202306341>.
- [61] M.S. Patil, N. Kitchamsetti, S.R. Mulani, S.R. Rondiya, N.G. Deshpande, R.A. Patil, R.W. Cross, N.Y. Dzade, K.K. Sharma, P.S. Patil, Y.R. Ma, H.K. Cho, R.S. Devan, Photocatalytic behavior of Ba(Sb/Ta)₂O₆ perovskite for reduction of organic pollutants: experimental and DFT correlation, *J. Taiwan Inst. Chem. Eng.* 122 (2021) 201–209, <https://doi.org/10.1016/j.jtice.2021.04.032>.
- [62] F.Y. Ren, Y.J. Ji, F. Chen, Y.Y. Qian, J.J. Tian, J.C. Wang, Flower-like bimetal Ni/Co-based metal-organic-framework materials with adjustable components toward high performance solid-state supercapacitors, *Mater. Chem. Front.* 5 (2021) 7333–7342, <https://doi.org/10.1039/D1QM00940K>.
- [63] C. Chen, Y.X. Tuo, Q. Lu, H. Lu, S.Y. Zhang, Y. Zhou, J. Zhang, Z. Liu, Z. Kang, X. Feng, D. Chen, Hierarchical trimetallic Co-Ni-Fe oxides derived from core-shell structured metal-organic frameworks for highly efficient oxygen evolution reaction, *Appl. Catal. B Environ.* 287 (2021) 119953, <https://doi.org/10.1016/j.apcatb.2021.119953>.
- [64] R. Xiao, H.I. Abdu, L.P. Wei, T.Y. Wang, S.H. Huo, J. Chen, X.Q. Lu, Fabrication of magnetic trimetallic metal-organic frameworks for the rapid removal of tetracycline from water, *Analyst* 145 (2020) 2398–2404, <https://doi.org/10.1039/C9AN02481F>.
- [65] H. Shu, T.R. Lai, J. Ren, X.X. Cui, X. Tian, Z.C. Yang, X.C. Xiao, Y. Wang, Trimetallic metal-organic frameworks (Fe, Co, Ni-MOF) derived as efficient electrochemical determination for ultra-micro imidacloprid in vegetables, *Nanotechnology* 33 (2022) 135502, <https://doi.org/10.1088/1361-6528/ac4350>.
- [66] W. Zhang, J.S. Luo, X. Zhang, W. Guo, N. Han, S. Xie, Z.Y. Zhou, Z. Anwer, Z. H. Xue, J. Franssaer, Metal-organic framework-derived CoP₂@N-doped carbon hollow spheres for efficient oxygen evolution reaction, *J. Mater. Sci. Technol.* 164 (2023) 240–245, <https://doi.org/10.1016/j.jmst.2023.04.024>.
- [67] K.Y. Shen, Y. Tang, Q.H. Zhou, Y. Zhang, W. Ge, X.X. Shai, S.P. Deng, P.Z. Yang, S. K. Deng, J.S. Wang, Metal-organic framework-derived S-NiFe PBA coupled with NiFe layered double hydroxides as Mott-Schottky electrocatalysts for efficient alkaline oxygen evolution reaction, *Chem. Eng. J.* 471 (2023) 144827, <https://doi.org/10.1016/j.cej.2023.144827>.
- [68] J. Yun, J. Park, M. Ryoo, N. Kitchamsetti, T.S. Goh, D. Kim, Piezo-triboelectric hybridized nanogenerator embedding MXene based bifunctional conductive filler in polymer matrix for boosting electrical power, *Nano Energy* 105 (2023) 108018, <https://doi.org/10.1016/j.nanoen.2022.108018>.
- [69] J. Park, S. Jo, N. Kitchamsetti, S. Zaman, D. Kim, The development of NiCo₂O₄/PVP/PANI heterogeneous nanocomposites as an advanced battery-type electrode material for high-performing supercapacitor application, *J. Alloys Compd.* 926 (2022) 166815, <https://doi.org/10.1016/j.jallcom.2022.166815>.
- [70] N.Y.W. Zaw, S. Jo, J. Park, N. Kitchamsetti, N. Jayababu, D. Kim, Clay-assisted hierarchical growth of metal-telluride nanostructures as an anode material for hybrid supercapacitors, *Appl. Clay Sci.* 225 (2022) 106539, <https://doi.org/10.1016/j.clay.2022.106539>.
- [71] J.X. Li, T. Bao, C. Zhang, H. Song, Y.Y. Zou, L. Yuan, Y. Xi, C.Z. Yu, C. Liu, A general strategy for direct growth of yolk-shell MOF-on-MOF hybrids, *Chem. Eng. J.* 472 (2023) 144926, <https://doi.org/10.1016/j.cej.2023.144926>.
- [72] S.F.N. Ana, S. Zeinali, Synthesis of a novel one-dimensional ternary MOF-on-MOF in form of direct and carbonization derived structure towards promising catalytic efficiency of HER, *Appl. Energy* 350 (2023) 121755, <https://doi.org/10.1016/j.apenergy.2023.121755>.
- [73] R. Chavan, N. Bhat, S. Parit, K. Narasimharao, R.S. Devan, R.B. Patil, V.C. Karade, N.V. Pawar, J.H. Kim, J.P. Jadhav, A.D. Chougale, Development of magnetically recyclable nanocatalyst for enhanced Fenton and photo-Fenton degradation of MB and Cr(VI) photo-reduction, *Mater. Chem. Phys.* 293 (2023) 126964, <https://doi.org/10.1016/j.matchemphys.2022.126964>.
- [74] S. Vallem, J. Bae, The active role of conjugate polymer composites in electrochemical storage: a themed perspective on polymer-MOF nanocomposites for metal-ion batteries, *Recent Adv. Polym. Mater. Electrochem. Energy Storage* (2023) 211–228, https://doi.org/10.1007/978-981-99-4193-3_12.
- [75] N. Kitchamsetti, A.L.F. de Barros, Recent advances in MXenes based composites as photocatalysts: synthesis, properties and photocatalytic removal of organic contaminants from wastewater, *ChemCatChem* 15 (2023) e202300690, <https://doi.org/10.1002/cctc.202300690>.
- [76] L.M. Xu, Z.B. Ding, Y.Y. Chen, X.T. Xu, Y. Liu, J.B. Li, T. Lu, L.K. Pan, Carbon nanotube bridged nickel hexacyanoferrate architecture for high-performance hybrid capacitive deionization, *J. Colloid Interface Sci.* 630 (2023) 372–381, <https://doi.org/10.1016/j.jcis.2022.10.140>.
- [77] Y.Q. Wang, Y.L. Yang, M. Miao, X. Feng, Carbon nanotube arrays@cobalt hybrids derived from metal-organic framework ZIF-67 for enhanced electromagnetic wave absorption, *Mater. Today Phys.* 35 (2023) 101110, <https://doi.org/10.1016/j.mtphys.2023.101110>.
- [78] I. Kim, H.W. Cho, N. Kitchamsetti, J.H. Yun, J.M. Lee, W. Park, D. Kim, A robust triboelectric impact sensor with carbon dioxide precursor-based calcium carbonate layer for slap match application, *Micromachines* 14 (2023) 1778, <https://doi.org/10.3390/mi14091778>.
- [79] F.S. Farahani, M.S. Rahmanifar, A. Noori, M.F. El-Kady, N. Hassani, M.N. Amal, R.B. Kaner, M.F. Mousavi, Trilayer metal-organic frameworks as multifunctional electrocatalysts for energy conversion and storage applications, *J. Am. Chem. Soc.* 144 (2022) 3411–3428, <https://doi.org/10.1021/jacs.1c10963>.
- [80] H. Zhang, W.Q. Zhao, Y.Z. Wu, Y.S. Wang, M.C. Zou, A.Y. Cao, Dense monolithic MOF and carbon nanotube hybrid with enhanced volumetric and areal capacities for lithium-sulfur battery, *J. Mater. Chem. A* 7 (2019) 9195–9201, <https://doi.org/10.1039/C9TA00485H>.
- [81] J.M. Palomba, D.M. Wirth, J.Y. Kim, M. Kalaj, E.M. Clarke, G.W. Peterson, J. K. Pokorski, S.M. Cohen, Strong, ductile MOF-poly(urethane urea) composites, *Chem. Mater.* 33 (2021) 3164–3171, <https://doi.org/10.1021/acs.chemmater.0c04874>.
- [82] N. Liu, J.J. Zhao, S. Osman, L. Wang, G. Jiang, Y.Z. Sun, X.G. Liu, J.Q. Pan, Honeycomb-like porous carbon derived from fluorinated magnesium-based metal organic frameworks as an electrode material for supercapacitors, *J. Energy Storage* 63 (2023) 106939, <https://doi.org/10.1016/j.est.2023.106939>.
- [83] X.J. Xie, H. Zeng, W.G. Lu, D. Li, Metal-organic frameworks for hydrocarbon separation: design, progress, and challenges, *J. Mater. Chem. A* 11 (2023) 20459–20469, <https://doi.org/10.1039/D3TA03852A>.

- [84] H. Rabiee, J.K. Heffernan, L. Ge, X.Q. Zhang, P.H. Yan, E. Marcellin, S.H. Hu, Z. H. Zhu, H. Wang, Z.G. Yuan, Tuning flow-through Cu-based hollow fiber gas-diffusion electrode for high-efficiency carbon monoxide (CO) electroreduction to C₂+ products, *Appl. Catal. B Environ.* 330 (2023) 122589, <https://doi.org/10.1016/j.apcatb.2023.122589>.
- [85] D.J. Tranchemontagne, J.R. Hunt, O.M. Yaghi, Room temperature synthesis of metal-organic frameworks: MOF-5, MOF-74, MOF-177, MOF-199, IRMOF-0, *Tetrahedron* 64 (2008) 8553–8557, <https://doi.org/10.1016/j.tet.2008.06.036>.
- [86] J.J. Duan, Y.T. Sun, S. Chen, X.J. Chen, C. Zhao, A zero-dimensional nickel, iron-metal-organic framework (MOF) for synergistic N₂ electrofixation, *J. Mater. Chem. A* 8 (2020) 18810–18815, <https://doi.org/10.1039/D0TA05010E>.
- [87] X.H. Zhang, C.Y. Chuah, P.P. Dong, Y.H. Cha, T.H. Bae, M.K. Song, Hierarchically porous Co-MOF-74 hollow nanorods for enhanced dynamic CO₂ separation, *ACS Appl. Mater. Interfaces* 10 (2018) 43316–43322, <https://doi.org/10.1021/acsmi.8b17180>.
- [88] R.C. Arbulu, Y.B. Jiang, E.J. Peterson, Y. Qin, Metal-organic framework (MOF) nanorods, nanotubes, and nanowires, *Angew. Chem. Int. Ed.* 57 (2018) 5813–5817, <https://doi.org/10.1002/anie.201802694>.
- [89] H.C. Xia, J. Zhang, Z. Yang, S.Y. Guo, S.H. Guo, Q. Xu, 2D MOF nanoflake-assembled spherical microstructures for enhanced supercapacitor and electrocatalysis performances, *Nano-Micro Lett.* 9 (2017) 43, <https://doi.org/10.1007/s40820-017-0144-6>.
- [90] J.Y. Cheng, S.M. Chen, D. Chen, L.B. Dong, J.J. Wang, T. Zhang, T.P. Jiao, B. Liu, H. Wang, J.J. Kai, D.Q. Zhang, G.P. Zheng, L.J. Zhi, F.Y. Kang, W.J. Zhang, Editable asymmetric all-solid-state supercapacitors based on high-strength, flexible, and programmable 2D-metal-organic framework/reduced graphene oxide self-assembled papers, *J. Mater. Chem. A* 6 (2018) 20254–20266, <https://doi.org/10.1039/C8TA06785F>.
- [91] J.R. He, W.Q. Lv, Y.F. Chen, J. Xiong, K.C. Wen, C. Xu, W.L. Zhang, Y.R. Li, W. Qin, W.D. He, Direct impregnation of SeS₂ into a MOF-derived 3D nanoporous Co-N-C architecture towards superior rechargeable lithium batteries, *J. Mater. Chem. A* 6 (2018) 10466–10473, <https://doi.org/10.1039/C8TA02434K>.
- [92] H. Zhang, W.Q. Zhao, M.C. Zou, Y.S. Wang, Y.J. Chen, L. Xu, H.S. Wu, A.Y. Cao, 3D, mutually embedded MOF@carbon nanotube hybrid networks for high-performance lithium-sulfur batteries, *Adv. Energy Mater.* 8 (2018) 1800013, <https://doi.org/10.1002/aenm.201800013>.
- [93] W.B. Lv, Y.F. Song, H.B. Pei, Z.L. Mo, Synthesis strategies and applications of metal-organic framework-quantum dot (MOF@QDs) functional composites, *J. Ind. Eng. Chem.* (2023), <https://doi.org/10.1016/j.jiec.2023.07.055>.
- [94] B. Siu, A.R. Chowdhury, Z.W. Yan, S.M. Humphrey, T. Hutter, Selective adsorption of volatile organic compounds in metal-organic frameworks (MOFs), *Coord. Chem. Rev.* 485 (2023) 215119, <https://doi.org/10.1016/j.ccr.2023.215119>.
- [95] A.J. Amali, H. Hoshino, C. Wu, M. Ando, Q. Xu, From metal-organic framework to intrinsically fluorescent carbon nanodots, *Chem. Eur. J.* 20 (2014) 8279–8282, <https://doi.org/10.1002/chem.201402982>.
- [96] Y.F. Chen, X. Feng, X.Q. Huang, Z.G. Lin, X.K. Pei, S. Li, J.K. Li, S. Wang, R. Li, B. Wang, A tale of copper coordination frameworks: controlled single-crystal-to-single-crystal transformations and their catalytic C-H bond activation properties, *Chem. Eur. J.* 21 (2015) 13894–13899, <https://doi.org/10.1002/chem.201501672>.
- [97] C.H. Wang, Y.Y. Yao, J.S. Li, Y. Yamauchi, Metal-organic frameworks: a robust platform for creating nanoarchitected carbon materials, *Acc. Mater. Res.* 3 (2022) 426–438, <https://doi.org/10.1021/accountsmr.1c00258>.
- [98] L. Huang, J. Yang, Y. Asakura, Q. Shuai, Y. Yamauchi, Nanoarchitectonics of hollow covalent organic frameworks: synthesis and applications, *ACS Nano* 17 (2023) 8918–8934, <https://doi.org/10.1021/acsnano.3c01758>.
- [99] A. Saad, S. Biswas, E. Gkanitsou, C. Sicard, E. Dumas, N. Menguy, N. Steunou, Metal-organic framework based 1D nanostructures and their superstructures: synthesis, microstructure, and properties, *Chem. Mater.* 33 (2021) 5825–5849, <https://doi.org/10.1021/acs.chemmater.1c01034>.
- [100] J.B. Shi, J.L. Zhang, D.X. Tan, X.Y. Cheng, X.I. Tan, B.X. Zhang, B.X. Han, L.F. Liu, F.Y. Zhang, M.R. Liu, J.F. Xiang, Rapid, room-temperature and template-free synthesis of metal-organic framework nanowires in alcohol, *ChemCatChem* 11 (2019) 2058–2062, <https://doi.org/10.1002/cctc.201900124>.
- [101] W. Zhang, Z.Y. Wu, H.L. Jiang, S.H. Yu, Nanowire-directed templating synthesis of metal-organic framework nanofibers and their derived porous doped carbon nanofibers for enhanced electrocatalysis, *J. Am. Chem. Soc.* 136 (2014) 14385–14388, <https://doi.org/10.1021/ja5084128>.
- [102] Y.L. Liu, X.Y. Liu, L. Feng, L.X. Shao, S.J. Li, J. Tang, H. Cheng, Z. Chen, R. Huang, H.C. Xu, J.L. Zhuang, Two-dimensional metal-organic framework nanosheets: synthesis and applications in electrocatalysis and photocatalysis, *ChemSusChem* 15 (2022) e202102603, <https://doi.org/10.1002/cssc.202102603>.
- [103] J.H. Cai, S.Z. Song, L. Zhu, Q.P. Lu, Z. Lu, Y.Y. Wei, H.H. Wang, Two-dimensional Cu-porphyrin nanosheet membranes for nanofiltration, *Nano Res.* 16 (2023) 6290–6297, <https://doi.org/10.1007/s12274-023-5447-y>.
- [104] J.J. Liu, X.Y. Song, T. Zhang, S.Y. Liu, H.R. Wen, L. Chen, 2D conductive metal-organic frameworks: an emerging platform for electrochemical energy storage, *Angew. Chem. Int. Ed.* 60 (2021) 5612–5624, <https://doi.org/10.1002/anie.202006102>.
- [105] J.W. Guo, H.B. Zhao, Z.W. Yang, Y.W. Wang, X.L. Liu, L.F. Wang, Z.H. Zhao, A. Z. Wang, L.H. Ding, H. Liu, X. Yu, Hierarchical porous 3D Ni₃N-CoN/NC heterojunction nanosheets with nitrogen vacancies for high-performance flexible supercapacitor, *Nano Energy* 116 (2023) 108763, <https://doi.org/10.1016/j.nanoen.2023.108763>.
- [106] S.F. Wu, Z. Li, M.Q. Li, Y.X. Diao, F. Lin, T.T. Liu, J. Zhang, P. Tieu, W.P. Gao, F. Qi, X.Q. Pan, Z.T. Xu, Z.L. Zhu, A.K.Y. Jen, 2D metal-organic framework for stable perovskite solar cells with minimized lead leakage, *Nat. Nanotechnol.* 15 (2020) 934–940, <https://doi.org/10.1038/s41565-020-0765-7>.
- [107] H. Szalad, A. Uscategui, J. Albero, H. Garcia, 2D/2D Cu-tetrahydroxyquinone MOF/N-doped graphene heterojunction as photocatalyst for overall water splitting, *Int. J. Hydrog. Energy* 48 (2023) 12374–12384, <https://doi.org/10.1016/j.ijhydene.2022.12.168>.
- [108] C.Y. Li, J. Wang, Y. Yan, P.W. Huo, X.K. Wang, MOF-derived NiZnCo-P nanorod array for asymmetric supercapacitor, *Chem. Eng. J.* 446 (2022) 137108, <https://doi.org/10.1016/j.cej.2022.137108>.
- [109] F.L. Li, C.G. Li, Q. Xie, X.L. Chen, X.Z. Tang, T. Guo, MOF-derived core-shell Co₉S₈@MoS₂ nanocubes anchored on RGO to construct heterostructure for high-efficiency microwave attenuation, *J. Alloys Compd.* 935 (2023) 168106, <https://doi.org/10.1016/j.jallcom.2022.168106>.
- [110] Z. Zuhra, S. Ali, S. Ali, H. Xu, R.Z. Wu, Y.Y. Tang, Exceptionally amino-quantitated 3D MOF@CNT-sponge hybrid for efficient and selective recovery of Au(III) and Pd(II), *Chem. Eng. J.* 431 (2022) 133367, <https://doi.org/10.1016/j.cej.2021.133367>.
- [111] K. Chen, Y. Jiang, W. Tao, T.S. Wang, F.M. Liu, C.G. Wang, X. Yan, G. Lu, P. Sun, MOF structure engineering to synthesize core-shell heterostructures with controllable shell layer thickness: regulating gas selectivity and sensitivity, *Sensors Actuators B Chem.* 378 (2023) 133117, <https://doi.org/10.1016/j.snb.2022.133117>.
- [112] K. Narasimharao, G.V. Ramana, D. Sreedhar, V. Vasudevarao, Synthesis of graphene oxide by modified hummers method and hydrothermal synthesis of graphene-NiO nano composite for supercapacitor application, *J. Mater. Sci. Eng.* 5 (2016) 1000284, <https://doi.org/10.4172/2169-0022.1000284>.
- [113] J.J. Zhao, N. Liu, Y.Z. Sun, Q.H. Xu, J.Q. Pan, Nitrogen-modified spherical porous carbon derived from aluminum-based metal-organic frameworks as activation-free materials for supercapacitors, *J. Energy Storage* 73 (2023) 109070, <https://doi.org/10.1016/j.est.2023.109070>.
- [114] L. Wang, G.Y. Zhu, Y.H. Lin, Y. Wang, Q.S. Zhu, Z.H. Dai, MOF-derived hierarchical porous carbon octahedrons for aluminum-ion batteries, *Carbon* 202 (2023) 305–313, <https://doi.org/10.1016/j.carbon.2022.10.069>.
- [115] X.Y. Qin, D. Kim, Y.Z. Piao, Metal-organic frameworks-derived novel nanostructured electrocatalysts for oxygen evolution reaction, *Carbon Energy* 3 (2021) 66–100, <https://doi.org/10.1002/cey2.80>.
- [116] H.D. Mai, K. Rafiq, H. Yoo, Nano metal-organic framework-derived inorganic hybrid nanomaterials: synthetic strategies and applications, *Chem. Eur. J.* 23 (2017) 5631–5651, <https://doi.org/10.1002/chem.201604703>.
- [117] D. He, Y. Gao, Y.C. Yao, L. Wu, J. Zhang, Z.H. Huang, M.X. Wang, Asymmetric supercapacitors based on hierarchically nanoporous carbon and ZnCo₂O₄ from a single biometallic metal-organic frameworks (Zn/Co-MOF), *Front. Chem.* 8 (2020) 719, <https://doi.org/10.3389/fchem.2020.00719>.
- [118] M.J. Wang, Z.X. Mao, L. Liu, L.S. Peng, N. Yang, J.H. Deng, W. Ding, J. Li, Z. D. Wei, Preparation of hollow nitrogen doped carbon via stresses induced orientation contraction, *Small* 14 (2018) 1804183, <https://doi.org/10.1002/sml.201804183>.
- [119] J.S. Meng, C.J. Niu, L.H. Xu, J.T. Li, X. Liu, X.P. Wang, Y.Z. Wu, X.M. Xu, W. Y. Chen, Q. Li, Z.Z. Zhu, D.Y. Zhao, L.Q. Mai, General oriented formation of carbon nanotubes from metal-organic frameworks, *J. Am. Chem. Soc.* 139 (2017) 8212–8221, <https://doi.org/10.1021/jacs.7b01942>.
- [120] S.X. Bao, J.Y. Li, B.Y. Guan, M.J. Jia, O. Terasaki, J.H. Yu, A green selective water-etching approach to MOF@mesoporous SiO₂ yolk-shell nanoreactors with enhanced catalytic stabilities, *Matter* 3 (2020) 498–508, <https://doi.org/10.1016/j.matt.2020.06.021>.
- [121] X.J. Li, L.M. Ye, Z. Ye, S.H. Xie, Y.M. Qiu, F.Z. Liao, C.X. Lin, M.H. Liu, N. P. co-doped core/shell porous carbon as a highly efficient peroxydisulfate activator for phenol degradation, *Sep. Purif. Technol.* 276 (2021) 119286, <https://doi.org/10.1016/j.seppur.2021.119286>.
- [122] Y.Y. Yi, W. Zhao, Z.H. Zeng, C.H. Wei, C. Lu, Y.L. Shao, W.Y. Guo, S.X. Dou, J. Y. Sun, ZIF-67 derived nitrogen doped porous carbon confined CoP polyhedron targeting superior potassium-ion storage, *Small* 16 (2020) 1906566, <https://doi.org/10.1002/sml.201906566>.
- [123] A. Aijaz, J. Masa, C. Rosler, W. Xia, P. Weide, R.A. Fischer, W. Schuhmann, M. Muhler, Metal-organic framework derived carbon nanotube grafted cobalt/carbon polyhedra grown on nickel foam: an efficient 3D electrode for full water splitting, *ChemElectroChem* 4 (2017) 188–193, <https://doi.org/10.1002/celec.201600452>.
- [124] P. Pachfule, D. Shinde, M. Majumder, Q. Xu, Fabrication of carbon nanorods and graphene nanoribbons from a metal-organic framework, *Nat. Chem.* 8 (2016) 718–724, <https://doi.org/10.1038/nchem.2515>.
- [125] J.S. Meng, C.J. Niu, L.H. Xu, J.T. Li, X. Liu, X.P. Wang, Y.Z. Wu, X.M. Xu, W. Y. Chen, Q. Li, Z.Z. Zhu, D.Y. Zhao, L.Q. Mai, General oriented formation of carbon nanotubes from metal-organic frameworks, *J. Am. Chem. Soc.* 139 (2017) 8212–8221, <https://doi.org/10.1021/jacs.7b01942>.
- [126] Y. Qiu, H.B. Yang, L. Ma, Y. Lin, H.W. Zong, B. Wen, X.Y. Bai, M.Q. Wang, In situ-derived carbon nanotube-decorated nitrogen-doped carbon-coated nickel hybrids from MOF/melamine for efficient electromagnetic wave absorption, *J. Colloid Interface Sci.* 581 (2021) 783–793, <https://doi.org/10.1016/j.jcis.2020.07.151>.
- [127] C. Liu, X.D. Hang, J. Wang, H. Song, Y.N. Yang, Y. Liu, J.S. Li, L.J. Wang, C.Z. Yu, Hollow mesoporous carbon nanocubes: rigid-interface induced outward contraction of metal-organic frameworks, *Adv. Funct. Mater.* 28 (2018) 1705253, <https://doi.org/10.1002/adfm.201705253>.

- [128] Y.N. Hou, Z.B. Zhao, Z.F. Yu, S. Zhang, S.F. Li, J. Yang, H. Zhang, C. Liu, Z. Y. Wang, J.S. Qiu, Microporous MOFs engaged in the formation of nitrogen doped mesoporous carbon nanosheets for high-rate supercapacitors, *Chem. Eur. J.* 24 (2018) 2681–2686, <https://doi.org/10.1002/chem.201705006>.
- [129] Q.L. Zhu, P. Pachfule, P. Strubel, Z.P. Li, R.Q. Zou, Z. Liu, S. Kaskel, Q. Xu, Fabrication of nitrogen and sulfur co-doped hollow cellular carbon nanocapsules as efficient electrode materials for energy storage, *Energy Storage Mater.* 13 (2018) 72–79, <https://doi.org/10.1016/j.ensm.2017.12.027>.
- [130] M.X. Liu, F. Zhao, D.Z. Zhu, H. Duan, Y.K. Lv, L.C. Li, L.H. Gan, Ultramicroporous carbon nanoparticles derived from metal-organic framework nanoparticles for high-performance supercapacitors, *Mater. Chem. Phys.* 211 (2018) 234–241, <https://doi.org/10.1016/j.matchemphys.2018.02.030>.
- [131] X.Q. Yang, W. Chen, H.D. Bian, T.Y. Sun, Y.Y. Du, Z.Y. Zhang, W.J. Zhang, Y.Y. Li, X.F. Chen, F. Wang, Synthesis of mesoporous ZIF-8 nanoribbons and their conversion into carbon nanoribbons for high-performance supercapacitors, *Chem. Eur. J.* 24 (2018) 11185–11192, <https://doi.org/10.1002/chem.201801869>.
- [132] X. Li, G. Xu, J. Peng, S. Liu, H.Y. Zhang, J.W. Mao, H. Niu, W.P. Lv, X.Y. Zhao, R. Wu, Highly porous metal-free graphitic carbon derived from metal-organic framework for profiling of N-linked glycans, *ACS Appl. Mater. Interfaces* 10 (2018) 11896–11906, <https://doi.org/10.1021/acsami.8b02423>.
- [133] H.M. Tang, W.Y. Li, H.S. Jiang, R.J. Lin, Z. Wang, J.H. Wu, G.J. He, P.R. Shearing, D.J.L. Brett, ZIF-8-derived hollow carbon for efficient adsorption of antibiotics, *Nanomaterials* 9 (2019) 117, <https://doi.org/10.3390/nano9010117>.
- [134] X.M. Cao, Z.J. Sun, S.Y. Zhao, B. Wang, Z.B. Han, MOF-derived sponge-like hierarchical porous carbon for flexible all-solid-state supercapacitors, *Mater. Chem. Front.* 2 (2018) 1692–1699, <https://doi.org/10.1039/C8QM00284C>.
- [135] L.Y. Fei, C. Chen, L.G. Shen, Y.Y. Zhang, B. Wang, J.J. Xu, B.S. Li, S. Raza, H. J. Lin, Graphene oxide assisted assembly of superhydrophilic MOF-based membrane with 2D/3D hybrid nanochannels for enhanced water purification, *Chem. Eng. J.* 460 (2023) 141694, <https://doi.org/10.1016/j.cej.2023.141694>.
- [136] C. Yang, Q. Wang, K.L. Zhang, Preparation, characterization, and electrochemical sensing performance of a novel pristine Cd-MOF and its composite with carbon nanotubes, *Dalton Trans.* 52 (2023) 5687–5703, <https://doi.org/10.1039/D3DT00353A>.
- [137] P.F. Zhang, H.S. Cheng, F. Gu, S.H. Hong, H.J. Dong, C.M. Li, Progress on iron-series metal-organic frameworks materials towards electrocatalytic hydrogen evolution reaction, *Surf. Interfaces* 42 (2023) 103368, <https://doi.org/10.1016/j.surfin.2023.103368>.
- [138] B. Hosseinzadeh, B. Nagar, R.B. Vilau, P.G. Romero, S.H. Kazemi, MOF-derived conformal cobalt oxide/C composite material as high-performance electrode in hybrid supercapacitors, *Electrochim. Acta* 389 (2021) 138657, <https://doi.org/10.1016/j.electacta.2021.138657>.
- [139] M.Q. Huang, L. Wang, K. Pei, W.B. You, X.F. Yu, Z.C. Wu, R.C. Che, Multidimension-controllable synthesis of MOF-derived Co@N-doped carbon composite with magnetic-dielectric synergy toward strong microwave absorption, *Small* 16 (2020) 2000158, <https://doi.org/10.1002/sml.202000158>.
- [140] K.B. Wang, X.R. Yi, X.F. Luo, Y. Shi, J.Y. Xu, Fabrication of Co₃O₄ pseudocapacitor electrodes from nanoscale cobalt-organic frameworks, *Polyhedron* 109 (2016) 26–32, <https://doi.org/10.1016/j.poly.2016.01.046>.
- [141] M.K. Wu, C. Chen, J.J. Zhou, F.Y. Yi, K. Tao, L. Han, MOF-derived hollow double-shelled NiO nanospheres for high-performance supercapacitors, *J. Alloys Compd.* 734 (2018) 1–8, <https://doi.org/10.1016/j.jallcom.2017.10.171>.
- [142] S. Maiti, A. Pramanik, S. Mahanty, Extraordinarily high pseudocapacitance of metal organic framework derived nanostructured cerium oxide, *Chem. Commun.* 50 (2014) 11717–11720, <https://doi.org/10.1039/C4CC005363J>.
- [143] C. Singh, S. Mukhopadhyay, I. Hod, Metal-organic framework derived nanomaterials for electrocatalysis: recent developments for CO₂ and N₂ reduction, *Nano Converg.* 8 (2021) 1, <https://doi.org/10.1186/s40580-020-00251-6>.
- [144] V. Shrivastav, S. Sundriyal, U.K. Tiwari, K.H. Kim, A. Deep, Metal-organic framework derived zirconium oxide/carbon composite as an improved supercapacitor electrode, *Energy* 235 (2021) 121351, <https://doi.org/10.1016/j.energy.2021.121351>.
- [145] J.E. Zhou, J.H. Chen, Y.H. Peng, Y.Q. Zheng, A. Zeb, X.M. Lin, Metal-organic framework-derived transition metal sulfides and their composites for alkali-ion batteries: a review, *Coord. Chem. Rev.* 472 (2022) 214781, <https://doi.org/10.1016/j.ccr.2022.214781>.
- [146] Z.X. Cheng, A. Saad, S. Adimi, H.C. Guo, S. Liu, T. Thomas, M.H. Yang, Metal organic framework-derived porous Fe₂N nanocubes by rapid-nitridation for efficient photocatalytic hydrogen evolution, *Mater. Adv.* 1 (2020) 1161–1167, <https://doi.org/10.1039/D0MA00074D>.
- [147] S.K. Park, J.K. Kim, Y.C. Kang, Metal-organic framework-derived CoSe₂/(NiCo)Se₂ box-in-box hollow nanocubes with enhanced electrochemical properties for sodium-ion storage and hydrogen evolution, *J. Mater. Chem. A* 5 (2017) 18823–18830, <https://doi.org/10.1039/C7TA05571D>.
- [148] W.T. Deng, J. Chen, L. Yang, X.X. Liang, S.Y. Yin, X.L. Deng, G.Q. Zou, H.S. Hou, X.B. Ji, Solid solution metal chalcogenides for sodium-ion batteries: the recent advances as anodes, *Small* 17 (2021) 2101058, <https://doi.org/10.1002/sml.202101058>.
- [149] L. Zhao, C. Gong, X.W. Chen, X. He, H. Chen, X. Du, D.H. Wang, W. Fang, H. J. Zhang, W.X. Li, ZIF-67 derived Mo-CoS₂ nanoparticles embedded in hierarchically porous carbon hollow sphere for efficient overall water splitting, *Appl. Surf. Sci.* 623 (2023) 157030, <https://doi.org/10.1016/j.apsusc.2023.157030>.
- [150] L. Shen, Y.T. Qian, Z. Lyu, D.H. Kim, D.J. Kang, Two-dimensional metal-organic frameworks and their derivative electrocatalysts for water splitting, *Appl. Sci.* 13 (2023) 9343, <https://doi.org/10.3390/app13169343>.
- [151] Z. Li, X.W. Hu, Z.N. Shi, J.L. Lu, Z.W. Wang, MOF-derived iron sulfide nanocomposite with sulfur-doped carbon shell as a promising anode material for high-performance lithium-ion batteries, *J. Alloys Compd.* 868 (2021) 159110, <https://doi.org/10.1016/j.jallcom.2021.159110>.
- [152] F.P. Xiao, X.M. Yang, T.H. Yao, H.K. Wang, A.L. Rogach, Encapsulation of selenium in MOF-derived N,O-codoped porous flower-like carbon host for Na-Se batteries, *Chem. Eng. J.* 430 (2022) 132737, <https://doi.org/10.1016/j.cej.2021.132737>.
- [153] U. Ravon, M.E. Domine, C. Gaudillere, A.D. Chomel, D. Farrusseng, MOFs as acid catalysts with shape selectivity properties, *New J. Chem.* 32 (2008) 937–940, <https://doi.org/10.1039/B803953B>.
- [154] P. Choudhary, S.K. Ola, I. Chopra, V. Dhayal, D.S. Shekhawat, Metal-organic framework (MOF)/graphene-oxide (GO) nanocomposites materials: a potential formulation for anti-corrosive coatings-a review, *Mater. Today Proc.* 79 (2023) 172–178, <https://doi.org/10.1016/j.matpr.2022.09.603>.
- [155] C.Y. Wang, B.Y. Yu, H.F. Fu, P. Wang, C.C. Wang, A mixed valence Tb (III)/Tb (IV) metal-organic framework: crystal structure, luminescence property and selective detection of naproxen, *Polyhedron* 159 (2019) 298–307, <https://doi.org/10.1016/j.poly.2018.11.064>.
- [156] M.K. Kim, S.H. Kim, M.K. Park, S.G. Ryu, H.S. Jung, Degradation of chemical warfare agents over cotton fabric functionalized with UiO-66-NH₂, *RSC Adv.* 8 (2018) 41633–41638, <https://doi.org/10.1039/C8RA06805D>.
- [157] M. Esmailzadeh, A composite prepared from a metal-organic framework of type MIL-101 (Fe) and morin-modified magnetite nanoparticles for extraction and speciation of vanadium (IV) and vanadium (V), *Microchim. Acta* 186 (2019) 14, <https://doi.org/10.1007/s00604-018-3093-y>.
- [158] D.X. Wang, H.Y. He, X.H. Chen, S.Y. Feng, Y.Z. Niu, D.F. Sun, A 3D porous metal-organic framework constructed of 1D zigzag and helical chains exhibiting selective anion exchange, *CrystEngComm* 12 (2010) 1041–1043, <https://doi.org/10.1039/B910988A>.
- [159] L.P. Lopez, Z.A. Castillo, M.C. Munoz, J.A. Real, Clathration of five-membered aromatic rings in the bimetallic spin crossover metal-organic framework [Fe (TPT)₂]/[M^I(CN)₂]₂]. G (M^I = Ag, Au), *Cryst. Growth Des.* 14 (2014) 6311–6319, <https://doi.org/10.1021/cg5010616>.
- [160] W.W. Li, C.C. Zhou, C. Li, W.R. Zhu, J.Q. Shi, G.J. Liu, Synthesis of UiO-66 series metal-organic framework composites and the adsorption effect on gallium, *Chem. Eng. J.* 455 (2023) 140881, <https://doi.org/10.1016/j.cej.2022.140881>.
- [161] C.J. Qu, X.Y. Lv, R.Y. Wang, R.J. Zhang, W.L. Guo, Controllable synthesis of FeMn bimetallic ferrocene-based metal-organic frameworks to boost the catalytic efficiency for removal of organic pollutants, *Environ. Sci. Pollut. Res.* 30 (2023) 17449–17458, <https://doi.org/10.1007/s11356-022-23315-y>.
- [162] P.T. Phan, J.S. Hong, N. Tran, T.H. Le, The properties of microwave-assisted synthesis of metal-organic frameworks and their applications, *Nanomaterials* 13 (2023) 352, <https://doi.org/10.3390/nano13020352>.
- [163] W. Guo, W. Monns, W. Zhang, S. Xie, N. Han, Z.Y. Zhou, N. Chanut, K. Vanstreels, R. Ameloot, X. Zhang, J. Franssaer, Anodic electrodeposition of continuous metal-organic framework films with robust adhesion by pre-anchored strategy, *Microporous Mesoporous Mater.* 350 (2023) 112443, <https://doi.org/10.1016/j.micromeso.2023.112443>.
- [164] R.S. Kumar, S.S. Kumar, M.A. Kulandainathan, Efficient electrosynthesis of highly active Cu₃(BTC)₂-MOF and its catalytic application to chemical reduction, *Microporous Mesoporous Mater.* 168 (2013) 57–64, <https://doi.org/10.1016/j.micromeso.2012.09.028>.
- [165] W.P. Wang, M. Chai, M.Y.B. Zulkifli, K.J. Xu, Y.L. Chen, L.Z. Wang, V. Chen, J. W. Hou, Metal-organic framework composites from a mechanochemical process, *Mol. Syst. Des.* 8 (2023) 560–579, <https://doi.org/10.1039/D2ME00211F>.
- [166] P. Kumari, A. Kareem, P. Jhariat, S.S. Kumar, T. Panda, Phase purity regulated by mechano-chemical synthesis of metal-organic frameworks for the electrocatalytic oxygen evolution reaction, *Inorg. Chem.* 62 (2023) 3457–3463, <https://doi.org/10.1021/acs.inorgchem.2c03609>.
- [167] G. Kaur, P. Kandwal Komal, D. Sud, Sonochemically synthesized Zn (II) and Cd (II) based metal-organic frameworks as fluoroprobes for sensing of 2,6-dichlorophenol, *J. Solid State Chem.* 319 (2023) 123833, <https://doi.org/10.1016/j.jssc.2022.123833>.
- [168] S. Glowinski, B. Szczesniak, J. Choma, M. Jaroniec, Recent developments in sonochemical synthesis of nanoporous metal-organic materials, *Molecules* 28 (2023) 2639, <https://doi.org/10.3390/molecules28062639>.
- [169] H.L. Li, M. Eddaoudi, M.O. Keffe, O.M. Yaghi, Design and synthesis of an exceptionally stable and highly porous metal-organic framework, *Nature* 402 (1999) 276–279, <https://doi.org/10.1038/46248>.
- [170] C. Ajpi, N. Leiva, A. Lundblad, G. Lindbergh, S. Cabrera, Synthesis and spectroscopic characterization of Fe³⁺-BDC metal organic framework as material for lithium ion batteries, *J. Mol. Struct.* 1272 (2023) 134127, <https://doi.org/10.1016/j.molstruc.2022.134127>.
- [171] Z. Dong, W. Hu, H.J. Liu, Z.Z. Yang, D. Moitra, D. Jiang, S. Dai, J.Z. Hu, D. Wu, H. F. Lin, Solvent-treated zirconium-based nanoporous UiO-66 metal-organic frameworks for enhanced CO₂ capture, *ACS Appl. Nano Mater.* 6 (2023) 12159–12167, <https://doi.org/10.1021/acsanm.3c01909>.
- [172] P.P. Long, H.W. Wu, Q. Zhao, Y.X. Wang, J.X. Dong, J.P. Li, Solvent effect on the synthesis of MIL-96(Cr) and MIL-100(Cr), *Microporous Mesoporous Mater.* 142 (2011) 489–493, <https://doi.org/10.1016/j.micromeso.2010.12.036>.
- [173] C.K. Brozek, L. Bellarosa, T. Soejima, T.V. Clark, N. Lopez, M. Dinca, Solvent-dependent cation exchange in metal-organic frameworks, *Chem. Eur. J.* 20 (2014) 6871–6874, <https://doi.org/10.1002/chem.201402682>.

- [174] H. Guo, H. Zhang, N. Wu, Z. Pan, C.L. Li, Y. Chen, Y.J. Cao, W. Yang, Trimesic acid-modified 2D NiCo-MOF for high-capacity supercapacitors, *J. Alloys Compd.* 934 (2023) 167779, <https://doi.org/10.1016/j.jallcom.2022.167779>.
- [175] W.Y. Ren, Y. Wang, J. Wang, R.X. Sun, Hydrothermally synthesized Mo/Zr-MOF photocatalyst for promoting the removal of Cr⁶⁺ under visible light, *Green Mater.* 29 (2023), <https://doi.org/10.1680/jgrma.22.00074>.
- [176] S.A.E. Naser, K.O. Badmus, L. Khotseng, Synthesis, properties, and applications of metal organic frameworks supported on graphene oxide, *Coatings* 13 (2023) 1456, <https://doi.org/10.3390/coatings13081456>.
- [177] X.R. Tang, N. Li, H. Pang, Metal-organic frameworks-derived metal phosphides for electrochemistry application, *Green Energy Environ.* 7 (2022) 636–661, <https://doi.org/10.1016/j.gee.2021.08.003>.
- [178] M. Eddaoudi, J. Kim, N. Rosi, D. Vodak, J. Wachter, M.O. Keffe, O.M. Yaghi, Systematic design of pore size and functionality in isorecticular MOFs and their application in methane storage, *Science* 295 (2002) 469–472, <https://doi.org/10.1126/science.1067208>.
- [179] Y. Qi, F. Luo, Y.X. Che, J. Zheng, Hydrothermal synthesis of metal-organic frameworks based on aromatic polycarboxylate and flexible bis(imidazole) ligands, *Cryst. Growth Des.* 8 (2008) 606–611, <https://doi.org/10.1021/cg700758c>.
- [180] Y.W. Chen, D.F. Lv, J.L. Wu, J. Xiao, H.X. Xi, Q.B. Jia, Z. Li, A new MOF-505@GO composite with high selectivity for CO₂/CH₄ and CO₂/N₂ separation, *Chem. Eng. J.* 308 (2017) 1065–1072, <https://doi.org/10.1016/j.cej.2016.09.138>.
- [181] Z.Y. Li, K.R. Shi, L.Y. Zhai, Z.Z. Wang, H.Y. Wang, Y. Zhao, J.J. Wang, Constructing multiple sites of metal-organic frameworks for efficient adsorption and selective separation of CO₂, *Sep. Purif. Technol.* 307 (2023) 122725, <https://doi.org/10.1016/j.seppur.2022.122725>.
- [182] K. Kamal, M.A. Bustam, M. Ismail, D. Grekov, A.M. Shariff, P. Pre, Optimization of washing processes in solvothermal synthesis of nickel-based MOF-74, *Materials* 13 (2020) 2741, <https://doi.org/10.3390/ma13122741>.
- [183] L.N. Appelhans, L. Hughes, B. McKenzie, M. Rodriguez, J. Griego, J. Briscoe, M. Moorman, E. Frederick, J.B. Wright, Facile microwave synthesis of zirconium metal-organic framework thin films on gold and silicon and application to sensor functionalization, *Microporous Mesoporous Mater.* 323 (2021) 111133, <https://doi.org/10.1016/j.micromeso.2021.111133>.
- [184] R. Gaikwad, S. Gaikwad, Y.H. Kim, S. Han, Electrospun fiber mats with multistep seeded growth of UTSA-16 metal organic frameworks by microwave reaction with excellent CO₂ capture performance, *Microporous Mesoporous Mater.* 323 (2021) 111233, <https://doi.org/10.1016/j.micromeso.2021.111233>.
- [185] J.E. Efome, D. Rana, T. Matsuura, C.Q. Lan, Insight studies on metal-organic framework nanofibrous membrane adsorption and activation for heavy metal ions removal from aqueous solution, *ACS Appl. Mater. Interfaces* 10 (2018) 18619–18629, <https://doi.org/10.1021/acsami.8b01454>.
- [186] S. Gaikwad, S.J. Kim, S. Han, Novel metal-organic framework of UTSA-16 (Zn) synthesized by a microwave method: outstanding performance for CO₂ capture with improved stability to acid gases, *J. Ind. Eng. Chem.* 87 (2020) 250–263, <https://doi.org/10.1016/j.jiec.2020.04.015>.
- [187] W.L. Teo, W.Q. Zhou, C. Qian, Y.L. Zhao, Industrializing metal-organic frameworks: scalable synthetic means and their transformation into functional materials, *Mater. Today* 47 (2021) 170–186, <https://doi.org/10.1016/j.mattod.2021.01.010>.
- [188] L.J. Guo, W. Chen, C.Q. Wang, B. Dong, Application of electrochemically assisted synthesis of MOFs-derived phosphides as catalyst for CH₄-CO₂ reforming, *Int. J. Electrochem. Sci.* 18 (2023) 26–32, <https://doi.org/10.1016/j.ijeoes.2023.01.005>.
- [189] Y. Zhang, N. Li, Y. Xu, M. Yang, X.G. Luo, C.J. Hou, D.Q. Huo, An ultra-sensitive electrochemical aptasensor based on Co-MOF/ZIF-8 nano-thin-film by the in-situ electrochemical synthesis for simultaneous detection of multiple biomarkers of breast cancer, *Microchem. J.* 187 (2023) 108316, <https://doi.org/10.1016/j.microc.2022.108316>.
- [190] N. Campagnol, T.V. Assche, T. Boudewijns, J. Denayer, K. Binnemans, D.D. Vos, J. Franss, High pressure, high temperature electrochemical synthesis of metal-organic frameworks: films of MIL-100 (Fe) and HKUST-1 in different morphologies, *J. Mater. Chem. A* 1 (2013) 5827–5830, <https://doi.org/10.1039/C3TA10419B>.
- [191] A.M. Joaristi, J.J. Alcaniz, P.S. Crespo, F. Kaptejin, J. Gascon, Electrochemical synthesis of some archetypical Zn²⁺, Cu²⁺, and Al³⁺ metal organic frameworks, *Cryst. Growth Des.* 12 (2012) 3489–3498, <https://doi.org/10.1021/cg300552w>.
- [192] Y.X. Liu, Y.N. Wei, M.H. Liu, Y.C. Bai, X.Y. Wang, S.C. Shang, J.Y. Chen, Y.Q. Liu, Electrochemical synthesis of large area two-dimensional metal-organic framework films on copper anodes, *Angew. Chem. Int. Ed.* 60 (2021) 2887–2891, <https://doi.org/10.1002/anie.202012971>.
- [193] M. Adams, M. Kozłowska, N. Baroni, M. Oldenburg, R. Ma, D. Busko, A. Turshatov, G. Emandi, M.O. Senge, R. Halder, C. Woll, G.U. Nienhaus, B. S. Richards, I.A. Howard, Highly efficient one-dimensional triplet exciton transport in a palladium-porphyrin-based surface-anchored metal-organic framework, *ACS Appl. Mater. Interfaces* 11 (2019) 15688–15697, <https://doi.org/10.1021/acsami.9b03079>.
- [194] Y. Zhong, B.R. Cheng, C.B. Park, A. Ray, S. Brown, F. Muijd, J.U. Lee, H. Zhou, J. Suh, K.H. Lee, A.J. Mannix, K.B. Kang, S.J. Sibener, D.A. Muller, J.W. Park, Wafer-scale synthesis of monolayer two-dimensional porphyrin polymers for hybrid superlattices, *Science* 366 (2019) 1379–1384, <https://doi.org/10.1126/science.aax9385>.
- [195] A. Pichon, A.L. Garay, S.L. James, Solvent-free synthesis of a microporous metal-organic framework, *CrystEngComm* 8 (2006) 211–214, <https://doi.org/10.1039/B513750K>.
- [196] M. Klimakow, P. Klobes, K. Rademann, F. Emmerling, Characterization of mechanochemically synthesized MOFs, *Microporous Mesoporous Mater.* 154 (2012) 113–118, <https://doi.org/10.1016/j.micromeso.2011.11.039>.
- [197] P.F. Zhang, H.Y. Li, G.M. Veith, S. Dai, Soluble porous coordination polymers by mechanochemistry: from metal-containing films/membranes to active catalysts for aerobic oxidation, *Adv. Mater.* 27 (2015) 234–239, <https://doi.org/10.1002/adma.201403299>.
- [198] F. Delogu, G. Gorras, A. Sorrentino, Fabrication of polymer nanocomposites via ball milling: present status and future perspectives, *Prog. Mater. Sci.* 86 (2017) 75–126, <https://doi.org/10.1016/j.pmatsci.2017.01.003>.
- [199] D. Braga, S.L. Giffreda, F. Grepioni, A. Pettersen, L. Maini, M. Curzi, M. Polito, Mechanochemical preparation of molecular and supramolecular organometallic materials and coordination networks, *Dalton Trans.* 10 (2006) 1249–1263, <https://doi.org/10.1039/B516165G>.
- [200] T. Friscic, S.L. Childs, S.A.A. Rizvi, W. Jones, The role of solvent in mechanochemical and sonochemical cocrystal formation: a solubility-based approach for predicting cocrystallisation outcome, *CrystEngComm* 11 (2009) 418–426, <https://doi.org/10.1039/B815174A>.
- [201] P.J. Beldon, L. Fabian, R.S. Stein, A. Thirumugan, A.K. Cheetham, T. Friscic, Rapid room-temperature synthesis of zeolitic imidazolate frameworks by using mechanochemistry, *Angew. Chem. Int. Ed.* 49 (2010) 9640–9643, <https://doi.org/10.1002/anie.201005547>.
- [202] Q. Li, Y.W. Tao, S.P. Luo, A.J. Xie, Y. Tu, 3D sulfur and nitrogen doped carbon materials Ni-MOF electrocatalysts for oxygen evolution reaction, *Ionics* 29 (2023) 1077–1087, <https://doi.org/10.1007/s11581-022-04872-1>.
- [203] A. Gowdhaman, S.A. Kumar, D. Elumalai, C. Balaji, M. Sabarinathan, R. Ramesh, M. Navaneethan, Ni-MOF derived NiO/Ni-r-GO nanocomposite as a novel electrode material for high-performance asymmetric supercapacitor, *J. Energy Storage* 60 (2023) 106769, <https://doi.org/10.1016/j.est.2023.106769>.
- [204] M.D. Li, X.Y. Jiang, J.J. Liu, Q. Liu, N.J. Lv, N. Qi, Z.Q. Chen, A flower-like Co/Ni bimetallic metal-organic framework based electrode material with superior performance in supercapacitors, *J. Alloys Compd.* 930 (2023) 167354, <https://doi.org/10.1016/j.jallcom.2022.167354>.
- [205] L.N. Jin, Q. Liu, W.Y. Sun, Room temperature solution-phase synthesis of flower-like nanostructures of [Ni₃(BTC)₂·12H₂O] and their conversion to porous NiO, *Chin. Chem. Lett.* 24 (2013) 663–667, <https://doi.org/10.1016/j.ccllet.2013.05.001>.
- [206] S.Y. Song, X.Y. Ma, W.Y. Li, B.Y. Zhang, B. Shao, X.Y. Chang, X.J. Liu, Novel stylophora coral-like furan-based Ni/Co bimetallic metal organic framework for high-performance capacitive storage and non-enzymatic glucose electrochemical sensing, *J. Alloys Compd.* 931 (2023) 167413, <https://doi.org/10.1016/j.jallcom.2022.167413>.
- [207] R. Zhang, C.A. Tao, R. Chen, L.F. Wu, X.X. Zou, J.F. Wang, Ultrafast synthesis of Ni-MOF in one minute by ball milling, *Nanomaterials* 8 (2018) 1067, <https://doi.org/10.3390/nano8121067>.
- [208] Y.R. Lee, M.S. Jang, H.Y. Cho, H.J. Kwon, S.H. Kim, W.S. Ahn, ZIF-8: a comparison of synthesis methods, *Chem. Eng. J.* 271 (2015) 276–280, <https://doi.org/10.1016/j.cej.2015.02.094>.
- [209] D.Y. Fang, C.L. Liu, Y. Chen, Q.L. Peng, K.G. Wu, Y.X. Chen, H. Jiang, Y. Wu, B. X. Shen, Q.M. Wu, D. Wu, H. Sun, Elucidating and manipulating pressure-induced water intrusion-extrusion in tunable hydrophobic Co/Zn bimetallic ZIFs: roles of pore size and hydrogen bond, *Nano Res.* (2023), <https://doi.org/10.1007/s12274-023-5967-5>.
- [210] T. Friscic, D.G. Reid, I. Halasz, R.S. Stein, R.E. Dinnebier, M.J. Duer, Ion- and liquid-assisted grinding: improved mechanochemical synthesis of metal-organic frameworks reveals salt inclusion and anion templating, *Angew. Chem. Int. Ed.* 49 (2010) 712–715, <https://doi.org/10.1002/anie.200906583>.
- [211] K. Imawaka, M. Sugita, T. Takewaki, S. Tanaka, Mechanochemical synthesis of bimetallic CoZn-ZIFs with sodalite structure, *Polyhedron* 158 (2019) 290–295, <https://doi.org/10.1016/j.poly.2018.11.018>.
- [212] S. Tanaka, T. Nagaoka, A. Yasuyoshi, Y. Hasegawa, J.F.M. Denayer, Hierarchical pore development of ZIF-8 MOF by simple salt-assisted mechanochemistry, *Cryst. Growth Des.* 18 (2018) 274–279, <https://doi.org/10.1021/acs.cgd.7b01211>.
- [213] D.W. Jung, D.A. Yang, J. Kim, J.H. Kim, W.S. Ahn, Facile synthesis of MOF-177 by a sonochemical method using 1-methyl-2-pyrrolidinone as a solvent, *Dalton Trans.* 39 (2010) 2883–2887, <https://doi.org/10.1039/B925088C>.
- [214] J. Kim, S.T. Yang, S.B. Choi, J. Sim, J.H. Kim, W.S. Ahn, Control of catenation in CuTATB-n metal-organic frameworks by sonochemical synthesis and its effect on CO₂ adsorption, *J. Mater. Chem.* 21 (2011) 3070–3076, <https://doi.org/10.1039/C0JM03318A>.
- [215] M.Y. Masoomi, M. Bagheri, A. Morsali, High adsorption capacity of two Zn-based metal-organic frameworks by ultrasound assisted synthesis, *Ultrason. Sonochem.* 33 (2016) 54–60, <https://doi.org/10.1016/j.ultsonch.2016.04.013>.
- [216] X. Zhang, B. Wang, A. Alsalmeh, S.C. Xiang, Z.J. Zhang, B.L. Chen, Design and applications of water-stable metal-organic frameworks: status and challenges, *Coord. Chem. Rev.* 423 (2020) 213507, <https://doi.org/10.1016/j.ccr.2020.213507>.
- [217] L. Feng, K.Y. Wang, E. Joseph, H.C. Zhou, Catalytic porphyrin framework compounds, *Trends Chem.* 2 (2020) 555–568, <https://doi.org/10.1016/j.trechm.2020.01.003>.
- [218] C. Jia, T. He, G.M. Wang, Zirconium-based metal-organic frameworks for fluorescent sensing, *Coord. Chem. Rev.* 476 (2023) 214930, <https://doi.org/10.1016/j.ccr.2022.214930>.
- [219] P. Chen, Y. Wang, X.Q. Zhuang, H.J. Liu, G.G. Liu, W.Y. Lv, Selective removal of heavy metals by Zr-based MOFs in wastewater: new acid and amino

- functionalization strategy, *J. Environ. Sci.* 124 (2023) 268–280, <https://doi.org/10.1016/j.jes.2021.10.010>.
- [220] K.S. Yu, Y.R. Lee, J.Y. Seo, K.Y. Baek, Y.M. Chung, W.S. Ahn, Sonochemical synthesis of Zr-based porphyrinic MOF-525 and MOF-545: enhancement in catalytic and adsorption properties, *Microporous Mesoporous Mater.* 316 (2021) 110985, <https://doi.org/10.1016/j.micromeso.2021.110985>.
- [221] H.Q. Xu, K.C. Wang, M. Ding, D.W. Feng, H.L. Jiang, H.C. Zhou, Seed-mediated synthesis of metal-organic frameworks, *J. Am. Chem. Soc.* 138 (2016) 5316–5320, <https://doi.org/10.1021/jacs.6b01414>.
- [222] F. Israr, D. Chun, Y.M. Kim, D.K. Kim, High yield synthesis of Ni-BTC metal-organic framework with ultrasonic irradiation: role of polar aprotic DMF solvent, *Ultrason. Sonochem.* 31 (2016) 93–101, <https://doi.org/10.1016/j.ultrasonch.2015.12.007>.
- [223] G. Sargazi, D. Afzali, A. Mostafavi, A novel synthesis of a new thorium (IV) metal organic framework nanostructure with well controllable procedure through ultrasound assisted reverse micelle method, *Ultrason. Sonochem.* 41 (2018) 234–251, <https://doi.org/10.1016/j.ultrasonch.2017.09.046>.
- [224] J.W. Ren, X. Dyosiba, N.M. Musyoka, H.W. Langmi, M. Mathe, S. Liao, Review on the current practices and efforts towards pilot-scale production of metal-organic frameworks (MOFs), *Coord. Chem. Rev.* 352 (2017) 187–219, <https://doi.org/10.1016/j.ccr.2017.09.005>.
- [225] A. Li, M.K. Huang, D. Hu, Z. Tang, J.H. Xu, Y. Li, X.W. Zhang, X. Chen, G. Wang, Polydopamine-coated metal-organic framework-based composite phase change materials for photothermal conversion and storage, *Chin. Chem. Lett.* 34 (2023) 107916, <https://doi.org/10.1016/j.ccl.2022.107916>.
- [226] I.M. Honicke, I. Senkovska, V. Bon, I.A. Baburin, N. Bonisch, S. Raschke, J. D. Evans, S. Kaskel, Balancing mechanical stability and ultrahigh porosity in crystalline framework materials, *Angew. Chem. Int. Ed.* 57 (2018) 13780–13783, <https://doi.org/10.1002/anie.201808240>.
- [227] Q.L. Ma, T. Zhang, B. Wang, Shaping of metal-organic frameworks, a critical step toward industrial applications, *Matter* 5 (2022) 1070–1091, <https://doi.org/10.1016/j.matt.2022.02.014>.
- [228] S. Mubarak, D. Dhamodharan, P.N.P. Ghoderao, H.S. Byun, A systematic review on recent advances of metal-organic frameworks-based nanomaterials for electrochemical energy storage and conversion, *Coord. Chem. Rev.* 471 (2022) 214741, <https://doi.org/10.1016/j.ccr.2022.214741>.
- [229] O.K. Farha, I. Eryazici, N.C. Jeong, B.G. Hauser, C.E. Wilmer, A.A. Sarjeant, R. Q. Snurr, S.T. Nguyen, A.O. Yazaydin, J.T. Hupp, Metal-organic framework materials with ultrahigh surface areas: is the sky the limit? *J. Am. Chem. Soc.* 134 (2012) 15016–15021, <https://doi.org/10.1021/ja3055639>.
- [230] A. Kirchon, L. Feng, H.F. Drake, E.A. Joseph, H.C. Zhou, From fundamentals to applications: a toolbox for robust and multifunctional MOF materials, *Chem. Soc. Rev.* 47 (2018) 8611–8638, <https://doi.org/10.1039/C8CS00688A>.
- [231] W. Kukulka, K. Cendrowski, B. Michalkiewicz, E. Mijowska, MOF-5 derived carbon as material for CO₂ absorption, *RSC Adv.* 9 (2019) 18527–18537, <https://doi.org/10.1039/C9RA01786K>.
- [232] J.J. Wang, J.H. Zhao, J. Yang, J. Cheng, Y.Z. Tan, H.H. Feng, Y.C. Li, An electrochemical sensor based on MOF-derived NiO@ZnO hollow microspheres for isoniazid determination, *Microchim. Acta* 187 (2020) 380, <https://doi.org/10.1007/s00604-020-04305-8>.
- [233] T. Segakweng, N.M. Musyoka, J.W. Ren, P. Crouse, H.W. Langmi, Comparison of MOF-5 and Cr-MOF-derived carbons for hydrogen storage application, *Res. Chem. Intermed.* 42 (2016) 4951–4961, <https://doi.org/10.1007/s11164-015-2338-1>.
- [234] R.Z. Rao, S.T. Ma, B. Gao, F.K. Bi, Y.F. Chen, Y. Yang, N. Liu, M.H. Wu, X. D. Zhang, Recent advances of metal-organic framework-based and derivative materials in the heterogeneous catalytic removal of volatile organic compounds, *J. Colloid Interface Sci.* 636 (2023) 55–72, <https://doi.org/10.1016/j.jcis.2022.12.167>.
- [235] S.R. Wu, J.B. Liu, H. Wang, H. Yan, A review of performance optimization of MOF-derived metal oxide as electrode materials for supercapacitors, *Int. J. Energy Res.* 43 (2019) 697–716, <https://doi.org/10.1002/er.4232>.
- [236] F. Yu, X.T. Bae, M.X. Liang, J. Ma, Recent progress on metal-organic framework-derived porous carbon and its composite for pollutant adsorption from liquid phase, *Chem. Eng. J.* 405 (2021) 126960, <https://doi.org/10.1016/j.cej.2020.126960>.
- [237] S.J. Yang, S.H. Nam, T.H. Kim, J.H. Im, H.S. Jung, J.H. Kang, S.G. Wi, B.W. Park, C.R. Park, Preparation and exceptional lithium anodic performance of porous carbon-coated ZnO quantum dots derived from a metal-organic framework, *J. Am. Chem. Soc.* 135 (2013) 7394–7397, <https://doi.org/10.1021/ja311550t>.
- [238] F.C. Zheng, Y. Yang, Q.W. Chen, High lithium anodic performance of highly nitrogen-doped porous carbon prepared from a metal-organic framework, *Nat. Commun.* 5 (2014) 5261, <https://doi.org/10.1038/ncomms5261>.
- [239] X. Sun, Y.F. Li, J. Dou, D. Shen, M.D. Wei, Metal-organic frameworks derived carbon as a high-efficiency counter electrode for dye-sensitized solar cells, *J. Power Sources* 322 (2016) 93–98, <https://doi.org/10.1016/j.jpowsour.2016.05.025>.
- [240] S.K. Park, J.K. Kim, Y.C. Kang, Excellent sodium-ion storage performances of CoSe₂ nanoparticles embedded within N-doped porous graphitic carbon nanocube/carbon nanotube composite, *Chem. Eng. J.* 328 (2017) 546–555, <https://doi.org/10.1016/j.cej.2017.07.079>.
- [241] B.Y. Xia, Y. Yan, N. Li, H.B. Wu, X.W. Lou, X. Wang, A metal-organic framework-derived bifunctional oxygen electrocatalyst, *Nat. Energy* 1 (2016) 15006, <https://doi.org/10.1038/energy.2015.6>.
- [242] A. Aijaz, J. Masa, C. Rosler, W. Xia, P. Weide, A.J.R. Botz, R.A. Fischer, W. Schuhmann, M. Muhler, Co@Co₃O₄ encapsulated in carbon nanotube-grafted nitrogen-doped carbon polyhedra as an advanced bifunctional oxygen electrode, *Angew. Chem. Int. Ed.* 55 (2016) 4087–4091, <https://doi.org/10.1002/anie.201509382>.
- [243] H.Y. Zhao, L. Zhao, Magnetic N-doped Co-carbon composites derived from metal organic frameworks as highly efficient catalysts for p-nitrophenol reduction reaction, *Dalton Trans.* 47 (2018) 3321–3328, <https://doi.org/10.1039/C7DT04272H>.
- [244] M. Zhong, W.W. He, W. Shuang, Y.Y. Liu, T.L. Hu, X.H. Bu, Metal-organic framework derived core-shell Co/Co₃O₄@N-C nanocomposites as high performance anode materials for lithium ion batteries, *Inorg. Chem.* 57 (2018) 4620–4628, <https://doi.org/10.1021/acs.inorgchem.8b00365>.
- [245] W. Tian, H. Hu, Y.X. Wang, P. Li, J.Y. Liu, J.L. Liu, X.B. Wang, X.D. Xu, Z.T. Li, Q. S. Zhao, H. Ning, W.T. Wu, M.B. Wu, Metal-organic frameworks mediated synthesis of one-dimensional molybdenum-based/carbon composites for enhanced lithium storage, *ACS Nano* 12 (2018) 1990–2000, <https://doi.org/10.1021/acsnano.7b09175>.
- [246] Q. Li, P. Xu, W. Gao, S.G. Ma, G.Q. Zhang, R.G. Cao, J.P. Cho, H.L. Wang, G. Wu, Graphene/graphene-tube nanocomposites templated from cage-containing metal-organic frameworks for oxygen reduction in Li-O₂ batteries, *Adv. Mater.* 26 (2014) 1378–1386, <https://doi.org/10.1002/adma.201304218>.
- [247] P.P. Zhao, X. Hua, W. Xu, W. Luo, S.L. Chen, G.Z. Cheng, Metal-organic framework-derived hybrid of Fe₃C nanorod-encapsulated, N-doped CNTs on porous carbon sheets for highly efficient oxygen reduction and water oxidation, *Catal. Sci. Technol.* 6 (2016) 6365–6371, <https://doi.org/10.1039/C6CY01031H>.
- [248] L.J. Kong, C.C. Xie, H.C. Gu, C.P. Wang, X.L. Zhou, J. Liu, Z. Zhou, Z.Y. Li, J. Zhu, X.H. Bu, Thermal instability induced oriented 2D pores for enhanced sodium storage, *Small* 14 (2018) 1800639, <https://doi.org/10.1002/smll.201800639>.
- [249] S.T. Liu, J.S. Zhou, H.H. Song, Tailoring highly N-doped carbon materials from hexamine-based MOFs: superior performance and new insight into the roles of N configurations in Na-ion storage, *Small* 14 (2018) 1703548, <https://doi.org/10.1002/smll.201703548>.
- [250] L.H. Choi, S.Y. Jang, H.C. Kim, S. Huh, In₂S₃ nanoparticle-embedded and sulfur and nitrogen co-doped microporous carbons derived from In(tdc)₂ metal-organic framework, *Dalton Trans.* 47 (2018) 1140–1150, <https://doi.org/10.1039/C7DT03910G>.
- [251] H.X. Li, J.W. Lang, S.L. Lei, J.T. Chen, K.J. Wang, L.Y. Liu, T.Y. Zhang, W.S. Liu, X. B. Yan, A high-performance sodium-ion hybrid capacitor constructed by metal-organic framework-derived anode and cathode materials, *Adv. Funct. Mater.* 28 (2018) 1800757, <https://doi.org/10.1002/adfm.201800757>.
- [252] Y. Xu, W.G. Tu, B.W. Zhang, S.M. Yin, Y.Z. Huang, M. Kraft, R. Xu, Nickel nanoparticles encapsulated in few-layer nitrogen-doped graphene derived from metal-organic frameworks as efficient bifunctional electrocatalysts for overall, *Adv. Mater.* 29 (2017) 1605957, <https://doi.org/10.1002/adma.201605957>.
- [253] H.C. Pang, B.Q. Guan, W.W. Sun, Y. Wang, Metal-organic-frameworks derivation of mesoporous NiO nanorod for high-performance lithium ion batteries, *Electrochim. Acta* 213 (2016) 351–357, <https://doi.org/10.1016/j.electacta.2016.06.163>.
- [254] M.D. Zhang, Q.B. Dai, H. Zheng, M.D. Chen, L.M. Dai, Novel MOF-derived Co@N-C bifunctional catalysts for highly efficient Zn-air batteries and water splitting, *Adv. Mater.* 30 (2018) 1705431, <https://doi.org/10.1002/adma.201705431>.
- [255] Y.J. Chen, S.F. Ji, Y.G. Wang, J.C. Dong, W.X. Chen, Z. Li, R.G. Shen, L.R. Zheng, Z.B. Zhuang, D.S. Wang, Y.D. Li, Isolated single iron atoms anchored on N-doped porous carbon as an efficient electrocatalyst for the oxygen reduction reaction, *Angew. Chem. Int. Ed.* 56 (2017) 6937–6941, <https://doi.org/10.1002/anie.201702473>.
- [256] W.X. Chen, J.J. Pei, C.T. He, J.W. Wan, H.L. Ren, Y. Wang, J.C. Dong, K.L. Wu, W. C. Cheong, J.J. Mao, X.S. Zheng, W.S. Yan, Z.B. Zhuang, C. Chen, Q. Peng, D. S. Wang, Y.D. Li, Single tungsten atoms supported on MOF-derived N-doped carbon for robust electrochemical hydrogen evolution, *Adv. Mater.* 30 (2018) 1800396, <https://doi.org/10.1002/adma.201800396>.
- [257] F. Zou, Y.M. Chen, K.W. Liu, Z.T. Yu, W.F. Liang, S.M. Bhaway, M. Gao, Y. Zhu, Metal organic frameworks derived hierarchical hollow NiO/Ni/graphene composites for lithium and sodium storage, *ACS Nano* 10 (2016) 377–386, <https://doi.org/10.1021/acsnano.5b05041>.
- [258] L.J. Kong, J. Zhu, W. Shuang, X.H. Bu, Nitrogen-doped wrinkled carbon foils derived from MOF nanosheets for superior sodium storage, *Adv. Energy Mater.* 8 (2018) 1801515, <https://doi.org/10.1002/aenm.201801515>.
- [259] K. Zhang, M.H. Park, J. Zhang, G.H. Lee, J.Y. Shin, Y.M. Kang, Cobalt phosphide nanoparticles embedded in nitrogen-doped carbon nanosheets: promising anode material with high rate capability and long cycle life for sodium-ion batteries, *Nano Res.* 10 (2017) 4337–4350, <https://doi.org/10.1007/s12274-017-1649-5>.
- [260] S.W. Liu, X. Zhang, G.Z. Wang, Y.X. Zhang, H.M. Zhang, High-efficiency Co/Co₃S₂@S,N-codoped porous carbon electrocatalysts fabricated from controllably grown sulfur- and nitrogen-including cobalt-based MOFs for rechargeable zinc-air batteries, *ACS Appl. Mater. Interfaces* 9 (2017) 34269–34278, <https://doi.org/10.1021/acsami.7b11101>.
- [261] H. Li, Y. Su, W.W. Sun, Y. Wang, Carbon nanotubes rooted in porous ternary metal sulfide@N/S-doped carbon dodecahedron: bimetal-organic frameworks derivation and electrochemical application for high-capacity and long-life lithium-ion batteries, *Adv. Funct. Mater.* 26 (2016) 8345–8353, <https://doi.org/10.1002/adfm.201601631>.
- [262] X. Li, Q. Sun, J. Liu, B.W. Xiao, R.Y. Li, X.L. Sun, Tunable porous structure of metal organic framework derived carbon and the application in lithium-sulfur batteries, *J. Power Sources* 302 (2016) 174–179, <https://doi.org/10.1016/j.jpowsour.2015.10.049>.

- [263] X.W. Sun, H. Huang, C.P. Wang, Y.Y. Liu, T.L. Hu, X.H. Bu, Effective Co_3S_4 HER electrocatalysts fabricated by in-situ sulfuration of a metal-organic framework, *ChemElectroChem* 5 (2018) 3639–3644, <https://doi.org/10.1002/celec.201801238>.
- [264] A. Tayal, Y. Chen, C.H. Song, S. Hiroi, L.S.R. Kumara, N. Palina, O. Seo, M. Mukoyoshi, H. Kobayashi, H. Kitagawa, O. Sakata, Local geometry and electronic properties of nickel nanoparticles prepared via thermal decomposition of Ni-MOF-74, *Inorg. Chem.* 57 (2018) 10072–10080, <https://doi.org/10.1021/acs.inorgchem.8b01230>.
- [265] P. Ge, H.S. Hou, S. Li, L. Yang, X.B. Ji, Tailoring rod-like FeSe_2 coated with nitrogen-doped carbon for high-performance sodium storage, *Adv. Funct. Mater.* 28 (2018) 1801765, <https://doi.org/10.1002/adfm.201801765>.
- [266] P. Yang, X.L. Song, C.C. Jia, H.S. Chen, Metal-organic framework-derived hierarchical ZnO/NiO composites: morphology, microstructure and electrochemical performance, *J. Ind. Eng. Chem.* 62 (2018) 250–257, <https://doi.org/10.1016/j.jiec.2018.01.002>.
- [267] C.F. Dong, Y.L. Zhou, W. Liu, W. Du, X.T. Zhang, X.Q. Sun, L.T. Kang, X.Y. Zhang, F. Jiang, Zn-Ce based bimetallic organic frameworks derived ZnSe/CeO_2 nanoparticles encapsulated by reduced graphene oxide for enhanced sodium-ion and lithium-ion storage, *J. Alloys Compd.* 875 (2021) 159903, <https://doi.org/10.1016/j.jallcom.2021.159903>.
- [268] X.F. Lu, Y.J. Fang, D. Luan, X.W.D. Lou, Metal-organic frameworks derived functional materials for electrochemical energy storage and conversion: a mini review, *Nano Lett.* 21 (2021) 1555–1565, <https://doi.org/10.1021/acs.nanolett.0c04898>.
- [269] Y. Nishi, The development of lithium ion secondary batteries, *Chem. Rec.* 1 (2001) 406–413, <https://doi.org/10.1002/tcr.1024>.
- [270] T. Chen, J. Wu, Q.L. Zhang, X. Su, Recent advancement of SiO_x based anodes for lithium-ion batteries, *J. Power Sources* 363 (2017) 126–144, <https://doi.org/10.1016/j.jpowsour.2017.07.073>.
- [271] L.Y. Zhu, T.L. Han, Y.Y. Ding, J.W. Long, X.R. Lin, J.Y. Liu, A metal-organic-framework derived $\text{NiFe}_2\text{O}_4/\text{NiCo-LDH}$ nanocube as high-performance lithium-ion battery anode under different temperatures, *Appl. Surf. Sci.* 599 (2022) 153953, <https://doi.org/10.1016/j.apsusc.2022.153953>.
- [272] A. Li, M. Zhong, W. Shuang, C.P. Wang, J. Liu, Z. Chang, X.H. Bu, Facile synthesis of Co_3O_4 nanosheets from MOF nanolates for high performance anodes of lithium-ion batteries, *Inorg. Chem. Front.* 5 (2018) 1602–1608, <https://doi.org/10.1039/C8QI000196K>.
- [273] J. Shao, Z.M. Wan, H.M. Liu, H.Y. Zheng, T. Gao, M. Shen, Q.T. Qu, H.H. Zheng, Metal organic frameworks-derived Co_3O_4 hollow dodecahedrons with controllable interiors as outstanding anodes for Li storage, *J. Mater. Chem. A* 2 (2014) 12194–12200, <https://doi.org/10.1039/C4TA01966K>.
- [274] C.C. Sun, J. Yang, X.H. Rui, W.N. Zhang, Q.Y. Yan, P. Chen, F.W. Huo, W. Huang, X.C. Dong, MOF-directed templating synthesis of a porous multicomponent dodecahedron with hollow interiors for enhanced lithium-ion battery anodes, *J. Mater. Chem. A* 3 (2015) 8483–8488, <https://doi.org/10.1039/C5TA00455A>.
- [275] Y.Z. Han, J. Li, T.Y. Zhang, P.F. Qi, S. Li, X. Gao, J.W. Zhou, X. Feng, B. Wang, Zinc/nickel-doped hollow core-shell Co_3O_4 derived from a metal-organic framework with high capacity, stability, and rate performance in lithium/sodium-ion batteries, *Chem. Eur. J.* 24 (2018) 1651–1656, <https://doi.org/10.1002/chem.201704416>.
- [276] B. Wang, X.Y. Wang, X.Z. Yu, Metal-organic frameworks derived $(\text{Cu}_{0.30}\text{Co}_{0.7})\text{Co}_3\text{O}_4/\text{CuO}$ composite rectangular pyramid grass as high performance anode materials for lithium ion battery, *Electrochim. Acta* 250 (2017) 35–41, <https://doi.org/10.1016/j.electacta.2017.08.029>.
- [277] G. Huang, Q. Li, D.M. Yin, L.M. Wang, Hierarchical porous $\text{Te}/\text{ZnCo}_2\text{O}_4$ nanofibers derived from Te -metal-organic frameworks for superior lithium storage capability, *Adv. Funct. Mater.* 27 (2017) 1604941, <https://doi.org/10.1002/adfm.201604941>.
- [278] J.P. Wang, H. Zhou, M.Z. Zhu, A.H. Yuan, X.P. Shen, Metal-organic framework-derived Co_3O_4 covered by MoS_2 nanosheets for high-performance lithium-ion batteries, *J. Alloys Compd.* 744 (2018) 220–227, <https://doi.org/10.1016/j.jallcom.2018.02.086>.
- [279] L.L. Wu, Z. Wang, Y. Long, J. Li, Y. Liu, Q.S. Wang, X. Wang, S.Y. Song, X.G. Liu, H.J. Zhang, Multishelled $\text{Ni}_3\text{Co}_3\text{O}_4$ hollow microspheres derived from bimetal organic frameworks as anode materials for high-performance lithium-ion batteries, *Small* 13 (2017) 1604270, <https://doi.org/10.1002/smll.201604270>.
- [280] S. Maiti, A. Pramanik, T. Dhawa, M. Sreemany, S. Mahanty, Bi-metal organic framework derived nickel manganese oxide spinel for lithium-ion battery anode, *Mater. Sci. Eng. B* 229 (2018) 27–36, <https://doi.org/10.1016/j.mseb.2017.12.018>.
- [281] G.Y. Zhao, X. Sun, L. Zhang, X. Chen, Y.C. Mao, K. Sun, A self-supported metal-organic framework derived Co_3O_4 film prepared by an in-situ electrochemically assistant process as Li ion battery anodes, *J. Power Sources* 389 (2018) 8–12, <https://doi.org/10.1016/j.jpowsour.2018.04.001>.
- [282] W.B. Zhang, H.C. Pang, W.W. Sun, L.P. Lv, Y. Wang, Metal-organic frameworks derived germanium oxide nanosheets for large reversible Li-ion storage, *Electrochem. Commun.* 84 (2017) 80–85, <https://doi.org/10.1016/j.elecom.2017.09.019>.
- [283] Y.Y. Chen, Y. Wang, X.P. Shen, R. Cai, H.X. Yang, K.Q. Xu, A.H. Yuan, Z.Y. Ji, Cyanide-metal framework derived $\text{CoMoO}_4/\text{Co}_3\text{O}_4$ hollow porous octahedrons as advanced anodes for high performance lithium ion batteries, *J. Mater. Chem. A* 6 (2018) 1048–1056, <https://doi.org/10.1039/C7TA08868J>.
- [284] Y. Xia, B.B. Wang, G. Wang, X.J. Liu, H. Wang, MOF-derived porous $\text{Ni}_3\text{Fe}_3\text{O}_4$ nanotubes with excellent performance in lithium-ion batteries, *ChemElectroChem* 3 (2016) 299–308, <https://doi.org/10.1002/celec.201500419>.
- [285] S.K. Park, J.K. Kim, Y.C. Kang, Electrochemical properties of uniquely structured Fe_2O_3 and FeSe_2 /graphitic-carbon microrods synthesized by applying a metal-organic framework, *Chem. Eng. J.* 334 (2018) 2440–2449, <https://doi.org/10.1002/celec.201500419>.
- [286] M. Zhong, D.H. Yang, L.J. Kong, W. Shuang, Y.H. Zhang, X.H. Bu, Bimetallic metal-organic framework derived Co_3O_4 - CoFe_2O_4 composites with different Fe/Co molar ratios as anode materials for lithium ion batteries, *Dalton Trans.* 46 (2017) 15947–15953, <https://doi.org/10.1039/C7DT03047A>.
- [287] F.C. Zheng, D.Q. Zhu, X.H. Shi, Q.W. Chen, Metal-organic framework-derived porous $\text{Mn}_{1.8}\text{Fe}_{1.2}\text{O}_4$ nanocubes with an interconnected channel structure as high-performance anodes for lithium ion batteries, *J. Mater. Chem. A* 3 (2015) 2815–2824, <https://doi.org/10.1039/C4TA06150K>.
- [288] A. Banerjee, V. Aravindan, S. Bhatnagar, D. Mhamane, S. Madhavi, S. Ogale, Superior lithium storage properties of $\alpha\text{-Fe}_2\text{O}_3$ nano-assembled spindles, *Nano Energy* 2 (2013) 890–896, <https://doi.org/10.1016/j.nanoen.2013.03.006>.
- [289] V. Soundharajan, B. Sambandam, J. Song, S.J. Kim, J.G. Jo, S.H. Kim, S.G. Lee, V. Mathew, J.K. Kim, $\text{Co}_3\text{V}_2\text{O}_8$ sponge network morphology derived from metal-organic framework as an excellent lithium storage anode material, *ACS Appl. Mater. Interfaces* 8 (2016) 8546–8553, <https://doi.org/10.1021/acsami.6b01047>.
- [290] L. Zhang, H.B. Wu, R. Xu, X.W. Lou, Porous Fe_2O_3 nanocubes derived from MOFs for highly reversible lithium storage, *CrystEngComm* 15 (2013) 9332–9335, <https://doi.org/10.1039/C3CE40996A>.
- [291] H. Cao, S. Zhu, C. Yang, R.Q. Bao, L.N. Tong, L.R. Hou, X.G. Zhang, C.Z. Yuan, Metal-organic-framework-derived two-dimensional ultrathin mesoporous hetero- $\text{ZnFe}_2\text{O}_4/\text{ZnO}$ nanosheets with enhanced lithium storage properties for Li-ion batteries, *Nanotechnology* 27 (2016) 465402, <https://doi.org/10.1088/0957-4884/27/46/465402>.
- [292] Z.L. Xiu, M.H. Alfaruqi, J.H. Gim, J. Song, S.J. Kim, T.V. Thi, P.T. Duong, J. P. Baboo, V. Mathew, J.K. Kim, Hierarchical porous anatase TiO_2 derived from a titanium metal-organic framework as a superior anode material for lithium ion batteries, *Chem. Commun.* 51 (2015) 12274–12277, <https://doi.org/10.1039/C5CC03381K>.
- [293] Q. Li, G. Huang, D.M. Yin, Y.M. Wu, L.M. Wang, Synthesis of porous NiO nanorods as high-performance anode materials for lithium-ion batteries, *Part. Part. Syst. Charact.* 33 (2016) 764–770, <https://doi.org/10.1002/ppsc.201600084>.
- [294] H. Li, M. Liang, W.W. Sun, Y. Wang, Bimetal-organic framework: one-step homogenous formation and its derived mesoporous ternary metal oxide nanorod for high-capacity, high-rate, and long-cycle-life lithium storage, *Adv. Funct. Mater.* 26 (2016) 1098–1103, <https://doi.org/10.1002/adfm.201504312>.
- [295] Z.C. Bai, Y.H. Zhang, Y.W. Zhang, C.L. Guo, B. Tang, D. Sun, MOFs-derived porous Mn_2O_3 as high-performance anode material for Li-ion battery, *J. Mater. Chem. A* 3 (2015) 5266–5269, <https://doi.org/10.1039/C4TA06292B>.
- [296] G. Huang, L.L. Zhang, F.F. Zhang, L.M. Wang, Metal-organic framework derived $\text{Fe}_2\text{O}_3/\text{NiCo}_2\text{O}_4$ porous nanocages as anode materials for Li-ion batteries, *Nanoscale* 6 (2014) 5509–5515, <https://doi.org/10.1039/C3NR06041A>.
- [297] K.Z. Cao, L.F. Jiao, H. Xu, H.Q. Liu, H.Y. Kang, Y. Zhao, Y.C. Liu, Y.J. Wang, H. T. Yuan, Reconstruction of mini-hollow polyhedron Mn_2O_3 derived from MOFs as a high-performance lithium anode material, *Adv. Sci.* 3 (2016) 1500185, <https://doi.org/10.1002/advs.201500185>.
- [298] X.D. Xu, R.G. Cao, S.Y. Jeong, J.P. Cho, Spindle-like mesoporous $\alpha\text{-Fe}_2\text{O}_3$ anode material prepared from MOF template for high-rate lithium batteries, *Nano Lett.* 12 (2012) 4988–4991, <https://doi.org/10.1021/nl302618s>.
- [299] B. Liu, X.B. Zhang, H. Shioyama, T. Mukai, T. Sakai, Q. Xu, Converting cobalt oxide subunits in cobalt metal-organic framework into agglomerated Co_3O_4 nanoparticles as an electrode material for lithium ion battery, *J. Power Sources* 195 (2010) 857–861, <https://doi.org/10.1016/j.jpowsour.2009.08.058>.
- [300] Y. Han, M.L. Zhao, L. Dong, J.M. Feng, Y.J. Wang, D.J. Li, X.F. Li, MOF-derived porous hollow Co_3O_4 parallelepipeds for building high-performance Li-ion batteries, *J. Mater. Chem. A* 3 (2015) 22542–22546, <https://doi.org/10.1039/C5TA06205E>.
- [301] D. Tian, X.L. Zhou, Y.H. Zhang, Z. Zhou, X.H. Bu, MOF-derived porous Co_3O_4 hollow tetrahedra with excellent performance as anode materials for lithium-ion batteries, *Inorg. Chem.* 54 (2015) 8159–8161, <https://doi.org/10.1021/acs.inorgchem.5b00544>.
- [302] C. Li, T.Q. Chen, W.J. Xu, X.B. Lou, L.K. Pan, Q. Chen, B.W. Hu, Mesoporous nanostructured Co_3O_4 derived from MOF template: a high-performance anode material for lithium-ion batteries, *J. Mater. Chem. A* 3 (2015) 5585–5591, <https://doi.org/10.1039/C4TA06914E>.
- [303] Y. Li, Y.X. Xu, W.P. Yang, W.X. Shen, H.G. Xue, H. Pang, MOF-derived metal oxide composites for advanced electrochemical energy storage, *Small* 14 (2018) 1704435, <https://doi.org/10.1002/smll.201704435>.
- [304] G.H. Zhang, S.C. Hou, H. Zhang, W. Zeng, F.L. Yan, C.C. Li, H.G. Duan, High-performance and ultra-stable lithium-ion batteries based on MOF-derived ZnO/ZnO quantum dots/C core-shell nanorod arrays on a carbon cloth anode, *Adv. Mater.* 27 (2015) 2400–2405, <https://doi.org/10.1002/adma.201405222>.
- [305] A. Banerjee, U. Singh, V. Aravindan, M. Srinivasan, S. Ogale, Synthesis of CuO nanostructures from Cu-based metal organic framework (MOE-199) for application as anode for Li-ion batteries, *Nano Energy* 2 (2013) 1158–1163, <https://doi.org/10.1016/j.nanoen.2013.04.008>.
- [306] R.B. Wu, X.K. Qian, F. Yu, H. Liu, K. Zhou, J. Wei, Y.Z. Huang, MOF-templated formation of porous CuO hollow octahedra for lithium-ion battery anode materials, *J. Mater. Chem. A* 1 (2013) 11126–11129, <https://doi.org/10.1039/C3TA12621H>.

- [307] G.Z. Fang, J. Zhou, C.W. Liang, A.Q. Pan, C. Zhang, Y. Tang, X.P. Tan, J. Liu, S. Q. Liang, MOFs nanosheets derived porous metal oxide-coated three-dimensional substrates for lithium-ion battery applications, *Nano Energy* 26 (2016) 57–65, <https://doi.org/10.1016/j.nanoen.2016.05.009>.
- [308] Y. Guo, G.H. Qin, E. Liang, M.W. Li, C.Y. Wang, MOFs-derived MgFe_2O_4 microboxes as anode material for lithium-ion batteries with superior performance, *Ceram. Int.* 43 (2017) 12519–12525, <https://doi.org/10.1016/j.ceramint.2017.06.124>.
- [309] M.J. Du, H. Dan, L.Y. Bing, C. Jinxi, Porous nanostructured ZnCo_2O_4 derived from MOF-74: high-performance anode materials for lithium ion batteries, *J. Energy Chem.* 26 (2017) 673–680, <https://doi.org/10.1016/j.jechem.2017.02.001>.
- [310] G. Huang, F.F. Zhang, L.L. Zhang, X.C. Du, J.W. Wang, L.M. Wang, Hierarchical $\text{NiFe}_2\text{O}_4/\text{Fe}_2\text{O}_3$ nanotubes derived from metal organic frameworks for superior lithium ion battery anodes, *J. Mater. Chem. A* 2 (2014) 8048–8053, <https://doi.org/10.1039/C4TA00200H>.
- [311] L. Wang, Y.Z. Han, X. Feng, J.W. Zhou, P.F. Qi, B. Wang, Metal-organic frameworks for energy storage: batteries and supercapacitors, *Coord. Chem. Rev.* 307 (2016) 361–381, <https://doi.org/10.1016/j.ccr.2015.09.002>.
- [312] C.Y. Zhang, J. Dai, P.G. Zhang, S.Y. Zhang, H. Zhang, Y.H. Shen, A. Xie, Porous $\text{Fe}_2\text{O}_3/\text{ZnO}$ composite derived from MOFs as an anode material for lithium ion batteries, *Ceram. Int.* 42 (2016) 1044–1049, <https://doi.org/10.1016/j.ceramint.2015.09.028>.
- [313] X.X. Li, S. Zheng, L. Jin, Y. Li, P.B. Geng, H.G. Xue, H. Pang, Q. Xu, Metal-organic framework-derived carbons for battery applications, *Adv. Energy Mater.* 8 (2018) 1800716, <https://doi.org/10.1002/aenm.201800716>.
- [314] B. Liu, H. Shioyama, T. Akita, Q. Xu, Metal-organic framework as a template for porous carbon synthesis, *J. Am. Chem. Soc.* 130 (2008) 5390–5391, <https://doi.org/10.1021/ja7106146>.
- [315] Z.Q. Xie, Z.Y. He, X.H. Feng, W.W. Xu, X.D. Cui, J.H. Zhang, C. Yan, M.A. Carreon, Z. Liu, Y. Wang, Hierarchical sandwich-like structure of ultrafine N-rich porous carbon nanospheres grown on graphene sheets as superior lithium-ion battery anodes, *ACS Appl. Mater. Interfaces* 8 (2016) 10324–10333, <https://doi.org/10.1021/acsami.6b01430>.
- [316] H.J. Peng, G.X. Hao, Z.H. Chu, Y.W. Lin, X.M. Lin, Y.P. Cai, Porous carbon with large surface area derived from a metal-organic framework as a lithium-ion battery anode material, *RSC Adv.* 7 (2017) 34104–34109, <https://doi.org/10.1039/C7RA05090A>.
- [317] X. Liu, S.C. Zhang, Y. Xing, S.B. Wang, P.H. Yang, H.L. Li, MOF-derived, N-doped porous carbon coated graphene sheets as high-performance anodes for lithium-ion batteries, *New J. Chem.* 40 (2016) 9679–9683, <https://doi.org/10.1039/C6NJ01896C>.
- [318] C. Shen, C.C. Zhao, F.X. Xin, C. Cao, W.Q. Han, Nitrogen-modified carbon nanostructures derived from metal-organic frameworks as high performance anodes for Li-ion batteries, *Electrochim. Acta* 180 (2015) 852–857, <https://doi.org/10.1016/j.electacta.2015.09.036>.
- [319] Y.L. Tong, D. Ji, P. Wang, H. Zhou, K. Akhtar, X.P. Shen, J.H. Zhang, A.H. Yuan, Nitrogen-doped carbon composites derived from 7,7,8,8-tetracyanoquinodimethane-based metal-organic frameworks for supercapacitors and lithium-ion batteries, *RSC Adv.* 7 (2017) 25182–25190, <https://doi.org/10.1039/C7RA02543B>.
- [320] A. Li, Y. Tong, B. Cao, H.H. Song, Z.H. Li, X.H. Chen, J.S. Zhou, G. Chen, H. M. Luo, MOF-derived multifractal porous carbon with ultrahigh lithium-ion storage performance, *Sci. Rep.* 7 (2017) 40574, <https://doi.org/10.1038/srep40574>.
- [321] H.H. Shangguan, W. Huang, C. Engelbrekt, X.W. Zheng, F. Shen, X.X. Xiao, L.J. Ci, P.C. Si, J.D. Zhang, Well-defined cobalt sulfide nanoparticles locked in 3D hollow nitrogen-doped carbon shells for superior lithium and sodium storage, *Energy Storage Mater.* 18 (2019) 114–124, <https://doi.org/10.1016/j.ensm.2019.01.012>.
- [322] R. Tian, Y. Zhou, H. Duan, Y.P. Guo, H. Li, K.F. Chen, D.F. Xue, H.Z. Liu, MOF-derived hollow Co_3S_4 quasi-polyhedron/MWCNT nanocomposites as electrodes for advanced lithium ion batteries and supercapacitors, *ACS Appl. Energy Mater.* 1 (2018) 402–410, <https://doi.org/10.1021/acs.aem.7b00072>.
- [323] W.W. Sun, C. Cai, X.X. Tang, L.P. Lv, Y. Wang, Carbon coated mixed-metal selenide microrod: bimetal-organic-framework derivation approach and applications for lithium-ion batteries, *Chem. Eng. J.* 351 (2018) 169–176, <https://doi.org/10.1016/j.cej.2018.06.093>.
- [324] X. Wang, Y. Chen, Y.J. Fang, J.T. Zhang, S. Gao, X.W. Lou, Synthesis of cobalt sulfide multi-shelled nanoboxes with precisely controlled two to five shells for sodium-ion batteries, *Angew. Chem. Int. Ed.* 58 (2019) 2675–2679, <https://doi.org/10.1002/anie.201812387>.
- [325] D. Sarkar, D. Das, S. Nagarajan, D. Mitlin, Thermally fabricated cobalt telluride in nitrogen-rich carbon dodecahedra as high-rate potassium and sodium ion battery anodes, *Sustain. Energy Fuel* 6 (2022) 3582–3590, <https://doi.org/10.1039/D2SE00267A>.
- [326] S. Gu, Y. Chen, R. Hao, J. Zhao, I. Hussain, N. Qin, M.Q. Li, J.J. Chen, Z.Q. Wang, W. Zheng, Q.M. Gan, Z.Q. Li, H. Guo, Y.Z. Li, K. Zhang, Z.G. Li, Redox of naphthalenediimide radicals in a 3D polyimide for stable Li-ion batteries, *Chem. Commun.* 57 (2021) 7810–7813, <https://doi.org/10.1039/D1CC02426D>.
- [327] F.Y. Cheng, J. Liang, Z.L. Tao, J. Chen, Functional materials for rechargeable batteries, *Adv. Mater.* 23 (2011) 1695–1715, <https://doi.org/10.1002/adma.201003587>.
- [328] X.J. Xu, J. Liu, J.W. Liu, L.Z. Ouyang, R.Z. Hu, H. Wang, L.C. Yang, M. Zhu, A general metal-organic framework (MOF)-derived selenidation strategy for in situ carbon-encapsulated metal selenides as high-rate anodes for Na-ion batteries, *Adv. Funct. Mater.* 28 (2018) 1707573, <https://doi.org/10.1002/adfm.201707573>.
- [329] Z.N. Cao, J. Cui, D.B. Yu, Y. Wang, J.Q. Liu, J.C. Zhang, J. Yan, Y. Zhang, S. H. Sun, Y.C. Wu, Synergistic engineering of architecture and composition in bimetallic selenide@carbon hybrid nanotubes for enhanced lithium- and sodium-ion batteries, *Adv. Funct. Mater.* (2023), <https://doi.org/10.1002/adfm.202306862>.
- [330] J. Jin, Y. Zheng, L.B. Kong, N. Srikanth, Q.Y. Yan, K. Zhou, Tuning ZnSe/CoSe in MOF-derived N-doped porous carbon/CNTs for high-performance lithium storage, *J. Mater. Chem. A* 6 (2018) 15710–15717, <https://doi.org/10.1039/C8TA04425B>.
- [331] L. Yu, J.F. Yang, X.W. Lou, Formation of CoS_2 nanobubble hollow prisms for highly reversible lithium storage, *Angew. Chem. Int. Ed.* 55 (2016) 13422–13426, <https://doi.org/10.1002/anie.201606776>.
- [332] S. Foley, H. Geaney, G. Bree, K. Stokes, S. Connolly, M.J. Zaworotko, K.M. Ryan, Copper sulfide (Cu_2S) nanowire-in-carbon composites formed from direct sulfurization of the metal-organic framework HKUST-1 and their use as Li-ion battery cathodes, *Adv. Funct. Mater.* 28 (2018) 1800587, <https://doi.org/10.1002/adfm.201800587>.
- [333] J. Liu, C. Wu, D.D. Xiao, P. Kopold, L. Gu, P.A.V. Ken, J. Maier, Y. Yu, MOF-derived hollow Co_9S_8 nanoparticles embedded in graphitic carbon nanocages with superior Li-ion storage, *Small* 12 (2016) 2354–2364, <https://doi.org/10.1002/sml.201503821>.
- [334] Q. He, J.S. Liu, Z.H. Li, Q. Li, L. Xu, B.X. Zhang, J.S. Meng, Y.Z. Wu, L.Q. Mai, Solvent-free synthesis of uniform MOF shell-derived carbon confined SnO_2/Co nanocubes for highly reversible lithium storage, *Small* 13 (2017) 1701504, <https://doi.org/10.1002/sml.201701504>.
- [335] R.L. Dai, W.W. Sun, L.P. Lv, M.H. Wu, H. Liu, G.X. Wang, Y. Wang, Bimetal-organic-framework derivation of ball-cactus-like Ni-Sn-P@C-CNT as long-cycle anode for lithium ion battery, *Small* 13 (2017) 2106491, <https://doi.org/10.1002/sml.202106491>.
- [336] D.H. Yang, X.L. Zhou, M. Zhong, Z. Zhou, X.H. Bu, A robust hybrid of SnO_2 nanoparticles sheathed by N-doped carbon derived from ZIF-8 as anodes for Li-ion batteries, *ChemNanoMat* 3 (2017) 252–258, <https://doi.org/10.1002/cnma.201600371>.
- [337] Y.Y. Guo, Q.Q. Zeng, Y. Zhang, Z.F. Dai, H.S. Fan, Y. Huang, W. Zhang, H. Zhang, J. Lu, F.W. Huo, Q.Y. Yan, Sn nanoparticles encapsulated in 3D nanoporous carbon derived from a metal-organic framework for anode material in lithium-ion batteries, *ACS Appl. Mater. Interfaces* 9 (2017) 17173–17178, <https://doi.org/10.1021/acsami.7b04561>.
- [338] Y.T. Zhong, B. Li, S.M. Li, S.Y. Xu, Z.H. Pan, Q.M. Huang, L. Xing, C.S. Wang, W. S. Li, Bi nanoparticles anchored in N-doped porous carbon as anode of high energy density lithium ion battery, *Nano Micro Lett.* 10 (2018) 56, <https://doi.org/10.1007/s40820-018-0209-1>.
- [339] K. Chayambuka, G. Mulder, D.L. Danilov, P.H.L. Notten, Sodium-ion battery materials and electrochemical properties reviewed, *Adv. Energy Mater.* 8 (2018) 1800079, <https://doi.org/10.1002/aenm.201800079>.
- [340] G.Q. Zou, H.S. Hou, P. Ge, Z.D. Huang, G.G. Zhao, D.L. Yin, X.B. Ji, Metal-organic framework-derived materials for sodium energy storage, *Small* 14 (2018) 1702648, <https://doi.org/10.1002/sml.201702648>.
- [341] Y.W. Park, D.S. Shin, S.H. Woo, N.S. Choi, K.H. Shin, S.M. Oh, K.T. Lee, S.Y. Hong, Sodium terephthalate as an organic anode material for sodium ion batteries, *Adv. Mater.* 24 (2012) 3562–3567, <https://doi.org/10.1002/adma.201201205>.
- [342] X.J. Zhang, D.S. Li, G. Zhu, T. Lu, L.K. Pan, Porous CoFe_2O_4 nanocubes derived from metal-organic frameworks as high-performance anode for sodium ion batteries, *J. Colloid Interface Sci.* 499 (2017) 145–150, <https://doi.org/10.1016/j.jcis.2017.03.104>.
- [343] X.J. Zhang, W. Qin, D.S. Li, D. Yan, B.W. Hu, Z. Sun, L.K. Pan, Metal-organic framework derived porous $\text{CuO}/\text{Cu}_2\text{O}$ composite hollow octahedrons as high performance anode materials for sodium ion batteries, *Chem. Commun.* 51 (2015) 16413–16416, <https://doi.org/10.1039/C5CC006924F>.
- [344] Z.S. Hong, M. Kang, X.H. Chen, K.Q. Zhou, Z.G. Huang, M.D. Wei, Synthesis of mesoporous Co^{2+} -doped TiO_2 nanodisks derived from metal organic frameworks with improved sodium storage performance, *ACS Appl. Mater. Interfaces* 9 (2017) 32071–32079, <https://doi.org/10.1021/acsami.7b06290>.
- [345] X.X. Lu, F. Luo, Q.Q. Xiong, H.Z. Chi, H.Y. Qin, Z.G. Ji, L.C. Tong, H.G. Pan, Sn-MOF derived bimodal-distributed SnO_2 nanosphere as a high performance anode of sodium ion batteries with high gravimetric and volumetric capacities, *Mater. Res. Bull.* 99 (2018) 45–51, <https://doi.org/10.1016/j.materresbull.2017.10.040>.
- [346] Y. Guo, Y.Y. Zhu, C. Yuan, C.Y. Wang, MgFe_2O_4 hollow microboxes derived from metal-organic-frameworks as anode material for sodium-ion batteries, *Mater. Lett.* 199 (2017) 101–104, <https://doi.org/10.1016/j.matlet.2017.04.069>.
- [347] X.J. Zhang, M. Wang, G. Zhu, D.S. Li, D. Yan, T. Lu, L.K. Pan, Porous cake-like TiO_2 derived from metal-organic frameworks as superior anode material for sodium ion batteries, *Ceram. Int.* 43 (2017) 2398–2402, <https://doi.org/10.1016/j.ceramint.2016.11.028>.
- [348] G.Z. Fang, J. Zhou, Y.S. Cai, S.N. Liu, X.P. Tan, A.Q. Pan, S.Q. Liang, Metal-organic framework-templated two-dimensional hybrid bimetallic metal oxides with enhanced lithium/sodium storage capability, *J. Mater. Chem. A* 5 (2017) 13983–13993, <https://doi.org/10.1039/C7TA01961K>.
- [349] S.T. Liu, J.S. Zhou, H.H. Song, 2D Zn-hexamine coordination frameworks and their derived N-rich porous carbon nanosheets for ultrafast sodium storage, *Adv. Energy Mater.* 8 (2018) 1800569, <https://doi.org/10.1002/aenm.201800569>.
- [350] G.Q. Zou, H.S. Hou, X.Y. Cao, P. Ge, G.G. Zhao, D. Yin, X.B. Ji, 3D hollow porous carbon microspheres derived from Mn-MOFs and their electrochemical behavior

- for sodium storage, *J. Mater. Chem. A* 5 (2017) 23550–23558, <https://doi.org/10.1039/C7TA08352A>.
- [351] X.D. Shi, Y.X. Chen, Y.Q. Lai, K. Zhang, J. Li, Z. Zhang, Metal organic frameworks templated sulfur-doped mesoporous carbons as anode materials for advanced sodium ion batteries, *Carbon* 123 (2017) 250–258, <https://doi.org/10.1016/j.carbon.2017.07.056>.
- [352] Y.M. Hu, Y.P. Chen, Y. Liu, W.X. Li, M.Y. Zhu, P.F. Hu, H.M. Jin, Y. Li, Accordion-like nanoporous carbon derived from Al-MOF as advanced anode material for sodium ion batteries, *Microporous Mesoporous Mater.* 270 (2018) 67–74, <https://doi.org/10.1016/j.micromeso.2018.04.046>.
- [353] G.Q. Zou, X. Jia, Z.D. Huang, S. Li, H.X. Liao, H.S. Hou, L.P. Huang, X.B. Ji, Cube-shaped porous carbon derived from MOF-5 as advanced material for sodium-ion batteries, *Electrochim. Acta* 196 (2016) 413–421, <https://doi.org/10.1016/j.electacta.2016.03.016>.
- [354] J.M. Fan, J.J. Chen, Q. Zhang, B.B. Chen, J. Zang, M.S. Zheng, Q.F. Dong, An amorphous carbon nitride composite derived from ZIF-8 as anode material for sodium-ion batteries, *ChemSusChem* 8 (2015) 1856–1861, <https://doi.org/10.1002/cssc.201500192>.
- [355] X. Gu, P.C. Dai, L.J. Li, J.Q. Li, D.W. Li, H.Y. Zhang, X.B. Zhao, Porous carbon polyhedrons with high-level nitrogen-doping for high-performance sodium-ion battery anodes, *ChemistrySelect* 1 (2016) 6442–6447, <https://doi.org/10.1002/slct.201601758>.
- [356] C.H. Wang, Y.V. Kaneti, Y. Bando, J.J. Lin, C. Liu, J.S. Li, Y. Yamauchi, Metal-organic framework-derived one-dimensional porous or hollow carbon-based nanofibers for energy storage and conversion, *Mater. Horiz.* 5 (2018) 394–407, <https://doi.org/10.1039/C8MH00133B>.
- [357] W. Zhang, X.F. Jiang, Y.Y. Zhao, A.C. Sanchez, V. Malgras, J.H. Kim, J.H. Kim, S. B. Wang, J. Liu, J.S. Jiang, Y. Yamauchi, M. Hu, Hollow carbon nanobubbles: monocrystalline MOF nanobubbles and their pyrolysis, *Chem. Sci.* 8 (2017) 3538–3546, <https://doi.org/10.1039/C6SC04903F>.
- [358] A. Mahmood, S. Li, Z. Ali, H. Tabassum, B.J. Zhu, Z. Liang, W. Meng, W. Aftab, W. H. Guo, H. Zhang, M. Yousaf, S. Gao, R.Q. Zou, Y.S. Zhao, Ultrafast sodium/potassium-ion intercalation into hierarchically porous thin carbon shells, *Adv. Mater.* 31 (2019) 1805430, <https://doi.org/10.1002/adma.201805430>.
- [359] Y.M. Chen, X.Y. Li, K.S. Park, W. Lu, C. Wang, W.J. Xue, F. Yang, J. Zhou, L. M. Suo, T.Q. Lin, H.T. Huang, J. Li, J.B. Goodenough, Nitrogen-doped carbon for sodium-ion battery anode by self-etching and graphitization of bimetallic MOF-based composite, *Chem* 3 (2017) 152–163, <https://doi.org/10.1016/j.chempr.2017.05.021>.
- [360] J.B. Li, J.L. Li, D. Yan, S.J. Hou, X.T. Xu, T. Lu, Y.F. Yao, W.J. Mai, L.K. Pan, Design of pomegranate-like clusters with NiS₂ nanoparticles anchored on nitrogen-doped porous carbon for improved sodium ion storage performance, *J. Mater. Chem. A* 6 (2018) 6595–6605, <https://doi.org/10.1039/C8TA00557E>.
- [361] Y.Y. Wang, W.P. Kang, D.W. Cao, M.H. Zhang, Z. Kang, Z.Y. Xiao, R.M. Wang, D. F. Sun, A yolk-shelled Co₃S₂/MoS₂-CN nanocomposite derived from a metal-organic framework as a high performance anode for sodium ion batteries, *J. Mater. Chem. A* 6 (2018) 4776–4782, <https://doi.org/10.1039/C8TA00493E>.
- [362] X.Y. Gao, X.J. Zhang, J.L. Jiang, J. Chen, Rod-like carbon-coated MnS derived from metal-organic frameworks as high-performance anode material for sodium-ion batteries, *Mater. Lett.* 228 (2018) 42–45, <https://doi.org/10.1016/j.matlet.2018.05.077>.
- [363] R. Jin, X.F. Li, Y.X. Sun, H. Shan, L.L. Fan, D.J. Li, X.L. Sun, Metal organic frameworks-derived Co₂P@N-C@rGO with dual protection layers for improved sodium storage, *ACS Appl. Mater. Interfaces* 10 (2018) 14641–14648, <https://doi.org/10.1021/acsami.8b00444>.
- [364] Y.S. Cai, G.Z. Fang, J. Zhou, S. Liu, Z.G. Luo, A.Q. Pan, G.Z. Cao, S.Q. Liang, Metal-organic framework-derived porous shuttle-like vanadium oxides for sodium-ion battery application, *Nano Res.* 11 (2018) 449–463, <https://doi.org/10.1007/s12274-017-1653-9>.
- [365] L.M. Zhou, K. Zhang, J.Z. Sheng, Q. An, Z.L. Tao, Y.M. Kang, J. Chen, L.Q. Mai, Structural and chemical synergistic effect of CoS nanoparticles and porous carbon nanorods for high-performance sodium storage, *Nano Energy* 35 (2017) 281–289, <https://doi.org/10.1016/j.nanoen.2017.03.052>.
- [366] W. Huang, H.Y. Sun, H.H. Shangguan, X.Y. Cao, X.X. Xiao, F. Shen, K. Molhave, L. J. Ci, R.C. Si, J.D. Zhang, Three-dimensional iron sulfide-carbon interlocked graphene composites for high-performance sodium-ion storage, *Nanoscale* 10 (2018) 7851–7859, <https://doi.org/10.1039/C8NR00034D>.
- [367] F.X. Bu, P.T. Xiao, J.D. Chen, M.F.A. Aboud, I. Shakir, Y. Xu, Rational design of three-dimensional graphene encapsulated core-shell FeS@carbon nanocomposite as a flexible high-performance anode for sodium-ion batteries, *J. Mater. Chem. A* 6 (2018) 6414–6421, <https://doi.org/10.1039/C7TA11111H>.
- [368] L.T. Yu, J. Liu, X.J. Xu, L.G. Zhang, R.Z. Hu, J.W. Liu, L.Z. Ouyang, L.C. Yang, M. Zhu, Ilmenite nanotubes for high stability and high rate sodium-ion battery anodes, *ACS Nano* 11 (2017) 5120–5129, <https://doi.org/10.1021/acsnano.7b02136>.
- [369] Y.F. Zhang, A.Q. Pan, L. Ding, Z. Zhou, Y.P. Wang, S.Y. Niu, S.Q. Liang, G.Z. Cao, Nitrogen-doped yolk-shell-structured CoSe/C dodecahedra for high-performance sodium ion batteries, *ACS Appl. Mater. Interfaces* 9 (2017) 3624–3633, <https://doi.org/10.1021/acsami.6b13153>.
- [370] S.K. Park, J.K. Kim, Y.C. Kang, Metal-organic framework-derived CoSe₂/(NiCo)Se₂ box-in-box hollow nanocubes with enhanced electrochemical properties for sodium-ion storage and hydrogen evolution, *J. Mater. Chem. A* 5 (2017) 18823–18830, <https://doi.org/10.1039/C7TA05571D>.
- [371] W.N. Ren, H.F. Zhang, C. Guan, C.W. Cheng, Ultrathin MoS₂ nanosheets@metal organic framework-derived N-doped carbon nanowall arrays as sodium ion battery anode with superior cycling life and rate capability, *Adv. Funct. Mater.* 27 (2017) 1702116, <https://doi.org/10.1002/adfm.201702116>.
- [372] X.Y. Liu, F. Zou, K.W. Liu, Z. Qiang, C.J. Taubert, P. Ustiyana, B.D. Vogt, Y. Zhu, A binary metal organic framework derived hierarchical hollow Ni₃S₂/Co₃S₂/N-doped carbon composite with superior sodium storage performance, *J. Mater. Chem. A* 5 (2017) 11781–11787, <https://doi.org/10.1039/C7TA00201G>.
- [373] Y.V. Kaneti, J. Zhang, Y.B. He, Z. Wang, S. Tanaka, M.S.A. Hossain, Z.Z. Pan, B. Xiang, Q.H. Yang, Y. Yamauchi, Fabrication of an MOF-derived heteroatom-doped Co/CoO/carbon hybrid with superior sodium storage performance for sodium-ion batteries, *J. Mater. Chem. A* 5 (2017) 15356–15366, <https://doi.org/10.1039/C7TA03939E>.
- [374] X.L. Ge, Z.Q. Li, L.W. Yin, Metal-organic frameworks derived porous core/shell CoP@C polyhedrons anchored on 3D reduced graphene oxide networks as anode for sodium-ion battery, *Nano Energy* 32 (2017) 117–124, <https://doi.org/10.1016/j.nanoen.2016.11.055>.
- [375] Y.V. Lim, Y. Wang, D.Z. Kong, L. Guo, J.I. Wong, L.K. Ang, H.Y. Yang, Cubic-shaped WS₂ nanopetals on a Prussian blue derived nitrogen-doped carbon nanoporous framework for high performance sodium-ion batteries, *J. Mater. Chem. A* 5 (2017) 10406–10415, <https://doi.org/10.1039/C7TA01821E>.
- [376] S.H. Dong, C.X. Li, X.L. Ge, Z.Q. Li, X.G. Miao, L.W. Yin, ZnS-Sb₂S₃@C core-double shell polyhedron structure derived from metal-organic framework as anodes for high performance sodium ion batteries, *ACS Nano* 11 (2017) 6474–6482, <https://doi.org/10.1021/acsnano.7b03321>.
- [377] W.H. Li, S. Hu, X.Y. Luo, Z.L. Li, X.Z. Sun, M.S. Li, F.F. Liu, Y. Yu, Confined amorphous red phosphorus in MOF-derived N-doped microporous carbon as a superior anode for sodium-ion battery, *Adv. Mater.* 29 (2017) 1605820, <https://doi.org/10.1002/adma.201605820>.
- [378] Z.L. Chen, R.B. Wu, M. Liu, H. Wang, H.B. Xu, Y.H. Guo, Y. Song, F. Fang, X.B. Yu, D.L. Sun, General synthesis of dual carbon-confined metal sulfides quantum dots toward high-performance anodes for sodium-ion batteries, *Adv. Funct. Mater.* 27 (2017) 1702046, <https://doi.org/10.1002/adfm.201702046>.
- [379] G.Q. Zou, J. Chen, Y. Zhang, C. Wang, Z.D. Huang, S.M. Li, H.X. Liao, J.F. Wang, X.B. Ji, Carbon-coated rutile titanium dioxide derived from titanium-metal organic framework with enhanced sodium storage behavior, *J. Power Sources* 325 (2016) 25–34, <https://doi.org/10.1016/j.jpowsour.2016.06.017>.
- [380] Z. Zhang, Y.L. An, X.Y. Xu, C.L. Dong, J.K. Feng, L.J. Ci, S.L. Xiong, Metal-organic framework-derived graphene@nitrogen doped carbon@ultrafine TiO₂ nanocomposites as high rate and long-life anodes for sodium ion batteries, *Chem. Commun.* 52 (2016) 12810–12812, <https://doi.org/10.1039/C6CC07346H>.
- [381] A.Y. Kim, M.K. Kim, K. Cho, J.Y. Woo, Y.H. Lee, S.H. Han, D.J. Byun, W.C. Choi, J. K. Lee, One-step catalytic synthesis of CuO/Cu₂O in a graphitized porous C matrix derived from the Cu-based metal organic framework for Li- and Na-ion batteries, *ACS Appl. Mater. Interfaces* 8 (2016) 19514–19523, <https://doi.org/10.1021/acsami.6b05973>.
- [382] Y. Wang, C.Y. Wang, Y.J. Wang, H.K. Liu, Z. Huang, Superior sodium-ion storage performance of Co₃O₄@nitrogen-doped carbon: derived from a metal-organic framework, *J. Mater. Chem. A* 4 (2016) 5428–5435, <https://doi.org/10.1039/C6TA00236F>.
- [383] Y.S. Cai, H.L. Yang, J. Zhou, Z.G. Luo, G.Z. Fang, S.N. Liu, A.Q. Pan, S.Q. Liang, Nitrogen doped hollow MoS₂/C nanospheres as anode for long-life sodium-ion batteries, *Chem. Eng. J.* 327 (2017) 522–529, <https://doi.org/10.1016/j.cej.2017.06.146>.
- [384] L.Y. Qi, Y.W. Zhang, Z.C. Zuo, Y.L. Xin, C.K. Yang, B. Wu, X.X. Zhang, H.H. Zhou, In situ quantization of ferroelectric oxide embedded in 3D microcarbon for ultrahigh performance sodium-ion batteries, *J. Mater. Chem. A* 4 (2016) 8822–8829, <https://doi.org/10.1039/C6TA01836J>.
- [385] M. Shao, Y.Y. Cheng, T. Zhang, S. Li, W. Zhang, B. Zheng, J.S. Wu, W.W. Xiong, F. W. Huo, J. Lu, Designing MOFs-derived FeS₂@carbon composites for high-rate sodium ion storage with capacitive contributions, *ACS Appl. Mater. Interfaces* 10 (2018) 33097–33104, <https://doi.org/10.1021/acsami.8b10110>.
- [386] T.Q. Chen, X.J. Liu, L.Y. Niu, Y.Y. Gong, C. Li, S.Q. Xu, L.K. Pan, Recent progress on metal-organic framework-derived materials for sodium-ion batteries and, *Inorg. Chem. Front.* 7 (2020) 567–582, <https://doi.org/10.1039/C9QI01268K>.
- [387] Z.L. Jian, W. Luo, X.L. Ji, Carbon electrodes for K-ion batteries, *J. Am. Chem. Soc.* 137 (2015) 11566–11569, <https://doi.org/10.1021/jacs.5b06809>.
- [388] P.T. Xiao, S. Li, C.B. Yu, Y. Wang, Y. Xu, Interface engineering between the metal-organic framework nanocrystal and graphene toward ultrahigh potassium-ion storage performance, *ACS Nano* 14 (2020) 10210–10218, <https://doi.org/10.1021/acsnano.0c03488>.
- [389] Y.P. Li, C.H. Yang, F.H. Zheng, X. Ou, Q.C. Pan, Y.Z. Liu, G. Wang, High pyridine N-doped porous carbon derived from metal-organic frameworks for boosting potassium-ion storage, *J. Mater. Chem. A* 6 (2018) 17959–17966, <https://doi.org/10.1039/C8TA06652C>.
- [390] W. Zhang, X.F. Jiang, X.B. Wang, Y.V. Kaneti, Y.X. Chen, J. Liu, J.S. Jiang, Y. Yamauchi, M. Hu, Spontaneous weaving of graphitic carbon networks synthesized by pyrolysis of ZIF-67 crystals, *Angew. Chem. Int. Ed.* 56 (2017) 8435–8440, <https://doi.org/10.1002/anie.201701252>.
- [391] P.X. Xiong, X.X. Zhao, Y.H. Xu, Nitrogen-doped carbon nanotubes derived from metal-organic frameworks for potassium-ion battery anodes, *ChemSusChem* 11 (2018) 202–208, <https://doi.org/10.1002/cssc.201701759>.
- [392] G.F. Lu, H.L. Wang, Y.L. Zheng, H. Zhang, Y.P. Yang, J. Shi, M.H. Huang, W. Liu, Metal-organic framework derived N-doped CNT@ porous carbon for high-performance sodium- and potassium-ion storage, *Electrochim. Acta* 319 (2019) 541–551, <https://doi.org/10.1016/j.electacta.2019.07.026>.
- [393] S.T. Liu, B.B. Yang, J.S. Zhou, H.H. Song, Nitrogen-rich carbon-onion-constructed nanosheets: an ultrafast and ultrastable dual anode material for sodium and

- potassium storage, *J. Mater. Chem. A* 7 (2019) 18499–18509, <https://doi.org/10.1039/C9TA04699B>.
- [394] J.P. Li, Y.J. Li, X.D. Ma, K. Zhang, J.H. Hu, C.H. Yang, M.L. Liu, A honeycomb-like nitrogen-doped carbon as high-performance anode for potassium-ion batteries, *Chem. Eng. J.* 384 (2020) 123328, <https://doi.org/10.1016/j.cej.2019.123328>.
- [395] H.G. Tong, C.L. Wang, J. Lu, S. Chen, K. Yang, M.X. Huang, Q. Yuan, Q.W. Chen, Energetic metal-organic frameworks derived highly nitrogen-doped porous carbon for superior potassium storage, *Small* 16 (2020) 2002771, <https://doi.org/10.1002/smll.202002771>.
- [396] Q.Y. Yu, J. Hu, B. Wang, Y. Peng, Q. Liu, Y. Li, Fe-induced carbon nanotube/amorphous carbon polyhedral frame for superior potassium storage, *Nanotechnology* 31 (2020) 435406, <https://doi.org/10.1088/1361-6528/aba20f>.
- [397] Y.L. An, Y. Tian, Y. Li, S.L. Xiong, G.Q. Zhao, J.F. Feng, Y.T. Qian, Green and tunable fabrication of graphene-like N-doped carbon on a 3D metal substrate as a binder-free anode for high-performance potassium-ion batteries, *J. Mater. Chem. A* 7 (2019) 21966–21975, <https://doi.org/10.1039/C9TA08721D>.
- [398] X.F. Zhou, L.L. Chen, W.H. Zhang, J.W. Wang, Z.J. Liu, S.F. Zeng, R. Xu, Y. Wu, S. F. Ye, Y.Z. Feng, X.L. Cheng, Z.Q. Peng, X.F. Li, Y. Yu, Three-dimensional ordered macroporous metal-organic framework single crystal-derived nitrogen-doped hierarchical porous carbon for high-performance potassium-ion batteries, *Nano Lett.* 19 (2019) 4965–4973, <https://doi.org/10.1021/acs.nanolett.9b01127>.
- [399] J.F. Ruan, F.J. Mo, Z.L. Chen, M. Liu, S.Y. Zheng, R.B. Wu, F. Fang, Y. Song, D. Sun, Rational construction of nitrogen-doped hierarchical dual-carbon for advanced potassium-ion hybrid capacitors, *Adv. Energy Mater.* 10 (2020) 1904045, <https://doi.org/10.1002/aenm.201904045>.
- [400] Y.C. Liu, B. Huang, L. Zheng, M.Y. Shen, Z.H. Pu, Y. Shao, X.H. Li, S.J. Liao, UIO-66-NH₂-derived mesoporous carbon used as a high-performance anode for the potassium-ion battery, *RSC Adv.* 11 (2021) 1039–1049, <https://doi.org/10.1039/D0RA08808K>.
- [401] Z.B. Liang, Y.X. Wu, J.Q. Cheng, Y.Q. Tang, J.M. Shi, T.J. Qiu, W. Li, S. Gao, R. Q. Zhong, R.Q. Zou, A metal-organic framework nanorod-assembled superstructure and its derivative: unraveling the fast potassium storage mechanism in nitrogen-modified micropores, *Small* 17 (2021) 2100135, <https://doi.org/10.1002/smll.202100135>.
- [402] M.J. Shao, C.X. Li, T. Li, H. Zhao, W.Q. Yu, R.T. Wang, J. Zhang, L.W. Yin, Pushing the energy output and cycling lifespan of potassium-ion capacitor to high level through metal-organic framework derived porous carbon microspheres anode, *Adv. Funct. Mater.* 30 (2020) 2006561, <https://doi.org/10.1002/adfm.202006561>.
- [403] D.J. Li, X.L. Cheng, R. Xu, Y. Wu, X.F. Zhou, C. Ma, Y. Yu, Manipulation of 2D carbon nanolayers with a core-shell structure for high-performance potassium-ion batteries, *J. Mater. Chem. A* 7 (2019) 19929–19938, <https://doi.org/10.1039/C9TA04663A>.
- [404] J.L. Yang, Z.C. Ju, Y. Jiang, Z. Xing, B.J. Xi, J.K. Feng, S.L. Xiong, Enhanced capacity and rate capability of nitrogen/oxygen dual-doped hard carbon in capacitive potassium-ion storage, *Adv. Mater.* 30 (2018) 1700104, <https://doi.org/10.1002/adma.201700104>.
- [405] J. Lu, C.L. Wang, H.L. Yu, S.P. Gong, G.L. Xia, P. Jiang, P.P. Xu, K. Yang, Q. W. Chen, Oxygen/fluorine dual-doped porous carbon nanopolyhedra enabled ultrafast and highly stable potassium storage, *Adv. Funct. Mater.* 29 (2019) 1906126, <https://doi.org/10.1002/adfm.201906126>.
- [406] Y.Q. Zuo, P. Li, R. Zang, S.J. Wang, Z.M. Man, P.X. Li, S. Wang, W. Zhou, Sulfur-doped flowerlike porous carbon derived from metal-organic frameworks as a high-performance potassium-ion battery anode, *ACS Appl. Energy Mater.* 4 (2021) 2282–2291, <https://doi.org/10.1021/acsami.0c02799>.
- [407] G.J. Zheng, Z. Xing, X.R. Gao, C.H. Nie, Z.H. Xu, Z.C. Ju, Fabrication of 2D Cu-BDC MOF and its derived porous carbon as anode material for high-performance Li/K-ion batteries, *Appl. Surf. Sci.* 559 (2021) 149701, <https://doi.org/10.1016/j.apsusc.2021.149701>.
- [408] G.L. Xia, C.L. Wang, P. Jiang, J. Lu, J.F. Diao, Q.W. Chen, Nitrogen/oxygen co-doped mesoporous carbon octahedrons for high-performance potassium-ion batteries, *J. Mater. Chem. A* 7 (2019) 12317–12324, <https://doi.org/10.1039/C8TA12504J>.
- [409] Y.P. Li, W.T. Zhong, C.H. Yang, F.H. Zheng, Q.C. Pan, Y.Z. Liu, G. Wang, X. H. Xiong, M.L. Liu, N/S co-doped carbon microboxes with expanded interlayer distance toward excellent potassium storage, *Chem. Eng. J.* 358 (2019) 1147–1154, <https://doi.org/10.1016/j.cej.2018.10.135>.
- [410] X. Hu, G.B. Zhong, J.W. Li, Y.J. Liu, J. Yuan, J.X. Chen, H.B. Zhan, Z.H. Wen, Hierarchical porous carbon nanofibers for compatible anode and cathode of potassium-ion hybrid capacitor, *Energy Environ. Sci.* 13 (2020) 2431–2440, <https://doi.org/10.1039/D0EE00477D>.
- [411] K.Q. Zhou, R.X. Qiu, Y.C. Zhen, Z.G. Huang, S. Mathur, Z.S. Hong, Vitreum etching-assisted fabrication of porous hollow carbon architectures for enhanced capacitive sodium and potassium-ion storage, *Small* 17 (2021) 2100538, <https://doi.org/10.1002/smll.202100538>.
- [412] B.Y. Wang, Z.W. Deng, Y.T. Xia, J.X. Hu, H.J. Li, H. Wu, Q.B. Zhang, Y. Zhang, H. K. Liu, S.X. Dou, Realizing reversible conversion-alloying of Sb(V) in polyanionic acid for fast and durable lithium- and potassium-ion storage, *Adv. Energy Mater.* 10 (2020) 1903119, <https://doi.org/10.1002/aenm.201903119>.
- [413] Z.H. Sun, Y. Liu, W.B. Ye, J.Y. Zhang, Y.Y. Wang, Y. Lin, L.R. Hou, M.S. Wang, C. Z. Yuan, Unveiling intrinsic potassium storage behaviors of hierarchical nano Bi@N-doped carbon nanocages framework via in situ characterizations, *Angew. Chem. Int. Ed.* 60 (2021) 7180–7187, <https://doi.org/10.1002/anie.202016082>.
- [414] F.X. Zhang, B. Chen, D.L. Chao, Q.F. Gu, B. Johannessen, M. Jaroniec, S. Z. Qiao, Revealing the origin of improved reversible capacity of dual-shell bismuth boxes anode for potassium-ion batteries, *Mater.* 1 (2019) 1681–1693, <https://doi.org/10.1016/j.matt.2019.07.006>.
- [415] S.L. Su, Q. Liu, J. Wang, L. Fan, R.F. Ma, S.H. Chen, X. Han, B.G. Lu, Control of SEI formation for stable potassium-ion battery anodes by Bi-MOF-derived nanocomposites, *ACS Appl. Mater. Interfaces* 11 (2019) 22474–22480, <https://doi.org/10.1021/acsami.9b06379>.
- [416] N. Cheng, J.G. Zhao, L. Fan, Z.M. Liu, S.H. Chen, H.B. Ding, X.Z. Yu, Z.G. Liu, B. G. Lu, Sb-MOFs derived Sb nanoparticles@porous carbon for high performance potassium-ion batteries anode, *Chem. Commun.* 55 (2019) 12511–12514, <https://doi.org/10.1039/C9CC06561J>.
- [417] H.W. Huang, J. Wang, X.F. Yang, R.Z. Hu, J.L. Liu, L. Zhang, M. Zhu, Unveiling the advances of nanostructure design for alloy-type potassium-ion battery anodes via in situ TEM, *Angew. Chem. Int. Ed.* 59 (2020) 14504–14510, <https://doi.org/10.1002/anie.202004193>.
- [418] C.L. Yan, X. Gu, L. Zhang, Y. Wang, L.T. Yan, D.D. Liu, L.J. Li, P.C. Dai, X.B. Zhao, Highly dispersed Zn nanoparticles confined in a nanoporous carbon network: promising anode materials for sodium and potassium ion batteries, *J. Mater. Chem. A* 6 (2018) 17371–17377, <https://doi.org/10.1039/C8TA05297B>.
- [419] G.Y. Ma, C.J. Li, F. Liu, M.K. Majeed, Z.Y. Feng, Y.H. Cui, J. Yang, Y.T. Qian, Metal-organic framework-derived Co_{0.85}Se nanoparticles in N-doped carbon as a high-rate and long-lifespan anode material for potassium ion batteries, *Mater. Today Energy* 10 (2018) 241–248, <https://doi.org/10.1016/j.mtener.2018.09.013>.
- [420] Z.W. Liu, K. Han, P. Li, W. Wang, D.L. He, Q.W. Tan, L.Y. Wang, Y. Li, M.L. Qin, X. H. Qu, Tuning metallic Co_{0.85}Se quantum dots/carbon hollow polyhedrons with tertiary hierarchical structure for high-performance potassium ion batteries, *Nano Micro Lett.* 11 (2019) 96, <https://doi.org/10.1007/s40820-019-0326-5>.
- [421] C.H. Wang, B. Zhang, H.F. Xia, L. Cao, B. Luo, X.M. Fan, J.F. Zhang, X. Ou, Composition and architecture design of double-shelled Co_{0.85}Se_{1-x}S_x@carbon/graphene hollow polyhedron with superior alkali (Li, Na, K)-ion storage, *Small* 16 (2020) 1905853, <https://doi.org/10.1002/smll.201905853>.
- [422] J.H. Chu, W. Wang, Q.Y. Yu, C.Y. Lao, L. Zhang, K. Xi, K. Han, L.D. Xing, L. Song, M. Wang, Y.P. Bao, Open ZnSe/C nanocages: multi-hierarchy stress-buffer for boosting cycling stability in potassium-ion batteries, *J. Mater. Chem. A* 8 (2020) 779–788, <https://doi.org/10.1039/C9TA10088A>.
- [423] C.A. Etogo, H.W. Huang, H. Hong, G.X. Liu, L. Zhang, Metal-organic-frameworks-engaged formation of Co_{0.85}Se@C nanoboxes embedded in carbon nanofibers film for enhanced potassium-ion storage, *Energy Storage Mater.* 24 (2020) 167–176, <https://doi.org/10.1016/j.ensm.2019.08.022>.
- [424] Y.Y. He, L. Wang, C.F. Dong, C.C. Li, X.Y. Ding, Y.T. Qian, L.Q. Xu, In-situ rooting ZnSe/N-doped hollow carbon architectures as high-rate and long-life anode materials for half/full sodium-ion and potassium-ion batteries, *Energy Storage Mater.* 23 (2019) 35–45, <https://doi.org/10.1016/j.ensm.2019.05.039>.
- [425] Y. Hu, T.T. Lu, Y. Zhang, Y.W. Sun, J.L. Liu, D.H. Wei, Z.C. Ju, Q.C. Zhuang, Highly dispersed ZnSe nanoparticles embedded in N-doped porous carbon matrix as an anode for potassium ion batteries, *Part. Syst. Charact.* 36 (2019) 1900199, <https://doi.org/10.1002/ppsc.201900199>.
- [426] J.J. Yuan, W. Liu, X.K. Zhang, Y.H. Zhang, W.T. Yang, W.D. Lai, X.K. Li, J. J. Zhang, X.F. Li, MOF derived ZnSe-FeSe₂/RGO nanocomposites with enhanced sodium/potassium storage, *J. Power Sources* 455 (2020) 227937, <https://doi.org/10.1016/j.jpowsour.2020.227937>.
- [427] T. Yang, J.W. Liu, D.X. Yang, Q. Mao, J.S. Zhong, Y.J. Yuan, X.Y. Li, X. Zheng, Z. G. Ji, H. Liu, G.X. Wang, R.K. Zheng, Bi₂Se₃@C rod-like architecture with outstanding electrochemical properties in lithium/potassium-ion batteries, *ACS Appl. Energy Mater.* 3 (2020) 11073–11081, <https://doi.org/10.1021/acsami.0c02056>.
- [428] A. Mahmood, Z.S. Ali, H. Tabassum, A. Akram, W. Aftab, R. Ali, M.W. Khan, S. Loomba, A. Alluqmani, M.A. Riaz, M. Yousaf, N. Mahmood, Carbon fibers embedded with iron selenide (Fe₃Se₄) as anode for high-performance sodium and potassium ion batteries, *Front. Chem.* 8 (2020) 408, <https://doi.org/10.3389/fchem.2020.00408>.
- [429] J.M. Wang, B.B. Wang, X.J. Liu, J.T. Bai, H. Wang, G. Wang, Prussian blue analogs (PBA) derived porous bimetal (Mn, Fe) selenide with carbon nanotubes as anode materials for sodium and potassium ion batteries, *Chem. Eng. J.* 382 (2020) 123050, <https://doi.org/10.1016/j.cej.2019.123050>.
- [430] S.H. Yang, S.K. Park, Y.C. Kang, MOF-derived CoSe₂@N-doped carbon matrix confined in hollow mesoporous carbon nanospheres as high-performance anodes for potassium-ion batteries, *Nano Micro Lett.* 13 (2021) 9, <https://doi.org/10.1007/s40820-020-00539-6>.
- [431] L. Wang, Q.Q. Jiang, K. Yang, Y.F. Sun, T.F. Zhou, Z.X. Huang, H.J. Yang, J.C. Hu, Self-assembly of carbon nanotubes on a hollow carbon polyhedron to enhance the potassium storage cycling stability of metal organic framework-derived metallic selenide anodes, *J. Colloid Interface Sci.* 601 (2021) 60–69, <https://doi.org/10.1016/j.jcis.2021.05.064>.
- [432] H. Wang, X.K. Qian, H.Y. Wu, R.H. Zhang, R.B. Wu, MOF-derived rod-like composites consisting of iron sulfides embedded in nitrogen-rich carbon as high-performance lithium-ion battery anodes, *Appl. Surf. Sci.* 481 (2019) 33–39, <https://doi.org/10.1016/j.apsusc.2019.03.073>.
- [433] J.P. Xie, Y.Q. Zhu, N. Zhuang, H. Lei, W.L. Zhu, Y. Fu, M.S. Javed, J.L. Li, W. J. Mai, Rational design of metal organic framework-derived FeS₂ hollow nanocages@reduced graphene oxide for K-ion storage, *Nanoscale* 10 (2018) 17092–17098, <https://doi.org/10.1039/C8NR05239E>.
- [434] J.H. Chu, W.A. Wang, J.R. Feng, C.Y. Lao, K. Xi, L.D. Xing, K. Han, Q. Li, L. Song, P. Li, X. Li, Y.P. Bao, Deeply nesting zinc sulfide dendrites in tertiary hierarchical structure for potassium ion batteries: enhanced conductivity from interior to

- exterior, *ACS Nano* 13 (2019) 6906–6916, <https://doi.org/10.1021/acsnano.9b01773>.
- [435] B.L. Rui, J.H. Li, L.M. Chang, H.R. Wang, L. Lin, Y. Guo, P. Nie, Engineering MoS_2 nanosheets anchored on metal organic frameworks derived carbon polyhedra for superior lithium and potassium storage, *Front. Energy Res.* 7 (2019) 142, <https://doi.org/10.3389/fenrg.2019.00142>.
- [436] Y. Han, W.L. Li, K.H. Zhou, X.Y. Wu, H.Y. Wu, X. Wu, Q.F. Shi, G.W. Diao, M. Chen, Bimetallic sulfide $\text{Co}_9\text{S}_8/\text{N-C@MoS}_2$ dodecahedral heterogeneous nanocages for boosted Li/K storage, *ChemNanoMat* 6 (2020) 132–138, <https://doi.org/10.1002/cnma.201900601>.
- [437] W.F. Miao, Y. Zhang, H.T. Li, Z.H. Zhang, L. Li, Z. Yu, W.M. Zhang, ZIF-8/ZIF-67-derived 3D amorphous carbon-encapsulated CoS/NCNTs supported on CoS -coated carbon nanofibers as an advanced potassium-ion battery anode, *J. Mater. Chem. A* 7 (2019) 5504–5512, <https://doi.org/10.1039/C8TA12457D>.
- [438] S.P. Zhang, G. Wang, B.B. Wang, J.M. Wang, J.T. Bai, H. Wang, 3D carbon nanotube network bridged hetero-structured Ni-Fe-S nanocubes toward high-performance lithium, sodium, and potassium storage, *Adv. Funct. Mater.* 30 (2020) 2001592, <https://doi.org/10.1002/adfm.202001592>.
- [439] J.P. Xie, X.D. Li, H.J. Lai, Z.J. Zhao, J.L. Li, W.G. Zhang, W.G. Xie, Y.M. Liu, W. J. Mai, A robust solid electrolyte interphase layer augments the ion storage capacity of bimetallic-sulfide-containing potassium-ion batteries, *Angew. Chem. Int. Ed.* 58 (2019) 14740–14747, <https://doi.org/10.1002/anie.201908542>.
- [440] G.H. Qin, Y.T. Liu, P.Y. Han, F.S. Liu, Q. Yang, C.Y. Wang, Dispersed MoS_2 nanosheets in core shell $\text{Co}_3\text{O}_4/\text{C}$ nanocubes for superior potassium ion storage, *Appl. Surf. Sci.* 514 (2020) 145946, <https://doi.org/10.1016/j.apsusc.2020.145946>.
- [441] Y. Xu, B. Wang, H.R. Wu, R.X. Ti, Z.Z. Chen, $\text{Fe}_{1-x}\text{S}/\text{S}$ -doped carbon nanosheets derived from iron organic framework for high performance potassium-ion batteries anode, *Mater. Lett.* 291 (2021) 129419, <https://doi.org/10.1016/j.matlet.2021.129419>.
- [442] C. Yang, J.R. Feng, Y.L. Zhang, Q.F. Yang, P.H. Li, T. Arlt, F. Lai, J.J. Wang, C. C. Yin, W. Wang, G.Y. Qian, L.F. Cui, W.J. Yang, Y. Chen, I. Manke, Multidimensional integrated chalcogenides nanoarchitecture achieves highly stable and ultrafast potassium-ion storage, *Small* 15 (2019) 1903720, <https://doi.org/10.1002/smll.201903720>.
- [443] W.D. Li, D.Z. Wang, Z.J. Gong, Z.M. Yin, X.S. Guo, J. Liu, C.M. Mao, Z.H. Zhang, G.C. Li, A robust strategy for engineering $\text{Fe}_7\text{S}_8/\text{C}$ hybrid nanocages reinforced by defect-rich MoS_2 nanosheets for superior potassium-ion storage, *ACS Nano* 14 (2020) 16046–16056, <https://doi.org/10.1021/acsnano.0c07733>.
- [444] X.J. Zhang, W.O. Yang, G. Zhu, T. Lu, L.K. Pan, Shuttle-like carbon-coated FeP derived from metal-organic frameworks for lithium-ion batteries with superior rate capability and long-life cycling performance, *Carbon* 143 (2019) 116–124, <https://doi.org/10.1016/j.carbon.2018.11.005>.
- [445] Z.B. Yi, Y. Liu, Y.Z. Li, L.J. Zhou, Z.Y. Wang, J.Q. Zhang, H. Cheng, Flexible membrane consisting of MoP ultrafine nanoparticles highly distributed inside N and P codoped carbon nanofibers as high-performance anode for potassium-ion batteries, *Small* 16 (2020) 1905301, <https://doi.org/10.1002/smll.201905301>.
- [446] X.X. Chen, S.Y. Zeng, H. Muheiyati, Y.J. Zhai, C.C. Li, X.Y. Ding, L. Wang, D. B. Wang, L.Q. Xu, Y.Y. He, Y.T. Qian, Double-shelled Ni-Fe-P/N-doped carbon nanobox derived from a Prussian Blue analogue as an electrode material for K-ion batteries and Li-S batteries, *ACS Energy Lett.* 4 (2019) 1496–1504, <https://doi.org/10.1021/acsenergylett.9b00573>.
- [447] W.F. Miao, X.Y. Zhao, R. Wang, Y.Q. Liu, L. Li, Z.S. Zhang, W.M. Zhang, Carbon shell encapsulated cobalt phosphide nanoparticles embedded in carbon nanotubes supported on carbon nanofibers: a promising anode for potassium ion battery, *J. Colloid Interface Sci.* 556 (2019) 432–440, <https://doi.org/10.1016/j.jcis.2019.08.090>.
- [448] Y.Y. Yi, W. Zhao, Z.H. Zeng, C.H. Wei, C. Lu, Y.L. Shao, W.Y. Guo, S.X. Dou, J. Y. Sun, ZIF-8@ZIF-67-derived nitrogen-doped porous carbon confined CoP polyhedron targeting superior potassium-ion storage, *Small* 16 (2020) 1906566, <https://doi.org/10.1002/smll.201906566>.
- [449] Z.F. Zhang, C.X. Wu, Z.H. Chen, H.Y. Li, H.J. Cao, X.J. Luo, Z. Fang, Y.Y. Zhu, Spatially confined synthesis of a flexible and hierarchically porous three-dimensional graphene/FeP hollow nanosphere composite anode for highly efficient and ultrastable potassium ion storage, *J. Mater. Chem. A* 8 (2020) 3369–3378, <https://doi.org/10.1039/C9TA12191A>.



Narasimharao Kitchamsetti received his Ph.D. from Indian Institute of Technology Indore, India in June 2021. Later, he joined Kyung Hee University as a postdoctoral fellow. Since 2022, he has been working as a postdoctoral researcher at Chungbuk National University in the Department of Engineering Chemistry. His current research interests include design of core-shell heterostructures, MXenes, MOFs, energy storage and environmental applications such as supercapacitors, metal ion batteries, and photocatalytic water treatment.



Jung Sang Cho received his Ph. D. from Interdisciplinary Program for Bioengineering, College of Engineering, Seoul National University, Korea in 2013, and had post-doc experience at the Department of Materials Science and Engineering, Korea University, Korea (2014–2016). He is currently a professor at the Department of Engineering Chemistry, Chungbuk National University, Korea since 2016. His research group works on the development of nanostructured materials for the energy storage, sensor, catalyst, display, and biomaterials. For details, please see the lab website: <https://jjj777.wixsite.com/professor-cho/members>.